Inertial Hysteresis Couplings

by

Charles Michael Wheeler

B.S., University of Colorado at Boulder (2013)
S.M., Massachusetts Institute of Technology (2015)

Submitted to the Department of Mechanical Engineering
in partial fulfillment of the requirements for the degree of

Doctor of Philosophy in Mechanical Engineering

at the

MASSACHUSETTS INSTITUTE OF TECHNOLOGY

June 2023

Author . . . .

Charles M. Wheeler
Department of Mechanical Engineering
May 26, 2023

Certified by . . . .

Martin L. Culpepper
Professor of Mechanical Engineering
Thesis Supervisor

Accepted by . . . .

Nicolas Hadjiconstantinou
Professor of Mechanical Engineering
Chairman, Committee for Graduate Students

Inertial Hysteresis Couplings

by

Charles Michael Wheeler

Submitted to the Department of Mechanical Engineering
on May 26, 2023, in partial fulfillment of the
requirements for the degree of
Doctor of Philosophy in Mechanical Engineering

Abstract

This thesis presents the Inertial Hysteresis Coupling (IHC), a new family of variable-slip mechanical couplings/clutches aimed at achieving order-of-magnitude (∼10x) improvements in torque density (torque capacity / coupling diameter) over existing magnetic and fluid options. IHCs leverage combined normal, frictional, and inertial forces acting on sliding mechanical elements to realize this torque density improvement. The new design (a) allows for continuous modulation of these high-torque loads while (b) naturally achieving lockup at maximum engagement and (c) remaining well-suited to forced-convection cooling in high-heat-dissipation scenarios. Additionally, the base IHC design can be modified to achieve "one-way clutching" behavior while still retaining the ability to speed-synchronize (transmit load under partial slip) and achieve lockup. These characteristics make IHCs particularly well-suited to automotive and mobile robotics applications – for example, active control of vehicle differential slip – where high torque density and slip control are both of critical importance.

As the first investigation into IHCs, this research establishes multiple important foundations for analysis, simulation, and design. Starting from first principles, a ground-up model for IHC behavior is derived that encapsulates IHC geometry, relevant coordinate systems/transformations, kinematics, equilibrium equations, thermal loads, *etc.* Implemented in MATLAB, this model facilitates the selection of IHC parameters via performance projections, sensitivity studies, and a variety of different visualizations and animations. These tools enabled the design and fabrication of a physical IHC prototype, "ihcBENCH." Through testing of this prototype, the key desired behaviors were successfully demonstrated: linear torque modulation via control of the "clutch angle" β_O (max slip torque before lockup = 13.2 Nm, max/min slip torque ratio = 3.8, $R^2 = 0.986$); IHC lockup at high clutch engagement angles ($\beta_O \gtrapprox 37°$); and the one-way clutching behaviors previously described.

Thesis Supervisor: Martin L. Culpepper
Title: Professor of Mechanical Engineering

Acknowledgments

First, I would like to thank my advisor, Professor Martin Culpepper, who has supported me in endless ways throughout my time at MIT. I am incredibly fortunate to have had so many opportunities to learn from him – not only as an engineer, but as a researcher, teacher, manager, writer, presenter, and friend. His support has never wavered and this project would never have been possible without his trust and patience along the way. Although my time as a graduate student is ending, I still feel I have so much I could learn from him. I hope I will have many opportunities to do so in the future!

Second, my thesis committee members, Professor Warren Seering and Professor J. Kim Vandiver, have played vital roles in the success of this project. Finding the right committee members is crucial (especially for high-risk projects) and it's quite apparent that I could not have made better choices. Their questions, recommendations, and guidance have been invaluable for helping me navigate around many different pitfalls, and their continued enthusiasm provided me with the confidence needed to overcome every setback.

Next I would like to thank Dr. Timothy McFarland, my piano teacher throughout my time here in Cambridge. Not only has he been a great friend to me, but he has continued to guide me on this joyous path outside the "dayjob" of engineering. I am continually reminded – in the best kind of way – that "Life is a journey, not a destination."

Without many of my undergrad professors from CU Boulder I would have been neither prepared for, nor aware of, the path through graduate school. Most of all I would like to thank Professor Mark Rentschler, who went out of his way to encourage me on this journey – in addition to being an exceptional advisor, professor, and mentor. I would never have considered this route without him and owe him many thanks for his support and encouragement. Second, I owe a great deal to Professor Adam Norris, from whom I learned vector calculus and numerical methods (MATLAB). Almost all of this thesis relies on material from his courses in one way or another. It is no exaggeration to say that this project would never have been possible without the positive experiences and educational foundation I received from him. I would also like to especially thank Professors Wayne Ambler, Christopher Bell, Scott Bunch, Leland Giovannelli, Jean Hertzberg, Jeffrey Knutsen, Daria Kotys-Schwartz, and Derek Reamon, who have each taught me so much (both technical and otherwise) and given me lifelong memories and inspiration. As I will say so many times in these paragraphs, each of them has been a great friend to me.

To my labmates at MIT, especially Aaron Ramirez, Marcel Thomas, and Lauren Chai – I am so thankful to have had your comradeship during the Masters and PhD journeys. There would have been no way to make it through these experiences alone, and I could not have asked for anyone better to be there along the way. Thank you also to the many other past labmates, including Paula Countouris, Rachel Dias Carlson, Lucy Du, Brandon Evans, Jonathan Monti, and Joshua Nation for your friendship and many positive memories. To my newer labmates – Jesse de Alva, Luke Hardy, Alejandro Martinez, Jorge Nin, and Laura Rosado – although we did not have much overlap, you have been so kind to me, and I wish you all the best of luck in all your future endeavors.

There are so many folks at MIT who simply cannot be replaced – first and foremost are Saana McDaniel, Leslie Regan, and Una Sheehan, who are nothing short of heroes in my eyes. They repeatedly move heaven and earth to help everyone who needs it. Attempting to provide even a partial list of things they've made possible would only do them a disservice. MIT's motto *"Mens et Manus"* means "Mind and Hand" – perhaps the department could consider adopting a similar motto to reflect how steadily they've held us all up in their hands?

I would like to thank Sarah Gallaher, our lab admin for a number of years, who helped with so many aspects of research, teaching, and life as a graduate student. I would similarly like to thank Doug Foley who was recently passed this torch. Special thanks goes to Norma Ellis from Facilities, whose warm greetings during evening rounds always brightened my spirits and became a highlight of my time spent in lab.

Paul Carson and Dan Gilbert – expert machinists, mentors, and friends – made this project's prototyping elements possible. They guided me safely through countless hours of machining and ran multiple critical

CNC-machined parts, all while enduring my shop banter.

To the many friends I've made at MIT, each of you has given me treasured memories. Given our many various activities, my life would not be the same without you. In particular I'd like to thank: Raghav Aggarwal, Murthy Arelekatti, Peter Ascoli, Sabrina Ball, John Bell, Brij Bhushan, Michael Buchman, Lauren Chai, Brandon Chalifoux, Peter Chamberlain, Cecile Chazot, Phillip Daniel, Dan Dorsch, Lucy Du, Brandon Evans, Margaux Filippi, Amit Gandhi, Abe Gertler, Jamison Go, Maha Haji, Tyler Hamer, Yiou He, Greg Izatt, Jacob Izraelevitz, Mallory Jensen, Hilary Johnson, Robert Katzschmann, Philippe Kirschen, Ina Kundu, David Larson, Bethany Lettiere, Richard Li, Janille Maragh, John Mayo, Chris Merian, Sara Nagelberg, Joshua Nation, Scott Nill, Nigel Kojimoto, Larissa Nietner, Colm O'Rourke, Tyler Olsen, Max Opgenoord, Derek Paxson, Nina Petelina, John Peurifoy, Victor Prost, Shabnam Raayai, Aaron Ramirez, Joao Ramos, John Romanishin, Joseph Sandt, Joao Seixas de Medeiros, Sahil Shah, Kevin Simon, Jay Sircar, Sydney Sroka, Dale Thomas, Marcel Thomas, Albert Wang, Joshua Wiens, Natasha Wright, Shawn Zhang, and Rebecca Zubajlo.

I have been so lucky to have many lifelong friends outside of MIT who make life so very bright. Thank you especially to Shane and Natasha Butler, Dillon Campbell, Antony Chung, Matt Crane, Brad Crummy, Jeff Erbert, Jake Johnson, Cliff & Anette Lewis, Matt Samperi, Zack Stein, Bryce Suchomel, Anthony Vanicek, and Dylan Westbrook.

To my parents – how could I possibly capture my thanks in such a short space? The person I am today was nurtured by your boundless love, support, and kindness. You have always believed in me, no matter the circumstances. And in return, all you ever asked was that I be honest and try my best. I am thankful every day to have you as my parents!

Finally, and most of all, I would like to thank my partner, Jean Sack. Words cannot express how deeply I appreciate everything you have done for me over the last 10 years. Truly there is no one who can match your unwavering patience, compassion, and excitement for life. None of this would be remotely possible without you – many, many times over. Together, there is no hurdle we cannot overcome!

Contents

THIS PAGE INTENTIONALLY LEFT BLANK

List of Figures

THIS PAGE INTENTIONALLY LEFT BLANK

List of Tables

Table of Most Important Variables

$\boldsymbol{\beta_O}$	The IHC clutch angle. The tilt of the Orbit ring which modulates engagement between the Planet and Orbit.
$\boldsymbol{\beta_P}$	The Planet shape parameter (which cannot be changed once fabricated).
$\boldsymbol{\theta}$	Angular position about the global X axis. The subscript indicates the relevant component being referred to: *i.e.* $\theta_P/\theta_O/\theta_S$ indicates Planet/Orbit/Satellite, respectively. Relative positions are indicated with a pair of subscripts – for example, $\theta_{OP} = \theta_P - \theta_O$.
$\boldsymbol{\omega}$	Angular velocity about the global X axis. Subscript rules are the same as for θ.
$\boldsymbol{\omega_{OP}}$	The "slip rate." The difference in angular velocity between the Planet and Orbit.

Chapter 1

Introduction & Background

1.1 Thesis Motivation, Goals, and Outline

This research introduces a new type of mechanical coupling – the Inertial Hysteresis Coupling (IHC), for which a prototype is pictured in Figure 1-1. The IHC is a variable-slip coupling/clutch that aims to achieve similar functionality to existing magnetic and fluid options, but with substantially greater torque capacity and the in-built capacity to attain full lockup (zero slip). IHCs seek to enable widespread use of torque-dense variable-slip couplings in robotics and vehicle applications where the size and weight of existing variable-slip couplings makes their use prohibitive. IHCs achieve their improved torque density by harnessing normal and frictional forces developed between sliding contact surfaces between rigid mechanical components; peak torque is therefore limited by material strength rather than fluid or magnetic properties. Compared to existing magnetic/fluid couplings, this suggests potential torque density improvements of 2-10x or more (vs. existing options) with continued IHC development.

The IHC concept is a major departure from the design of any existing coupling, so no prior framework exists to model or design IHCs. This thesis lays the foundation for this framework by addressing a wide variety of both theoretical and practical considerations. It lays the groundwork for modeling, simulation, and design of IHCs, and concludes with validation testing that demonstrates the real-world behavior of a physical prototype. Unless specified otherwise, all of the modeling, simulation, design, and fabrication/testing frameworks presented in this document were developed from the ground-up by the author to fulfill the project goals. The contributions are organized into seven chapters:

- **Chapter 1** discusses the existing landscape of couplings, including their performance metrics (particularly torque density) and operating characteristics. It is shown that compact, high-torque-density, variable-slip couplings do not currently exist; this niche is the target

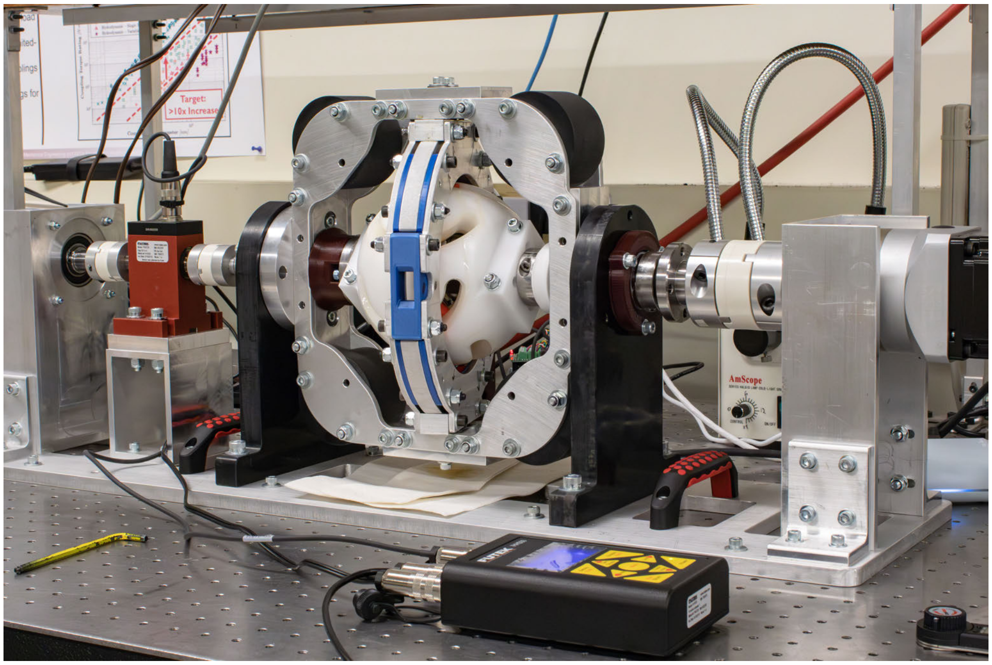

Figure 1-1 – Photograph of ihcBENCH, the prototype Inertial Hysteresis Coupling test system developed as part of this research.

for IHC development. Key impact areas that could benefit from such a coupling are presented, with a particular focus on vehicle and mobile robotics applications.

- **Chapter 2** lays out the operating principles behind IHCs using a series of "toy examples." IHC motion is easiest to understand via in-person observation or with video; with text and static images this is more difficult. This chapter attempts to bridge this "visualization gap" to convey the behavior of IHCs using several examples. Finally, a basic "damper model" is introduced, by which the performance of several coupling types can be described (mathematically). The chapter concludes with the introduction of IHC characteristic maps which, similar to pump charts, describe an IHC's torque/speed relationship across its full operating envelope. The most important goal of the modeling in Chapters 3 and 4 will be to produce characteristic maps such as these.
- **Chapter 3** lays the foundation for the mathematical analysis of IHCs, with a specific focus on geometry and kinematics. It includes definitions for coordinate systems, coordinate transforms, parameterized IHC geometries, the setup of the kinematics model, and solution process for the kinematics model.
- **Chapter 4** builds on Chapter 3 to arrive at the IHC characteristic map and various other parameters of interest (contact forces, energy dissipation, and sensitivity studies). In this chapter, the equilibrium equations are solved and the interal forces of the IHC determined.

- **Chapter 5** introduces ihcBENCH, an instrumented prototype IHC designed for the testing and validation of the concepts introduced in the earlier chapters of this thesis. Discussion includes design considerations for IHC components (Planet/Orbit/Satellites), the test system layout, constraint & degrees-of-freedom, actuation, electronics, and software.
- **Chapter 6** presents results from the testing of ihcBENCH, including successful demonstrations of torque modulation and coupling lockup.
- **Chapter 7** concludes the thesis and makes recommendations for both immediate and long-term future work.

1.2 Summary of Research Contributions

Several of the most important research contributions made are summarized in Figure 1-2.

Concept Synthesis	• IHC Synthesis • Determine degrees of freedom / constraint / actuation • Identify key opportunities (torque density, overload protection)
Mathematical Modeling	• Mathematical descriptions of geometry & motion • Definitions for coordinate frames & coordinate transforms • Deterministic approach for solving kinematics • Derivation of equilibrium equations incl. friction
Simulation Package	• Comprehensive MATLAB implementation of analytical models • Estimates vibration, wear, & thermal effects • Presents instantaneous and time-averaged results • Numerous visualizations & animations to aid communication
Test System Design	• Identify concerns for manufacturability & assembly • Major design, fabrication, assembly, and testing takeaways
Validation Testing	• Prove working principle via operation • Validation of analytical and numerical models • Observe important expected & unexpected behaviors

Figure 1-2 – Summary of key research contributions.

1.3 Background: Rotary Couplings

1.3.1 What is a Rotary Coupling?

A rotary coupling (or more simply, a **coupling**) is a mechanical device which connects two pieces of rotating equipment and enables the transmission of torque between them. Couplings date back to ancient times – primitive universal joints are known to have existed in Greece at least as early as 300 BCE [1]. Today, couplings are ubiquitous and some variant can be found in nearly every machine, from office printers, bicycles, and automobiles to steel mills, industrial pumps, and heavy-duty conveyor systems. The humble coupling fulfills the often-overlooked, yet crucial role of connecting rotating parts in the modern mechanical world. If a machine has a motor or engine, there's a good chance it also has at least one coupling. A variety of different examples can be seen in Figure 1-3.

In operation, a coupling transmits torque between two mechanical connections: its "input" and "output," which are connected to the power source and mechanical load, respectively. Here, the terms "input" and "output" indicate the direction of instantaneous torque transmission. Torque transmission is often unidirectional, though this is not always the case. In many applications torque may "flow" in either direction depending on the immediate circumstances. For example, when an electric vehicle utilizes regenerative braking, its wheels briefly become the torque inputs and back-drive their motor(s) for energy recovery (most of the time, power flows the other way – out from the motors to the wheels).

Aside from transmitting torque, couplings provide several other high-level benefits, of which many are listed in Table 1.1. Of particular interest is *clutching,* where torque transmission can be modulated or interrupted entirely (the clutch in an automobile transmission is one very common example). The benefits of clutching are discussed in more detail in Section 1.5.2.

Couplings play particularly crucial roles in industrial applications, where the large loads, inertias, and energies involved necessitate paying special attention to the mechanical connections between equipment. Example applications include: misalignment couplings for motors; hoist clutches for cranes; torque-limiting couplings for roller tension control in metal-forming processes; overrunning clutches for marine drives; safety couplings for conveyor systems; tension control in filament manufacture; fluid couplings for smooth startup of heavy equipment (*e.g.* electrical generators); and many others [8].

Table 1.1 – Several Important Benefits of Using Couplings

Clutching	Torque transmission can be engaged, disengaged, and/or modulated.
Modularity	A wide variety of off-the-shelf parts can be mated together.
Serviceability	Installation, assembly, and maintenance of any connected equipment can be performed swiftly and easily.
Compensation	Errors in the alignment and positioning of connected equipment (parallel, angular, and/or axial misalignment) can be accommodated.
Isolation	Loads *other than the desired driving torque* can be isolated. Torsional vibration can also be mitigated via built-in compliance and damping.
Motion	Driveshafts can transmit uninterrupted torque despite changing their positions or orientations (for example, constant-velocity joints on front-wheel-drive automobiles).
Safety	Protecting against overload, undesired reverse rotation, and/or system runaway.

(a) Photo [2] of a mountain bike freehub, whose ratcheting gear-and-pawl mechanism lets the rear wheel spin when the rider is not pedaling.

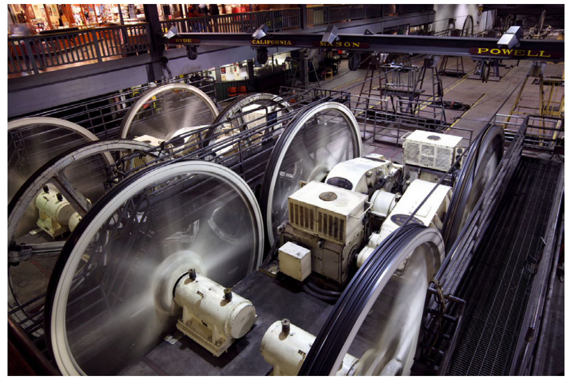

(b) Photo [3] of the San Francisco Cable Car "Power House," overhauled with new gearboxes and flexible gear couplings as of 2019.

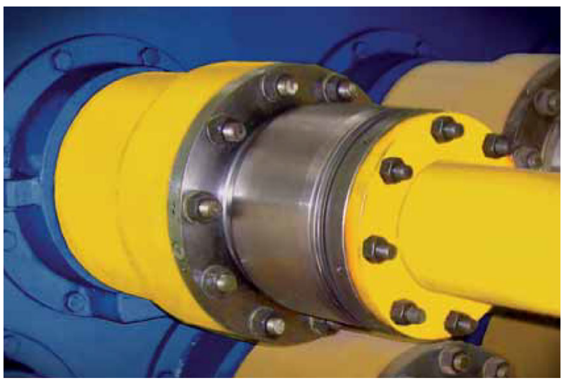

(c) Photo [4] of a coupling driving a leveler machine in a hot strip steel mill. The coupling does not slip or clutch on/off in normal operation, but incorporates anti-overload emergency disconnect functionality.

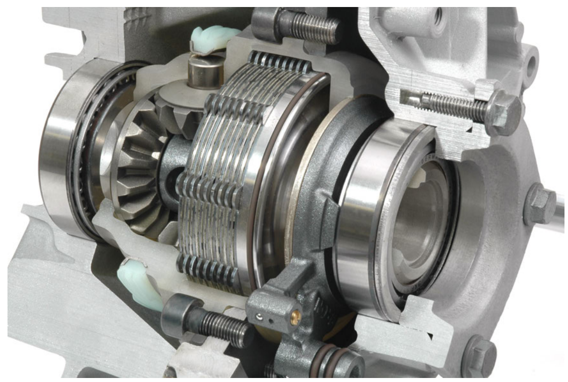

(d) Cutaway [5] of an automobile electronically-operated limited-slip differential. Computer-controlled friction clutch packs actively redistribute power between the vehicle's left and right wheels, enhancing the vehicle's traction control, stability control, and torque-vectoring capabilities.

(e) Photo [6] of an excavator wheel driven through a hydrodynamic (fluid) coupling at an open-pit lignite mine.

(f) Photo [7] of a magnetic coupling (with its protective shroud removed) driving a $\sim$120 kW water pump at a power plant.

Figure 1-3 – Common Couplings & Applications

1.4 Important Definitions

Certain terminology will be frequently used to discuss couplings and their characteristics – see Table 1.2.

1.5 Coupling Modes and the Tradeoff Between Versatility & Torque Capacity

Arguably the most important decision to be made when selecting a coupling is choosing whether clutching capability is needed. Must the coupling be capable of fully engaging and fully disengaging torque transmission? Must it be capable of running partially engaged? Must it be able to actively moderate torque by continuously varying the level of engagement? Ideally the choice of whether to select a clutching coupling would be straightforward – as simple as "ticking a box on the options sheet." In practice this is not so easy. Couplings are usually designed from the ground-up around their intended clutching behavior (or lack thereof). As a result, the choice of coupling "Mode Type" imposes constraints onto nearly every other performance characteristic. This thesis classifies couplings into three categories based on their clutching/non-clutching behavior: Single-Mode, Dual-Mode, and Variable-Mode, as described in Table 1.3.

1.5.1 Mode Type and Torque Density

After Mode Type, two of the most important metrics of coupling performance are torque capacity and size. These values, when combined, give a measure of a coupling's "torque density." Torque density is essentially a measure of volumetric efficiency, *i.e.* how effectively a coupling transmits torque given the packaging space afforded to it. As part of this research, several industrial couplings from a variety of manufacturers were surveyed and their torque densities compared. The results – plotted in Figures 1-4 and 1-5 – show clear performance stratification between different coupling types. Several important observations can be made:

- At a given size, single-mode mechanical couplings drastically out-perform dual-mode friction couplings and achieve $\sim 10x$ higher torque. In turn, dual-mode friction couplings drastically out-perform variable-mode couplings, again by a factor of $\sim 10x$. The torque capacity gap between single-mode and variable-mode couplings of the same size is a substantial $\sim 100x$. **This factor is so large that it cannot be ignored; a particular application must demonstrate critical need for variable-mode operation to justify the selection of such a coupling, given the magnitude of this performance gap.**
- At a given torque level, single-mode mechanical couplings are $\sim 1/2$ the diameter of equally-rated dual-mode friction couplings, which are themselves $\sim 1/2$ the diameter of equally-rated variable-mode couplings. **Single-mode couplings are roughly $\sim 1/4$ the**

Table 1.2 – Important Coupling Terminology

(Dis)engage	Used in this thesis as shorthand for "engage/disengage."
Speed	For couplings, speed refers to rate-of-rotation and can be used to describe a single coupling shaft, the coupling as a whole, *etc.* Speed is an absolute value so it is always positive.
Clutch	The ability to (dis)engage torque transmission and/or actively modulate the slip rate. Can also refer to a coupling that exhibits this ability.
Input	The side of a coupling from which net energy flows in.
Output	The side of a coupling from which net energy flows out.
Operating Point	The steady-state behavior of a coupling under a given set of conditions. Typical "inputs" are the level of coupling engagement and coupling slip speed, while the "output" is the transmitted torque.
Slip	A phenomenon where the input and output rotate at different speeds. Note that slip is distinct from backlash/slop.
Speed Ratio	The steady-state Output Speed divided by the Input Speed. If the speeds differ, the Input is considered to be the faster component, so this ratio ranges from $[0, 1]$. *If the Speed Ratio is* 10%, *the output speed is* 10% *of the input speed.*
Slip Rate	The difference between the input/output rotation speeds. In practice this is typically expressed in units of *rotations per minute (RPM)*. In mathematical models and expressions, *radians per second* is often used.
Slip-Rotation	A rotation of the input shaft *relative to the output shaft*, or vice-versa.
Slip Ratio	The Slip Rate divided by the Input Speed. *If the slip ratio is* 10%, *the output speed is* 90% *of the input speed.*
Slip Limit	The maximum torque a coupling can transmit before slipping.
Fully Engaged	For a clutch, the operating point at which maximum torque is transmitted. At full engagement, different coupling types may continuously slip, lockup without positive engagement, or lockup with positive engagement. Examples of couplings exhibiting these behaviors are variable hydrodynamic couplings, friction clutches, and dog clutches, respectively.
Fully Disengaged	For a clutch, the operating point at which minimum torque is transmitted.
Lockup	A clutch state where there is no slip under normal operation; input/output speeds are synchronized. Depending on the clutch design, it may still slip if overloaded (*e.g.* friction clutches).
Partially Engaged	An intermediate clutch state between Fully Disengaged and Fully Engaged. Partial engagement is usually accompanied by clutch slip, meaning power is dissipated while torque is transmitted.
Positively Engaged	A coupling state where the input and output are physically locked together and cannot slip without some mechanical component breaking. A special case of "Fully Engaged." *Note, depending on the coupling type, there may still be some backlash, but continuous slip cannot occur.*
Engagement Quality	A subjective rating of a clutch's ability to modulate transmitted torque while slipping. Related to engagement sensitivity, linearity, predictability, and other factors.

Table 1.3 – Coupling Mode Types

Mode Type:	Operating Points:	Mode Description:
Single-Mode *"Always On"*	**1**	*"Permanent Couplings"* – A single-mode coupling always operates in one configuration and torque cannot be modulated. This category includes most non-friction couplings (rigid, alignment-compensating, one-way), as well as constant-fill fluid couplings and synchronous magnetic couplings. Note that many permanent couplings can still slip, but the level of slip cannot be controlled via direct manipulation of the coupling.
Dual-Mode *"On/Off"*	**2**	*"Digital Clutches"* – A dual-mode coupling can transition between two steady-state operating configurations. Partial engagement occurs *briefly* during mode transition (*i.e.* speed synchronization, such as shifting gears in an automobile). Especially for friction clutches, these transients must be short, infrequent, and specifically designed to avoid overheating and damage. This category includes most friction clutches, some synchronous magnetic couplings, and some rigid couplings (*e.g.* tooth clutches). Note that although Dual-Mode couplings can (dis)engage, they cannot necessarily perform speed-synchronization on their own (tooth clutches again serve as good examples of this).
Variable-Mode *"Infinitely Variable"*	∞	*"Analog Clutches"* – Variable-mode couplings may traverse "through" different operating points, many of which can be sustained continuously in steady-state operation (subject to other constraints, such as the thermal limits of the design). Varying the level of coupling engagement allows for modulation of the torque transmitted. This category includes many variable-fill fluid couplings, and variable-magnetic couplings, and certain specialty friction clutches.

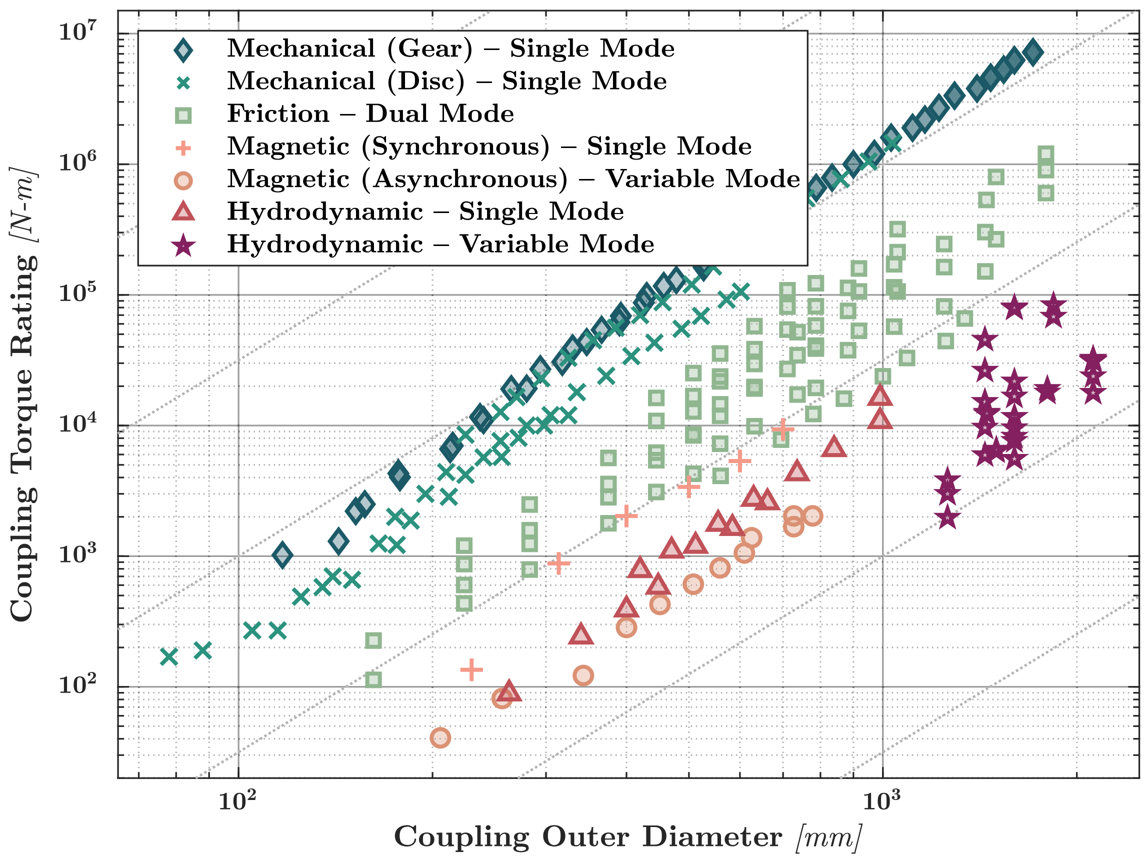

Figure 1-4 – Plot of torque capacity vs. diameter for several industrial couplings. This plot compares the performance of several industrial couplings, including single-mode mechanical couplings, dual-mode friction couplings, and various fluid/magnetic couplings (of single and variable-mode varieties). The values plotted were sourced directly from manufacturer data [9]–[14]:

Flender GmbH:	*Gear, Disc, and Single-Mode Hydrodynamic*
MagnaDrive Corp.:	*Single and Variable-Mode Magnetic*
Voith Group:	*Variable-Mode Hydrodynamic*
Wichita Clutch:	*Friction*

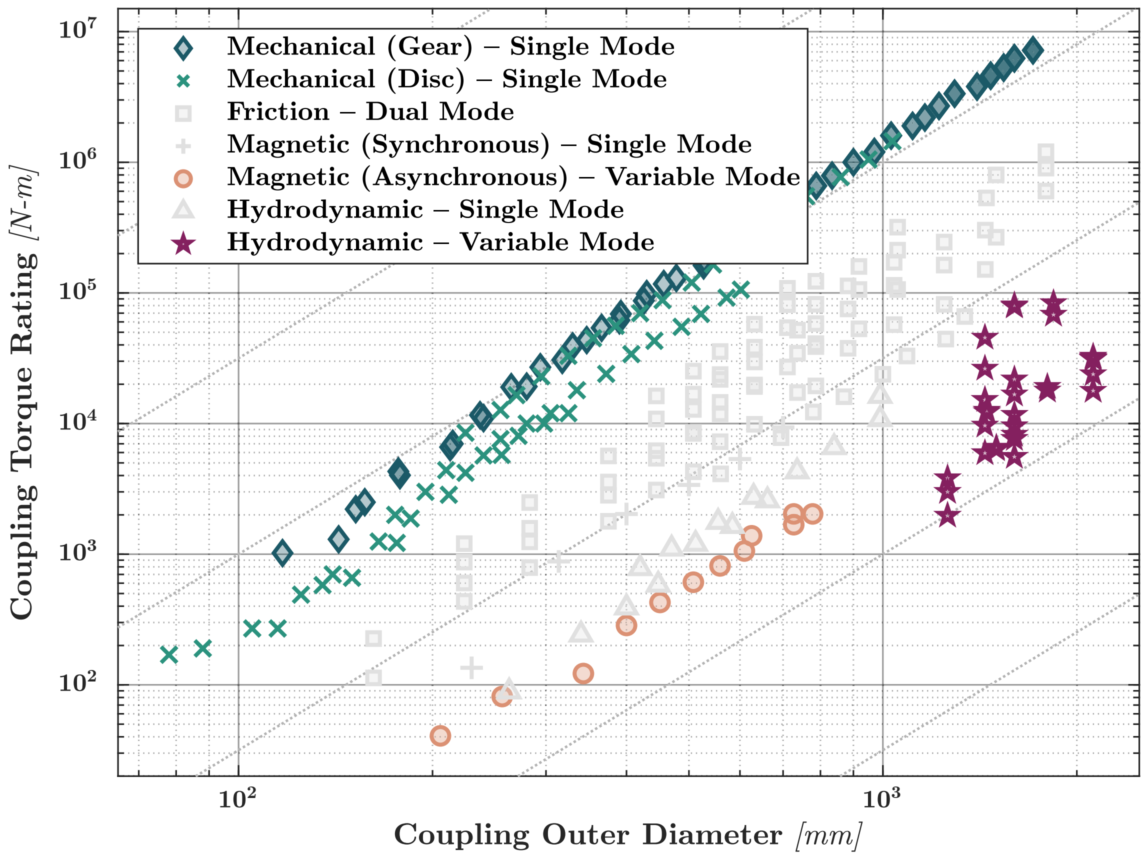

Figure 1-5 – Plot of torque capacity vs. diameter, focusing on Single vs. Variable-Mode couplings. This plot uses the same data as Figure 1-4 and particularly highlights the steep performance price paid for versatility; single-mode couplings bear **∼100*x* the torque** of similarly-sized variable-mode couplings.

diameter of variable-mode couplings; assuming roughly equal proportions, this corresponds to ∼1/64 the volume of variable-mode couplings.

- The torque-diameter scaling – the slope on this log-log chart – is third-order ($T \propto D^3$), so torque capacity scales roughly proportionally with coupling volume. This relationship holds steady regardless of coupling type or size; each coupling very closely follows (or falls below) the "trendline" of its associated group.[1 2] **In other words, coupling performance is fundamentally limited by the underlying physics. Outside of a truly revolutionary innovation in fluid/magnetic couplings, it is unlikely that continued iteration on the current designs will produce variable-mode couplings with massively improved performance (vs. the current benchmarks).**
- The torque-dense, single-mode mechanical couplings not only achieve the highest torque ratings, but also span the widest range of available sizes. **Many variable-mode couplings are non-viable due to size constraints alone, even before considering their shortfalls in terms of torque capacity.**

As alluded to, the comparatively low torque density of variable-mode couplings is readily explained. Hydrodynamic and magnetic couplings are fundamentally limited by commercially achievable material properties, specifically fluid density and magnetic maximum energy product [15], [16]. Friction clutches offer better torque density but are limited by their ability to continuously evacuate dissipated heat while slipping, especially at the friction interface [17]. Cooling can be enhanced via fluid immersion and forced-convection at the cost of a reduction in friction coefficient and torque capacity. Even then, friction clutches are overwhelmingly used in dual-mode applications where slip events are brief and infrequent. The ratings shown anticipate dual-mode operation only and do not represent friction torque capacity under continuous slip.

Demonstrating the viability of a new coupling type, that delivers true variable-mode operation alongside the potential for order-of-magnitude improvements in torque density is the key overarching goal of this research effort.

1.5.2 The Utility of Coupling Engagement/Disengagement and Slip

Where dual or variable-mode couplings are used, the ability to (dis)engage and/or modulate torque on-command is usually essential to machine function. Without a clutch, a manual-transmission automobile could never shift gears, idle at a stoplight, or even start its engine (at least, from a standstill). Clutch

[1] Friction couplings appear to show more variation, but this is because the data include clutches with different numbers of friction clutch plates (from 1-4 clutch plates). Adding clutch plates increases clutch length but does not increase diameter, so this metric slightly favors multi-plate clutches. Clutches sharing the same plate count fall tightly on their respective trendlines.

[2] At first glance, variable-mode hydrodynamic couplings appear grouped rather than falling on a distinct trendline. However, extending the trendline from single-mode hydrodynamic couplings, one can see that the variable-mode counterparts only match this line at best (most fall below it).

(dis)engagement and slip are two sides of the same coin, with slip being the phenomenon that occurs *during the process of* coupling (dis)engagement. In the same example of a stick-shift car, precise clutch control (slip control) is what makes smooth takeoffs and gearshifts possible – a diagram of friction clutch operation can be seen in Figure 1-6.

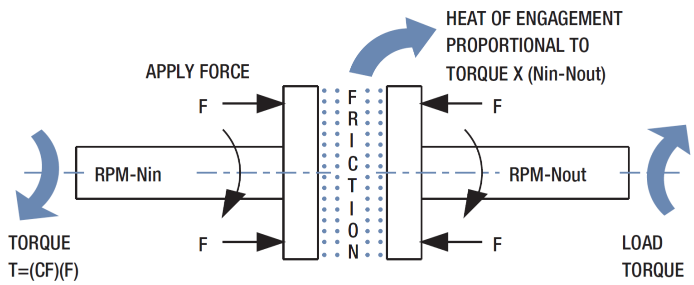

Figure 1-6 – Diagram of typical friction clutch operation [18]. When the clutch plates are clamped together, the resulting friction transmits torque. During the engagement process, the clutch slips and dissipates heat at a rate proportional to the slip speed. No heat is dissipated at the friction interface when the clutch is fully engaged (input/output speeds match) or completely disengaged.

Particularly in industrial applications, coupling (dis)engagement allows many power sources and/or loads to be connected together on-demand to form mechanical networks. This provides opportunities for improved flexibility and reliability/redundancy. In the Industrial Age, textile factories distributed mechanical power via systems of driveshafts, pulleys, gears, and belts (see Figure 1-7a). All were connected to a common power source, such as a water wheel, turbine, or steam engine. Individual machines were powered using a rudimentary friction-based clutching scheme, whereby engagement was controlled by sliding the drive belt between sections of a so-called "fast-and-loose pulley"[1] [19].

Dual and variable-mode couplings can also be used to connect multiple drives to a single load. This can be used to add system redundancy, improve efficiency at different operating points (*i.e.* swapping between low- and high-speed optimized drives), and increase power output of an existing drive system by adding another power source in parallel.

Slip is also useful for reasons beyond clutching. In fluid and magnetic couplings, the ability to slip serves as a safeguard against shock/overload, dampens torsional vibrations, and passively facilitates smooth acceleration and deceleration of high-inertia loads. Safety couplings (one-way couplings, torque-limiting couplings, *etc.*) specifically slip in certain conditions and lock in others. For example, backstopping clutches are used in inclined conveyor systems for raw materials. In normal operation, the backstopping clutch slips and permits the conveyor to transport material up an incline. If the drive ever fails, the backstopping clutch

[1] The "fast-and-loose pulley" is actually two adjacent flat-rimmed pulleys, one free-spinning (loose) and the other locked to a driveshaft (fast). The belt would freewheel while running on the loose pulley and the machine would not be driven. Then, sliding the belt over to the fast pulley would start the machine running again.

(a) Photo [20] from the Boott Cotton Mills Museum in Lowell, Massachusetts. A lineshaft running along the ceiling distributes power via flat belts to the machines below.

(b) Rendering [21] of an SSS (Synchro-Self-Shifting) Clutch, a type of overrunning clutch that transmits power in one rotational direction only. U.S. Naval vessels make extensive use of these couplings in various multiple-power-source Combined Marine Propulsion systems [22].

Figure 1-7 – Example applications where couplings are used to transmit mechanical power across a network of multiple loads and/or power sources.

locks up and prevents the conveyor from running backwards, thereby avoiding potentially catastrophic reverse-runaway.

If substantial torque must be transmitted *while slipping continuously,* a fluid or magnetic coupling is currently the preferred solution. Both are non-contact and so exhibit minimal wear and excellent service life. For heavy-slip applications, fluid couplings are particularly attractive because the working fluid can serve double-duty as a recirculating cooling agent. However, the governing physics of both fluid and magnetic couplings fundamentally limits their achievable torque density. For large stationary applications (*e.g.* chemical plants, power plants, factories), size and weight are not always crucial design constraints so this drawback is not as substantial. However, the prohibitive size and weight of fluid and magnetic couplings frequently precludes their use in mobile and/or space-constrained applications. On the other hand, friction clutches offer substantially greater torque capacity, but as mentioned, they struggle to manage thermal loads while operating at continuous slip – see Figure 1-8.

The Inertial Hysteresis Coupling presented in this thesis seeks to combine different aspects of rigid, friction, and fluid couplings to achieve high torque density and variable-mode operation, while facilitating efficient cooling. It harnesses both frictional and normal forces to efficiently transmit loads (*i.e.* driving heavy loads even with low friction coefficients) while using a geometry that is much easier to cool compared to friction clutches.

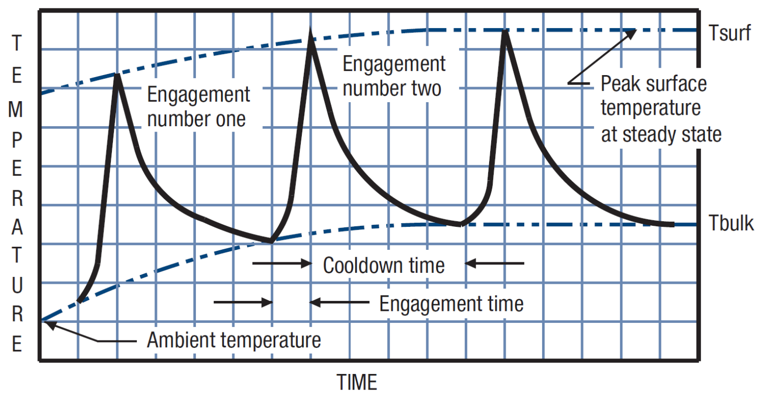

Figure 1-8 – Cyclic heating & cooling cycles of a friction clutch [23]. The engagement-disengagement cycle shown is typical for friction clutches. During engagement, the friction lining experiences rapid heating as the input/output shaft speeds synchronize. This is followed by an extended period of gradual cooling (which is typically much longer than the heating period). Friction couplings are designed to endure thermal load under brief transient events such as these – but not for continuous operation at slip.

1.5.3 The Utility of Coupling Lockup and Positive Engagement

While coupling slip is undoubtedly useful, there are many situations where slip is unacceptable. The drawbacks of undesired slip include losses in efficiency, an inability to ensure synchronization of speeds and/or positions, generation of (potentially substantial) waste heat, and accelerated wear. In such cases, a "lockup-capable" coupling – which permits the input and output to be locked together with no slip – may be desired.

Returning to the example of a stick-shift car, clutch slip is essential during key periods such as takeoff, gearshifts, *etc*. Outside of these short events however, the clutch should lockup such that there is no slip between the engine and transmission. Lockup maximizes the power delivered to the wheels, preserves consistent and predictable throttle response, improves fuel efficiency, and most importantly, avoids needless clutch heating and wear. When operated correctly, a clutch can last tens of thousands of miles. Yet, as many people can attest, less than a minute spent "slipping the clutch" (uninterrupted) can permanently damage it and require it to be replaced.

"Slipping" and "lockup" couplings can be combined together in a single assembly to achieve the benefits of both in exchange for increased cost and complexity. Many modern automobiles combine fluid and friction elements in their transmissions for this very reason: the torque converter (a fluid coupling) will allow slip between the engine and transmission when idling, accelerating from rest, or shifting gears. Then, once the vehicle is up to speed, a separate parallel friction clutch mechanism locks out the fluid coupling and eliminates slip for more efficient cruising. The Inertial Hysteresis Coupling presented in this thesis not only exhibits variable-mode operation, but is also capable of achieving lockup without any separate mechanisms.

Note that a friction coupling under lockup will still slip if sufficiently overloaded. Sometimes this is desirable as it can limit torque transmission, thereby preventing damage or injury. When undesirable, a positively-engaged solution such as a Hirth coupling may be preferred. Positively-engaged connections will physically break before slipping (technically a more “strict” lockup condition).

1.5.4 Power Dissipation of Couplings Under Slip

It is crucial to note that coupling slip always corresponds to power dissipation via heat generation. The dissipation rate can be determined from the operating point alone, *i.e.* the coupling’s input speed, output speed, and torque transmitted. In other words, if the operating point parameters are known, the power dissipation can be calculated without any information about the coupling itself.[1] The power P_d is dissipated as heat within the coupling. Managing this heat is absolutely crucial for any coupling that slips, whether continuously or in short bursts.

$$\boxed{P_d = |T\Delta\omega|} \tag{1.1}$$

Where:

$$\begin{aligned} P_d &= \text{Power dissipation (thermal load)} \\ T &= \text{Torque transmitted} \\ \Delta\omega &= \text{Slip rate (difference between input/output speeds)} \end{aligned}$$

The power dissipated in Equation (1.1) represents a loss in the overall system efficiency of a machine. However, again, this efficiency loss is a function purely of the operating point; efficiency cannot be “magically recouped” by changing the coupling design if the operating point remains the same.

1.5.5 Couplings, Clutches, Brakes, and Transmissions

To prevent confusion, the distinction between couplings, clutches, brakes, and transmissions is briefly discussed here. For purposes of this thesis, clutches and brakes fall under the umbrella of “couplings,” while “true transmissions” are considered separate devices entirely.

Although the design criteria and functional requirements for clutches and brakes may differ substantially, they are functionally very similar in operation. Both facilitate (dis)engagement of torque transmission

[1] Note that the coupling design is likely to change which operating point the coupling settles at in a given scenario. However, if the operating point parameters are firmly set, the power dissipation rate can be calculated without needing to consider any details of the coupling’s actual design.

between rotating mechanical elements. The main differentiator is whether the connection is to something fixed (brake) or rotating (clutch) – see Figures 1-9 and 1-10.

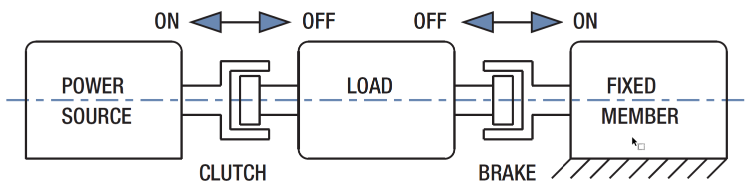

Figure 1-9 – Simple diagram [23] of a mechanism with both clutch and brake connections. Although the terms “clutch” and “brake” imply different goals, the mechanisms themselves are closely related – in fact, brakes can be thought of as a subset of clutches. While clutches usually drive loads, brakes are designed to stop them. In some cases the same mechanism can be used for clutching and/or braking (see Figure 1-10).

“True” transmissions are distinct from couplings in that input/output speed differences are the result of torque multiplication rather than slip. The input/output speed ratio is balanced by an inverse input/output torque ratio, with a persistent goal of approaching 100% overall efficiency.[1] Torque multiplication and efficiency maximization are often, but not always, desirable. For example, a transmission cannot interrupt torque transmission or modulate the power passed from source to load, for example to shift gears or to protect equipment against shock loads. For this reason, couplings are frequently paired with transmissions so the benefits of both can be realized.

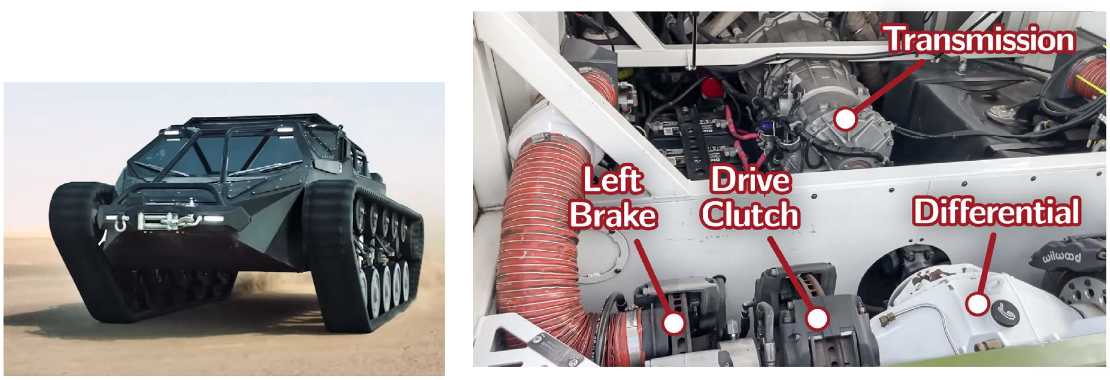

(a) [24] **(b)** [25]

Figure 1-10 – The Ripsaw EV2, a tracked vehicle that uses sets of friction-based rotor & caliper assemblies as both drive clutches and as brakes [24], [25]. The EV2 accelerates, turns, and brakes using sprockets to drive its treads. Mounted to the vehicle’s rear axles – which power the drive sprockets – are four separate rotor/caliper sets. Each side has a fully independent rotor/caliper set for clutching and another set for braking. The hardware used in the clutch/brake assemblies is nearly identical, but their layouts differ.

[1] In most cases “couplings” and “transmissions” are quite distinct and comply with the descriptions given. However, some exceptions exist, such as the torque converter – a special type of fluid coupling that incorporates an extra component called the “stator.” At low speeds and high slip rates, the stator multiplies torque similarly to a transmission. However, at high speeds, the stator locks out and the device behaves like a normal hydrodynamic coupling.

1.6 Key Applications for IHCs

As mentioned, couplings are virtually ubiquitous devices, found nearly everywhere machinery performs useful work. In 2018, the estimated global market size for couplings was approximately $3.9 billion, a number that is projected to grow to $5.7 billion by 2026 [26]. Additionally, every existing major coupling type sees widespread use across a variety of industries. Thus, the potential applications for IHCs are quite numerous. That said, the areas offering the greatest potential impact are those that would leverage the projected performance advantages of IHCs: active modulation of torque transmission; efficient cooling via forced fluid convection; and a compact, high-torque-density footprint. Applications that would benefit most from these qualities are those which simultaneously demand wide operating flexibility, high torque capacity, and excellent size/weight characteristics. The automotive and mobile robotics markets are two prime examples of areas where these factors are given high priority.

Perhaps the most impactful application of IHCs in the automotive market would be for next-generation mechanical torque vectoring systems. In recent decades, substantial work has been devoted to the development of electronic limited-slip differentials such as the Audi Sport Differential pictured in Figure 1-11. Using an electronically-controlled clutch pack, the sport differential allows the vehicle to control the distribution of torque between the driven wheels for the purpose of maximizing traction. The friction clutch pack connects the left and right axles and modulates torque transmission between them via the friction clutch pack. This allows the vehicle to combat the undesirable "differential spin" phenomenon suffered by open differentials, particularly in traction-compromised conditions such as the example in Figure 1-12. If only an open differential were used here, the vehicle's (propulsive) traction would be limited by the wheel with the least grip.[1]

Though well-known, Audi is far from the only manufacturer to develop systems with active differentials and/or torque-vectoring features. Other offerings include:

- **BMW:** Active M Differential
- **BorgWarner:** eTVD
- **Ferrari:** E-Diff
- **General Motors:** eLSD
- **GKN Automotive:** Twinster All-Wheel Drive
- **Haldex:** LSC
- **Honda/Acura:** SH-AWD
- **Mercedes-Benz:** AMG Electronic Limited-Slip Differential
- **Nissan:** ATTESA E-TS Pro
- **Porsche:** PTV Plus
- **ZF:** eLSD and eVD

[1] Those familiar with the term "One-Wheel Peel" may relate to this!

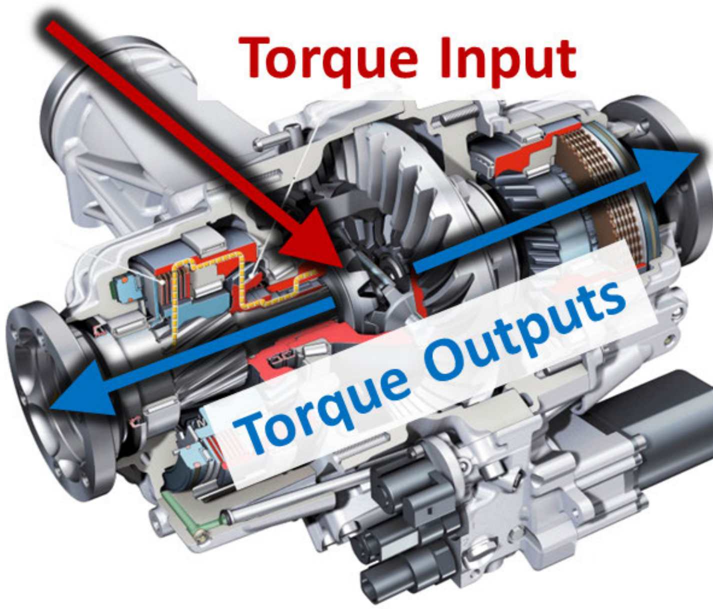

(a) [27]

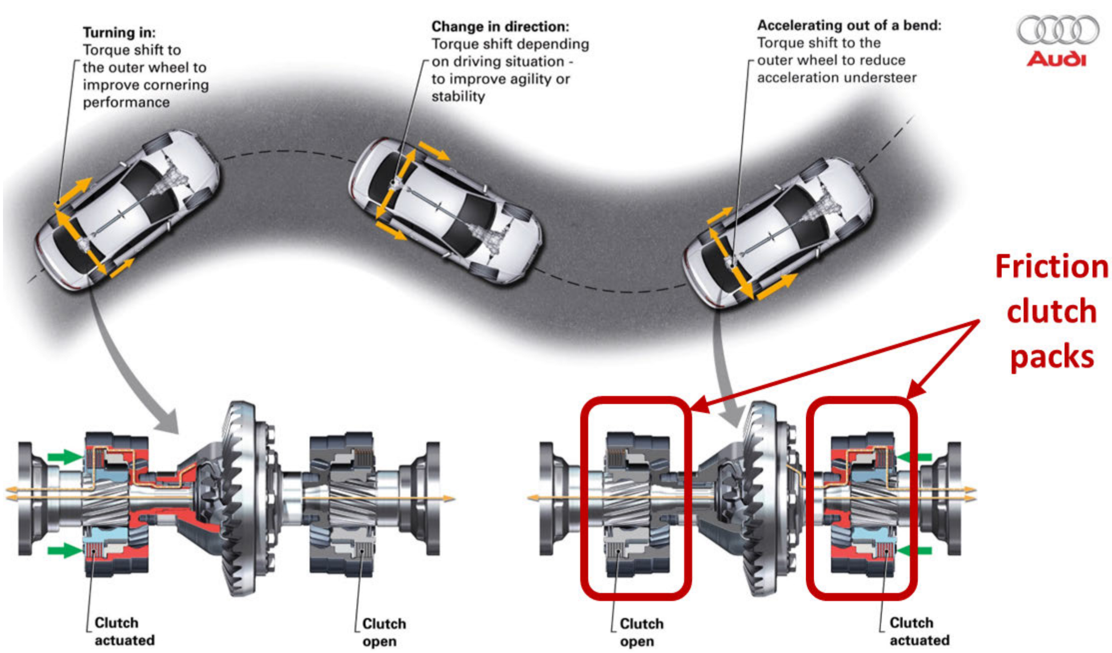

(b) [28]

Figure 1-11 – Various illustrations showing the Audi Sport Differential and the means by which it improves vehicle handling via torque vectoring.

Figure 1-12 – Porsche Cayman undergoing testing on a split-mu test track. Split-mu test tracks are explicitly designed to subject vehicles to drastically different friction conditions at different wheels. Such conditions are very difficult to manage for vehicles with open differentials because power delivery is limited by the wheel with the least traction.

These solutions all lean heavily on friction clutches for modulating torque; with such tight packaging constraints, only friction clutches currently offer sufficient torque density for this application. Yet, they still have severe limitations when it comes to high-duty-cycle use. As mentioned previously, friction couplings are not particularly well-suited for continuous-slip operation for thermal reasons; in the automotive sector, there are simply no other options, so this compromise is accepted.

The thermal issues of friction-clutch torque-vectoring systems are highlighted in Figures 1-13 and 1-14. In short, common clutch friction materials experience significant performance degradation and accelerated wear when temperatures surpass $\sim$200 °C – a threshold which is rapidly breached under heavy load. In practice, these systems work best under only moderate, intermittent loading.

As the world continues the transition to primarily electric automobiles, the challenge of heat management in active differentials will, if anything, become even more pressing. While per-wheel electric drives offer a variety of advantages, there still remain significant practical reasons a design team might opt for a topology using a single electric motor that distributes power via a differential. This includes reduced cost, reduced vehicle moments-of-inertia (due to the motor's weight being more centralized), a reduced total part count, and more efficient use of vehicle space (*i.e.* only one motor housing, set of mounts, *etc.*). Additionally, electric vehicles typically exhibit substantially greater torque output than their gasoline-powered counterparts, meaning the requirements for torque capacity will only increase.

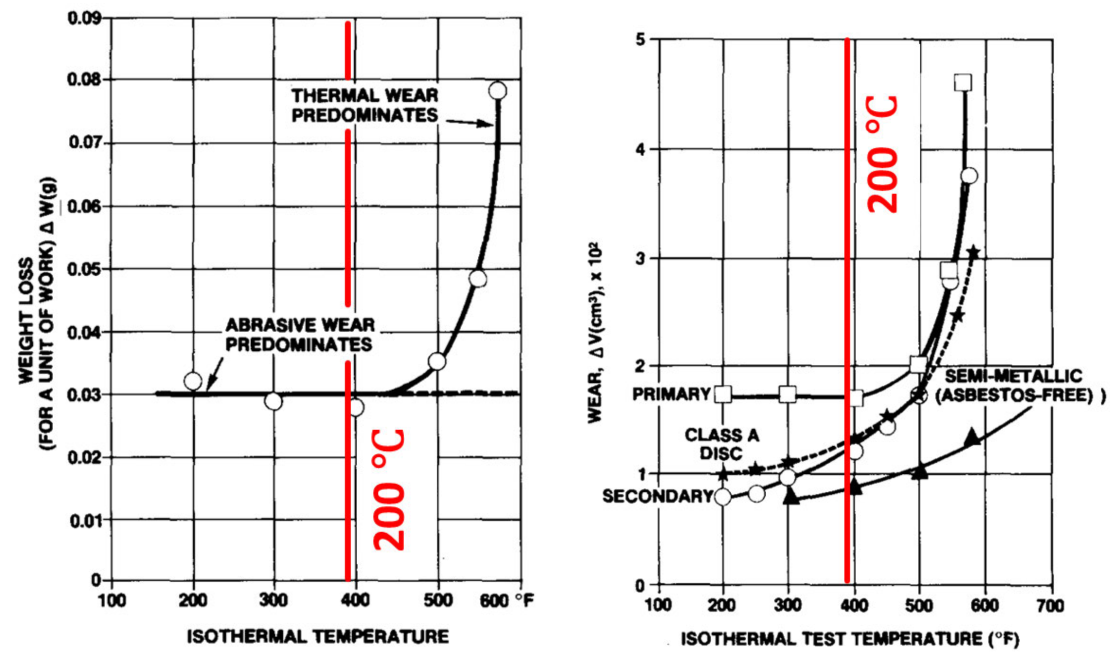

(a) [29] **(b)** [29]

Figure 1-13 – Graphs highlighting the rapid degradation of friction clutches at elevated temperatures.

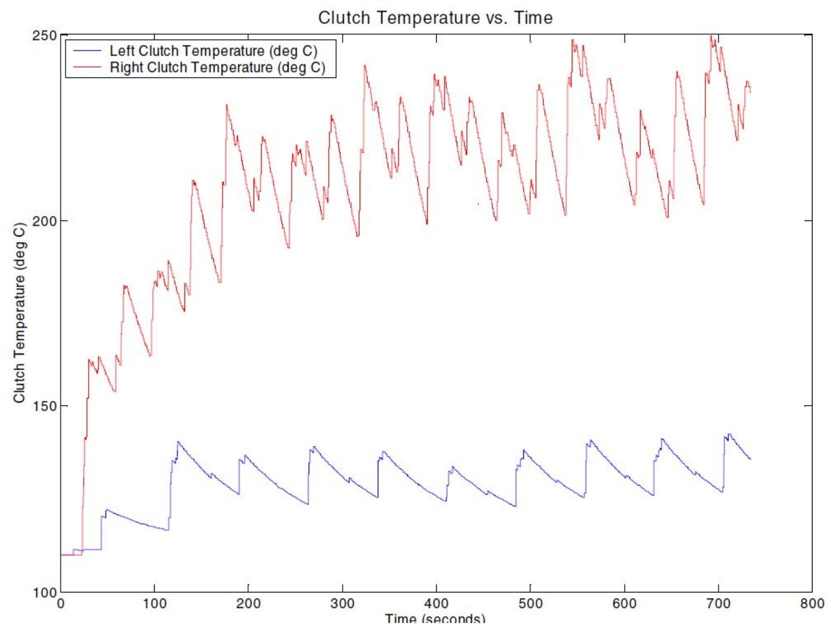

(a) [30] (No clutch cooling)

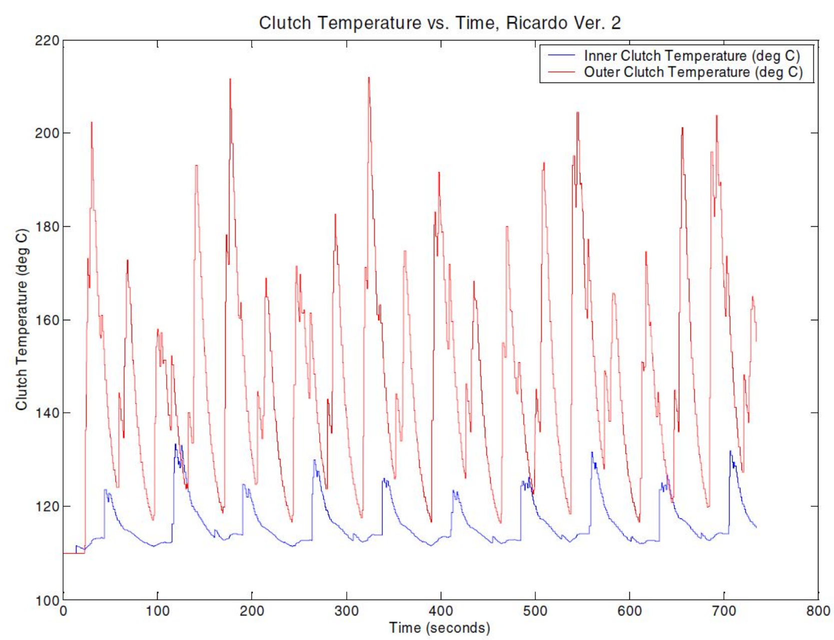

(b) [30] (Oil convective cooling)

Figure 1-14 – Thermal simulations of a torque-vectoring clutch pack by Ricardo Driveline and Transmission Systems. The authors of this paper simulated the expected heating effects of a torque-vectoring rear differential based on real-world data collected at a race track. In the uncooled case (Figure 1-14a), clutch temperatures rapidly breach 200°C and never fall back to acceptable levels. The cooled case (Figure 1-14b) performs much better on average, yet still experiences transient spikes to over 200°C.

THIS PAGE INTENTIONALLY LEFT BLANK

Chapter 2

The Inertial Hysteresis Coupling (IHC) Concept

2.1 Inspiration: The Ball-Type Constant-Velocity Joint

The seed for the Inertial Hysteresis Coupling concept was originally planted when the author viewed an animation of a ball-type constant-velocity joint (AKA "CV joint") in operation. This type of coupling, pictured in Figure 2-1, has grooves in the inner and outer race components which ball bearings contact mechanically. The ball-and-groove geometry provides firm constraint in the rotation direction associated with torque transmission (*i.e.* rotation about the shaft axes), while permitting angular deflection in the other two directions. CV joints can maintain smooth and constant 1:1 input/output speed ratios even when shaft pivot angles approach $\sim 40°$. For this reason, ball-type CV joints are widely used in front-wheel drive automobiles; they permit constant and smooth power delivery to the front wheels without inhibiting the vehicle's ability to turn.

The behavior of the ball-type CV joint can be described by the phrase:

A CV joint is a mechanism that...
...maintains a ***constant speed ratio***...
...despite a ***variable shaft geometry.***

In other words, **careful design of the rigid contact scheme permits power transmission despite relative motion** (in this case, change of the axle angle). The IHC, on the other hand, sought to re-imagine this phrase as:

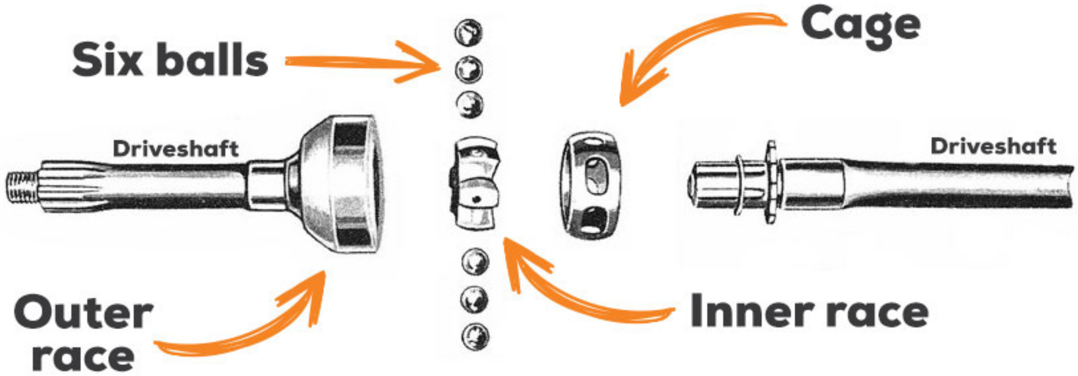

Figure 2-1 – Illustration [31] of the components of a ball-type CV joint. The inner and outer races each have meridianal grooves which resemble the lines between the slices of an orange. Ball bearings span the gap between these grooves, allowing the mechanism to transmit rotational power while leaving the driveshafts free to pivot. The ball-type CV joint's ability to maintain a smooth and constant 1:1 speed ratio makes it popular for use in front-wheel-drive automobiles.

Is there a similar geometry that can...

...produce a ***variable speed ratio***...

...while maintaining a ***constant shaft geometry?***

2.2 A Mechanical Analog to the Fluid Coupling

For achieving a variable speed ratio – *i.e.* controlling slip – it's useful to first consider the physical basis on which fluid couplings operate (see Figure 2-2). Fluid couplings consist of three elements: a Pump (input), a Turbine (output), and a working fluid. During operation, the working fluid continuously recirculates. With each cycle, the Pump (input) imparts energy to the fluid by accelerating it, after which the Turbine harvests this energy (as torque) by slowing the fluid down and redirecting its flow. The fluid itself endures this repeated pattern of acceleration, deceleration, and direction change, serving as the medium through which the Pump and Turbine interact (they never directly touch one another). Thus, the reaction loads on the Pump and Turbine act on each other indirectly by means of the working fluid (which serves as a sort of "intermediary").

Translating this to the mechanical domain, one might replace "working fluid" with "sliding connector." Could a mechanism be devised such that it has input/output features (equivalent to the pump/turbine) which do not interact directly, but instead transmit loads via this "sliding connector?" The input could propel the connecting object, then the output would "catch it" and harvest its energy, ultimately resulting in a net transmission of torque across the assembly. In short, the answer is yes! The Inertial Hysteresis Coupling (IHC) is one such concept that physically realizes this.

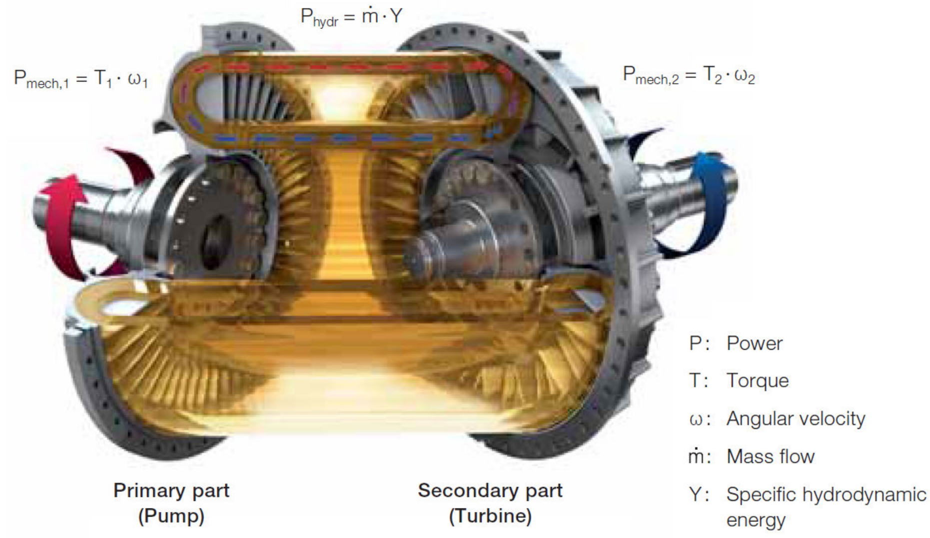

Figure 2-2 – Exploded-view diagram of a hydrodynamic coupling [32]. In a hydrodynamic (AKA fluid) coupling, the input and output shafts never interact directly. Instead, torque is transmitted via circulation of a working fluid. The coupling's input side (the pump) drives the fluid, and the output side (the turbine) harvests energy from the fluid to produce torque.

A surprisingly simple analogy can be made to a basic mechanical device – the bead maze pictured in Figure 2-3. Bead mazes are simple but popular children's toys found throughout the USA in dentist and doctor offices. Each consists of a set of colorful twisted guidewires along which painted beads can slide. Each bead can be easily moved by hand, but is constrained to move along its guidewire.

Though it is simple, the bead maze in some ways acts very similarly to the proposed "sliding connector" concept. Consider Figure 2-3 – the helical red section in particular. If the bead is dropped through this section of its guidewire, it will accelerate and travel down through the spiral before reaching the bottom. Along the way, the guidewire directs the bead while friction impedes motion. Though the magnitudes are miniscule, gravity pulls the bead along the guidewire, thereby imparting normal and frictional forces onto the guidewire itself. It could be said that:

- **Gravity** is the **Energy Input**
- **The bead** is the **"Sliding Connector"**
- **The guidewire** is the **Energy Output**[1]

At the scale of a children's toy, forces are miniscule and the bead-guidewire interactions are almost forgettable. However, consider what would happen if the bead were somehow to be fired into helical section at high speed (say, 50+ m/s). Assuming the helix does not break outright, the bead will endure comparatively massive centrifugal and frictional loads as it follows the guidewire helix. The guidewire

[1] For now, ignore the fact that a bead maze cannot do much of anything useful with this energy!

Figure 2-3 – Photograph of a bead maze toy [33]. This bead maze toy serves as a simple example of how loads can be transmitted via contact forces between constrained masses. As a bead falls down along the helical guidewire, normal and frictional forces keep it on-track. These forces also impede its motion, causing equal-and-opposite reaction forces to act upon the guidewire in return.

experiences equal and opposite reaction loads, which will likewise be massive. Again, even though the guidewire in this example can't do anything particularly *useful* with all this reaction force, it should at least be clear that the bead/guidewire pair can transmit forces to one another while the bead slips along. Additionally, the forces experienced by the bead arise specifically due to the motion constraints enforced on it by the helical track. Just as was done with the working fluid in a hydrodynamic coupling, a solid mass can be intentionally redirected for the purpose of generating forces on other solid mechanical objects.

2.2.1 Preview of ihcBENCH, a Prototype Inertial Hysteresis Coupling

Figure 2-4 depicts ihcBENCH, the physical test system built as part of this research effort (and discussed at length in Chapter 5). At the center of this assembly is the prototype Inertial Hysteresis Coupling AKA IHC, a device which extends the bead maze concept into a useful device. The IHC consists of three major subassemblies:

- **The "Planet,"** analogous to the "pump" in a fluid coupling[1]
- **The "Orbit,"** analogous to the "turbine" in a fluid coupling
- **"The Satellites,"** which act as the Connecting Objects (analogous to the "working fluid")

[1] In practice either the Planet or Orbit can act as the power input/output (*i.e.* pump/turbine). But, this analogy is sufficient for now.

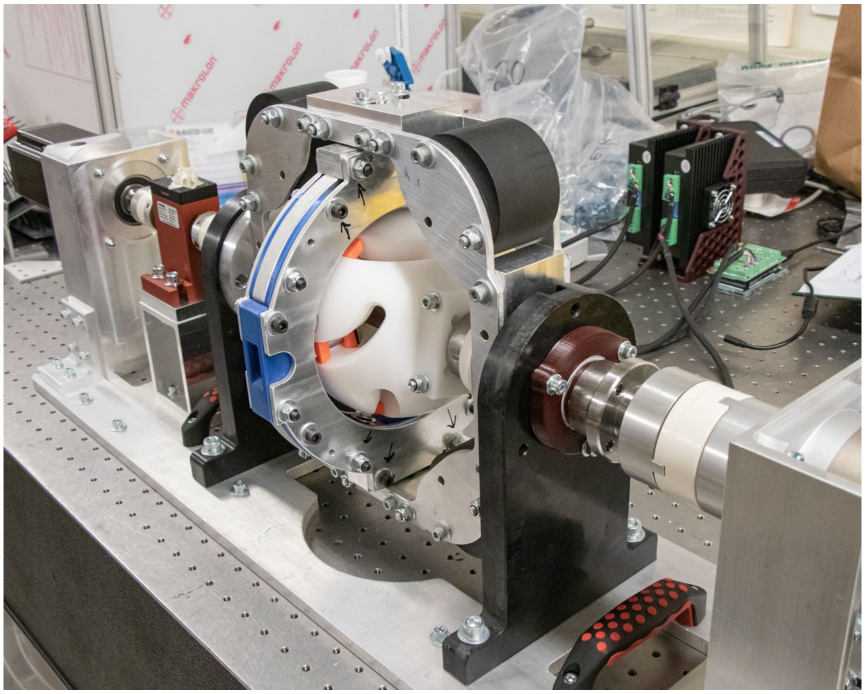

Figure 2-4 – Photo of the ihcBENCH prototype system. The Planet is the white "ball" at the center of the assembly; the blue and silver ring wrapping around it is the Orbit; and the Satellites are orange.

Input power is supplied to the Planet, which rotates about its central axis and drives a set of Satellites. Each Satellite may slide along a track in the Planet, while also traversing the larger Orbit ring. As the Planet spins, the Satellites experience continuous acceleration and deceleration as they track along both the Planet and Orbit constraints. In the process, they interact with the Planet and Orbit by means of normal and frictional forces. These interactions produce net torque transmission across the device, allowing the Planet to drive the Orbit via the intermediary Satellites (the Planet and Orbit never touch one another directly).

An IHC relies on its Satellites to transmit torque. ***The Satellites are inertial masses*** – they not only transmit contact loads from the Planet/Orbit, but will also induce inertial loads due their non-zero mass.[1] The presence of some[2] friction is also crucial for this process; as it turns out, without friction, average torque transmission actually sums to zero (the mechanism simply cycles between equal periods of positive and negative torque, averaging to zero – see Figure 2-5). The ***hysteresis that friction provides*** is ultimately essential to an IHC's core functionality. **Hence, the "Inertial Hysteresis Coupling" is so named!**

As the rigid mechanical "sliding connector" moves it experiences kinetic friction. However, a wide contact

[1] The prototype discussed in this thesis uses lightweight Satellites (50 grams each) and reaches only ~75 RPM. As a result, inertial effects have not yet been deeply explored, but are expected to be important in future work.

[2] A small, but non-zero, amount.

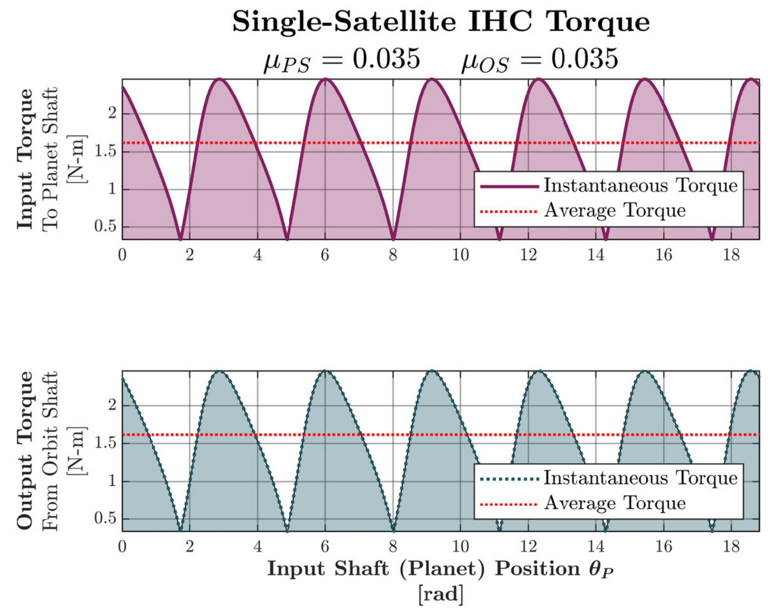

(a)

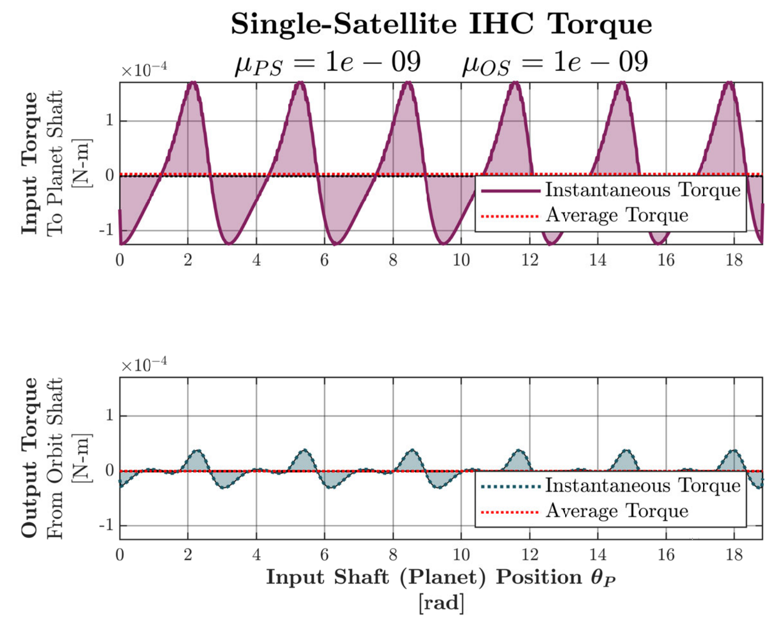

(b)

Figure 2-5 – Simulation plots showing the importance of friction for transmitting torque with an IHC. These plots show the total torque output for a hypothetical IHC with only a single Satellite element. The only difference between these simulations is the friction coefficient. The results demonstrate the need to have friction – without it, a force-hysteresis loop is not developed and no meaningful net torque can be transmitted by the IHC (hence the name!). When the friction value is set vanishingly-low, constant input/output speeds result in near-zero average torque transmission. Instead, the Satellite cycles between periods of positive and negative torque which almost fully cancel each other out. By contrast, more realistic friction values produce a hysteresis effect and meaningful net-positive torque transmission.

area can be utilized to reduce contact stress, to maintain a supporting lubricant film, and to achieve a long wear life. Second, the incident angles / friction contact angles can be manipulated to modulate the friction forces produced. While slipping, the lubricant not only reduces friction and wear, but can also serve as a convective cooling agent. The sliding contact surfaces can be continually flushed with oil or the entire mechanism submerged in an oil bath.[1] When the incident angle falls below a critical threshold, the sliding connector locks in place and the Input/Output are rigidly linked.[2] While locked in this fashion, the load capacity of the device as a whole is ultimately limited by the mechanical strength of its parts (the same limitation that applies to rigid single-mode couplings). Finally, because most of the coupling load is supported by normal contact forces (which remain effective even with very low friction coefficients, < 0.05), the materials selection process can favor high-temperature, high-wear-resistance materials such as hardened steels and bearing bronzes. This is in contrast to friction couplings, which transmit 100% of their torque via friction and frequently use much less resilient organic friction materials.

In short, the "sliding connector" concept combines several of the key desirable aspects of various existing coupling types:

- **Like variable-mode fluid couplings,** the concept can modulate slip and is readily adapted for convective cooling.
- **Like dual-mode friction couplings,** the concept can transition into full lockup (zero slip).
- **Like single-mode rigid couplings,** the concept is fundamentally limited by the mechanical strength of its rigid materials rather than fluid or magnetic properties. This enables potentially order-of-magnitude improvements in torque density over existing variable-slip couplings.

2.3 Fundamental IHC Parts and Motions

As mentioned, a simple theoretical Inertial Hysteresis Coupling (IHC) consists of the three parts shown in Figure 2-6. The components' names were picked based on the loose resemblances to their namesakes:

- **Planet:** A sphere with straight slot, depicted in green.
- **Orbit:** A ring with straight slot around the inner circumference, depicted in blue.
- **Satellite:** A peg, depicted in red.

The Planet and Orbit function as the IHC Input/Output via shafts attached to each as shown in Figure 2-7. They are then placed together (their centers co-located) with their shafts pointing in opposite directions

[1] Oil could even be pumped to orifices in the various contact surfaces so each can operate as a hydrostatic bearing. Such an approach is left for future work.

[2] Note that, in general, the static coefficient of friction between two surfaces is higher than the dynamic coefficient of friction. Thus, the sliding connector truly does "lock in," as it is more difficult to get moving again back in the direction it came from.

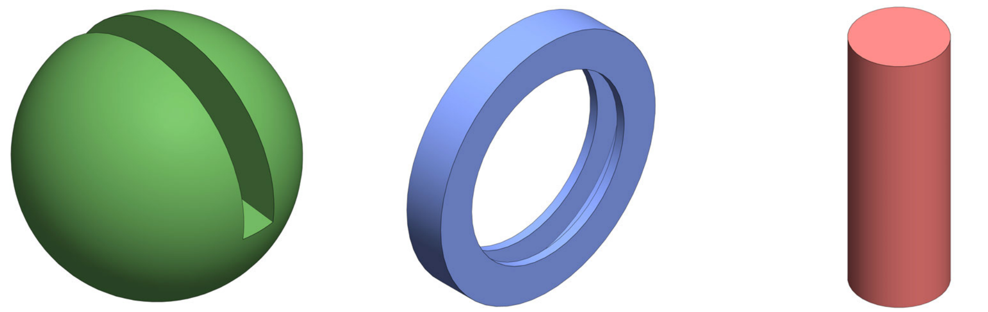

(a) Planet sphere with slot **(b)** Orbit ring with slot **(c)** Satellite peg

Figure 2-6 – The Three Fundamental IHC Components.

along a common central axis. For simplicity, in the following examples, the Orbit will remain fixed in place while the Planet and Satellite(s) move (in practice, both the Planet and Orbit can rotate independently). In terms of degrees-of-freedom, the Planet and Orbit can each only rotate about their shaft axis – all other degrees-of-freedom are constrained. Finally, the Satellite is added, completing the conceptual IHC assembly in Figure 2-8. The Satellite runs along the Planet and Orbit slots, sliding freely within each of them and always pointing towards the center of the planet. The Satellite is assumed to have non-zero mass and non-zero friction coefficient (it can experience normal, frictional, and inertial forces).

2.3.1 Assumptions for Example Motion Cases

A few example cases will now be presented to demonstrate various IHC motions. In each case, the Satellite is constrained to follow the slots in both the Planet and Orbit. We will qualitatively consider these motions and the potential forces that arise from them. A few other assumptions, listed in Table 2.1, also apply.

Table 2.1 – Assumptions for IHC Conceptual Examples

1	All components are assumed to be infinitely rigid.
2	The Satellite peg fits *exactly* within the Planet and Orbit slots, with zero backlash, lateral force, or preload/nesting/interference force.
3	The Satellite cannot tilt within either slot, and always remains pointed towards the center of the Planet sphere.
4	The Satellite always tracks inside both slots at once, placing it deterministically at the "intersection" of the two slots.

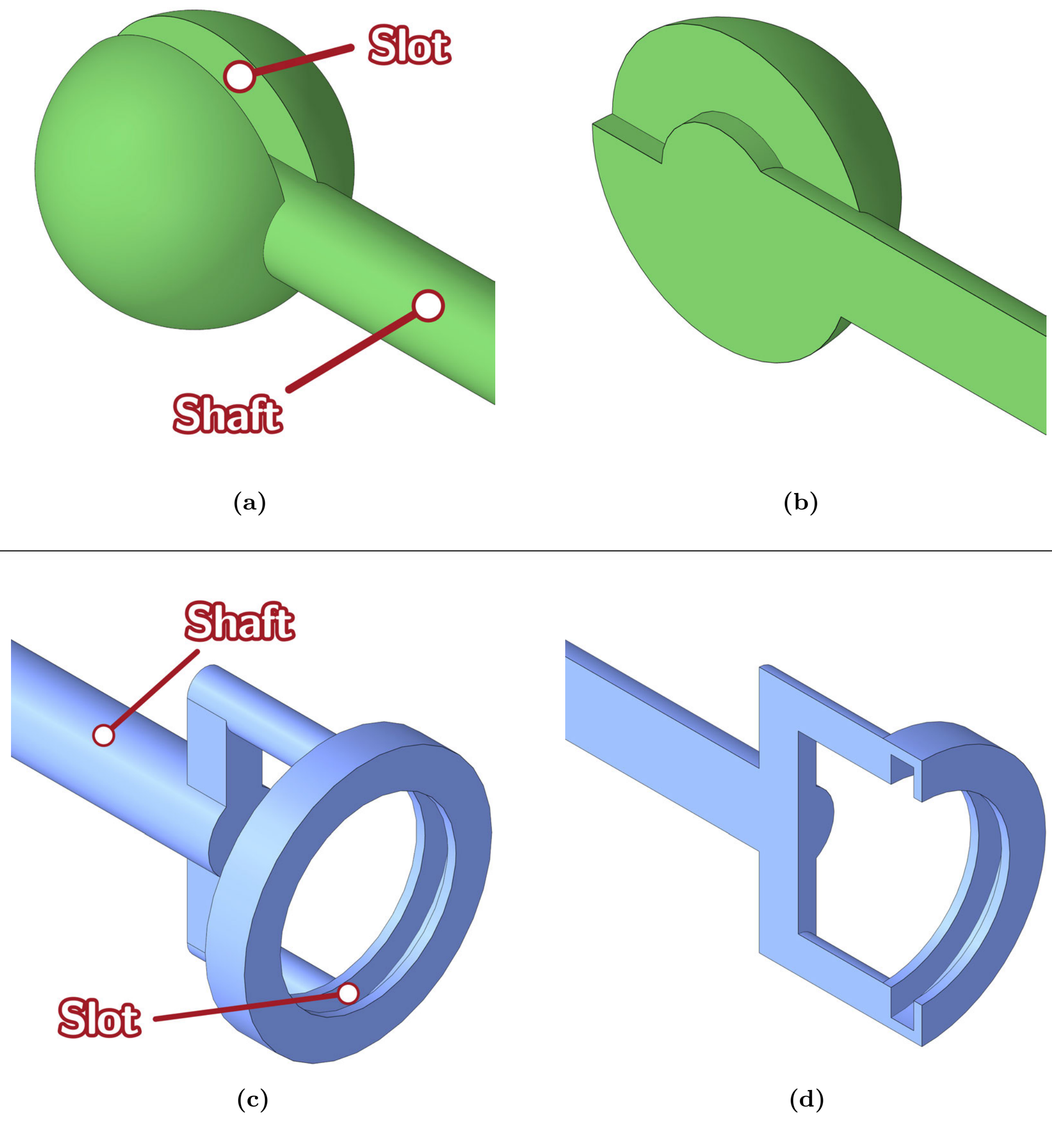

Figure 2-7 – Cutaway views showing the Satellite slots designed into the Planet and Orbit.

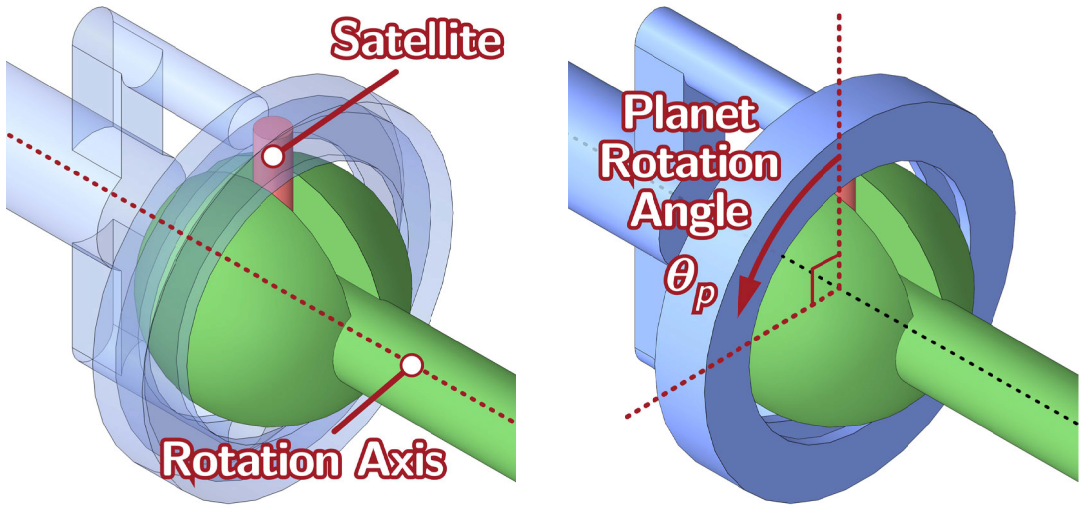

(a) (b)

Figure 2-8 – Isometric views of the Planet/Orbit/Satellite assembly. In this example and those following, the Satellite can slide along the Planet and Orbit slots. Any acceleration it experiences must result from normal and/or friction forces acting at these interfaces. (Note that in these examples, the Satellite is assumed to always point towards the "center" of the Planet).

2.3.2 Example Case #1 – Zero Torque Transmission

The first case considered is that presented in Figures 2-9 to 2-11, where the Orbit ring is exactly aligned with the "equator" of the Planet. When the Planet rotates, the Satellite follows a simple path and advances through the Orbit at constant speed. The Satellite does not move relative to the Planet and it experiences no lateral forces or acceleration. With no normal force acting between the Satellite and the Orbit sidewalls, there is no friction and the Satellite moves without resistance. In other words, for this hypothetical example, this is the minimally-engaged state where no torque is transmitted.

2.3.3 Example Case #2 – Orbit Engagement

Example Case #2 considers Figures 2-12 to 2-14. Here, the Orbit ring has been tilted by 40°. Although the orientation of the Orbit ring has changed, the component as a whole can still only rotate about the same central axis as the Planet. The tilt of the Orbit ring is subtle but has numerous cascading effects. A few of these include:

- The Satellite no longer moves along the "equator" of the Planet. It still moves through the Orbit's circular path but the motion is now inclined with respect to the Planet. It moves across the Planet's "equator" at rotation angles of 0° and 180°.
- The apparent Orbit-Satellite contact angle is no longer constant and now varies with position. It is most inclined at angles 0° and 180° (Figure 2-13a) and most shallow at angles 90° and 270°.

Example Case #1 – Zero Torque Transmission

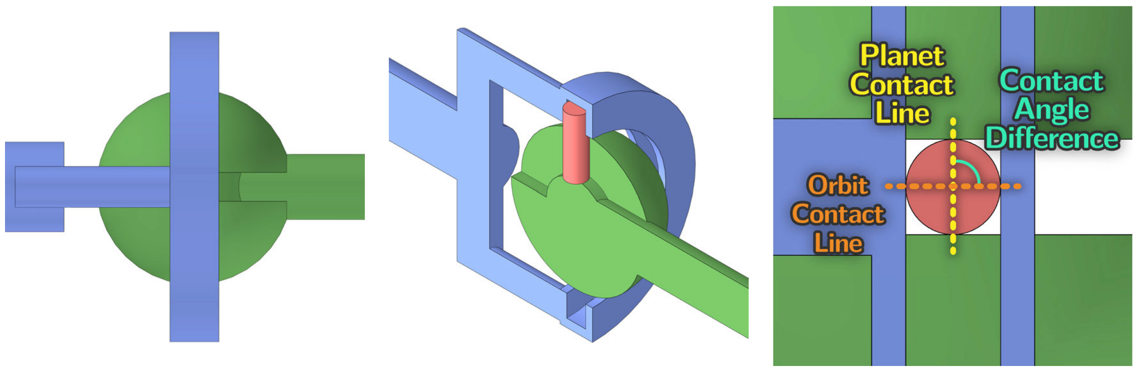

(a) (b) (c)

Figure 2-9 – Views of the Planet/Orbit/Satellite with 0° of Orbit tilt.
Figure 2-9a: Top view.
Figure 2-9b: Isometric view with cutaway along the Planet slot.
Figure 2-9c: Satellite axis cutaway view with Planet/Orbit contact lines marked.

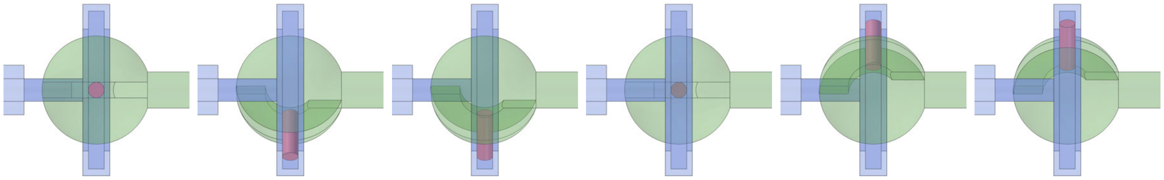

(a) $\theta_P = 0°$ **(b)** $\theta_P = 60°$ **(c)** $\theta_P = 120°$ **(d)** $\theta_P = 180°$ **(e)** $\theta_P = 240°$ **(f)** $\theta_P = 300°$

Figure 2-10 – Top view snapshots of one complete rotation by the Planet/Satellite (0° of Orbit tilt).

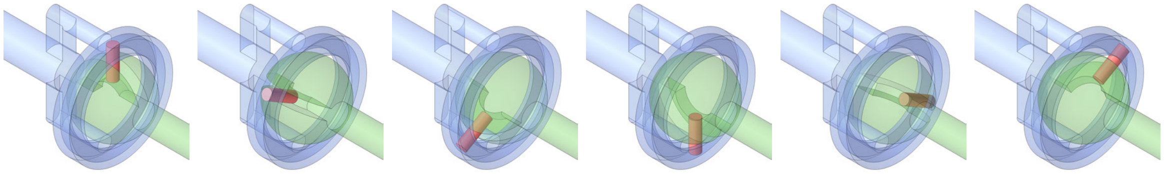

(a) $\theta_P = 0°$ **(b)** $\theta_P = 60°$ **(c)** $\theta_P = 120°$ **(d)** $\theta_P = 180°$ **(e)** $\theta_P = 240°$ **(f)** $\theta_P = 300°$

Figure 2-11 – Isometric view snapshots of one complete rotation by the Planet/ Satellite (0° of Orbit tilt).

- The Satellite no longer moves at constant velocity, which is not an immediately intuitive result. In the images shown, consider the location of Satellite's center-of-mass (CM), which could be assumed to be halfway along its length. In certain locations (90° and 270°) the CM is close to the Planet/Orbit rotation axis, while at others (0° and 180°) it is farther away. Since the Planet driving the Satellite maintains a *constant angular speed*, the Satellite's absolute speed therefore must vary based on its distance from the rotation axis. Therefore, it must undergo cycles of acceleration and deceleration. The normal and frictional contact forces are the only loads acting laterally on the Satellite, so they must drive this acceleration/deceleration process. The equal and opposite reactions must then be acting on the Planet/Orbit, meaning some net transmission of torque from Planet to Orbit occurs.
- The close-up cutaway pictured in Figure 2-12 hints at a potential mechanism for achieving lock-up and positive engagement. This scenario is not so different from that of a block on a shallow inclined plane; when the inclination angle gets low enough, the block can no longer slide from purely vertical applied load. This foreshadows that Satellites will exhibit critical contact angles beyond which they will lock up and be unable to slip, no matter how much load is imposed.

Note that all of these effects occur simply by tilting the Orbit ring. **This tilt corresponds to the IHC "clutch angle" – in these examples it is shown as fixed in place, but in practice can be actively controlled to smoothly modulate torque transmission.**

2.3.4 Example Case #3 – Multiple Satellites

Third, we consider the same geometry as in the previous example, but add five more satellites running in their own evenly-spaced Planet slots as shown in Figure 2-16. The use of multiple satellites is a natural extension to the concept, bringing many benefits:

- Greater torque can be transmitted as more Satellites carry load at each moment in time.
- Certain loads from opposing Satellites will cancel one another out due to symmetry, reducing vibration and bearing loads.
- A single Satellite results in strongly cyclical torque output, *i.e.* significant ripple. With many Satellites in one system, the total IHC torque is "handed off" between individual satellites and the net torque output is smoothed. Minimization of torque ripple remains a potential area of exploration for future work.

Example Case #2 – Orbit Engagement

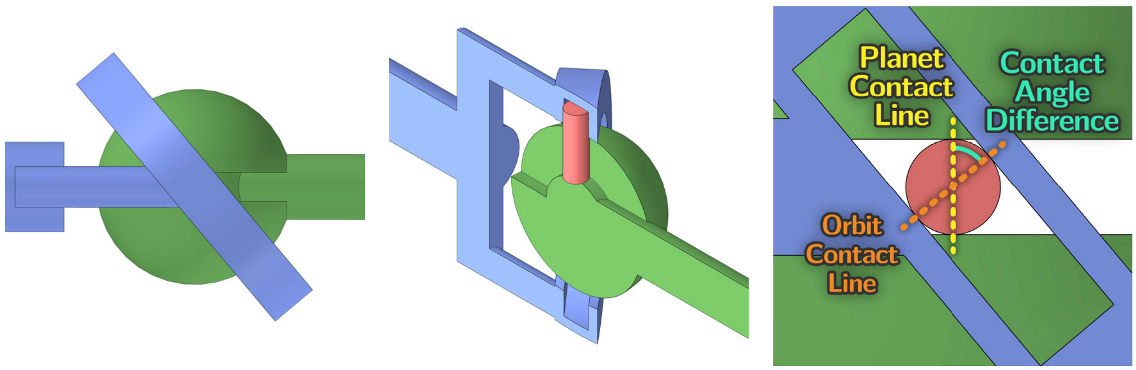

(a) **(b)** **(c)**

Figure 2-12 – Views of the Planet/Orbit/Satellite with 40° of Orbit tilt.
Figure 2-12a: Top View. 40° Orbit tilt is clearly visible.
Figure 2-12b: Isometric view with cutaway along the Planet slot.
Figure 2-12c: Satellite axis cutaway-view with Planet/Orbit contact lines marked.

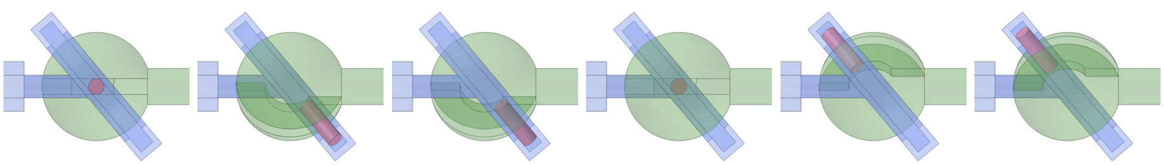

(a) $\theta_P = 0°$ **(b)** $\theta_P = 60°$ **(c)** $\theta_P = 120°$ **(d)** $\theta_P = 180°$ **(e)** $\theta_P = 240°$ **(f)** $\theta_P = 300°$

Figure 2-13 – Top view snapshots of one complete rotation by the Planet/Satellite (40° of Orbit tilt).

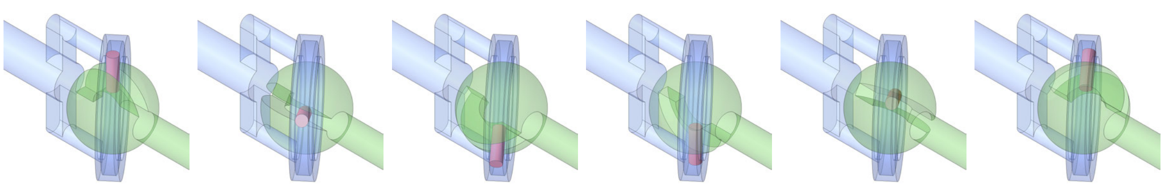

(a) $\theta_P = 0°$ **(b)** $\theta_P = 60°$ **(c)** $\theta_P = 120°$ **(d)** $\theta_P = 180°$ **(e)** $\theta_P = 240°$ **(f)** $\theta_P = 300°$

Figure 2-14 – Isometric view snapshots of one complete rotation by the Planet/Satellite (40° of Orbit tilt).

Example Case #2 – Partial Engagement

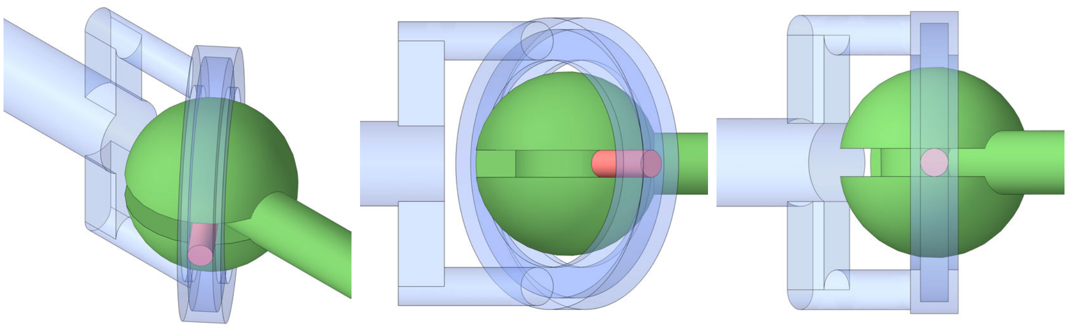

(a) (b) (c)

Figure 2-15 – Isometric, side, and on-axis views (respectively) of Example Case #2. Here, the Planet sits at the 90° rotation position; in this and the 270° position, the Orbit/ Satellite Contact Line is horizontal despite the tilt of the Orbit ring. Together with Figure 2-12, it's clear the orientation of the Orbit /Satellite Contact Line changes as the Planet/Satellite rotate relative to the Orbit.

Example Case #3 – Multiple Satellites

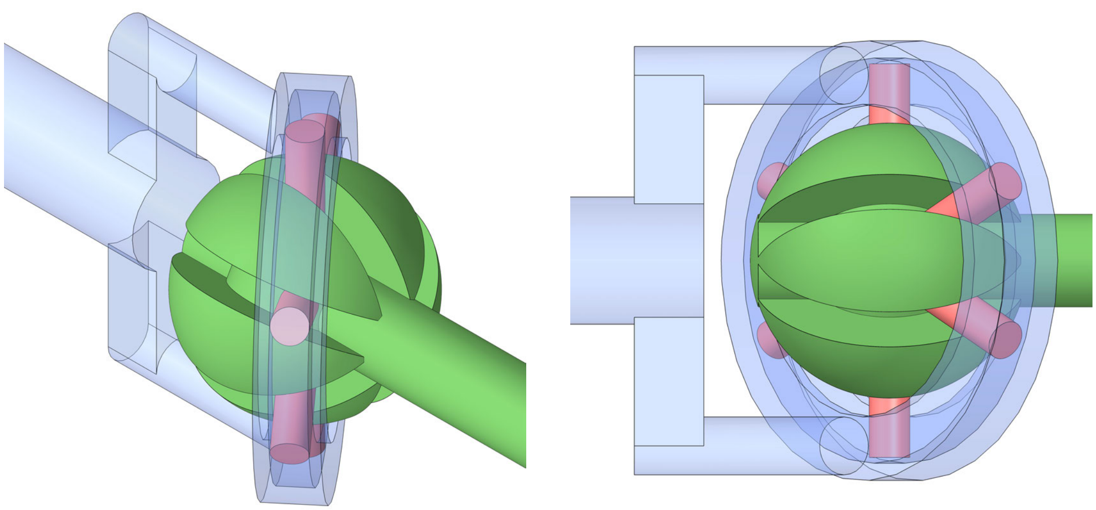

(a) (b)

Figure 2-16 – Isometric and front views of Example Case #3 with six satellites present. Symmetry is achieved by incorporating five additional satellites. This helps to balance out non-torque reaction loads, increases the total torque capacity, and reduces torque ripple in operation (the Satellites "hand off" load to one another as they traverse the Orbit).

2.3.5 Example Case #4 – Altered Planet Slot Shape

Finally, we consider one last modification – changing the shape of the Planet slot. This change has far-reaching implications in terms of modeling, design, fabrication, assembly, *etc.* Functionally, it allows the Satellite to achieve extremely shallow contact angles, such as those shown in Figure 2-17. Even for very low coefficients of friction, such shallow contact angles allow high forces to be developed and lockup to be achieved. Whereas the contact angles in earlier examples were limited by the rotation range of the Orbit ring, this modification allows arbitrarily shallow contact angles to be obtained.

Case #4 – Altered Planet Slot Shape

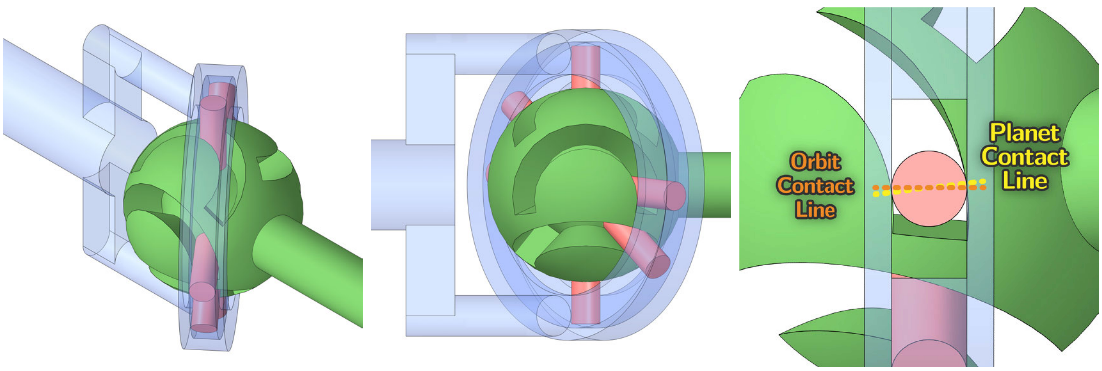

(a) **(b)** **(c)**

Figure 2-17 – Front, isometric, and Satellite-axis views of Example Case #4 with curved Planet slot geometry. By curving the Planet slots, extremely shallow contact angles can be achieved – pictured are the near-parallel Planet and Orbit contact lines. This modification not only increases the mechanism's torque capacity, but also allows it lock up completely even when very low friction coefficients are observed.

2.4 Modeling Couplings as Rotary Dampers

In several of the previous examples, "mechanical impedance" played a key role. These impedances will now be considered quantitatively – to do so, a rotary dashpot/damper model (Figure 2-18 and Table 2.2) is presented.

A rotary dashpot is a mechanical element that produces torque as the result of different rotation speeds of its input/output. An ideal dashpot, being massless, behaves like a spring or any other two-load element – its input and output torques are exactly equal. Real mechanical dampers are more complicated due to having non-zero compliance and rotational inertia. This allows their *instantaneous* input and output torques to differ. Their input load is not transmitted *immediately* to the output, and some energy can briefly be stored internally as elastic and kinetic energy (though this is very quickly re-released to the output). **However, if input/output shaft rotation speeds are constant, the time-averaged, steady-state values for torque input and torque output are equal.**

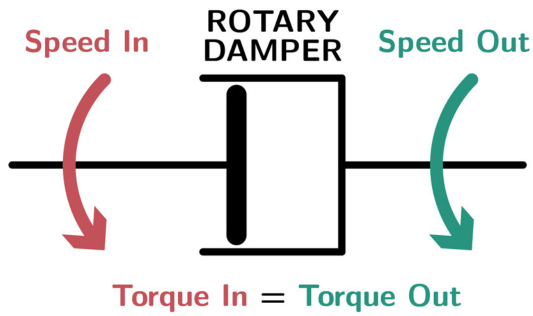

Figure 2-18 – Diagram of an ideal Rotary Damper. The torque transmitted by an ideal rotary damper is proportional to the slip speed, *i.e.* the difference between its input and output speeds. Ideal rotary dampers are two-force members and have equal input and output torques.

The behavior of a basic rotary dashpot is given by Equations (2.1) and (2.2). These equations convey the relationship between the three most important operating parameters – input speed, output speed, torque – with the help of the damping coefficient c_d.

$$\bar{T}_d = c_d(\omega_2 - \omega_1) \tag{2.1}$$

$$\bar{T}_d = c_d(\Delta\omega_{12}) \tag{2.2}$$

Where:

$$\begin{aligned}
\bar{T}_d &= \text{Time-average of torque transmitted through the damper} \\
c_d &= \text{Damping coefficient} \\
\omega_1, \omega_2 &= \text{Angular velocities of damper input/output (constant)} \\
\Delta\omega_{12} &= \text{Angular slip rate, } (\omega_2 - \omega_1)
\end{aligned}$$

For ideal dampers c_d is constant, but that is often not true for real couplings. Various models for c_d can instead be used to incorporate speed sensitivity, full coupling (dis)engagement, and even variable-mode operation. Examples for several of these behaviors are given in Table 2.2.

2.5 Characteristic Maps for Slipping Couplings

Conceptually, c_d proves most useful for "connecting the dots" between the qualitative and quantitative behaviors of couplings in operation. However, slip-coupling performance is usually expressed directly using plots of the coupling's slip speed vs. torque output relationship. These plots capture a coupling's performance across all its possible operating points, the boundaries of which denote the coupling's performance envelope. **Such charts are called "characteristic maps."** They are similar to, and

Table 2.2 – Damping Coefficients for Several Coupling Types

Equivalent c_d	**Notes**	**Behavior**
$\boldsymbol{c_d = 0}$	(Zero)	Torque is zero regardless of input or output speed. *Example: Fully-disengaged (open) friction clutch*
$\boldsymbol{c_d = \infty}$	(Infinity)	No defined relationship between speed and torque; they instead depend on the instantaneous operating conditions (inertias & torque efforts). *Examples: Rigid couplings; fully-engaged friction coupling (no slip); synchronous magnetic couplings (no slip)*
$\boldsymbol{c_d = k}$	$k > 0$ k is Constant	Torque scales linearly with the difference in input/output speed. *Example: Viscous coupling (fluid shearing)*
$\boldsymbol{c_d = k\Delta\omega}$	$k > 0$, k is Constant $\Delta\omega$ is slip rate	Damping coefficient c_d scales linearly with speed. Torque scales quadratically ($\bar{T}_d \propto \Delta\omega^2$). *Examples: Constant-fill fluid coupling; non-variable asynchronous magnetic coupling*
$\boldsymbol{c_d = k\Delta\omega}$	k is Positive k is Variable $\Delta\omega$ is slip rate	Similar to the previous example, except k can be actively controlled. Torque scales quadratically with speed ($\bar{T}_d \propto \Delta\omega^2$). *Example: Variable fluid coupling; variable asynchronous magnetic coupling*
$\boldsymbol{c_d = k\frac{\Delta\theta}{\Delta\omega}}$	k is Positive k is Constant $\Delta\omega$ is slip rate	Mathematical representation of an elastic coupling with a fixed spring constant. In the full torque expression, $\Delta\omega$ cancels out. $\bar{T}_d$ instead depends on angular displacement rather than slip rate. *Example: Elastic coupling (with rotary stiffness)*

analogous with, the characteristic curves used in fluid pump design. Figure 2-20 shows an example of a characteristic map for a constant-fill (non-variable) industrial hydrodynamic coupling from Voith.

When more than one variable parameter significantly affects torque output, a coupling's characteristic map can be charted along multiple axes. Surface or contour plots are often used for this. For example, the variable-fill hydrodynamic coupling shown in Figure 2-21 can pump fluid into or out of its housing to modulate torque transmission. The magnitude of torque transmitted scales with the housing's fill level – less fluid in the housing produces less torque, and vice-versa. This coupling's torque output depends on both slip speed and fill level, so its characteristic map is three-dimensional.

The characteristic map is the single most useful and efficient tool for communicating the performance of a variable-slip coupling. Thus, the goals of simulating IHC characteristic maps and testing them against a physical prototype were of the highest priority.

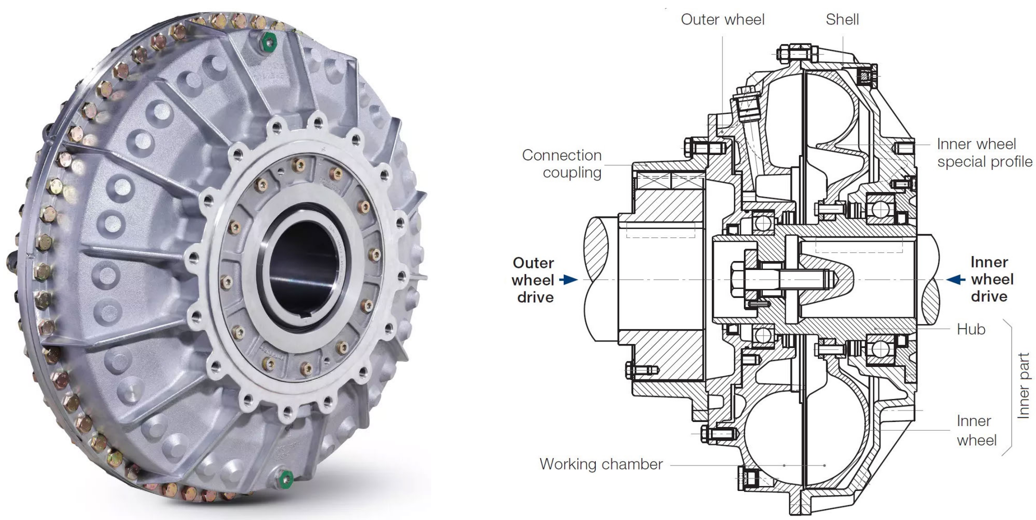

Figure 2-19 – Photo [34] and cutaway sketch [32] of a Voith Type-T constant-fill fluid coupling.

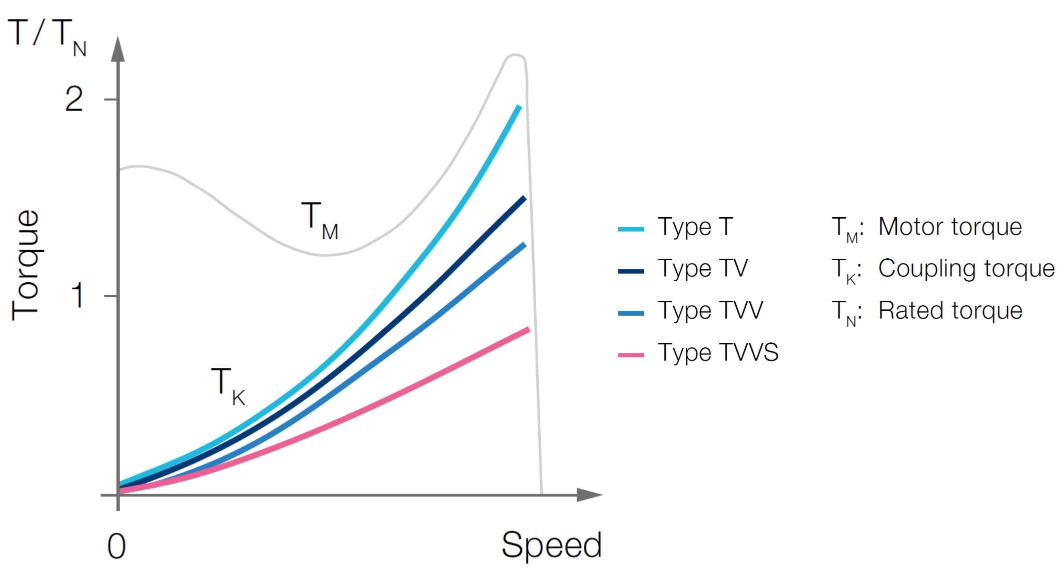

Figure 2-20 – Example characteristic plots for several Voith constant-fill fluid couplings. Being constant-fill couplings, these devices cannot actively modulate torque transmission – it varies only with slip rate.

(a) [34]

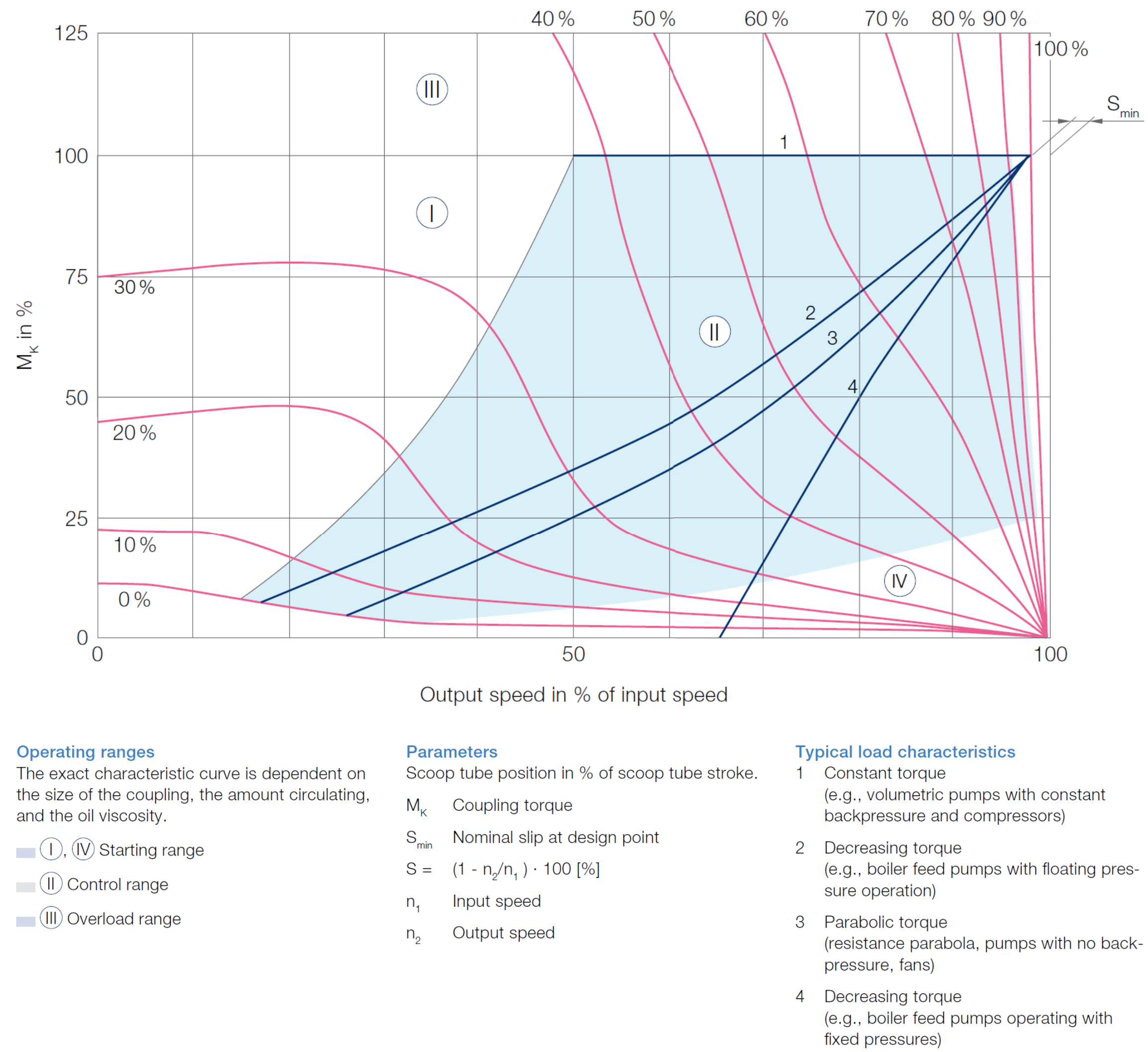

(b) [11]

Figure 2-21 – Photo of a cutaway Voith TPKL variable-fill fluid coupling alongside an example contour plot of a variable-fill coupling's characteristic map. Several contours are plotted, each describing the coupling's behavior at a different fill level (from 0% to 100% in increments of 10%). This data could also be represented using a 3D surface plot.

Chapter 3

Modeling Part 1:

Overview, Inputs, & Geometry/Kinematics

3.1 Modeling – Overview, Goals, & Scope

The modeling portion of this work covers numerous contributions that enable the quantitative and deterministic analysis of IHCs. This includes various definitions, derivations of transforms and geometry, solutions for kinematic & equilibrium equations, estimates of thermal behaviors, numerical techniques, and tools for analyzing the results in software. There is no preexisting body of work concerning IHC modeling, so the developments presented here are newly derived from the ground-up.

The goals of these modeling efforts were the following:

1. **Create a Modeling Framework:** Create a framework and toolset for quantitatively predicting and/or assessing IHC performance. The most important output from this is the IHC characteristic map. The creation of this model occupies the majority of this chapter and the next.
2. **Facilitate Optimization:** Enable the design of real-world IHCs via parameter sweeps and sensitivity analyses.
3. **Enhance Communication:** Generate plots, animations, and other visualizations to better understand and communicate IHC behaviors.
4. **Enable Future Work:** Create a common foundation upon which future work in the field can easily be built.

A primary result of these efforts is ***ihcMATLAB***, a custom-built MATLAB toolbox for analyzing, optimizing, and visualizing IHCs. It fully implements the model described in this chapter and the next in addition to offering a variety of other features. It can produce characteristic maps, conduct parameter sweeps, facilitate sensitivity analyses, and generate a multitude of illustrative charts and animations. Results for one or more IHC configurations can be easily investigated, including kinematics data, contact stresses, bearing loads, heat flux, and others. Essentially any parameter in the model can be analyzed on an instantaneous or time-averaged basis to assist with the IHC design process.

This chapter (Chapter 3) covers the model layout, conventions, definitions, geometry, and the derivation of the many kinematics variables. Chapter 4 introduces the Satellite geometry, then covers forces/moments, solutions to the equilibrium equations, the combined effect of many Satellites, IHC power input/output, thermal loads, and the selection of IHC parameters for a physical prototype.

3.2 Analysis Process & High-Level Assumptions

ihcMATLAB is structured according to the flowchart in Figure 3-1. It uses calculation loops at many different "layers" of the model, and the general sequence is:

1. Assign values and settings for a given test case.
2. Perform all calculations on a single Satellite at a single timestep.
3. Repeat step 2 for every timestep.
4. Extend the single-Satellite results to the other Satellites to obtain the results for the whole test case.
5. Repeat steps 1-4 for every IHC test case of interest. At a minimum this generally means varying β_O (the clutch angle). However, other design parameters can also be varied to investigate their effect on performance.

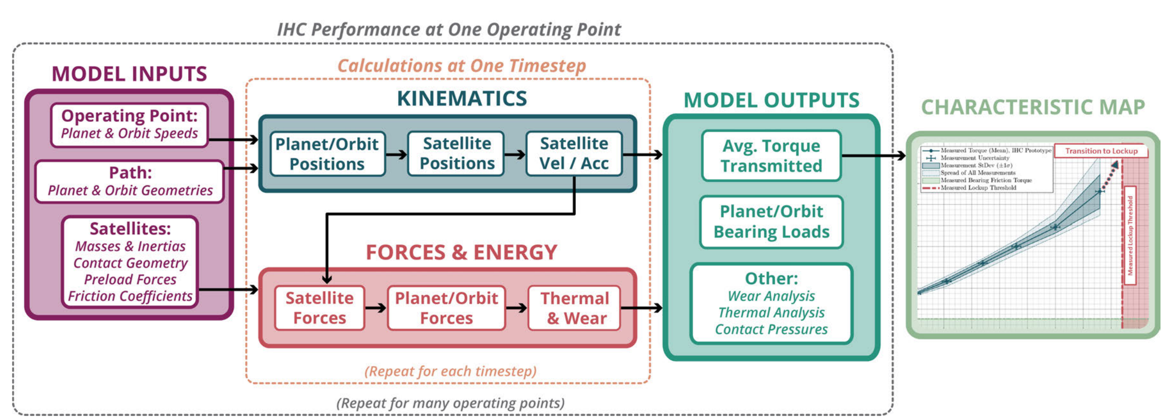

Figure 3-1 – Flowchart of the core ihcMATLAB calculation loops.

The analysis procedure makes the three key assumptions described in Table 3.1: (1) Causality, (2) Dynamic

Determinacy, and (3) Operation at Steady-State Equilibrium:

Table 3.1 – Key High-Level Model Assumptions

Causality	Each step of the flowchart proceeds in a strictly sequential and causal order. That is, there are no feedback loops or bidirectional "flows." The output of each step must be fully independent of any future steps.
Dynamic Determinacy	The system is considered to be dynamically determinate. Once the kinematics are known, all forces can be directly calculated from the equilibrium equations. This assumption, when accurate, substantially reduces model complexity by avoiding the difficult task of calculating loads from a dynamically indeterminate state (for example, needing to resolve varying contact pressures across the various sliding interfaces). Satisfying this assumption requires certain design choices to be made with respect to the physical mechanism itself (particularly the Satellites). This is discussed further in Chapter 4.
Steady-State Operation	The IHC simulates coupling behavior at steady-state equilibrium. That is, the Planet/Orbit shafts rotate at constant speeds throughout the duration of each simulation.

3.3 Notation

3.3.1 Subscripts & Superscripts

Numerous variables are introduced in the coming chapters which are accompanied by subscripts, superscripts, and/or other modifiers. In general:

- **Subscripts ($\boldsymbol{x_a}$)** are used to indicate the relevant physical part, frame(s)-of-reference, and/or direction of flow.
- **Superscripts ($\boldsymbol{x^a}$)** indicate subcomponents of various types. These include:
    - **Square-Bracket Superscripts** $\left(\boldsymbol{x^{[a]}}\right)$ reference discrete timesteps.
    - **Curly-Brace Superscripts** $\left(\boldsymbol{x^{\{a\}}}\right)$ are used flexibly to refer to indices, objects, *etc.* depending on context.
- **An asterisk in the subscript ($\boldsymbol{x_{S^*}}$)** indicates that the base component's local coordinate frame is referenced. For example, S^* refers to a Satellite's local coordinate frame. If no asterisk is used, global XYZ coordinates are implied.
- **A Satellite subscript without a number ($\boldsymbol{x_S}$)** refers to ***S1***, the "Primary" Satellite. Most Satellite-related calculations only need to be completed for this one Primary Satellite, then the results can be transferred to the other Satellites by applying a time-

shift “shortcut” as described in Chapter 4. Multi-Satellite numbering is typically avoided unless a particular derivation requires it.

A variety of notation examples are provided in Table 3.2.

Table 3.2 – Notation Examples

Example:	Description:
$\boldsymbol{x}^{\boldsymbol{A}}_{\boldsymbol{BC}}$	Component $\boldsymbol{A}$ of variable $\boldsymbol{x}$, corresponding to object $\boldsymbol{C}$, relative to object $\boldsymbol{B}$.
$\boldsymbol{x}^{\boldsymbol{A}[\mathbf{3}]}_{\boldsymbol{BC}}$	Component $\boldsymbol{A}$ of variable $\boldsymbol{x}$, at timestep $[\mathbf{3}]$, corresponding to object $\boldsymbol{C}$, relative to object $\boldsymbol{B}$.
$\omega_{\boldsymbol{OP}}$	Angular velocity $(\boldsymbol{\omega})$ of the Planet $(\boldsymbol{P})$ relative to the Orbit $(\boldsymbol{O})$.
$\vec{\boldsymbol{v}}^{\boldsymbol{x}}_{\boldsymbol{S1}}$	$\boldsymbol{x}$ component of the velocity vector $(\vec{\boldsymbol{v}})$ of Satellite #1 $(\boldsymbol{S1})$ in global coordinates.
$\vec{\boldsymbol{v}}^{\boldsymbol{y}}_{\boldsymbol{OS2}}$	$\boldsymbol{y}$ component of the velocity vector $(\vec{\boldsymbol{v}})$ for Satellite #2 $(\boldsymbol{S2})$, relative to the Orbit $(\boldsymbol{O})$, in global coordinates.
$\vec{\boldsymbol{r}}^{\boldsymbol{FN1}}_{\boldsymbol{S^*}}$	Position vector $\vec{\boldsymbol{r}}$ of Normal Force #1 $(\boldsymbol{FN1})$, relative to the Primary Satellite, in the Satellite’s local coordinate frame $(\boldsymbol{S^*})$.
$\vec{\boldsymbol{F}}^{\boldsymbol{N3}}_{\boldsymbol{PS1}}$	Vector of Normal Force #3 $(\boldsymbol{FN3})$ acting on Satellite #1 $(\boldsymbol{S1})$ by the Planet $(\boldsymbol{P})$.

3.3.2 Column Vector Orientation

Vectors and vector arrays are always organized in column-vector form. For example, the coordinate $\vec{\boldsymbol{r}} = (x, y, z)$ assumes the form:

$$\boxed{\vec{\boldsymbol{r}} = \begin{bmatrix} x \\ y \\ z \end{bmatrix}} \tag{3.1}$$

Coordinate arrays represent a variety of quantities, with the superscript indicating the type of array. Square bracket superscripts reference discrete timesteps – Equation (3.2) gives an example array whose columns represent the coordinates of a single point at n_t different timesteps:

$$\boxed{\vec{\boldsymbol{r}} = \begin{bmatrix} x^{[1]} & x^{[2]} & x^{[3]} & \dots & x^{[n_t]} \\ y^{[1]} & y^{[2]} & y^{[3]} & \dots & y^{[n_t]} \\ z^{[1]} & z^{[2]} & z^{[3]} & \dots & z^{[n_t]} \end{bmatrix}} \tag{3.2}$$

Brace superscripts reference indices, for example the coordinates of a curve's many points at a single timestep. Equation (3.3) is an example of such an array, which represents n_c different point coordinates at a single point in time:

$$\boxed{\vec{\boldsymbol{r}}(t) = \begin{bmatrix} x^{\{1\}} & x^{\{2\}} & x^{\{3\}} & \dots & x^{\{n_c\}} \\ y^{\{1\}} & y^{\{2\}} & y^{\{3\}} & \dots & y^{\{n_c\}} \\ z^{\{1\}} & z^{\{2\}} & z^{\{3\}} & \dots & z^{\{n_c\}} \end{bmatrix}} \tag{3.3}$$

Bracket and brace notation can be combined – see Equation (3.4). The array "slice" shown contains n_c point coordinates at timestep $t^{[i]}$. This slice is size $(3 \times n_c \times 1)$. The full array would be of size $(3 \times n_c \times n_t)$ (where n_c and n_t are the number of curve points and timesteps, respectively):

$$\boxed{\vec{\boldsymbol{r}}\left(t^{[i]}\right) = \begin{bmatrix} x^{\{1\}[i]} & x^{\{2\}[i]} & x^{\{3\}[i]} & \dots & x^{\{n_c\}[i]} \\ y^{\{1\}[i]} & y^{\{2\}[i]} & y^{\{3\}[i]} & \dots & y^{\{n_c\}[i]} \\ z^{\{1\}[i]} & z^{\{2\}[i]} & z^{\{3\}[i]} & \dots & z^{\{n_c\}[i]} \end{bmatrix}} \tag{3.4}$$

While multi-dimensional arrays can be very useful for implementing the model in software, this thesis generally avoids them to reduce the potential for confusion.

3.4 Global Coordinate Systems

A number of coordinate frames are used to derive important relationships, keep track of useful information, and visualize results in convenient and meaningful ways.

3.4.1 Global Cartesian Coordinates: (X, Y, Z)

The first coordinate system is the global XYZ frame shown in Figure 3-2. This Cartesian coordinate system serves as a static and inertial global reference frame. Each IHC is located within the global XYZ frame per three rules:

1. The center of the IHC Planet lies on the point $(X, Y, Z) = (0, 0, 0)$.
2. The Planet's "equatorial plane" coincides with the global $X = 0$ plane.
3. The Planet and Orbit are both oriented along, and rotate about, the X axis.

The direction of $+X$ can be chosen arbitrarily. However, care should be taken to ensure that, once chosen, its sign is always referenced correctly.

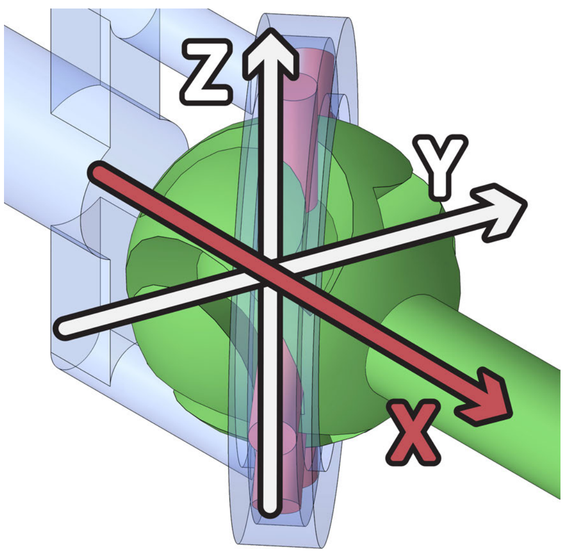

(a) IHC Conceptual Model

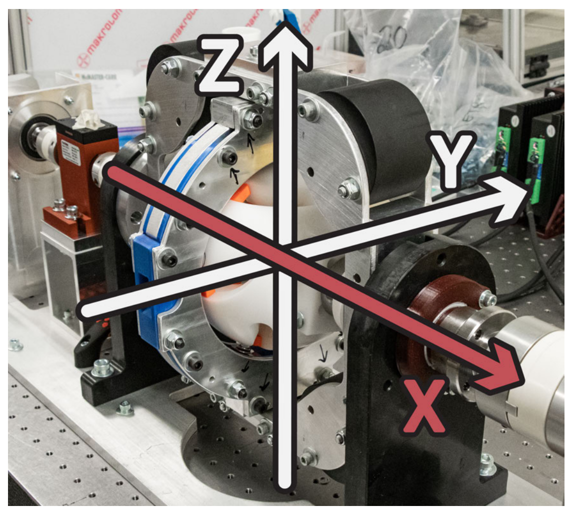

(b) ihcBENCH Prototype

Figure 3-2 – The convention for IHC global XYZ coordinates. The global X axis lies along the mechanism's axis of rotation, the Z axis points vertically upwards, and the Y axis points such that the system follows the right-hand-rule convention.

3.4.2 Global Spherical Coordinates: (ρ, θ, ϕ)

A global spherical coordinate system for IHCs is defined using the variables (ρ, θ, ϕ). The definitions used were specifically chosen to naturally map to IHC motions: θ corresponds to rotation, ϕ corresponds to angular tilt from the Planet centerline, and ρ corresponds to radial position from the Planet center (see Table 3.3 and Figure 3-3 for explanations and a visual example). The Planet, Orbit, and Satellites each have their own ρ[1] and θ,[2] while only the Satellite has a ϕ value.[3] This convention for (ρ, θ, ϕ) differs from

[1] ρ_P, ρ_O, and ρ_S
[2] θ_P, θ_O, and θ_S
[3] ϕ_S

Table 3.3 – Global Spherical Coordinate Variables (ρ, θ, ϕ)

Variable	Valid Range	Description
$\boldsymbol{\rho}$	***Constant***	Radial distance from the global XYZ origin $(0,0,0)$ to a point (x,y,z). (Note that the IHC design keeps all components at fixed radii).
$\boldsymbol{\theta}$	$\boldsymbol{0 \leq \theta < 2\pi}$	Rotation of an object about the global X axis, with $\theta = 0$ starting at the half-plane above the X axis. Rotation is counter-clockwise positive per the normal right-hand-rule convention. The subscript denotes the object referred to (the Planet, Orbit, and Satellite rotation angles are θ_P, θ_O, and θ_S, respectively).
$\boldsymbol{\phi}$	$\boldsymbol{\frac{-\pi}{2} \leq \phi \leq \frac{+\pi}{2}}$	Inclination from the $X = 0$ plane (the plane where the Planet's "equator" lies). Positive ϕ indicates inclination towards the $+X$ axis.

common standards such as ISO 80000-2:2019 [35].

3.4.3 Global Coordinate Transforms: $(x, y, z) \leftrightarrow (\rho, \theta, \phi)$

XYZ coordinates can be converted to (ρ, θ, ϕ) using Equations (3.5) to (3.7):

$$\rho = \sqrt{x^2 + y^2 + z^2} \tag{3.5}$$

$$\theta = atan2(-y, z) \tag{3.6}$$

$$\phi = atan2\left(x, \sqrt{y^2 + z^2}\right) \tag{3.7}$$

Here, $atan2()$ is the two-argument inverse tangent function, θ should be wrapped to $[0, 2\pi)$, and ϕ should be wrapped to $\left[\frac{-\pi}{2}, \frac{+\pi}{2}\right]$. The reverse transform, from (ρ, θ, ϕ) to XYZ, uses Equations (3.8) to (3.10):

$$x = \rho \sin(\phi) \tag{3.8}$$

$$y = -\rho \cos(\phi) \sin(\theta) \tag{3.9}$$

$$z = \rho \cos(\phi) \cos(\theta) \tag{3.10}$$

This transformation can also be expressed using a series of 4x4 Homogeneous Transformation Matrices (HTMs):

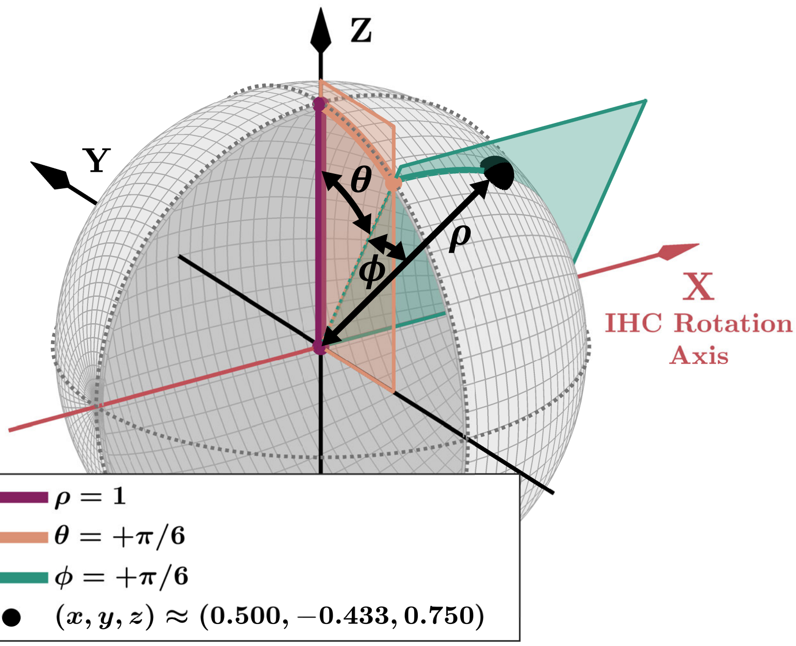

Figure 3-3 – Illustration of the (X, Y, Z) and (ρ, θ, ϕ) global coordinate systems using a cutaway sphere. Both the (X, Y, Z) and (ρ, θ, ϕ) systems are used to represent coordinates and motions.

$$\begin{bmatrix} x \\ y \\ z \\ 1 \end{bmatrix} = \begin{bmatrix} 1 & 0 & 0 & 0 \\ 0 & \cos(\theta) & -\sin(\theta) & 0 \\ 0 & \sin(\theta) & \cos(\theta) & 0 \\ 0 & 0 & 0 & 1 \end{bmatrix} \begin{bmatrix} \cos(\phi) & 0 & \sin(\phi) & 0 \\ 0 & 1 & 0 & 0 \\ -\sin(\phi) & 0 & \cos(\phi) & 0 \\ 0 & 0 & 0 & 1 \end{bmatrix} \begin{bmatrix} 1 & 0 & 0 & 0 \\ 0 & 1 & 0 & 0 \\ 0 & 0 & 1 & \rho \\ 0 & 0 & 0 & 1 \end{bmatrix} \begin{bmatrix} 0 \\ 0 \\ 0 \\ 1 \end{bmatrix} \tag{3.11}$$

3.5 Planet/Orbit Geometry

With the global coordinate systems defined, the virtual geometry of the Planet and Orbit can be envisioned and created. This research considers constant-curvature (circular/semicircular) geometries for both the Planet and Orbit. As a first investigation into IHCs, the choice of constant-curvature geometry offers a few important advantages:

- Constant-curvature arcs are sufficient for testing the validity of the IHC concept. Greater complexity would unnecessarily increase project risk.
- Constant-curvature geometries tend to be easier to create – mathematically, virtually, and physically.
- Constant-curvature mechanical interfaces remain conformal when moved relative to one

another. In other words, sliding parts can maintain large contact areas and low surface stresses as they move across one another.

3.5.1 Generating the Orbit Curve Geometry

The Orbit curve is a circular arc whose geometry and location are defined by three parameters: the **Orbit radius $\boldsymbol{\rho_O}$**, the **Orbit tilt angle $\boldsymbol{\beta_O}$**, and the **rotation angle $\boldsymbol{\theta_O}$**. As can be seen in Figure 3-4, it resembles a literal "orbit" and at $(\boldsymbol{t = 0})$ crosses through the $+\boldsymbol{Z}$ axis. The two-step process for constructing the initial Orbit curve is as follows:

1. Parameterize a circle of radius $\boldsymbol{\rho_O}$ in the $\boldsymbol{X = 0}$ plane, centered at $(\boldsymbol{Y}, \boldsymbol{Z}) = (\boldsymbol{0}, \boldsymbol{0})$
2. Rotate the circle about the $\boldsymbol{Z}$ axis by the angle $\boldsymbol{\beta_O}$.

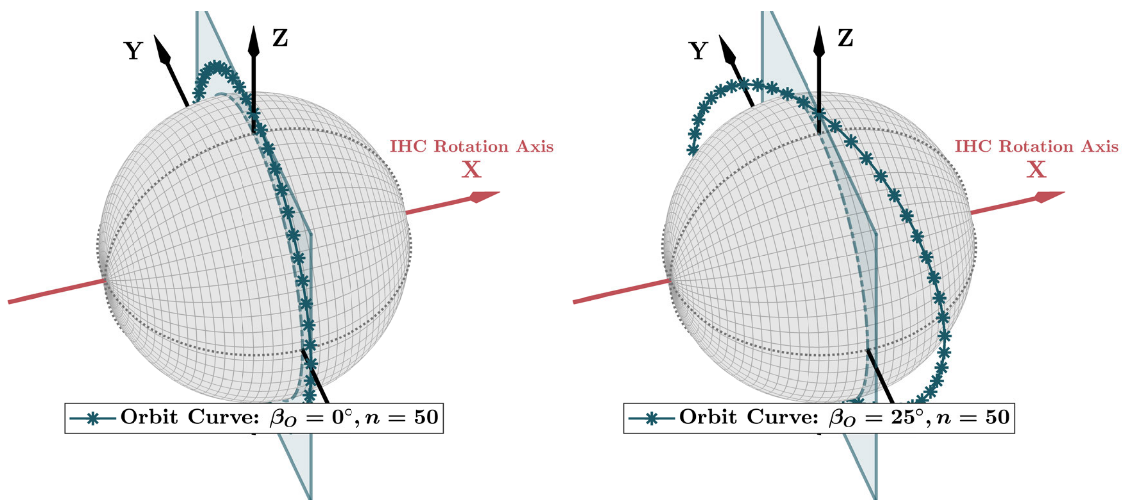

(a) (b)

Figure 3-4 – Example Orbit curves generated with various β_O values. In these examples, only $n_O = 50$ points are used so they can be clearly seen. The default in ihcMATLAB is $n_O = 1500$. The Orbit curves are generated with radius ρ_O. In this work, ρ_O is always larger than the Planet radius (ρ_P), so the Orbit curves are shown as being raised away from the surface of the sphere.

ihcMATLAB is a discrete numerical model, so geometries are represented as discrete parameterized curves (arrays of discrete points). Step 1 for creating the Orbit curve is the generation of the initial circle in the $\boldsymbol{X = 0}$ plane, represented by the coordinates in the 3-by-$\boldsymbol{n_O}$ matrix $\boldsymbol{S_{O'}}$ in Equation (3.12):

$$\boldsymbol{S_{O'}} = \begin{bmatrix} 0 & 0 & \cdots & 0 \\ \rho_O \cos\left(\tau_O^{\{1\}}\right) & \rho_O \cos\left(\tau_O^{\{2\}}\right) & \cdots & \rho_O \cos\left(\tau_O^{\{n_O\}}\right) \\ \rho_O \sin\left(\tau_O^{\{1\}}\right) & \rho_O \sin\left(\tau_O^{\{2\}}\right) & \cdots & \rho_O \sin\left(\tau_O^{\{n_O\}}\right) \end{bmatrix} \tag{3.12}$$

The entries of $S_{O'}$ are:

$$\boldsymbol{S_{O'}^{\{i\}}} = \begin{bmatrix} x_{O'}^{\{i\}} \\ y_{O'}^{\{i\}} \\ z_{O'}^{\{i\}} \end{bmatrix} = \begin{bmatrix} 0 \\ \rho_O \cos\left(\tau_O^{\{i\}}\right) \\ \rho_O \sin\left(\tau_O^{\{i\}}\right) \end{bmatrix} \tag{3.13}$$

In Equations (3.12) and (3.13), τ_O is a parameterizing variable – a 1-by-n_O vector of points from $[0, 2\pi)$. n_O is the number of parameterizing points and its value is specified by the user. The points in τ_O should be evenly spaced, with the difference between any two neighboring points being $\Delta\tau_O$. As the first point is $\tau_O^{\{1\}} = 0$, the last point $\tau_O^{\{n_O\}}$ should be $\Delta\tau_O$ less than 2π. This ensures the spacing between the first and last points on the Orbit curve matches the spacing between all other neighboring points.

Step 2 for creating the Orbit curve is the application of a rotation via the matrix $\left({}^{\boldsymbol{O}}\boldsymbol{H}_{\boldsymbol{O'}}^{\boldsymbol{\beta}}\right)$. This rotates the Orbit curve by an angle β_O about the Z axis. **The rotation angle $\boldsymbol{\beta_O}$ corresponds to the "IHC clutch angle." It is the parameter that modulates torque transmission through the IHC. This value is discussed extensively throughout the rest of the thesis and should be remembered.** The matrix associated with the clutch angle rotation is:

$${}^{\boldsymbol{O}}\boldsymbol{H}_{\boldsymbol{O'}}^{\boldsymbol{\beta}} = \begin{bmatrix} \cos(\beta_O) & -\sin(\beta_O) & 0 \\ \sin(\beta_O) & \cos(\beta_O) & 0 \\ 0 & 0 & 1 \end{bmatrix} \tag{3.14}$$

The resulting Orbit curve at $t = 0$ is given by $S_O|_{t=0}$ in Equation (3.15).

$$\boxed{\boldsymbol{S_O}|_{t=0} = \left({}^{\boldsymbol{O}}\boldsymbol{H}^{\boldsymbol{\beta}}_{\boldsymbol{O'}}\right)(S_{O'})} \tag{3.15}$$

Note that the rotation $\left({}^{\boldsymbol{O}}\boldsymbol{H}^{\boldsymbol{\beta}}_{\boldsymbol{O'}}\right)$ does not shift the location of the first Orbit curve coordinate $\boldsymbol{S}^{\{1\}}_{\boldsymbol{O}}$ because it lies along the $+Z$ axis at $(0, 0, \rho_O)$. This is intentional and is done for the Planet curve as well. It ensures the Planet, Orbit, and Satellite geometries are initialized directly along $+Z$ axis regardless of the geometry parameters chosen, so the initial positions are always the same.

At the initial condition $t = 0$, positive β_O follows the normal right-hand-rule and can theoretically be chosen from anywhere on the interval in Equation (3.16).[1] In practice, the maximum viable β_O will be less than $+\pi/2$ due to later geometric and mechanical constraints.

$$\boxed{0 \leq \beta_O < \frac{+\pi}{2}} \tag{3.16}$$

3.5.2 Generating the Planet Curve Geometry

The Planet arcs explored in this work are all half-circles and lie along the intersection of the Planet and a "splitting plane" (see Figures 3-5 and 3-6). The location and orientation of the splitting plane affect the size and orientation of the Planet arc but it always remains semicircular. In ihcMATLAB, this splitting plane follows the rules:

1. It intersects the point $(0, 0, \rho_P)$
2. It can be rotated about the axis which intersects $(0, 0, \rho_P)$ and lies parallel to the X axis.

The splitting plane angle is given by the Planet Shape Parameter β_P.[2] Figure 3-6 shows examples of many different planet curves generated with different β_P values. The simplest of these occurs when $\beta_P = 0$, wherein the curve lies along a Planet meridian. In physical mechanisms, non-zero β_P can greatly affect the device's behavior, particularly in terms of the Satellite/Planet contact angle.

Planet curves are parameterized in a similar fashion to Orbit curves – they use the vector τ_P, a 1-by-n_P vector of evenly-spaced points ranging from $\left\{\frac{-\pi}{2}, \frac{+\pi}{2}\right\}$. The value chosen for n_P should be odd to ensure a point is always initialized at $(0, 0, \rho_P)$. The parameterization itself depends on the value of β_P:

For $\boldsymbol{\beta_P = 0}$:

[1] Negative β_O values are technically permissible mathematically. However, they are not distinct "configurations" as each $-\beta_O$ case only differs from its $+\beta_O$ counterpart by 180 degrees of Orbit-Planet slip.

[2] The sign convention for $+\beta_P$ follows the normal counter-clockwise positive right-hand-rule convention. Its rotation axis is parallel to X.

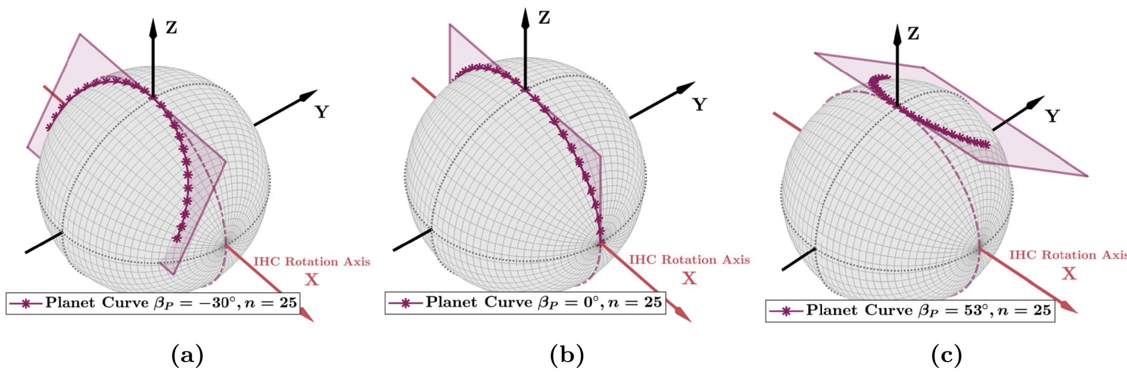

Figure 3-5 – Example Planet curves generated with various β_P values. In these examples, $n_P = 25$ so the points can be easily seen. The default in ihcMATLAB is $n_P = 1501$.

$$\boxed{\boldsymbol{S_P^{\{i\}}} = \begin{bmatrix} x_P^{\{i\}} \\ y_P^{\{i\}} \\ z_P^{\{i\}} \end{bmatrix} = \begin{bmatrix} \rho_P \sin\left(\tau_P^{\{i\}}\right) \\ 0 \\ \rho_P \cos\left(\tau_P^{\{i\}}\right) \end{bmatrix}} \tag{3.17}$$

For $\boldsymbol{\beta_P \neq 0}$:

$$\boxed{\boldsymbol{S_P^{\{i\}}} = \begin{bmatrix} x_P^{\{i\}} \\ y_P^{\{i\}} \\ z_P^{\{i\}} \end{bmatrix} = \begin{bmatrix} c_P\sqrt{2\left(\zeta_P^{\{i\}}\right)(\rho_P)(\cot(\beta_P)) - \left(\zeta_P^{\{i\}}\right)^2\left(1+\cot^2(\beta_P)\right)} \\ \zeta_P^{\{i\}} \\ \rho_P - \left(\zeta_P^{\{i\}}\right)(\cot(\beta_P)) \end{bmatrix}} \tag{3.18}$$

Where:

$$\zeta_P^{\{i\}} = (\rho_P)\left(\frac{\cot(\beta_P)}{1+\cot^2(\beta_P)}\right)\left(1-\cos\left(\tau_P^{\{i\}}\right)\right) \tag{3.19}$$

$$c_P = sign\left(\tau_P^{\{i\}}\right) \tag{3.20}$$

These equations produce points which are evenly-spaced, a fact that will make later calculations (such as heat flux) more straightforward. Despite the apparent complexity of the equations, there are only two geometry variables (ρ_P, β_P) and one parameterization variable (n_P) that need to be specified. Mathematical

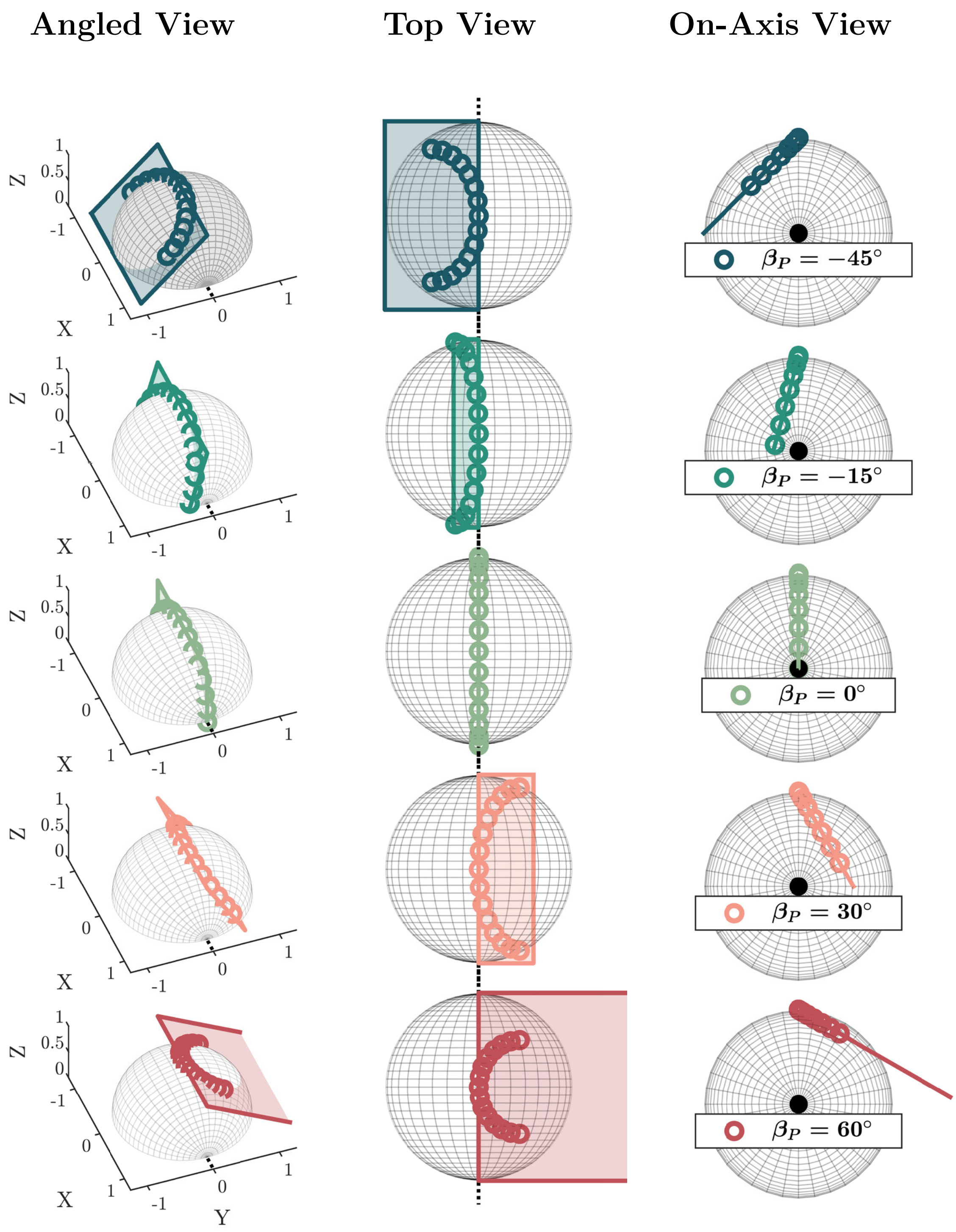

Figure 3-6 – Example Planet curves and the "splitting planes" which generate them.

limits for β_P are given in Equation (3.21). However, larger magnitudes of β_P result in physically smaller Planet curves, as seen Figure 3-6. Therefore, the practical limits for any particular design or application will usually be substantially below $|\beta_P| = \pi/2 = 90°$. For ihcBENCH (the prototype built during this project), $\beta_P = 53°$.

$$\boxed{\frac{-\pi}{2} < \beta_P < \frac{+\pi}{2}} \tag{3.21}$$

3.5.3 Planet & Orbit Geometry Together

Several examples showing both Planet and Orbit curves together are shown in Figure 3-7.

3.6 Planet & Orbit Motion

The terms "Planet speed" and "Orbit speed" refer to the angular rotation rates ω_P and ω_O, respectively. Both rotation rates have the following properties:

- The rotation axis is the global X axis, with the direction convention obeying the normal right-hand-rule.
- The rotation rates are predefined by the user.
- The rotation rates are constant. Thus, the angular accelerations α_P and α_O are zero.
- The Planet/Orbit experience no other motions or rotations.

3.6.1 Defining Slip Rate & Slip Rotation

In terms of kinematic and force analysis, it is very useful to derive the slip rate in Equation (3.22). Note that, since ω_O and ω_P are both constant, ω_{OP} is also constant.

$$\boxed{\textit{Slip Rate} = \omega_{OP} = (\omega_P - \omega_O)} \tag{3.22}$$

ihcMATLAB accepts both positive and negative slip rates. **However, the model formulation requires that the slip rate be non-zero.** For situations when the mechanism *must* lock up due to the balance of forces, this behavior is identified at a later stage of the calculations (in Chapter 4).

A second important term to become familiar with is **"slip-rotation."** One slip-rotation corresponds to one complete relative-rotation of the Planet with respect to the Orbit. In one slip-rotation, all Satellites complete exactly one loop through the Orbit ring:

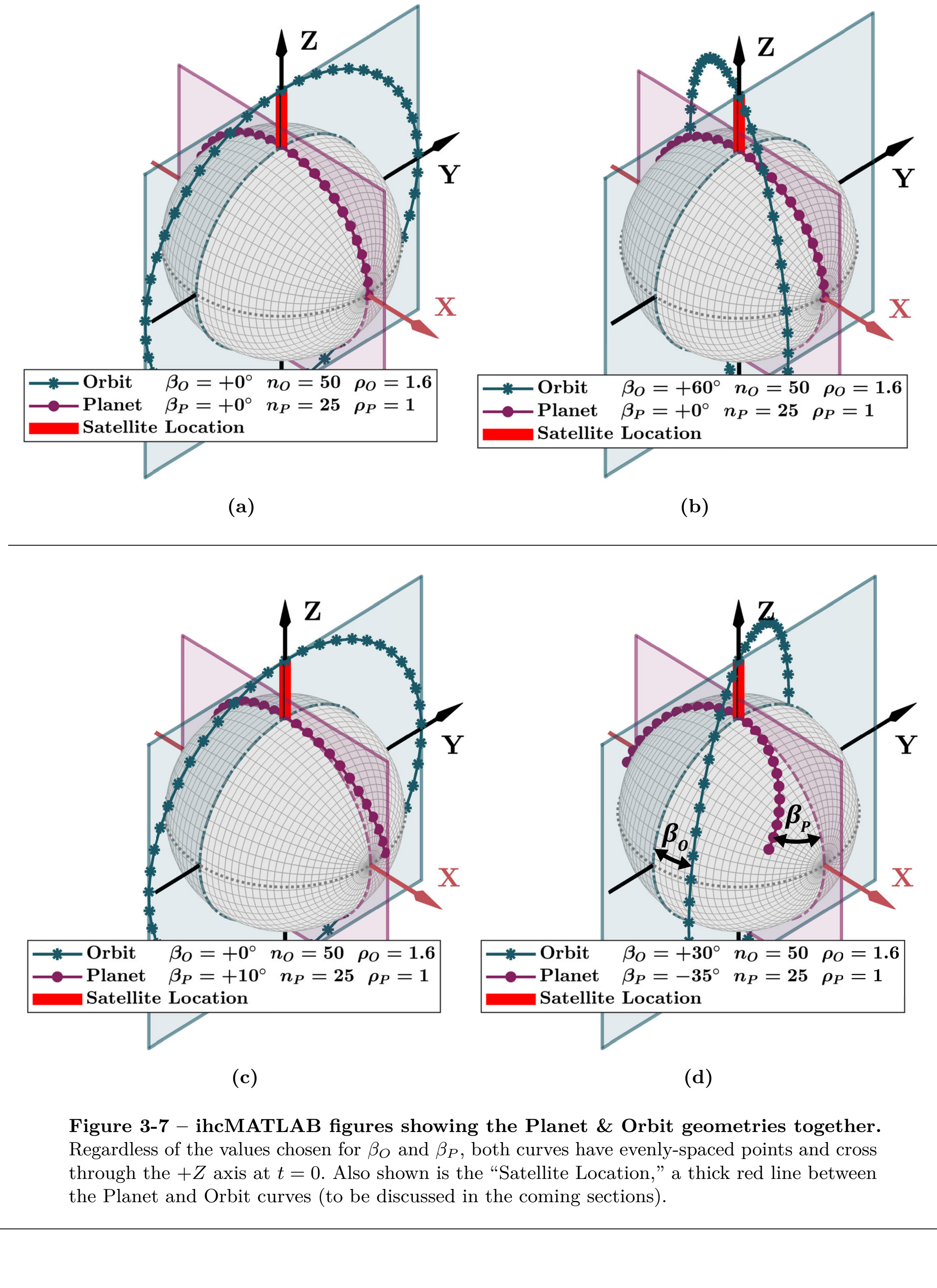

Figure 3-7 – ihcMATLAB figures showing the Planet & Orbit geometries together. Regardless of the values chosen for β_O and β_P, both curves have evenly-spaced points and cross through the $+Z$ axis at $t = 0$. Also shown is the “Satellite Location,” a thick red line between the Planet and Orbit curves (to be discussed in the coming sections).

$$\boxed{\begin{aligned} \textit{Period of one slip-rotation} &= \frac{\omega_{OP}}{2\pi} \qquad (3.23) \\ \textit{Relative angle change after one slip-rotation} &= \theta_{OP} = 2\pi \qquad (3.24) \end{aligned}}$$

In this model and the ihcMATLAB code, the variables for slip rate (ω_{OP}) and Planet rotation rate (ω_P) are very important. This is because:

- **Slip Rate** dictates the rate at which Satellites traverse the Orbit, thereby generating reaction loads and causing the IHC to transmit torque.
- $\boldsymbol{\omega_P}$ is the rotation rate for the Planet. It is also the average rotation rate for the Satellites, and therefore largely determines the amount of inertial loading (from centrifugal effects) experienced in operation. This is because each Satellite is driven by its associated Planet slot. The curvature of certain Planet shapes does permit Satellites to advance/retreat in θ (relative to a given reference point on the Planet slot), but the Planet and Satellites always start/end each slip-rotation at the same relative locations. Thus, they share the same average angular speed.

3.6.2 Model Timestep Size

Each simulation begins at $t = 0$ and proceeds in uniform timesteps Δt. In this work, the timestep is set by dividing each slip-rotation into a user-specified number of increments n_t:

$$\boxed{\Delta t_{OP} = \frac{2\pi}{(n_t)(\omega_{OP})}} \qquad (3.25)$$

For example, for $n_t = 360$, each timestep corresponds to $1°$ of relative Planet-Orbit slip.

n_t must provide enough point density to capture incremental motions with acceptable resolution. **Additionally, the number of timesteps should be equal to an integer-multiple of the satellite count n_S (see Section 4.7.1 for further discussion).** In ihcMATLAB a resolution of $n_t = 402$ was found to work well. However, the timestep definition may need to be adjusted depending on the geometry or operating point. For example, a much higher value for n_t may be needed when the slip rate ω_{OP} is very small and the Planet/Orbit speeds (ω_O, ω_P) are very high.

3.6.3 Incrementing the Planet/Orbit Positions

At each timestep, the Planet and Orbit rotational positions can be calculated as the products of the current time t and the prescribed velocities ω_P/ω_O:

$$\boxed{\begin{aligned}\theta_P(t) &= (t)(\omega_P) \quad (3.26)\\ \theta_O(t) &= (t)(\omega_O) \quad (3.27)\\ \theta_{OP}(t) &= (t)(\omega_{OP}) \quad (3.28)\end{aligned}}$$

The instantaneous locations of the Planet/Orbit curves are updated at each timestep by applying rotation matrices to the initial curves ($S_P|_{t=0}$ and $S_O|_{t=0}$), producing $S_P(t)$ and $S_O(t)$:

$$\boxed{\begin{aligned}S_P(t) &= \boldsymbol{H_P^{\theta}(t)} S_P|_{t=0} \quad (3.29)\\ S_O(t) &= \boldsymbol{H_O^{\theta}(t)} S_O|_{t=0} \quad (3.30)\end{aligned}}$$

The matrices in these equations – $\boldsymbol{H_P^{\theta}(t)}$ and $\boldsymbol{H_O^{\theta}(t)}$ – apply rotations by the angles θ_P and θ_O about the global X axis:

$$\boxed{\begin{aligned}\boldsymbol{H_P^{\theta}(t)} &= \begin{bmatrix} 1 & 0 & 0 \\ 0 & \cos(\theta_P(t)) & -\sin(\theta_P(t)) \\ 0 & \sin(\theta_P(t)) & \cos(\theta_P(t)) \end{bmatrix} \quad (3.31)\\ \boldsymbol{H_O^{\theta}(t)} &= \begin{bmatrix} 1 & 0 & 0 \\ 0 & \cos(\theta_O(t)) & -\sin(\theta_O(t)) \\ 0 & \sin(\theta_O(t)) & \cos(\theta_O(t)) \end{bmatrix} \quad (3.32)\end{aligned}}$$

At this point, the complete Planet and Orbit motions can be calculated, modeled, and animated across the entire simulation run. Note that this is possible without needing to consider anything about the Satellites or system forces.[1]

3.6.4 Vectorized Planet/Orbit Motions

Some later calculations are made easier by using vectorized forms for the Planet, Orbit, and slip motions. For the Planet, these are:

[1] Forces will be calculated based on the known motions rather than the other way around.

$$\boxed{\begin{aligned}\vec{\boldsymbol{\theta}}_P(t) &= \begin{bmatrix} \theta_P(t) \\ 0 \\ 0 \end{bmatrix} \quad (3.33)\\ \vec{\boldsymbol{\omega}}_P(t) &= \begin{bmatrix} \omega_P(t) \\ 0 \\ 0 \end{bmatrix} \quad (3.34)\\ \vec{\boldsymbol{\alpha}}_P(t) &= \begin{bmatrix} 0 \\ 0 \\ 0 \end{bmatrix} \quad (3.35)\end{aligned}}$$

For the Orbit, these are:

$$\boxed{\begin{aligned}\vec{\boldsymbol{\theta}}_O(t) &= \begin{bmatrix} \theta_O(t) \\ 0 \\ 0 \end{bmatrix} \quad (3.36)\\ \vec{\boldsymbol{\omega}}_O(t) &= \begin{bmatrix} \omega_O(t) \\ 0 \\ 0 \end{bmatrix} \quad (3.37)\\ \vec{\boldsymbol{\alpha}}_O(t) &= \begin{bmatrix} 0 \\ 0 \\ 0 \end{bmatrix} \quad (3.38)\end{aligned}}$$

In terms of slip, these are:

$$\boxed{\begin{aligned} \vec{\boldsymbol{\theta}}_{OP}(t) &= \begin{bmatrix} \theta_{OP}(t) \\ 0 \\ 0 \end{bmatrix} && (3.39) \\ \vec{\boldsymbol{\omega}}_{OP}(t) &= \begin{bmatrix} \omega_{OP}(t) \\ 0 \\ 0 \end{bmatrix} && (3.40) \\ \vec{\boldsymbol{\alpha}}_{OP}(t) &= \begin{bmatrix} 0 \\ 0 \\ 0 \end{bmatrix} && (3.41) \end{aligned}}$$

3.7 Satellite Location – Planet/Orbit Intersection

With the Planet and Orbit motions completely solved, determination of the Satellite motions comes next. Many of the following sections will only consider a single satellite at a time. This is for two reasons:

1. It is much less mentally taxing to develop a single satellite's full behavior in isolation, rather than considering all Satellites at once.
2. The Satellite assumptions enable a convenient "shortcut." As will be shown, only a single "Primary Satellite" needs to be fully solved. The results of all others are identical to the Primary, except with different time delays. Rather than solve each Satellite individually, we will "solve" for the rest by referencing the Primary Satellite data with appropriate time delays applied. This is covered in Chapter 4.

In this work, all Satellites are designed to obey the following rules:

- All satellites share identical geometry.
- Each satellite has a central axis which always points towards the Planet's center, $(0, 0, 0)$.
- Each satellite interfaces with a single common Orbit track. The interface location is along the Satellite axis.
- Each satellite interfaces with its own dedicated Planet track. The interface location is along the Satellite axis.
- All Planet tracks have identical geometries.

- All Planet tracks are spaced uniformly about the Planet's rotation axis X.

Given these rules, each Satellite's position can be fully determined using the Planet and Orbit geometry. Many of these rules exist to enforce the following:

> At any point in time $\boldsymbol{t}$, there will exist one (and only one) straight line which, starting from the origin $\mathbf{(0, 0, 0)}$, intersects (a) the Orbit arc and (b) one Planet arc. A single Satellite must lie along this line, so the line's current angular position $\boldsymbol{(\theta_S(t), \phi_S(t))}$, exactly matches that of the Satellite. The Satellite's radial coordinate $\boldsymbol{\rho_S}$ is predetermined from the physical design, so after $\boldsymbol{(\theta_S(t), \phi_S(t))}$ are found, the Satellite's position is known: $\boldsymbol{\vec{r}_S(t) = (\rho_S, \theta_S(t), \phi_S(t))}$.

Put simply, each Satellite tracks the intersection of its Planet curve and the Orbit curve, and this fact holds true at all times. Thus, determining a Satellite's position is equivalent to calculating the associated Planet/Orbit "intersection line" at each timestep. This task, described in Table 3.4, is performed numerically. Sections 3.7.1, 3-8 and 3-9 contain several illustrations to help visualize the process.

The requirement to always have a single intersection line is crucial. Situations with multiple (2+) intersections should be avoided as this implies the existence of at least one mechanical singularity. Situations with zero (0) intersections are physically unreachable – in a physical system, some component would break while attempting to reach this condition.

3.7.1 Determining the Planet/Orbit Arc Intersection

As mentioned, the process for determining a Satellite's instantaneous location is synonymous with locating the Planet/Orbit "intersection line." The process for doing so is summarized in Table 3.4. It ultimately produces the array $\vec{\boldsymbol{r}}_S$ which contains the Satellite coordinates at each timestep of the simulation.

3.7.2 Satellite Velocity & Acceleration

With the Satellite's position vector $\vec{\boldsymbol{r}}_S$ known, its velocity and acceleration can be calculated. Since $\vec{\boldsymbol{r}}_S$ was determined using global XYZ coordinates (an inertial reference frame), the Satellite's velocity and acceleration arrays ($\vec{\boldsymbol{v}}_S$, $\vec{\boldsymbol{a}}_S$) can be calculated as simple time-derivatives. See Equations (3.42) and (3.43).

$$\boxed{\vec{\boldsymbol{v}}_S = \frac{\mathrm{d}}{\mathrm{d}t}\vec{\boldsymbol{r}}_S} \tag{3.42}$$

$$\boxed{\vec{\boldsymbol{a}}_S = \frac{\mathrm{d}}{\mathrm{d}t}\vec{\boldsymbol{v}}_S} \tag{3.43}$$

Table 3.4 – Overview of Algorithm for Determining Satellite Locations

Step	Description
1	At the current time $\boldsymbol{t}$, take the Orbit curve in its current position and radially scale it to match the size of the Planet sphere. The Planet and Orbit curves now *very nearly* intersect – but not quite, as a result of line discretization.
2	Using a search and minimization process, locate the two the line segments (one in the Orbit and one in the Planet) which are nearest to one another.
3	Approximate the line segments' intersection point by locating the point in 3D space which is is minimally equidistant from both of them. This is a well-known problem and is frequently called the "closest point of approach" or "minimum distance between two skew lines" problem.
4	Convert the position of the intersection point to spherical coordinates. The resulting $\boldsymbol{\theta}$ and $\boldsymbol{\phi}$ coordinates $(\boldsymbol{\theta_S(t)}, \boldsymbol{\phi_S(t)})$ are shared by the Satellite, the Orbit intersection point, and the Planet intersection point.
5	Using the Satellite's radial position $\boldsymbol{\rho_S}$, its spherical coordinates are then $(\boldsymbol{\rho_S}, \boldsymbol{\theta_S(t)}, \boldsymbol{\phi_S(t)})$. Similar expressions for the Planet and Orbit intersection points can likewise be found, using $\boldsymbol{\rho_P}$ and $\boldsymbol{\rho_O}$ respectively.
6	Convert the Satellite's position in spherical coordinates back to $\boldsymbol{XYZ}$-space to obtain $\boldsymbol{\vec{r}_S(t)}$ at the current timestep.
7	Repeat Steps 1-6 at each timestep to get the Satellite position $\boldsymbol{\vec{r}_S}$ (size 3-by-$\boldsymbol{n_t}$) across the entire simulation.

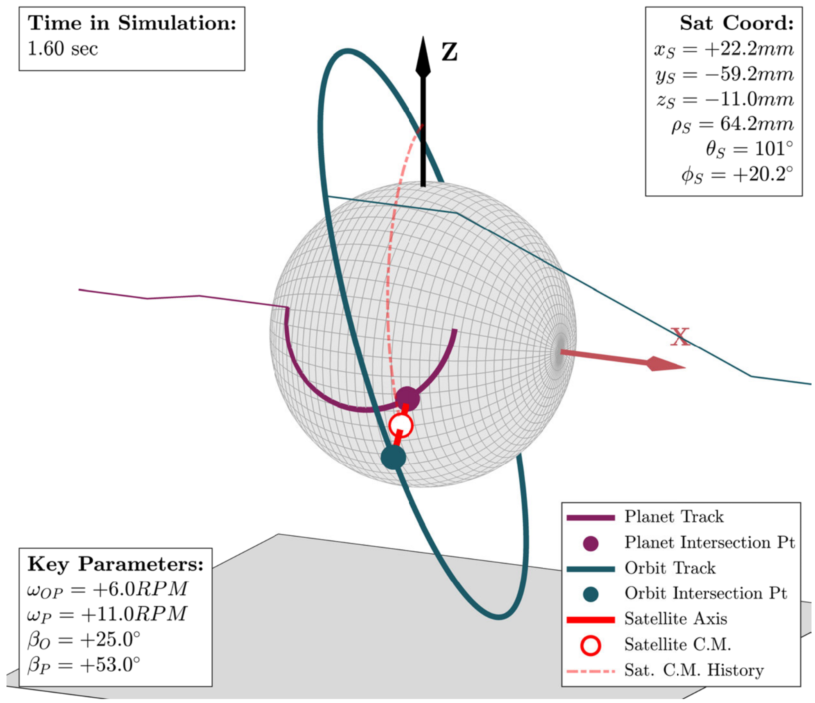

(a)

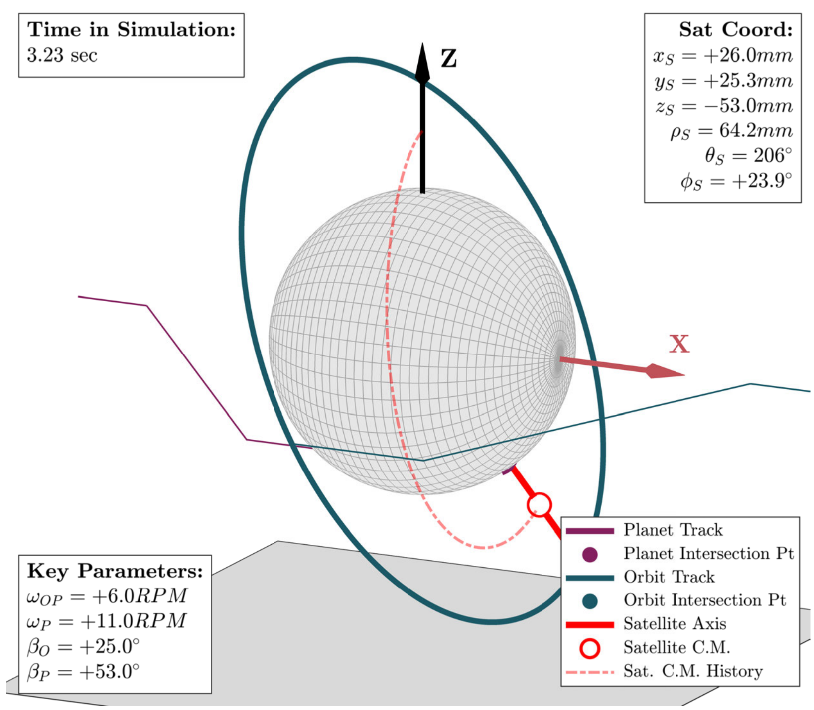

(b)

(Continued)

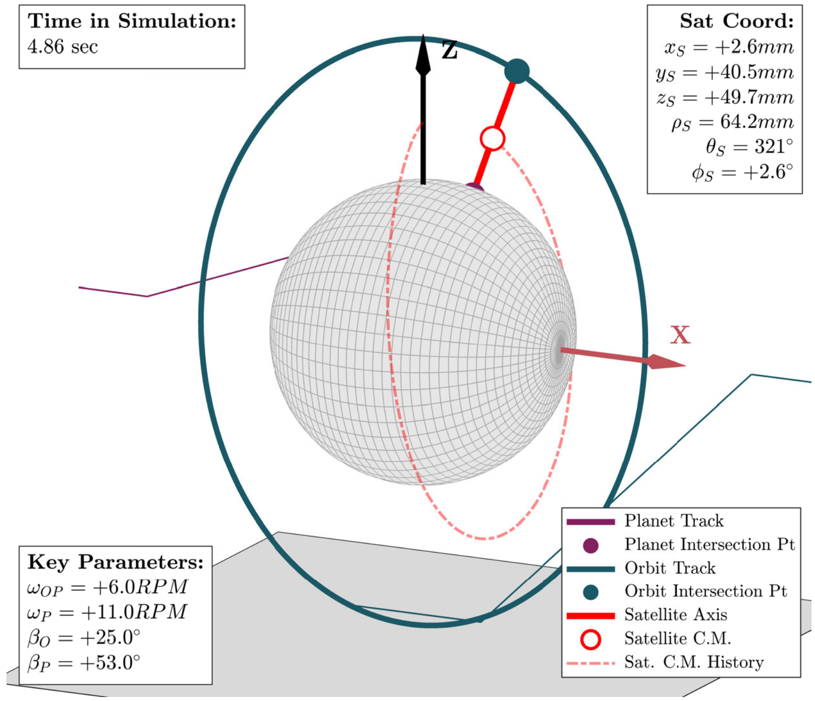

(c)

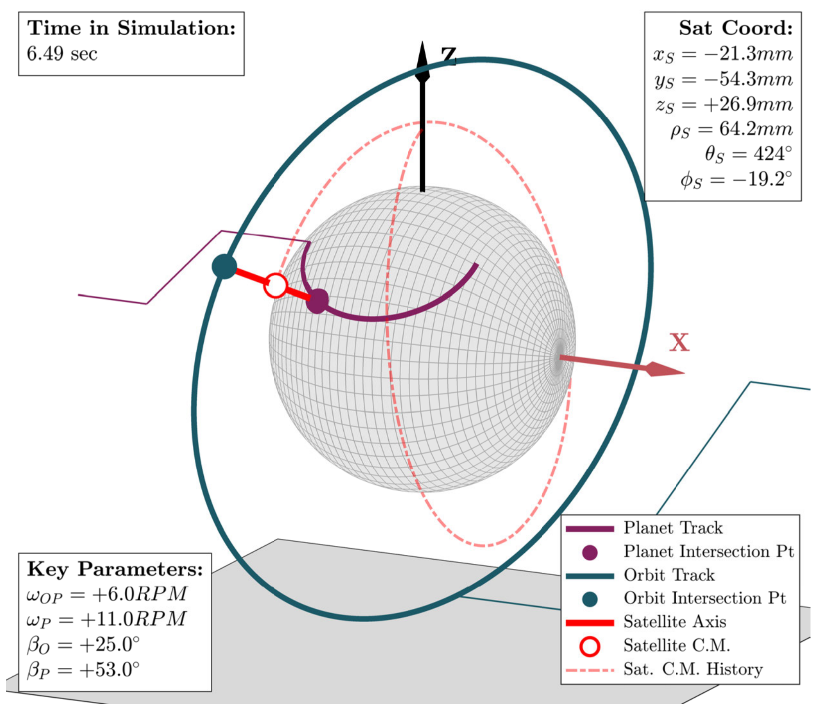

(d)

Figure 3-8 – Screenshots of an ihcMATLAB animation tool for visualizing Satellite positions and intersection lines.

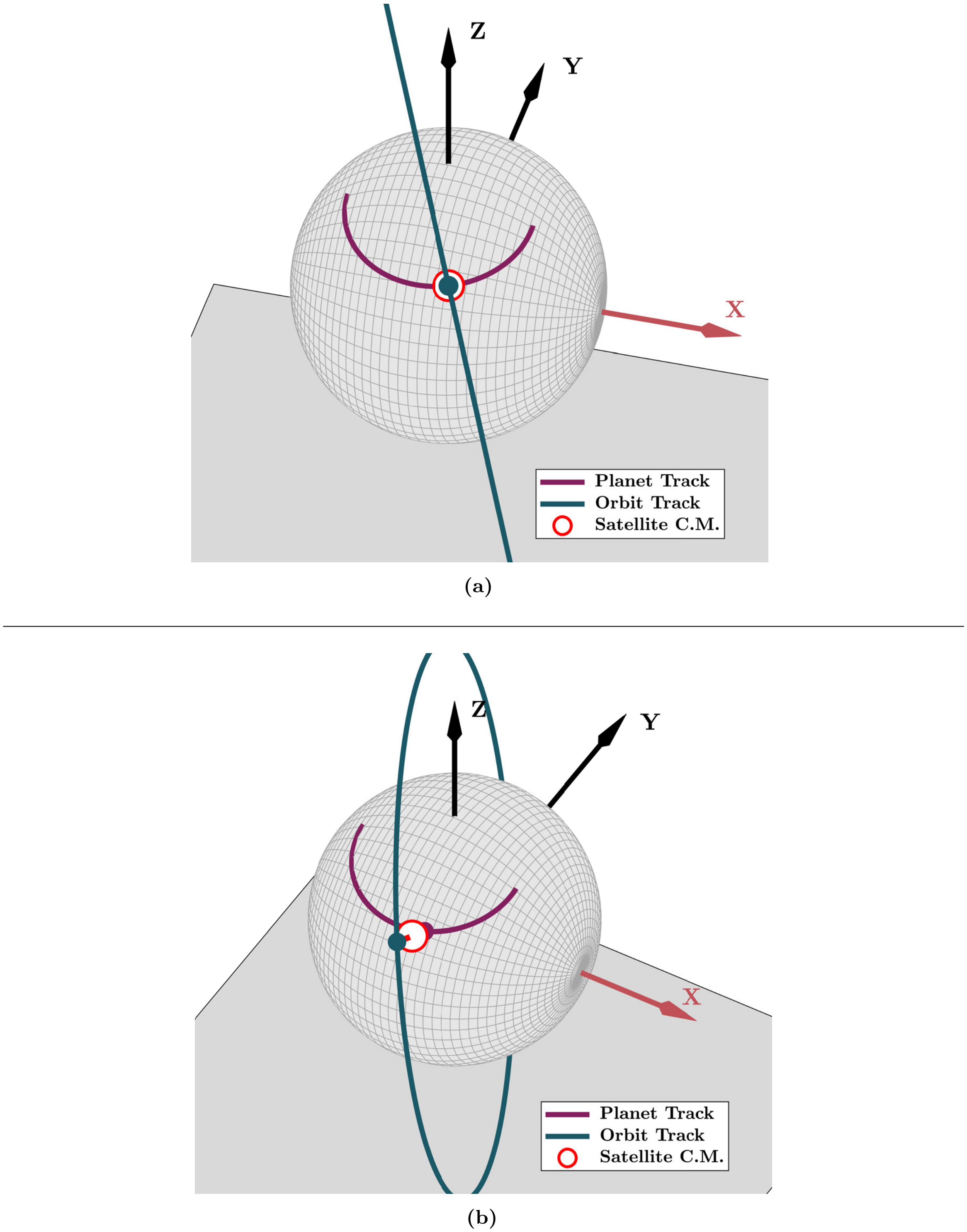

Figure 3-9 – On-Axis and Near-On-Axis views of the Satellite intersection line. The line intercepts all three of: (a) the global origin $(0, 0, 0)$, (b) the Planet curve, and (c) the Orbit curve.

Derivatives can also be taken in spherical coordinates. As ρ_S is constant, only the derivatives of (θ_S, ϕ_S) need to be calculated.

$$\boxed{\begin{aligned} \dot{\theta}_S &= \frac{\mathrm{d}}{\mathrm{d}t}\theta_S && (3.44) \\ \ddot{\theta}_S &= \frac{\mathrm{d}}{\mathrm{d}t}\dot{\theta}_S && (3.45) \end{aligned}}$$

$$\boxed{\begin{aligned} \dot{\phi}_S &= \frac{\mathrm{d}}{\mathrm{d}t}\phi_S && (3.46) \\ \ddot{\phi}_S &= \frac{\mathrm{d}}{\mathrm{d}t}\dot{\phi}_S && (3.47) \end{aligned}}$$

Throughout these calculations, care must be taken to unwrap angles when appropriate. For example, in Equations (3.44) and (3.45), θ should be unwrapped before taking derivatives to ensure no artificial "jumps" are introduced.

3.8 Satellite Orientation and the UVW Coordinate Frame

3.8.1 Satellite Local Coordinates – The UVW Frame

At this stage, the position, velocity, and acceleration of the Satellite's center-of-mass are fully determined. However, its orientation must now be considered – to do so, the Satellite is "upgraded" from a simple point-in-space to have a local coordinate frame, UVW. The Satellite's local coordinate frame represents the position and orientation of its center-of-mass, and an example is shown in Figure 3-10. The use of UVW anticipates three challenges:

1. Forces acting on a Satellite can't be placed at the correct locations and orientations if the Satellite's orientation is not known.
2. The angular equilibrium equations can't be solved without first knowing the Satellite's angular kinematics.
3. The Satellite's angular kinematics can't be determined without a basis for defining Satellite orientation.

The Satellite's local coordinate system UVW obeys the following rules:

1. UVW is local to the Satellite. Its origin always is located at, and moves along with, the Satellite's center-of-mass $\vec{\boldsymbol{r}}_S(t)$.
2. W is defined to point radially outwards from the Planet center (along the "intersection line" found previously).

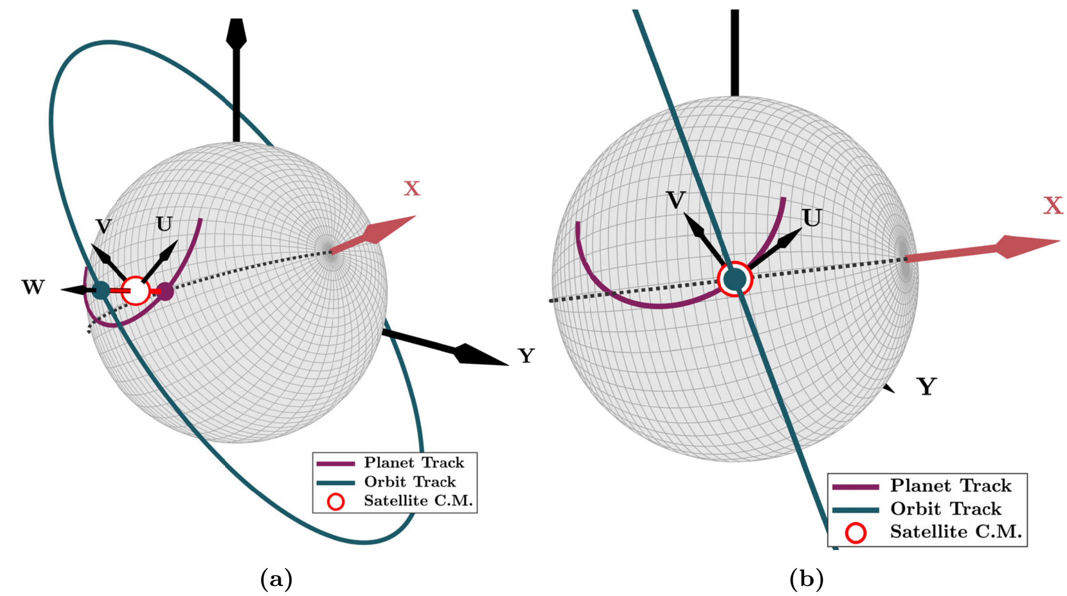

Figure 3-10 – Examples showing the location and orientation of the Satellite's local *UVW* coordinate system. The UVW origin is located at the Satellite's center-of-mass, $+W$ points radially outwards from the global origin $(0, 0, 0)$, and $+U$ lies parallel to the Planet curve (as viewed from along the $+W$ axis).

3. U is defined to point tangent to the Planet curve below it.

W is trivial to determine since the direction of the intersection line is already known. The orientations of U and V require one last parameter – a rotation angle. The variable created to represent this is γ_S, corresponding to Satellite rotation around W (per the normal right-hand-rule convention). Note that γ_S also describes the orientation of the Satellite/Planet interface relative to the direction of rotation, so it will be important for assigning the correct directions to forces in Chapter 4.

Examples of γ_S (as well as the related Orbit parameter γ_{OS}, discussed shortly) are shown in Figures 3-11 and 3-12. Note that when $\gamma_S = 0$, U simply points along a planet meridian (the dotted black line).

3.8.2 Determining γ_S

γ_S depends on the orientation of the Planet curve at the spot directly "below" the Satellite (where "below" means radially inwards). γ_S follows the Planet track due to the Satellite design constraints discussed in Chapter 4; in short, the Satellite follows the Planet slot, so its rotation angle γ_S does as well.

Notice that, when $\gamma_S = 0$, U points along a Planet meridian ("line of longitude"). Non-zero γ_S can be envisioned by "drawing" two unit vectors on the Planet, both of which start at the Planet intersection point. One unit vector points rightwards (towards $+X$) along a Planet meridian. The other points tangent to the Planet curve (of the two possible choices, the one pointing towards $+X$ is used). The angle between

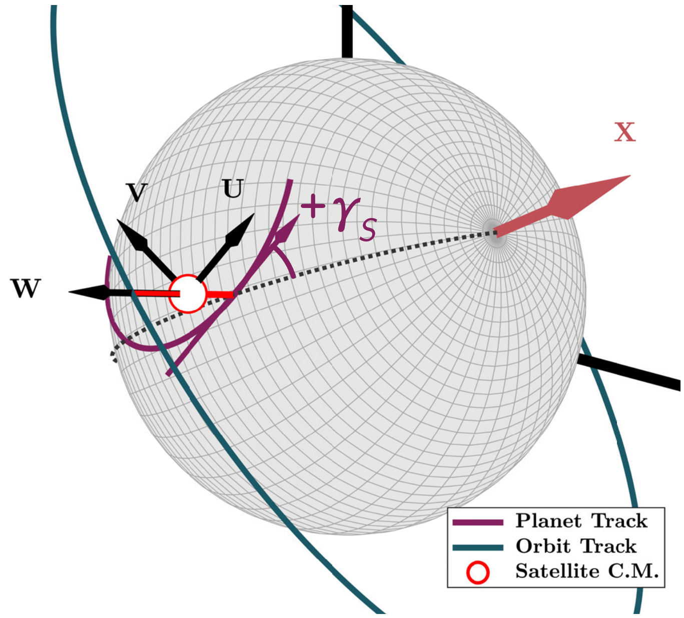

Figure 3-11 – Example diagram of γ_S. γ_S is the angle between the U axis and the Planet "meridian" at the current location (the black dotted line), as viewed from the $+W$ axis.

these unit vectors is γ_S. This qualitatively describes γ_S; Equation (3.48) is the equation used to calculate it.

$$\boxed{\gamma_S = \operatorname{sign}\left(\hat{\mathbf{W}}' \cdot \left(\hat{\mathbf{U}}' \times \hat{\mathbf{v}}^*_P\right)\right) \cos^{-1}\left(\hat{\mathbf{U}}' \cdot \hat{\mathbf{v}}^*_P\right)} \tag{3.48}$$

Where:

$\hat{\mathbf{v}}^*_P$ = Unit vector tangent to the Planet curve, pointing towards $+X$, and originating from the Planet intersection point $\vec{\boldsymbol{r}}^*_P$.

$\hat{\mathbf{U}}', \hat{\mathbf{V}}', \hat{\mathbf{W}}'$ = Unit vectors that point along the local directions U, V, W as if γ_S were 0.

3.8.3 Determining γ_{OS}

The Satellite also interacts with the Orbit, so the relative Satellite/Orbit orientation γ_{OS} is also needed. As will be described in Chapter 4, the Satellite component in contact with the Orbit is free to rotate (separately) about W. As a result, γ_{OS} affects only the directions of the Satellite/Orbit contact forces. It is not considered when finding the orientation of the Satellite's center-of-mass (only γ_S affects this).

γ_{OS} is formulated in a very similar process to γ_S, with a few key distinctions:

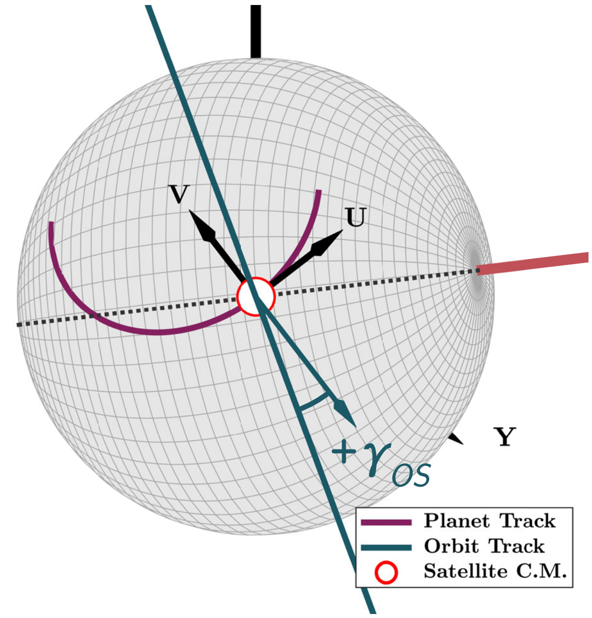

Figure 3-12 – Example diagram of γ_{OS}. γ_{OS} is the angle made between the $-V$ axis and the Orbit's path tangent, as viewed from the $+W$ axis.

- The reference vectors U, V, W reference the satellite's **true UVW coordinate frame, *i.e.* already rotated by γ_S.** γ_{OS} is the tilt of the Orbit relative to the Satellite.
- The Orbit track direction is compared against $-V$, rather than $+U$.

γ_{OS} is calculated using Equation (3.49).

$$\boxed{\gamma_{OS} = \text{sign}\Big(\hat{\mathbf{W}} \cdot \big(-\hat{\mathbf{V}} \times \hat{\mathbf{v}}_O^*\big)\Big) \cos^{-1}\big(-\hat{\mathbf{V}} \cdot \hat{\mathbf{v}}_O^*\big)} \tag{3.49}$$

Where:

$\hat{\mathbf{v}}_O^*$ = Unit vector tangent to the Orbit curve, pointing towards $+\theta$, and originating from the Orbit intersection point $\vec{\boldsymbol{r}}_O^*$.

$\hat{\mathbf{U}}, \hat{\mathbf{V}}, \hat{\mathbf{W}}$ = Unit vectors that point along the local directions U, V, W after rotating the Satellite by γ_S.

3.8.4 Deriving the Satellite Angular Kinematics

At this stage, the Satellite kinematics are not yet fully determined – we still lack the Satellite's angular velocities and accelerations relative to its local coordinate frame, UVW.[1] Determination of UVW rotation

[1] Chapter 4 will solve the Satellite equilibrium equations using the accelerations expressed in local UVW coordinates.

and acceleration rates is tricky because the coordinate frame is non-inertial. In other words, the fact that *the local coordinate system itself* moves and rotates in space means special care must be taken to correctly derive the missing angular parameters.

Luckily, this type of problem is well-understood; the spherical coordinates $(\rho_S, \phi_S, \gamma_S)$ are reminiscent of classical Euler angles. Landau and Lifshitz [36] provide derivations for angular velocities and accelerations using a slightly different set of Euler angles. Using their definitions as a reference, a new set of equations using the IHC angle definitions were derived – see Equations (3.50) to (3.55).

$$\boxed{\begin{aligned}
\dot{\theta}^U_{S*} &= \omega^U_{S*} = \quad \dot{\theta}_S \cos(\phi_S)\cos(\gamma_S) + \dot{\phi}_S \sin(\gamma_S) && (3.50)\\
\dot{\theta}^V_{S*} &= \omega^V_{S*} = -\dot{\theta}_S \cos(\phi_S)\sin(\gamma_S) + \dot{\phi}_S \cos(\gamma_S) && (3.51)\\
\dot{\theta}^W_{S*} &= \omega^W_{S*} = \quad \dot{\theta}_S \sin(\phi_S) + \dot{\gamma}_S && (3.52)
\end{aligned}}$$

Where:

$$\begin{aligned}
\omega^U_{S*}, \omega^V_{S*}, \omega^W_{S*} &= \text{Satellite angular velocities about the local axes } U, V, W.\\
\theta_S, \phi_S, \gamma_S &= \text{The Satellite's position coordinates in the global spherical frame.}\\
\dot{\theta}_S, \dot{\phi}_S, \dot{\gamma}_S &= \text{Time-derivatives of the Satellite's global spherical position coordinates.}
\end{aligned}$$

The calculations for local angular accelerations are straightforward; they are simply time-derivatives of the angular velocities:

$$\boxed{\begin{aligned}
\alpha^U_{S*} &= \dot{\omega}^U_{S*} = \frac{\mathrm{d}}{\mathrm{d}t}\left(\omega^U_{S*}\right) && (3.53)\\
\alpha^V_{S*} &= \dot{\omega}^V_{S*} = \frac{\mathrm{d}}{\mathrm{d}t}\left(\omega^V_{S*}\right) && (3.54)\\
\alpha^W_{S*} &= \dot{\omega}^W_{S*} = \frac{\mathrm{d}}{\mathrm{d}t}\left(\omega^W_{S*}\right) && (3.55)
\end{aligned}}$$

Expressed as a vector:

$$\boxed{\vec{\boldsymbol{\alpha}}_{S*} = \begin{bmatrix} \alpha^U_{S*} \\ \alpha^V_{S*} \\ \alpha^W_{S*} \end{bmatrix}} \tag{3.56}$$

Here:

$$\alpha_{S*}^{U}, \alpha_{S*}^{V}, \alpha_{S*}^{W} = \text{Satellite angular accelerations about the local axes } U, V, W.$$

As before, these calculations must be repeated at each timestep.

3.8.5 Satellite/Planet and Satellite/Orbit Relative Speeds

Next, the Satellite velocities relative to the Orbit and Planet tracks are still needed, as they determine the directions in which friction forces act. Without them, the friction forces in Chapter 4 cannot be assigned the correct orientations (opposing motion).

For this calculation, two points are tracked throughout the simulation. One is a point from the Planet curve, and one is a point from the Orbit curve. The coordinate vectors of these points are $\vec{\boldsymbol{r}}_{P'}$ and $\vec{\boldsymbol{r}}_{O'}$, respectively.[1] For convenience, the points initially located along the $+Z$ axis are chosen.

$$\boxed{\begin{aligned} \vec{\boldsymbol{r}}_{P'}|_{t=0} &= \begin{bmatrix} 0 \\ 0 \\ \rho_P \end{bmatrix} && (3.57) \\ \vec{\boldsymbol{r}}_{O'}|_{t=0} &= \begin{bmatrix} 0 \\ 0 \\ \rho_O \end{bmatrix} && (3.58) \end{aligned}}$$

These points can be kept track of using the full Planet/Orbit coordinate arrays, or separately (by applying the appropriate transformation matrices at each timestep). The velocities of these points can be found by taking the coordinates' time derivatives:

$$\boxed{\begin{aligned} \vec{\boldsymbol{v}}_{P'}(t) &= \frac{\mathrm{d}}{\mathrm{d}t}\vec{\boldsymbol{r}}_{P'}(t) && (3.59) \\ \vec{\boldsymbol{v}}_{O'}(t) &= \frac{\mathrm{d}}{\mathrm{d}t}\vec{\boldsymbol{r}}_{O'}(t) && (3.60) \end{aligned}}$$

The Planet/Satellite and Orbit/Satellite relative velocities are found by starting with the Planet and

[1] These coordinate vectors are in global XYZ coordinates and are relative to the Planet center.

Orbit intersection coordinates ($\vec{\boldsymbol{r}}^*_P(t)$ and $\vec{\boldsymbol{r}}^*_O(t)$ from Table 3.4).[1] Time derivatives are taken to find the following velocities:

$$\boxed{\begin{aligned} \vec{\boldsymbol{v}}^*_P(t) &= \frac{\mathrm{d}}{\mathrm{d}t}\vec{\boldsymbol{r}}^*_P(t) && (3.61) \\ \vec{\boldsymbol{v}}^*_O(t) &= \frac{\mathrm{d}}{\mathrm{d}t}\vec{\boldsymbol{r}}^*_O(t) && (3.62) \end{aligned}}$$

The relative Planet/Satellite and Orbit/Satellite velocities are therefore:

$$\boxed{\begin{aligned} \vec{\boldsymbol{v}}_{PS}(t) &= \vec{\boldsymbol{v}}^*_P(t) - \vec{\boldsymbol{v}}_{P'}(t) && (3.63) \\ \vec{\boldsymbol{v}}_{OS}(t) &= \vec{\boldsymbol{v}}^*_O(t) - \vec{\boldsymbol{v}}_{O'}(t) && (3.64) \end{aligned}}$$

These relative velocities are expressed in global XYZ coordinates – local expressions in UVW are needed. For this, transformations between the XYZ and UVW coordinate systems must be derived. These will allow various expressions to be converted from global to local coordinates, and vice-versa.

3.9 Satellite Coordinate Transforms: $(X, Y, Z) \leftrightarrow (U, V, W)$

In general, two entity types can be transformed between the XYZ and UVW coordinate frames:

- **Direction:** Conveys direction, but not position.
- **Location:** Conveys position, but not direction.

A slightly different transformation algorithm is used depending on whether the quantity being transformed is a "direction" or a "location" quantity. Note that some parameters are compound and consist of both a direction and a location – forces being the most prominent examples. For compound parameters, the location and direction components are converted separately using the appropriate transforms.

As a reminder, items with a bare subscript (*e.g.* $\vec{\boldsymbol{r}}_S$) are relative to the global XYZ coordinate frame, while those with an asterisk subscript (*e.g.* $\vec{\boldsymbol{r}}_{S^*}$) are relative to the Satellite's local UVW coordinate frame.

3.9.1 $XYZ \rightarrow UVW$ Transforms

For transforming vector orientations (directions) only a single rotation operation $\left({}^{\boldsymbol{S^*}}\boldsymbol{H}_{\boldsymbol{S}}\right)$ is needed:

[1] Not the Satellite's center-of-mass!

$$\boxed{\begin{bmatrix} \vec{\boldsymbol{v}}_{S^*} \\ \\ 1 \end{bmatrix} = \left({}^{\boldsymbol{S^*}}\boldsymbol{H_S}\right) \begin{bmatrix} \vec{\boldsymbol{v}}_{S} \\ \\ 1 \end{bmatrix}} \tag{3.65}$$

For transforming coordinate locations (positions), both a rotation operation $\left({}^{\boldsymbol{S^*}}\boldsymbol{H_S}\right)$ and a translation operation $\left({}^{\boldsymbol{S^*}}\boldsymbol{H_S^{XYZ}}\right)$ are needed:

$$\boxed{\begin{bmatrix} \vec{\boldsymbol{r}}_{S^*} \\ \\ 1 \end{bmatrix} = \left({}^{\boldsymbol{S^*}}\boldsymbol{H_S}\right)\left({}^{\boldsymbol{S^*}}\boldsymbol{H_S^{XYZ}}\right) \begin{bmatrix} \vec{\boldsymbol{r}}_{S} \\ \\ 1 \end{bmatrix}} \tag{3.66}$$

The entries of the associated transformation matrices are derived in Equations (3.67) to (3.71):

$$\boxed{{}^{\boldsymbol{S^*}}\boldsymbol{H_S} = \left({}^{\boldsymbol{S^*}}\boldsymbol{H_S^{\theta}}\right)\left({}^{\boldsymbol{S^*}}\boldsymbol{H_S^{\phi}}\right)\left({}^{\boldsymbol{S^*}}\boldsymbol{H_S^{\gamma}}\right)} \tag{3.67}$$

$$\boxed{{}^{\boldsymbol{S^*}}\boldsymbol{H_S^{XYZ}} = \begin{bmatrix} 1 & 0 & 0 & -r_S^X \\ 0 & 1 & 0 & -r_S^Y \\ 0 & 0 & 1 & -r_S^Z \\ 0 & 0 & 0 & 1 \end{bmatrix}} \tag{3.68}$$

$$\boxed{{}^{\boldsymbol{S^*}}\boldsymbol{H_S^{\theta}} = \begin{bmatrix} 1 & 0 & 0 & 0 \\ 0 & \cos(\theta_S) & \sin(\theta_S) & 0 \\ 0 & -\sin(\theta_S) & \cos(\theta_S) & 0 \\ 0 & 0 & 0 & 1 \end{bmatrix}} \tag{3.69}$$

$$
\boxed{{}^{S^*}\boldsymbol{H}_{\boldsymbol{S}}^{\phi} = \begin{bmatrix} \cos(\phi_S) & 0 & -\sin(\phi_S) & 0 \\ 0 & 1 & 0 & 0 \\ \sin(\phi_S) & 0 & \cos(\phi_S) & 0 \\ 0 & 0 & 0 & 1 \end{bmatrix}} \tag{3.70}
$$

$$
\boxed{{}^{S^*}\boldsymbol{H}_{\boldsymbol{S}}^{\gamma} = \begin{bmatrix} \cos(\gamma_S) & \sin(\gamma_S) & 0 & 0 \\ -\sin(\gamma_S) & \cos(\gamma_S) & 0 & 0 \\ 0 & 0 & 1 & 0 \\ 0 & 0 & 0 & 1 \end{bmatrix}} \tag{3.71}
$$

3.9.2 $UVW \rightarrow XYZ$ Transforms

For transforming vector orientations (directions) only a single rotation operation $\left({}^{\boldsymbol{S}}\boldsymbol{H}_{\boldsymbol{S^*}}\right)$ is needed:

$$
\boxed{\begin{bmatrix} \vec{\boldsymbol{r}}_S \\ 1 \end{bmatrix} = \left({}^{\boldsymbol{S}}\boldsymbol{H}_{\boldsymbol{S^*}}\right) \begin{bmatrix} \vec{\boldsymbol{r}}_{S^*} \\ 1 \end{bmatrix}} \tag{3.72}
$$

For transforming coordinate locations (positions), both a rotation operation $\left({}^{\boldsymbol{S}}\boldsymbol{H}_{\boldsymbol{S^*}}\right)$ and a translation operation $\left({}^{\boldsymbol{S}}\boldsymbol{H}_{\boldsymbol{S^*}}^{\boldsymbol{XYZ}}\right)$ are needed:

$$
\boxed{\begin{bmatrix} \vec{\boldsymbol{r}}_S \\ 1 \end{bmatrix} = \left({}^{\boldsymbol{S}}\boldsymbol{H}_{\boldsymbol{S^*}}^{\boldsymbol{XYZ}}\right)\left({}^{\boldsymbol{S}}\boldsymbol{H}_{\boldsymbol{S^*}}\right) \begin{bmatrix} \vec{\boldsymbol{r}}_{S^*} \\ 1 \end{bmatrix}} \tag{3.73}
$$

The entries of the various transformation matrices are derived in Equations (3.74) to (3.78):

$$\boxed{{}^{S}\boldsymbol{H}_{\boldsymbol{S^*}} = \left({}^{S}\boldsymbol{H}^{\boldsymbol{\theta}}_{\boldsymbol{S^*}}\right)\left({}^{S}\boldsymbol{H}^{\boldsymbol{\phi}}_{\boldsymbol{S^*}}\right)\left({}^{S}\boldsymbol{H}^{\boldsymbol{\gamma}}_{\boldsymbol{S^*}}\right)} \tag{3.74}$$

$$\boxed{{}^{S}\boldsymbol{H}^{\boldsymbol{XYZ}}_{\boldsymbol{S^*}} = \begin{bmatrix} 1 & 0 & 0 & r_S^X \\ 0 & 1 & 0 & r_S^Y \\ 0 & 0 & 1 & r_S^Z \\ 0 & 0 & 0 & 1 \end{bmatrix}} \tag{3.75}$$

$$\boxed{{}^{S}\boldsymbol{H}^{\boldsymbol{\theta}}_{\boldsymbol{S^*}} = \begin{bmatrix} 1 & 0 & 0 & 0 \\ 0 & \cos(\theta_S) & -\sin(\theta_S) & 0 \\ 0 & \sin(\theta_S) & \cos(\theta_S) & 0 \\ 0 & 0 & 0 & 1 \end{bmatrix}} \tag{3.76}$$

$$\boxed{{}^{S}\boldsymbol{H}^{\boldsymbol{\phi}}_{\boldsymbol{S^*}} = \begin{bmatrix} \cos(\phi_S) & 0 & \sin(\phi_S) & 0 \\ 0 & 1 & 0 & 0 \\ -\sin(\phi_S) & 0 & \cos(\phi_S) & 0 \\ 0 & 0 & 0 & 1 \end{bmatrix}} \tag{3.77}$$

$$\boxed{{}^{S}\boldsymbol{H}^{\boldsymbol{\gamma}}_{\boldsymbol{S^*}} = \begin{bmatrix} \cos(\gamma_S) & -\sin(\gamma_S) & 0 & 0 \\ \sin(\gamma_S) & \cos(\gamma_S) & 0 & 0 \\ 0 & 0 & 1 & 0 \\ 0 & 0 & 0 & 1 \end{bmatrix}} \tag{3.78}$$

A 3×3 version of Equation (3.78) is also defined that will prove helpful in Chapter 4:

$$
{}^{S}\boldsymbol{H}_{\boldsymbol{S^*}}^{\gamma^*} = \begin{bmatrix} \cos(\gamma_S) & -\sin(\gamma_S) & 0 \\ \sin(\gamma_S) & \cos(\gamma_S) & 0 \\ 0 & 0 & 1 \end{bmatrix} \tag{3.79}
$$

3.10 Satellite Local Sliding Velocity

The relative velocities from before can nnow be transformed into local UVW coordinates. For the Orbit/ Satellite interface, this is $\vec{\boldsymbol{v}}_{OS^*}$:

$$
\begin{bmatrix} \vec{\boldsymbol{v}}_{OS^*} \\ 1 \end{bmatrix} = {}^{\boldsymbol{S^*}}\boldsymbol{H}_{\boldsymbol{S}} \begin{bmatrix} \vec{\boldsymbol{v}}_{OS} \\ 1 \end{bmatrix} \tag{3.80}
$$

For the Planet/Satellite interface, this is:

$$
\begin{bmatrix} \vec{\boldsymbol{v}}_{PS^*} \\ 1 \end{bmatrix} = {}^{\boldsymbol{S^*}}\boldsymbol{H}_{\boldsymbol{S}} \begin{bmatrix} \vec{\boldsymbol{v}}_{PS} \\ 1 \end{bmatrix} \tag{3.81}
$$

$$
\tag{3.82}
$$

3.11 Satellite Local Acceleration

To round out the Satellite kinematics parameters, the Satellite's global linear acceleration is converted into local UVW coordinates. This will allow the equilibrium equations to be solved locally to the Satellite. An $XYZ \rightarrow UVW$ transform is performed on the XYZ Satellite acceleration ($\vec{\boldsymbol{a}}_S$), which was found in Equation (3.43):

$$
\begin{bmatrix} \vec{\boldsymbol{a}}_{S^*} \\ 1 \end{bmatrix} = \left({}^{\boldsymbol{S^*}}\boldsymbol{H}_{\boldsymbol{S}}\right) \begin{bmatrix} \vec{\boldsymbol{a}}_{S} \\ 1 \end{bmatrix} \tag{3.83}
$$

$\vec{\boldsymbol{a}}_{S^*}$ is the Satellite's linear acceleration in local UVW coordinates, and its entries are:

$$\boxed{\vec{\boldsymbol{a}}_{S^*} = \begin{bmatrix} a_{S^*}^{U} \\ \\ a_{S^*}^{V} \\ \\ a_{S^*}^{W} \end{bmatrix}} \tag{3.84}$$

The Satellite's linear acceleration ($\vec{\boldsymbol{a}}_{S^*}$) and angular acceleration ($\vec{\boldsymbol{\alpha}}_{S^*}$, from Equation (3.56)) will feed directly into the equilibrium equations solved in Chapter 4.

3.12 Example Satellite Kinematics Animation Tool

At this point, all kinematics for the IHC are determined. The various parameters will not only feed into the calculations in Chapter 4, but can also be used to visualize IHC motions and behaviors. An example of one such useful visualization is Figure 3-13.

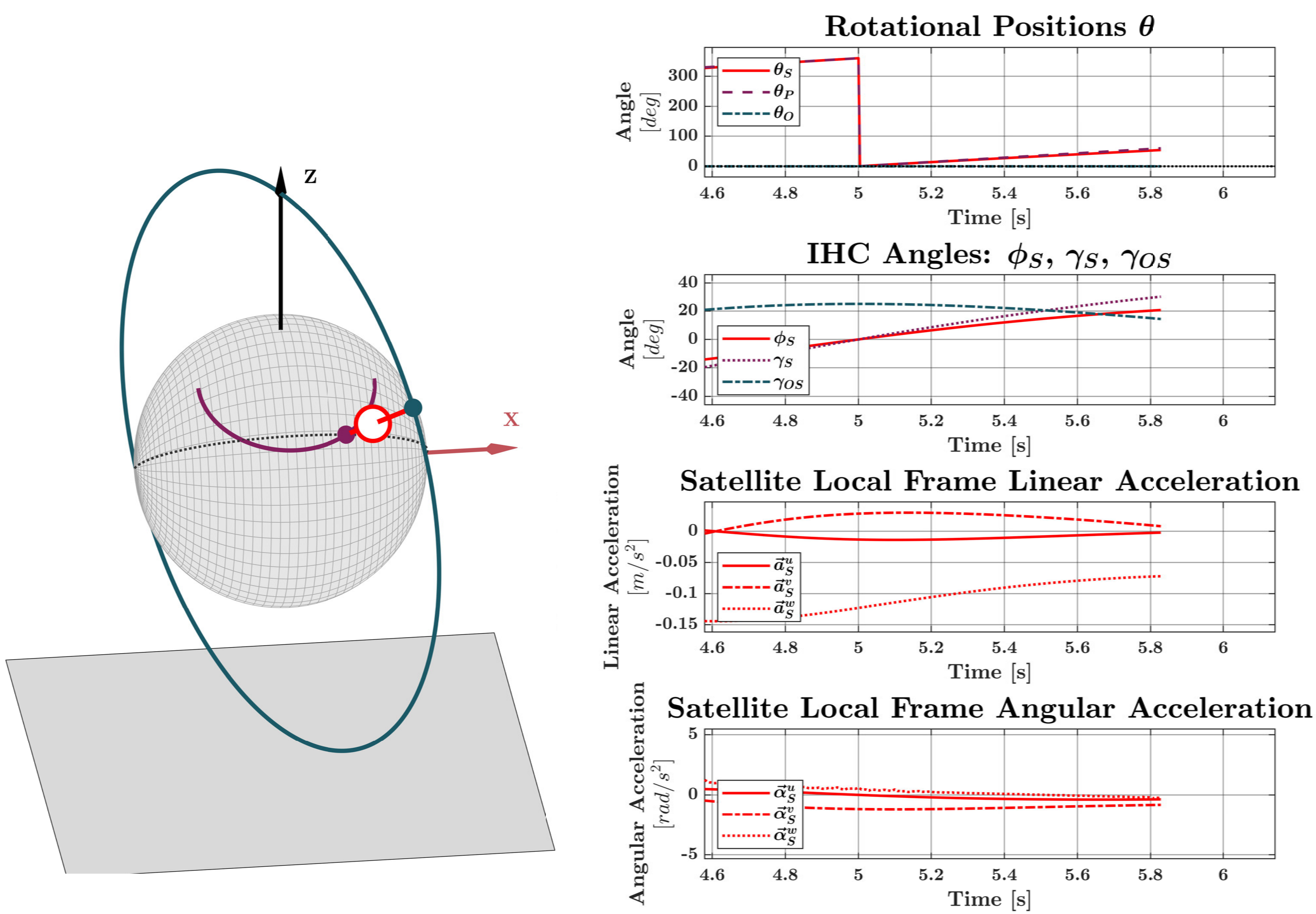

Figure 3-13 – Screenshot of an ihcMATLAB Kinematics Animation Tool. Displayed here is a screenshot from an ihcMATLAB animation. Animations such as this are invaluable for understanding the evolution of many parameters of interest. This readout gives clear feedback on the relative rotations (θ) of all components, the Satellite angle coordinates ($\phi_S, \gamma_S, \gamma_{OS}$), and the satellite accelerations (both linear and angular) relative to the local UVW coordinate frame. Animations like this one also provide valuable visual feedback when debugging.

THIS PAGE INTENTIONALLY LEFT BLANK

Chapter 4

Modeling Part 2:

Forces, Energy, Power, & Thermals

4.1 Satellite Geometry

Some design work must be completed before the IHC equilibrium equations can be solved. This is because the location and orientation of the various forces cannot be specified without having a clear picture of the real-world Satellite implementation. This suggests a potentially circular design issue: The goal of the model is to inform the IHC design, yet the model can't be run without first having created a design to simulate (in other words, a "chicken-and-the-egg" problem). To overcome this it's necessary to start with an "informed guess" at a viable Satellite geometry and then use the model to iterate through revisions, ultimately arriving at a final design.

This thesis considers only one IHC Satellite geometry. The selected design was expressly chosen for its pseudo-kinematic contact scheme, which allowed the project goals to be achieved with minimal excess complication and risk. However, it is important to note that the pseudo-kinematic design is not without its drawbacks (discussed later in this chapter). **Although the scope of this thesis is limited to the pseudo-kinematic design, future work should not be limited to this layout.** Other topologies offer potentially serious performance advantages in return for more difficult contact analysis. The contact force and equilibrium equation derivations will need to be reworked for each new topology explored in the future.

4.1.1 IHC Satellite Layout

Figures 4-1 to 4-3 show CAD screenshots of the Satellite geometry used in the final physical prototype. While discussion of many of the design details is left for Chapter 5, the core geometry related to contact forces is presented here. Each Satellite consists of four major components – three tapered blocks and a central shaft (see Figure 4-1a):

- **The lower two blocks are the "Planet" blocks.** They clamp to the Planet, which has a corresponding tapered slot. A preload force is provided by a spring acting on the lower Planet block, "squeezing" the Planet blocks into their slot. (See Figure 4-2)
- **The outer block is the "Orbit" block.** It slides inside a corresponding tapered slot in the Orbit subassembly. A preload force is provided by a spring, which presses the Orbit block outwards into the Orbit track slot. (See Figure 4-3)
- **The shaft serves as the core structure of the Satellite.** It lies coaxial to the Satellite "intersection line."

Each Satellite is tracked using its center-of-mass, the location of which can be estimated using computer-aided design (CAD) software. The Satellite's local coordinate system UVW is then placed exactly at this location, with its axes aligned to the Planet blocks (*i.e.* both UVW and the Planet blocks always have the same rotation γ_S). The Orbit block is free to rotate about the Satellite shaft axis (*i.e.* γ_{OS} rotation) so it can track the orientation of the Orbit slot (see Figure 4-1c).

4.1.2 Satellite Block Tapers

As can be clearly seen in Figures 4-2 and 4-3, each Satellite block is tapered. The tapers serve multiple purposes:

- **Most importantly, the tapers allow the contact scheme to be approximated as pseudo-kinematic, allowing the equilibrium equations to be easily solved.** This greatly simplifies the mathematics and avoids the need to consider pressure distributions or local deformations (though this is likely relevant in future work).
- Thanks to the two preload forces mentioned, each block is continuously pressed into its mating slot. This eliminates backlash from fabrication, assembly, etc.
- The preload forces are provided by springs. Each can act as a sort of "suspension" to absorb positional variation without admitting backlash. This allows the interfaces to self-compensate for changing geometric and alignment errors.

The main drawback of tapering the Satellite blocks is that the axial and lateral loads become coupled together. This means pure lateral loads can induce axial loads (along W). If an induced axial load is large enough to overcome the associated spring preload, the block will "lift off" and lose surface contact. The equilibrium equations presented later in this chapter forbid the loss of contact at any interface, so Satellite "liftoff" is a "soft failure condition." ihcMATLAB flags these cases so the boundary of pseudo-kinematic behavior can be tracked and identified.

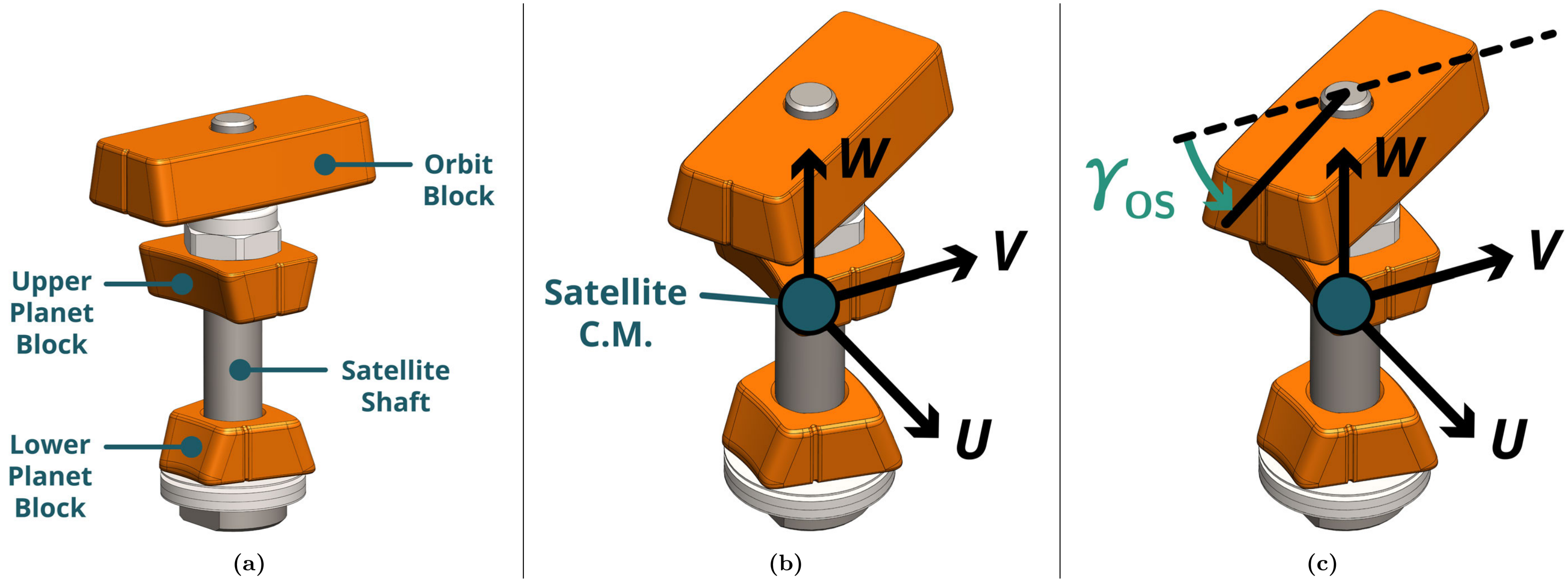

Figure 4-1 – Diagrams of the critical Satellite geometry, the coordinate system UVW, and the relative orientation γ_{OS} of the Orbit block.

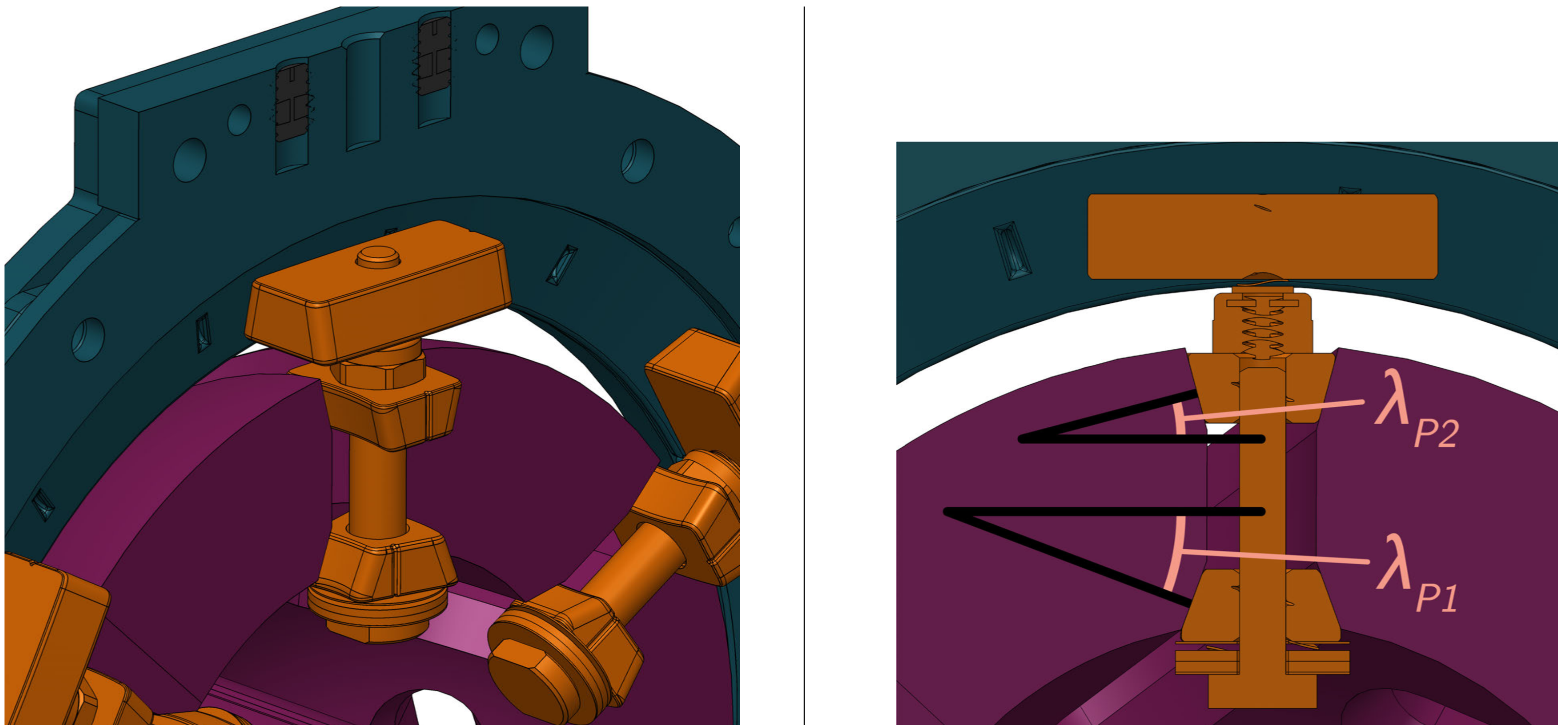

(a) (b)

Figure 4-2 – Diagrams of the contact angles $\boldsymbol{\lambda_{P1}}$ and $\boldsymbol{\lambda_{P2}}$, for the Lower and Upper Planet blocks, respectively. The angles chosen for the ihcBENCH prototype ($\lambda_{P1} = -20°, \lambda_{P2} = +15°$) allow the Satellite to "clamp" itself into the Planet slot.

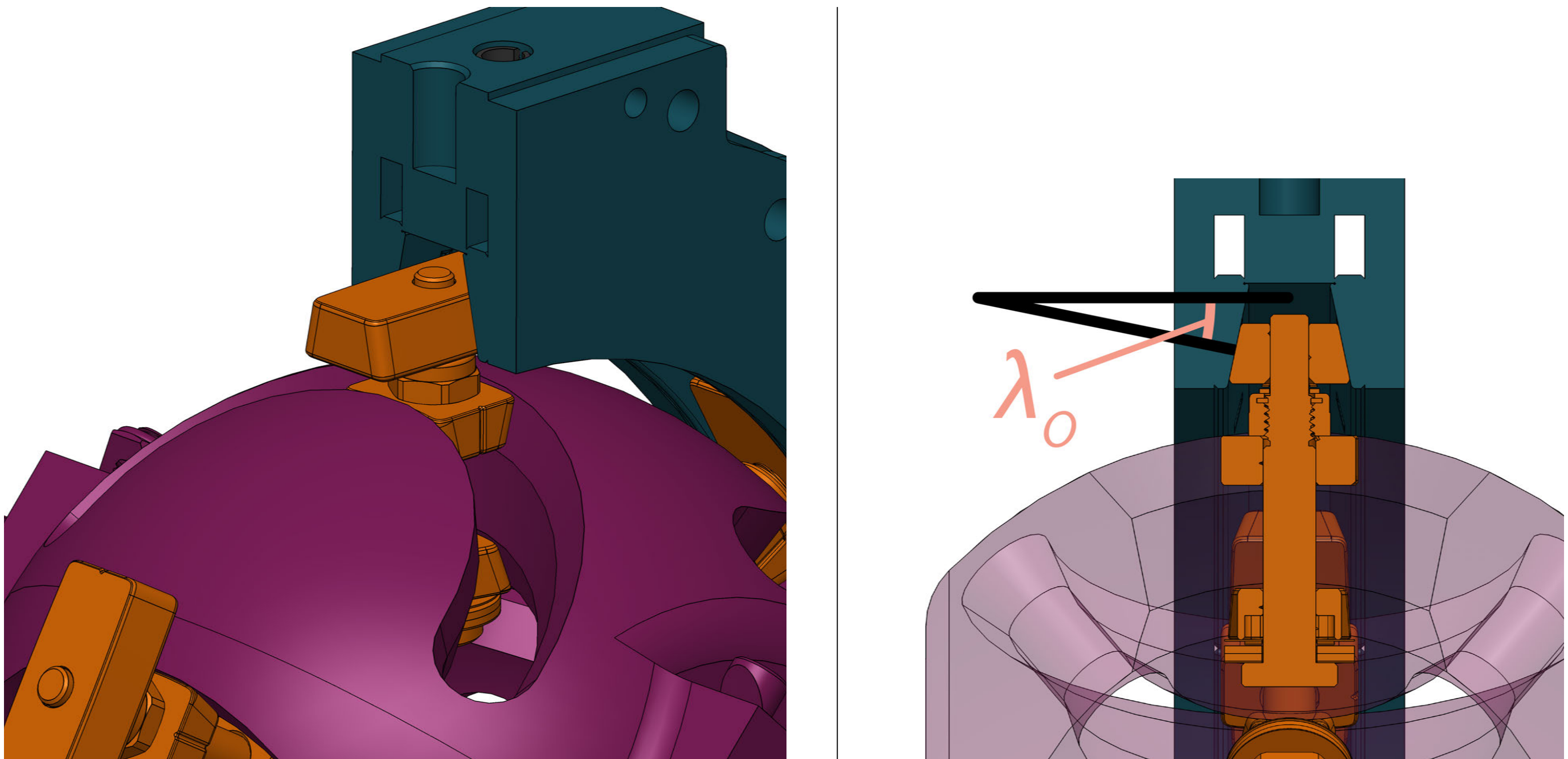

(a) (b)

Figure 4-3 – CAD screenshots showing cutaway views of the Satellite Orbit block contact angle, $\lambda_O = -12°$.

It is important to recognize that this “failure mode” is not inherent to IHCs in general – just those with tapered Satellite blocks. The implementation of a comprehensive solution to “liftoff” is left for future work. One potential option would be to use vertical Satellite faces. This would decouple the lateral and axial loads from one another, but would require many design aspects to be reevaluated, such as fits and tolerances, solutions to slop/backlash, ensuring proper Satellite degrees-of-freedom, and new derivations for the equilibrium equations. In this research effort, the performance drawback of tapered Satellite blocks was accepted in return for the substantially reduced burden for modeling, fabrication, and assembly.

The taper angle for each Satellite block is defined by a variable $\boldsymbol{\lambda}$, which corresponds to the inclination of a face’s *inward-pointing* normal vector from the horizontal UV plane:

- $\boldsymbol{\lambda > 0 \rightarrow}$ **Positive Taper:** Satellite block has a “downwards taper” (it is narrower at the bottom). The inward normal vector is inclined upwards.
- $\boldsymbol{\lambda = 0 \rightarrow}$ **Zero Taper:** Satellite block has no taper (there is no narrowing). The inward normal vector is horizontal.
- $\boldsymbol{\lambda < 0 \rightarrow}$ **Negative Taper:** Satellite block has an “upwards taper” (it is narrower at the top). The inward normal vector is inclined downwards.

The λ angles used for the IHC prototype are listed in Table 4.1. Further discussion on taper angle selection and associated practical considerations can be found in Section 5.4.1.

Table 4.1 – ihcBENCH Satellite Taper Angles

Contact Angle, Sat. Inner Planet Block	$\boldsymbol{\lambda_{P1}}$	$\mathbf{-20^\circ}$ Upwards Taper
Contact Angle, Sat. Outer Planet Block	$\boldsymbol{\lambda_{P2}}$	$\mathbf{+15^\circ}$ Downwards Taper
Contact Angle, Sat. Orbit Block	$\boldsymbol{\lambda_{O}}$	$\mathbf{-12^\circ}$ Upwards Taper

4.2 Satellite Contact Forces & Induced Moments

4.2.1 Contact Force Locations

This model simplifies the Satellite loads into point-loads acting at the locations shown in Figures 4-4 and 4-5 (related Satellite dimensions shown in Figures 4-6 and 4-7). Loads at Contact Points #1-2 act at the bottom edges of the front and rear faces of the Lower Planet block. Loads at Contact Points #3-6 act at the far corners of the Upper Planet block on its front/rear faces.[1] Loads acting at Contact Points #7-8

[1] Note that the blocks in Figure 4-4 have filleted edges. The forces are located at the extremities of the front/rear contact surfaces, just before each fillet begins.

act on the upper edges of the Orbit block's left/right faces. The eight load locations are placed at the extremities of their respective contact faces, reflecting the fact that the farthest-spaced points will provide most of the resistance to moment loads.

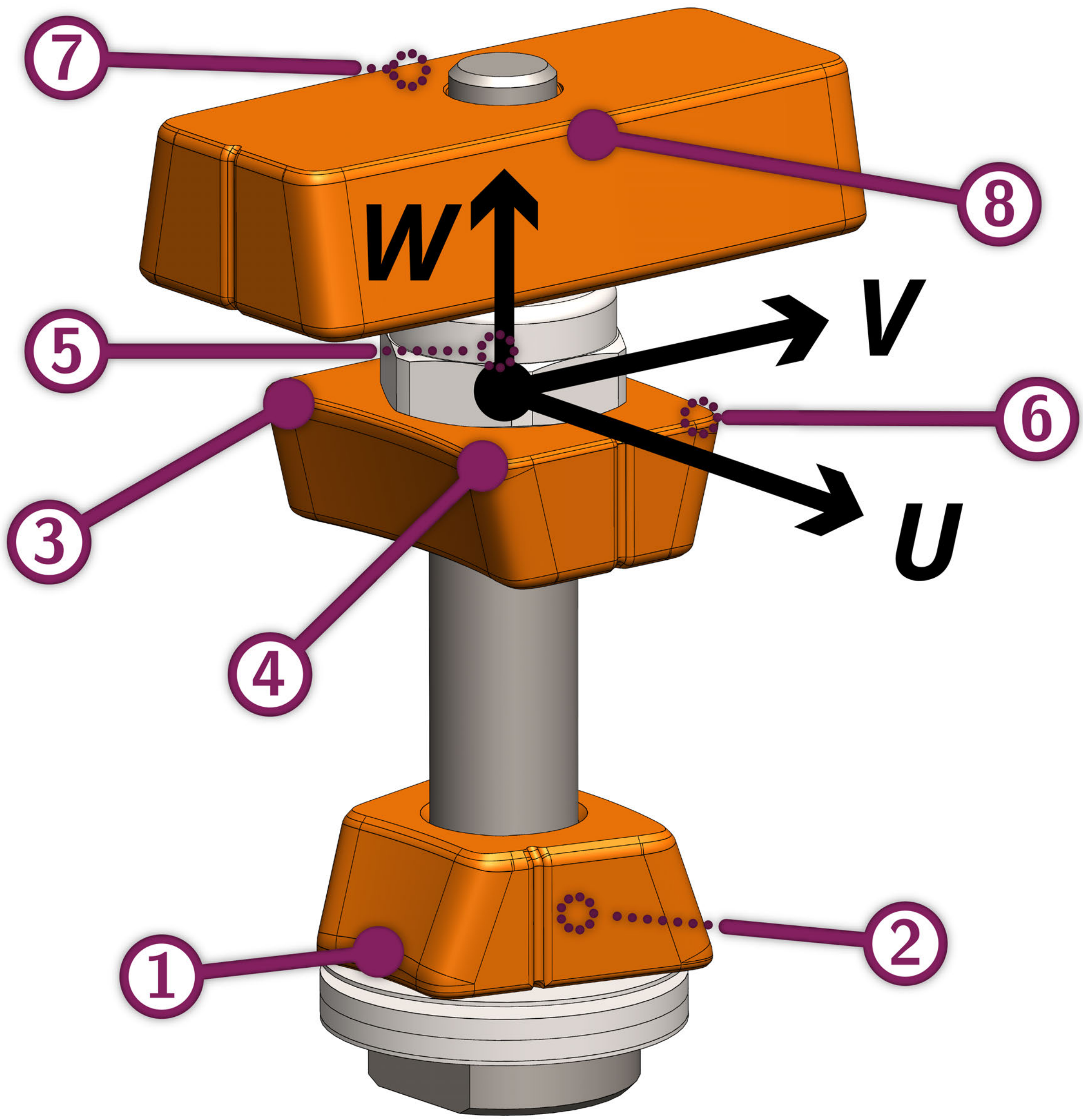

Figure 4-4 – Diagram of the locations of Contact Points #1-8 local to a Satellite. Each contact point has an associated normal force and an associated friction force.

4.2.2 Normal Forces, Friction Forces, & Effective Moments

At this stage of IHC analysis, the contact forces are the unknowns – all kinematics were found in Chapter 3 and the mass/inertia can be determined from CAD for any given design. However, only the forces' magnitudes need to be found – their locations (Contact Points #1-8) and directions (normal/parallel to

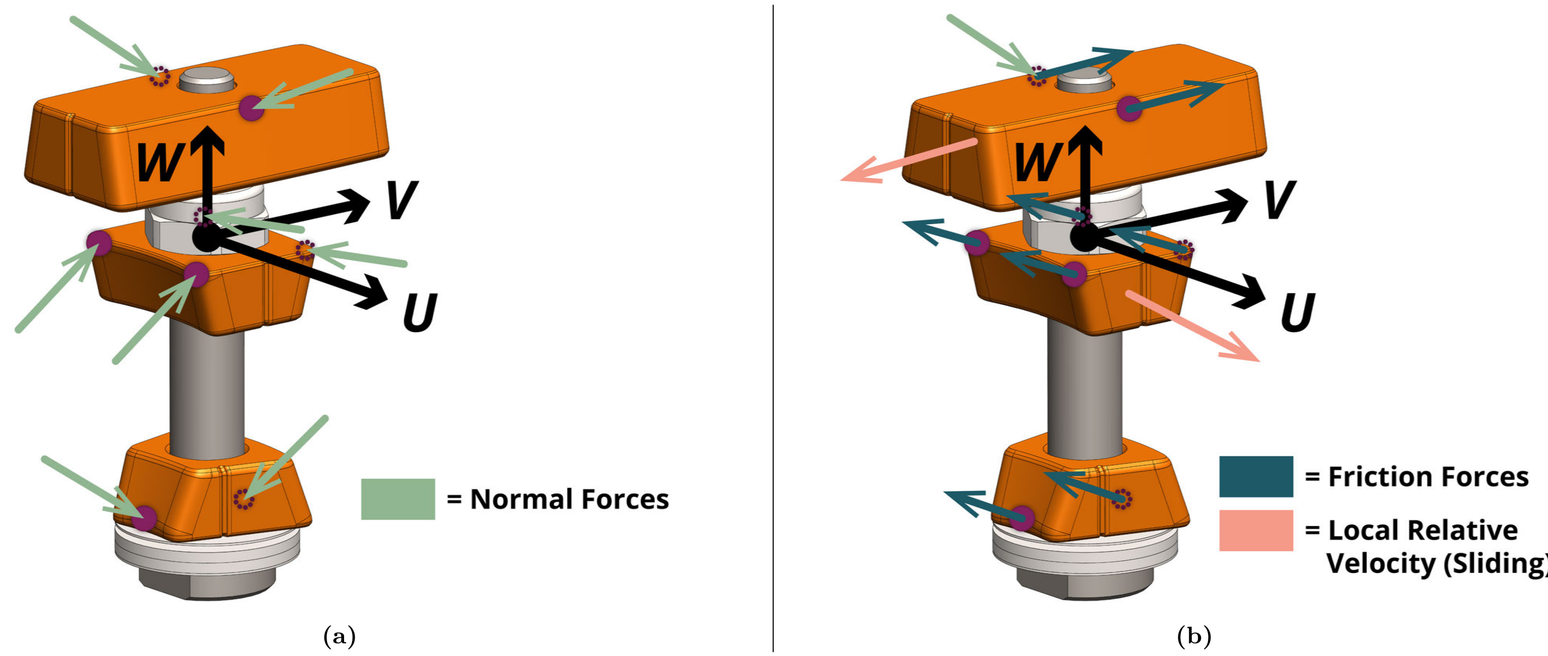

Figure 4-5 – Diagram of the Satellite normal and friction forces acting at the various Contact Points. Each normal force acts perpendicular to its contact face. Each friction force acts tangent to the face at the Contact Point location, in the direction opposing motion.

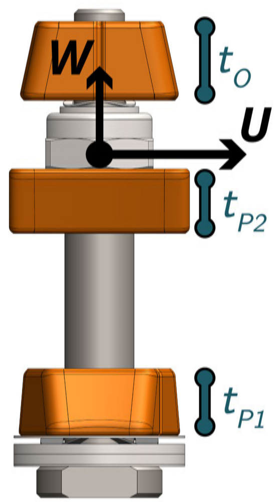

(a)

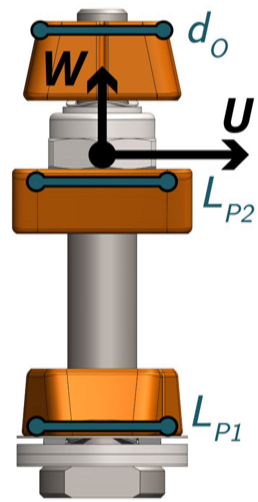

(b)

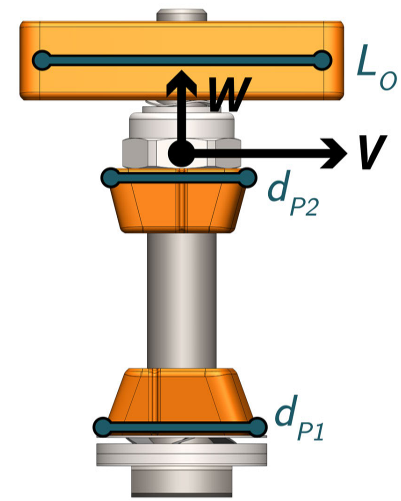

(c)

Figure 4-6 – Diagram of the Satellite block geometry variables.

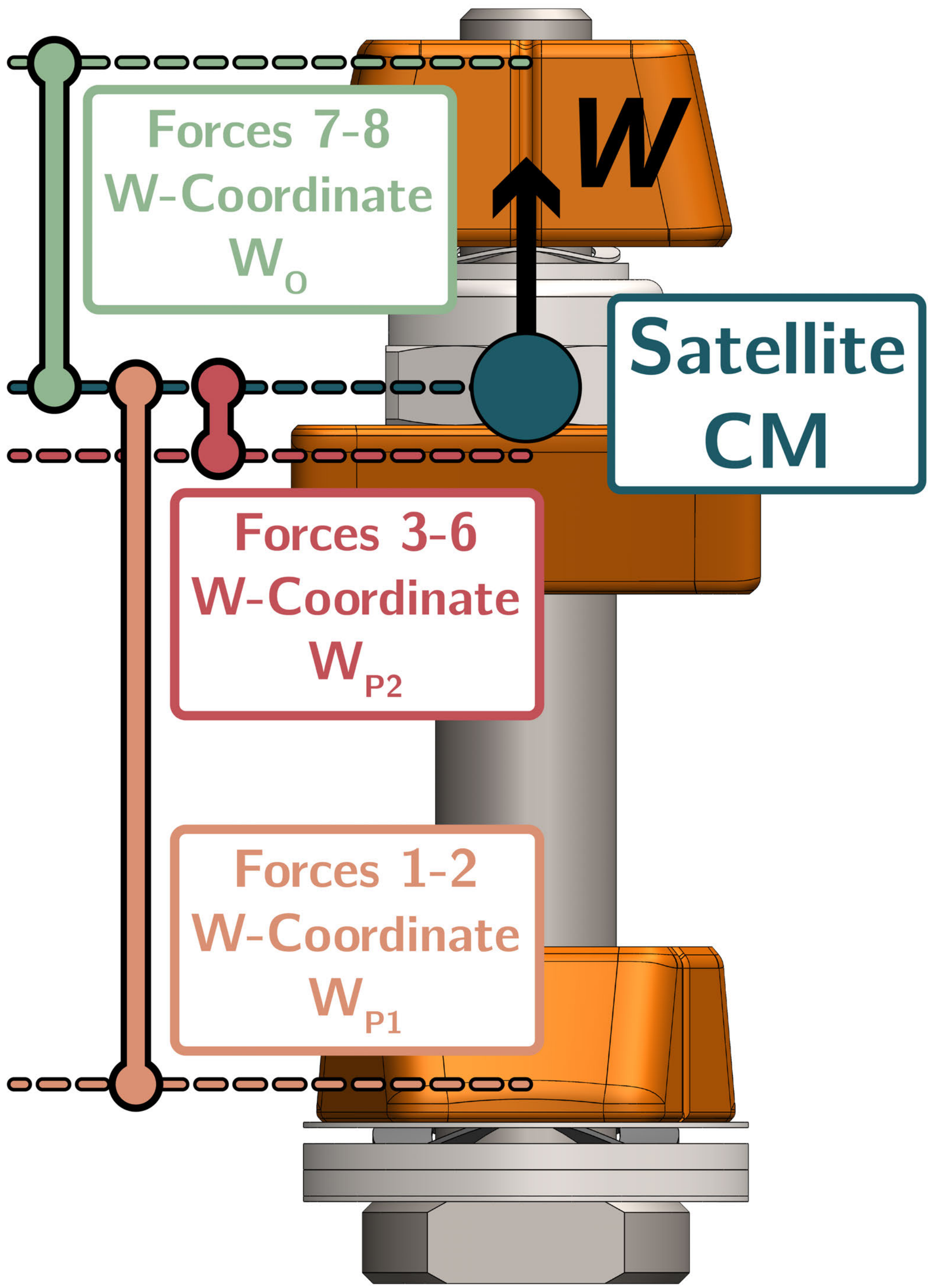

Figure 4-7 – Diagram of the Contact Point *W*-coordinates relative to the Satellite's center-of-mass.

the surface for normal/friction forces) are given from the model assumptions. **Note that this process will need to be repeated for each timestep of the model!**

Each contact point is associated with two contact forces: a compressive normal force and a friction force. Because a simple kinetic Coulomb model for friction is assumed $\left(|F^f| = \mu|F^N|\right)$, both forces depend on only a single unknown – the magnitude of the normal force. While the equilibrium equations can mathematically return negative values for normal force magnitudes, these represent invalid solutions for numerous reasons.[1] Every valid solution to the equilibrium equations must therefore produce eight compressive normal forces of varying magnitudes. Parameters such as the taper angles, preload values, block spacing, *etc.* all influence these magnitudes. As a result, they also determine which operating points are viable for the IHC as a whole.

The locations and orientations of the various contact forces are given in Table 4.2. The Planet block locations are straightforward to determine and depend only on the block geometry and spacing. The Orbit block locations are slightly trickier as they depend on the Orbit block rotation γ_{OS}.

In terms of the force direction vectors, the normal forces can be readily determined (again see Table 4.2). However, the friction forces reverse direction depending on the local velocity of each Satellite block relative to the slot in which it slides. In Table 4.2 this directionality is captured by the coefficients K_{PS} and K_{OS}. These coefficients can take values of ± 1 based on the dot products in Equations (4.1) and (4.2):

$$K_{PS} = \begin{cases} +1, & \text{if } \left(\vec{\boldsymbol{v}}_{PS^*} \cdot \hat{\mathbf{U}}\right) < 0 \\ -1, & \text{if } \left(\vec{\boldsymbol{v}}_{PS^*} \cdot \hat{\mathbf{U}}\right) \geq 0 \end{cases} \tag{4.1}$$

$$K_{OS} = \begin{cases} +1, & \text{if } \left(\vec{\boldsymbol{v}}_{OS^*} \cdot \hat{\mathbf{V}}\right) < 0 \\ -1, & \text{if } \left(\vec{\boldsymbol{v}}_{OS^*} \cdot \hat{\mathbf{V}}\right) \geq 0 \end{cases} \tag{4.2}$$

4.2.3 Expressions for Forces & Moments at Contact Points

In total, four quantities feed into the equilibrium equations at each contact location: the two contact forces (normal/frictional) and their two corresponding effective moments about the Satellite's center-of-mass. All four of these quantities depend on a single unknown – the normal force magnitude, which is given the symbol $\boldsymbol{\mathcal{F}}$. This magnitude can be divided out from the four entities to express them on a per-unit-normal-force basis in preparation for assembling the equilibrium equation matrices. Several expressions for the normal/friction forces and their effective moments will be walked through using Contact Point #1 as an example. The various contact forces and their effective moments are individually specified in

[1] A negative compressive force would mean the contact interfaces somehow transmit tensile loads. Equally importantly, the friction vector would also "flip" directions and aid motion, rather than oppose it.

Table 4.2 – Satellite Contact Force Locations & Directions in UVW-Space

Contact Point:	Contact Block:	Contact Location:	Normal Force Vector:	Normal Force Direction:	Friction Force Vector:	Friction Force Direction:
1	Lower Planet	$\vec{\boldsymbol{r}}_{S^*}^{\{1\}} = \begin{bmatrix} 0 \\ (\frac{-1}{2})d_{P1} \\ W_{P1} \end{bmatrix}$	$\vec{\boldsymbol{F}}_{PS^*}^{N1}$	$\hat{\mathbf{F}}_{PS^*}^{N1} = \begin{bmatrix} 0 \\ +\cos(\lambda_{P1}) \\ \sin(\lambda_{P1}) \end{bmatrix}$	$\vec{\boldsymbol{F}}_{PS^*}^{f1}$	$\hat{\mathbf{F}}_{PS^*}^{f1} = \begin{bmatrix} K_{PS} \\ 0 \\ 0 \end{bmatrix}$
2	Lower Planet	$\vec{\boldsymbol{r}}_{S^*}^{\{2\}} = \begin{bmatrix} 0 \\ (\frac{\pm 1}{2})d_{P1} \\ W_{P1} \end{bmatrix}$	$\vec{\boldsymbol{F}}_{PS^*}^{N2}$	$\hat{\mathbf{F}}_{PS^*}^{N2} = \begin{bmatrix} 0 \\ -\cos(\lambda_{P1}) \\ \sin(\lambda_{P1}) \end{bmatrix}$	$\vec{\boldsymbol{F}}_{PS^*}^{f2}$	$\hat{\mathbf{F}}_{PS^*}^{f2} = \begin{bmatrix} K_{PS} \\ 0 \\ 0 \end{bmatrix}$
3	Upper Planet	$\vec{\boldsymbol{r}}_{S^*}^{\{3\}} = \begin{bmatrix} (\frac{-1}{2})L_{P2} \\ (\frac{-1}{2})d_{P2} \\ W_{P2} \end{bmatrix}$	$\vec{\boldsymbol{F}}_{PS^*}^{N3}$	$\hat{\mathbf{F}}_{PS^*}^{N3} = \begin{bmatrix} 0 \\ +\cos(\lambda_{P2}) \\ \sin(\lambda_{P2}) \end{bmatrix}$	$\vec{\boldsymbol{F}}_{PS^*}^{f3}$	$\hat{\mathbf{F}}_{PS^*}^{f3} = \begin{bmatrix} K_{PS} \\ 0 \\ 0 \end{bmatrix}$
4	Upper Planet	$\vec{\boldsymbol{r}}_{S^*}^{\{4\}} = \begin{bmatrix} (\frac{\pm 1}{2})L_{P2} \\ (\frac{-1}{2})d_{P2} \\ W_{P2} \end{bmatrix}$	$\vec{\boldsymbol{F}}_{PS^*}^{N4}$	$\hat{\mathbf{F}}_{PS^*}^{N4} = \begin{bmatrix} 0 \\ +\cos(\lambda_{P2}) \\ \sin(\lambda_{P2}) \end{bmatrix}$	$\vec{\boldsymbol{F}}_{PS^*}^{f4}$	$\hat{\mathbf{F}}_{PS^*}^{f4} = \begin{bmatrix} K_{PS} \\ 0 \\ 0 \end{bmatrix}$
5	Upper Planet	$\vec{\boldsymbol{r}}_{S^*}^{\{5\}} = \begin{bmatrix} (\frac{-1}{2})L_{P2} \\ (\frac{\pm 1}{2})d_{P2} \\ W_{P2} \end{bmatrix}$	$\vec{\boldsymbol{F}}_{PS^*}^{N5}$	$\hat{\mathbf{F}}_{PS^*}^{N5} = \begin{bmatrix} 0 \\ -\cos(\lambda_{P2}) \\ \sin(\lambda_{P2}) \end{bmatrix}$	$\vec{\boldsymbol{F}}_{PS^*}^{f5}$	$\hat{\mathbf{F}}_{PS^*}^{f5} = \begin{bmatrix} K_{PS} \\ 0 \\ 0 \end{bmatrix}$
6	Upper Planet	$\vec{\boldsymbol{r}}_{S^*}^{\{6\}} = \begin{bmatrix} (\frac{\pm 1}{2})L_{P2} \\ (\frac{\pm 1}{2})d_{P2} \\ W_{P2} \end{bmatrix}$	$\vec{\boldsymbol{F}}_{PS^*}^{N6}$	$\hat{\mathbf{F}}_{PS^*}^{N6} = \begin{bmatrix} 0 \\ -\cos(\lambda_{P2}) \\ \sin(\lambda_{P2}) \end{bmatrix}$	$\vec{\boldsymbol{F}}_{PS^*}^{f6}$	$\hat{\mathbf{F}}_{PS^*}^{f6} = \begin{bmatrix} K_{PS} \\ 0 \\ 0 \end{bmatrix}$
7	Orbit	$\vec{\boldsymbol{r}}_{S^*}^{\{7\}} = \left({}^{\boldsymbol{S}}\boldsymbol{H}_{\boldsymbol{S^*}}^{\gamma^*}\right) \begin{bmatrix} (\frac{-1}{2})d_O \\ 0 \\ W_O \end{bmatrix}$	$\vec{\boldsymbol{F}}_{OS^*}^{N7}$	$\hat{\mathbf{F}}_{OS^*}^{N7} = \left({}^{\boldsymbol{S}}\boldsymbol{H}_{\boldsymbol{S^*}}^{\gamma^*}\right) \begin{bmatrix} +\cos(\lambda_O) \\ 0 \\ \sin(\lambda_O) \end{bmatrix}$	$\vec{\boldsymbol{F}}_{OS^*}^{f7}$	$\hat{\mathbf{F}}_{OS^*}^{f7} = \left({}^{\boldsymbol{S}}\boldsymbol{H}_{\boldsymbol{S^*}}^{\gamma^*}\right) \begin{bmatrix} 0 \\ K_{OS} \\ 0 \end{bmatrix}$
8	Orbit	$\vec{\boldsymbol{r}}_{S^*}^{\{8\}} = \left({}^{\boldsymbol{S}}\boldsymbol{H}_{\boldsymbol{S^*}}^{\gamma^*}\right) \begin{bmatrix} (\frac{\pm 1}{2})d_O \\ 0 \\ W_O \end{bmatrix}$	$\vec{\boldsymbol{F}}_{OS^*}^{N8}$	$\hat{\mathbf{F}}_{OS^*}^{N8} = \left({}^{\boldsymbol{S}}\boldsymbol{H}_{\boldsymbol{S^*}}^{\gamma^*}\right) \begin{bmatrix} -\cos(\lambda_O) \\ 0 \\ \sin(\lambda_O) \end{bmatrix}$	$\vec{\boldsymbol{F}}_{OS^*}^{f8}$	$\hat{\mathbf{F}}_{OS^*}^{f8} = \left({}^{\boldsymbol{S}}\boldsymbol{H}_{\boldsymbol{S^*}}^{\gamma^*}\right) \begin{bmatrix} 0 \\ K_{OS} \\ 0 \end{bmatrix}$

* ${}^{\boldsymbol{S}}\boldsymbol{H}_{\boldsymbol{S^*}}^{\gamma^*}$ is the 3x3 rotation matrix defined in Equation (3.79).

** K_{PS} and K_{OS} take values of ± 1 per Equations (4.1) and (4.2).

Tables 4.3 and 4.4.

At the first contact location, the normal and friction force vectors are:

$$\boxed{\begin{array}{ll} \vec{\boldsymbol{F}}^{N1}_{PS^*} & \textit{Normal Force Vector} \\ \vec{\boldsymbol{F}}^{f1}_{PS^*} & \textit{Friction Force Vector} \end{array}} \quad \begin{array}{r} (4.3) \\ (4.4) \end{array}$$

The normal force magnitude is:

$$\boxed{\boldsymbol{\mathcal{F}}^{N1} = \left\| \vec{\boldsymbol{F}}^{N1}_{PS^*} \right\|} \tag{4.5}$$

The normal and friction forces can be expressed in terms of this magnitude using coefficients of friction μ:

$$\boxed{\begin{aligned} \vec{\boldsymbol{F}}^{N1}_{PS^*} &= \boldsymbol{\mathcal{F}}^{N1}\left(\hat{\mathbf{F}}^{N1}_{PS^*}\right) \\ \vec{\boldsymbol{F}}^{f1}_{PS^*} &= \mu^{\{1\}}\boldsymbol{\mathcal{F}}^{N1}\left(\hat{\mathbf{F}}^{f1}_{PS^*}\right) \end{aligned}} \quad \begin{array}{r} (4.6) \\ (4.7) \end{array}$$

If $\vec{\boldsymbol{r}}^{\{1\}}_{S^*}$ is the coordinate of Contact Point #1 in the local UVW frame, the moments associated with the two forces are then:

$$\boxed{\begin{aligned} \vec{\boldsymbol{M}}^{N1}_{PS^*} &= \left(\vec{\boldsymbol{r}}^{\{1\}}_{S^*} \times \vec{\boldsymbol{F}}^{N1}_{PS^*}\right) = \boldsymbol{\mathcal{F}}^{N1}\left(\vec{\boldsymbol{r}}^{\{1\}}_{S^*} \times \hat{\mathbf{F}}^{N1}_{PS^*}\right) \\ \vec{\boldsymbol{M}}^{f1}_{PS^*} &= \left(\vec{\boldsymbol{r}}^{\{1\}}_{S^*} \times \vec{\boldsymbol{F}}^{f1}_{PS^*}\right) = \mu^{\{1\}}\boldsymbol{\mathcal{F}}^{N1}\left(\vec{\boldsymbol{r}}^{\{1\}}_{S^*} \times \hat{\mathbf{F}}^{f1}_{PS^*}\right) \end{aligned}} \quad \begin{array}{r} (4.8) \\ (4.9) \end{array}$$

The normal force magnitude can be divided out from the force and moment entities, allowing them to be expressed on a per-unit-normal-force basis (using the notation $\vec{\vec{\boldsymbol{F}}}$):

$$\vec{\boldsymbol{F}}^{N1}_{PS^*} = \left(\frac{\vec{\boldsymbol{F}}^{N1}_{PS^*}}{\boldsymbol{\mathcal{F}}^{N1}}\right) = \hat{\mathbf{F}}^{N1}_{PS^*} \tag{4.10}$$

$$\vec{\boldsymbol{F}}^{f1}_{PS^*} = \left(\frac{\vec{\boldsymbol{F}}^{f1}_{PS^*}}{\boldsymbol{\mathcal{F}}^{N1}}\right) = \mu^{\{1\}}\hat{\mathbf{F}}^{f1}_{PS^*} \tag{4.11}$$

$$\vec{\boldsymbol{M}}^{N1}_{PS^*} = \left(\frac{\vec{\boldsymbol{M}}^{N1}_{PS^*}}{\boldsymbol{\mathcal{F}}^{N1}}\right) = \left(\vec{\boldsymbol{r}}^{\{1\}}_{S^*} \times \hat{\mathbf{F}}^{N1}_{PS^*}\right) \tag{4.12}$$

$$\vec{\boldsymbol{M}}^{f1}_{PS^*} = \left(\frac{\vec{\boldsymbol{M}}^{f1}_{PS^*}}{\boldsymbol{\mathcal{F}}^{N1}}\right) = \mu^{\{1\}}\left(\vec{\boldsymbol{r}}^{\{1\}}_{S^*} \times \hat{\mathbf{F}}^{f1}_{PS^*}\right) \tag{4.13}$$

4.3 Satellite Preload Equations

The model presents 8 unknowns (the eight normal force magnitudes), yet there are currently only six equations of equilibrium – two additional equations are needed to solve the system. Two such equations can be gained by considering the balance of forces in the W-direction for individual satellite blocks. In particular, the two sprung Satellite blocks (those acted on by preload springs) are considered, with the relevant forces illustrated in Figure 4-8.

Three force types act on each sprung Satellite block in the W direction:

1. **Contact Forces**
2. **Gravitational & Inertial Forces**[1]
3. **Preload Spring Force**

Three simplifying assumptions are made:

- A Satellite block does not move relative to UVW.
- The preload spring force is known since it is specified from the IHC design.
- The preload spring force is assumed to be constant; the block does not move, therefore the spring does not compress/extend.[2]

With these assumptions, a force-balance in the W-direction can be written for each of the two sprung blocks.

For the Inner Planet block:

[1] Only inertial forces are considered in the model. Gravity is neglected but is mentioned here for completeness.
[2] This assumption neglects the fact that the Satellite shaft itself can move, thereby impacting the spring force. This is a possible area of exploration for future work.

Table 4.3 – Satellite Contact Force Expressions in UVW-Space

Contact Point:	Normal Force Magnitude:	Normal Force Vector:	Friction Force Vector:	Normal Force Per Unit $\mathcal{F}$:	Friction Force Per Unit $\mathcal{F}$:
1	$\boldsymbol{\mathcal{F}}^{N1} = \left\Vert \vec{\boldsymbol{F}}^{N1}_{PS^*} \right\Vert$	$\vec{\boldsymbol{F}}^{N1}_{PS^*} = \boldsymbol{\mathcal{F}}^{N1}\left(\hat{\mathbf{F}}^{N1}_{PS^*}\right)$	$\vec{\boldsymbol{F}}^{f1}_{PS^*} = \mu^{\{1\}}\boldsymbol{\mathcal{F}}^{N1}\left(\hat{\mathbf{F}}^{f1}_{PS^*}\right)$	$\vec{\vec{\boldsymbol{F}}}^{N1}_{PS^*} = \hat{\mathbf{F}}^{N1}_{PS^*}$	$\vec{\vec{\boldsymbol{F}}}^{f1}_{PS^*} = \mu^{\{1\}}\hat{\mathbf{F}}^{f1}_{PS^*}$
2	$\boldsymbol{\mathcal{F}}^{N2} = \left\Vert \vec{\boldsymbol{F}}^{N2}_{PS^*} \right\Vert$	$\vec{\boldsymbol{F}}^{N2}_{PS^*} = \boldsymbol{\mathcal{F}}^{N2}\left(\hat{\mathbf{F}}^{N2}_{PS^*}\right)$	$\vec{\boldsymbol{F}}^{f2}_{PS^*} = \mu^{\{2\}}\boldsymbol{\mathcal{F}}^{N2}\left(\hat{\mathbf{F}}^{f2}_{PS^*}\right)$	$\vec{\vec{\boldsymbol{F}}}^{N2}_{PS^*} = \hat{\mathbf{F}}^{N2}_{PS^*}$	$\vec{\vec{\boldsymbol{F}}}^{f2}_{PS^*} = \mu^{\{2\}}\hat{\mathbf{F}}^{f2}_{PS^*}$
3	$\boldsymbol{\mathcal{F}}^{N3} = \left\Vert \vec{\boldsymbol{F}}^{N3}_{PS^*} \right\Vert$	$\vec{\boldsymbol{F}}^{N3}_{PS^*} = \boldsymbol{\mathcal{F}}^{N3}\left(\hat{\mathbf{F}}^{N3}_{PS^*}\right)$	$\vec{\boldsymbol{F}}^{f3}_{PS^*} = \mu^{\{3\}}\boldsymbol{\mathcal{F}}^{N3}\left(\hat{\mathbf{F}}^{f3}_{PS^*}\right)$	$\vec{\vec{\boldsymbol{F}}}^{N3}_{PS^*} = \hat{\mathbf{F}}^{N3}_{PS^*}$	$\vec{\vec{\boldsymbol{F}}}^{f3}_{PS^*} = \mu^{\{3\}}\hat{\mathbf{F}}^{f3}_{PS^*}$
4	$\boldsymbol{\mathcal{F}}^{N4} = \left\Vert \vec{\boldsymbol{F}}^{N4}_{PS^*} \right\Vert$	$\vec{\boldsymbol{F}}^{N4}_{PS^*} = \boldsymbol{\mathcal{F}}^{N4}\left(\hat{\mathbf{F}}^{N4}_{PS^*}\right)$	$\vec{\boldsymbol{F}}^{f4}_{PS^*} = \mu^{\{4\}}\boldsymbol{\mathcal{F}}^{N4}\left(\hat{\mathbf{F}}^{f4}_{PS^*}\right)$	$\vec{\vec{\boldsymbol{F}}}^{N4}_{PS^*} = \hat{\mathbf{F}}^{N4}_{PS^*}$	$\vec{\vec{\boldsymbol{F}}}^{f4}_{PS^*} = \mu^{\{4\}}\hat{\mathbf{F}}^{f4}_{PS^*}$
5	$\boldsymbol{\mathcal{F}}^{N5} = \left\Vert \vec{\boldsymbol{F}}^{N5}_{PS^*} \right\Vert$	$\vec{\boldsymbol{F}}^{N5}_{PS^*} = \boldsymbol{\mathcal{F}}^{N5}\left(\hat{\mathbf{F}}^{N5}_{PS^*}\right)$	$\vec{\boldsymbol{F}}^{f5}_{PS^*} = \mu^{\{5\}}\boldsymbol{\mathcal{F}}^{N5}\left(\hat{\mathbf{F}}^{f5}_{PS^*}\right)$	$\vec{\vec{\boldsymbol{F}}}^{N5}_{PS^*} = \hat{\mathbf{F}}^{N5}_{PS^*}$	$\vec{\vec{\boldsymbol{F}}}^{f5}_{PS^*} = \mu^{\{5\}}\hat{\mathbf{F}}^{f5}_{PS^*}$
6	$\boldsymbol{\mathcal{F}}^{N6} = \left\Vert \vec{\boldsymbol{F}}^{N6}_{PS^*} \right\Vert$	$\vec{\boldsymbol{F}}^{N6}_{PS^*} = \boldsymbol{\mathcal{F}}^{N6}\left(\hat{\mathbf{F}}^{N6}_{PS^*}\right)$	$\vec{\boldsymbol{F}}^{f6}_{PS^*} = \mu^{\{6\}}\boldsymbol{\mathcal{F}}^{N6}\left(\hat{\mathbf{F}}^{f6}_{PS^*}\right)$	$\vec{\vec{\boldsymbol{F}}}^{N6}_{PS^*} = \hat{\mathbf{F}}^{N6}_{PS^*}$	$\vec{\vec{\boldsymbol{F}}}^{f6}_{PS^*} = \mu^{\{6\}}\hat{\mathbf{F}}^{f6}_{PS^*}$
7	$\boldsymbol{\mathcal{F}}^{N7} = \left\Vert \vec{\boldsymbol{F}}^{N7}_{OS^*} \right\Vert$	$\vec{\boldsymbol{F}}^{N7}_{OS^*} = \boldsymbol{\mathcal{F}}^{N7}\left(\hat{\mathbf{F}}^{N7}_{OS^*}\right)$	$\vec{\boldsymbol{F}}^{f7}_{OS^*} = \mu^{\{7\}}\boldsymbol{\mathcal{F}}^{N7}\left(\hat{\mathbf{F}}^{f7}_{OS^*}\right)$	$\vec{\vec{\boldsymbol{F}}}^{N7}_{OS^*} = \hat{\mathbf{F}}^{N7}_{OS^*}$	$\vec{\vec{\boldsymbol{F}}}^{f7}_{OS^*} = \mu^{\{7\}}\hat{\mathbf{F}}^{f7}_{OS^*}$
8	$\boldsymbol{\mathcal{F}}^{N8} = \left\Vert \vec{\boldsymbol{F}}^{N8}_{OS^*} \right\Vert$	$\vec{\boldsymbol{F}}^{N8}_{OS^*} = \boldsymbol{\mathcal{F}}^{N8}\left(\hat{\mathbf{F}}^{N8}_{OS^*}\right)$	$\vec{\boldsymbol{F}}^{f8}_{OS^*} = \mu^{\{8\}}\boldsymbol{\mathcal{F}}^{N8}\left(\hat{\mathbf{F}}^{f8}_{OS^*}\right)$	$\vec{\vec{\boldsymbol{F}}}^{N8}_{OS^*} = \hat{\mathbf{F}}^{N8}_{OS^*}$	$\vec{\vec{\boldsymbol{F}}}^{f8}_{OS^*} = \mu^{\{8\}}\hat{\mathbf{F}}^{f8}_{OS^*}$

Table 4.4 – Satellite Effective Moment Expressions in UVW-Space

Contact Point:	Moment From Normal Force:	Moment From Friction Force:	Normal Moment Per Unit $\mathcal{F}$:	Friction Moment Per Unit $\mathcal{F}$:
1	$\overrightarrow{\boldsymbol{M}}^{N1}_{PS^*} = \boldsymbol{\mathcal{F}}^{N1}\left(\vec{\boldsymbol{r}}^{\{1\}}_{S^*} \times \hat{\mathbf{F}}^{N1}_{PS^*}\right)$	$\overrightarrow{\boldsymbol{M}}^{f1}_{PS^*} = \mu^{\{1\}}\boldsymbol{\mathcal{F}}^{N1}\left(\vec{\boldsymbol{r}}^{\{1\}}_{S^*} \times \hat{\mathbf{F}}^{f1}_{PS^*}\right)$	$\overrightarrow{\tilde{\boldsymbol{M}}}^{N1}_{PS^*} = \left(\vec{\boldsymbol{r}}^{\{1\}}_{S^*} \times \hat{\mathbf{F}}^{N1}_{PS^*}\right)$	$\overrightarrow{\tilde{\boldsymbol{M}}}^{f1}_{PS^*} = \mu^{\{1\}}\left(\vec{\boldsymbol{r}}^{\{1\}}_{S^*} \times \hat{\mathbf{F}}^{f1}_{PS^*}\right)$
2	$\overrightarrow{\boldsymbol{M}}^{N2}_{PS^*} = \boldsymbol{\mathcal{F}}^{N2}\left(\vec{\boldsymbol{r}}^{\{2\}}_{S^*} \times \hat{\mathbf{F}}^{N2}_{PS^*}\right)$	$\overrightarrow{\boldsymbol{M}}^{f2}_{PS^*} = \mu^{\{2\}}\boldsymbol{\mathcal{F}}^{N2}\left(\vec{\boldsymbol{r}}^{\{2\}}_{S^*} \times \hat{\mathbf{F}}^{f2}_{PS^*}\right)$	$\overrightarrow{\tilde{\boldsymbol{M}}}^{N2}_{PS^*} = \left(\vec{\boldsymbol{r}}^{\{2\}}_{S^*} \times \hat{\mathbf{F}}^{N2}_{PS^*}\right)$	$\overrightarrow{\tilde{\boldsymbol{M}}}^{f2}_{PS^*} = \mu^{\{2\}}\left(\vec{\boldsymbol{r}}^{\{2\}}_{S^*} \times \hat{\mathbf{F}}^{f2}_{PS^*}\right)$
3	$\overrightarrow{\boldsymbol{M}}^{N3}_{PS^*} = \boldsymbol{\mathcal{F}}^{N3}\left(\vec{\boldsymbol{r}}^{\{3\}}_{S^*} \times \hat{\mathbf{F}}^{N3}_{PS^*}\right)$	$\overrightarrow{\boldsymbol{M}}^{f3}_{PS^*} = \mu^{\{3\}}\boldsymbol{\mathcal{F}}^{N3}\left(\vec{\boldsymbol{r}}^{\{3\}}_{S^*} \times \hat{\mathbf{F}}^{f3}_{PS^*}\right)$	$\overrightarrow{\tilde{\boldsymbol{M}}}^{N3}_{PS^*} = \left(\vec{\boldsymbol{r}}^{\{3\}}_{S^*} \times \hat{\mathbf{F}}^{N3}_{PS^*}\right)$	$\overrightarrow{\tilde{\boldsymbol{M}}}^{f3}_{PS^*} = \mu^{\{3\}}\left(\vec{\boldsymbol{r}}^{\{3\}}_{S^*} \times \hat{\mathbf{F}}^{f3}_{PS^*}\right)$
4	$\overrightarrow{\boldsymbol{M}}^{N4}_{PS^*} = \boldsymbol{\mathcal{F}}^{N4}\left(\vec{\boldsymbol{r}}^{\{4\}}_{S^*} \times \hat{\mathbf{F}}^{N4}_{PS^*}\right)$	$\overrightarrow{\boldsymbol{M}}^{f4}_{PS^*} = \mu^{\{4\}}\boldsymbol{\mathcal{F}}^{N4}\left(\vec{\boldsymbol{r}}^{\{4\}}_{S^*} \times \hat{\mathbf{F}}^{f4}_{PS^*}\right)$	$\overrightarrow{\tilde{\boldsymbol{M}}}^{N4}_{PS^*} = \left(\vec{\boldsymbol{r}}^{\{4\}}_{S^*} \times \hat{\mathbf{F}}^{N4}_{PS^*}\right)$	$\overrightarrow{\tilde{\boldsymbol{M}}}^{f4}_{PS^*} = \mu^{\{4\}}\left(\vec{\boldsymbol{r}}^{\{4\}}_{S^*} \times \hat{\mathbf{F}}^{f4}_{PS^*}\right)$
5	$\overrightarrow{\boldsymbol{M}}^{N5}_{PS^*} = \boldsymbol{\mathcal{F}}^{N5}\left(\vec{\boldsymbol{r}}^{\{5\}}_{S^*} \times \hat{\mathbf{F}}^{N5}_{PS^*}\right)$	$\overrightarrow{\boldsymbol{M}}^{f5}_{PS^*} = \mu^{\{5\}}\boldsymbol{\mathcal{F}}^{N5}\left(\vec{\boldsymbol{r}}^{\{5\}}_{S^*} \times \hat{\mathbf{F}}^{f5}_{PS^*}\right)$	$\overrightarrow{\tilde{\boldsymbol{M}}}^{N5}_{PS^*} = \left(\vec{\boldsymbol{r}}^{\{5\}}_{S^*} \times \hat{\mathbf{F}}^{N5}_{PS^*}\right)$	$\overrightarrow{\tilde{\boldsymbol{M}}}^{f5}_{PS^*} = \mu^{\{5\}}\left(\vec{\boldsymbol{r}}^{\{5\}}_{S^*} \times \hat{\mathbf{F}}^{f5}_{PS^*}\right)$
6	$\overrightarrow{\boldsymbol{M}}^{N6}_{PS^*} = \boldsymbol{\mathcal{F}}^{N6}\left(\vec{\boldsymbol{r}}^{\{6\}}_{S^*} \times \hat{\mathbf{F}}^{N6}_{PS^*}\right)$	$\overrightarrow{\boldsymbol{M}}^{f6}_{PS^*} = \mu^{\{6\}}\boldsymbol{\mathcal{F}}^{N6}\left(\vec{\boldsymbol{r}}^{\{6\}}_{S^*} \times \hat{\mathbf{F}}^{f6}_{PS^*}\right)$	$\overrightarrow{\tilde{\boldsymbol{M}}}^{N6}_{PS^*} = \left(\vec{\boldsymbol{r}}^{\{6\}}_{S^*} \times \hat{\mathbf{F}}^{N6}_{PS^*}\right)$	$\overrightarrow{\tilde{\boldsymbol{M}}}^{f6}_{PS^*} = \mu^{\{6\}}\left(\vec{\boldsymbol{r}}^{\{6\}}_{S^*} \times \hat{\mathbf{F}}^{f6}_{PS^*}\right)$
7	$\overrightarrow{\boldsymbol{M}}^{N7}_{OS^*} = \boldsymbol{\mathcal{F}}^{N7}\left(\vec{\boldsymbol{r}}^{\{7\}}_{S^*} \times \hat{\mathbf{F}}^{N7}_{OS^*}\right)$	$\overrightarrow{\boldsymbol{M}}^{f7}_{OS^*} = \mu^{\{7\}}\boldsymbol{\mathcal{F}}^{N7}\left(\vec{\boldsymbol{r}}^{\{7\}}_{S^*} \times \hat{\mathbf{F}}^{f7}_{OS^*}\right)$	$\overrightarrow{\tilde{\boldsymbol{M}}}^{N7}_{OS^*} = \left(\vec{\boldsymbol{r}}^{\{7\}}_{S^*} \times \hat{\mathbf{F}}^{N7}_{OS^*}\right)$	$\overrightarrow{\tilde{\boldsymbol{M}}}^{f7}_{OS^*} = \mu^{\{7\}}\left(\vec{\boldsymbol{r}}^{\{7\}}_{S^*} \times \hat{\mathbf{F}}^{f7}_{OS^*}\right)$
8	$\overrightarrow{\boldsymbol{M}}^{N8}_{OS^*} = \boldsymbol{\mathcal{F}}^{N8}\left(\vec{\boldsymbol{r}}^{\{8\}}_{S^*} \times \hat{\mathbf{F}}^{N8}_{OS^*}\right)$	$\overrightarrow{\boldsymbol{M}}^{f8}_{OS^*} = \mu^{\{8\}}\boldsymbol{\mathcal{F}}^{N8}\left(\vec{\boldsymbol{r}}^{\{8\}}_{S^*} \times \hat{\mathbf{F}}^{f8}_{OS^*}\right)$	$\overrightarrow{\tilde{\boldsymbol{M}}}^{N8}_{OS^*} = \left(\vec{\boldsymbol{r}}^{\{8\}}_{S^*} \times \hat{\mathbf{F}}^{N8}_{OS^*}\right)$	$\overrightarrow{\tilde{\boldsymbol{M}}}^{f8}_{OS^*} = \mu^{\{8\}}\left(\vec{\boldsymbol{r}}^{\{8\}}_{S^*} \times \hat{\mathbf{F}}^{f8}_{OS^*}\right)$

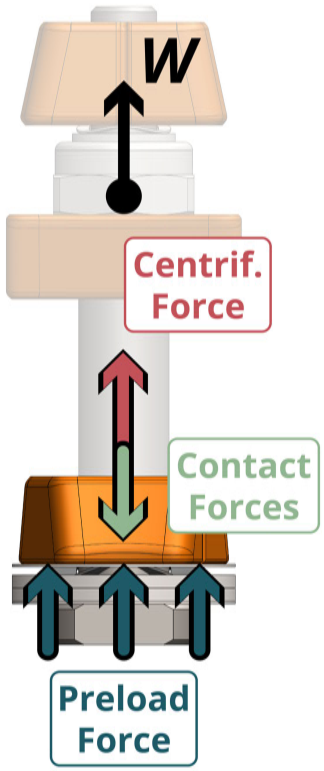

(a)

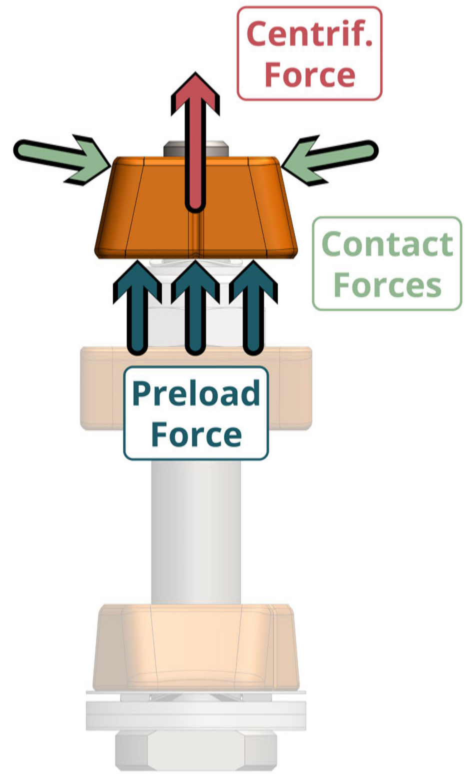

(b)

Figure 4-8 – Diagrams showing the forces involved in the Satellite preload equations. The Satellite preload equations (Equations (4.14) to (4.17)) consider equilibrium in the W-direction. In the local frame, the preload force, contact forces, and inertial load must balance to zero since the Satellite (nominally) does not change shape in operation. To avoid confusion, the contact forces here are drawn in the negative direction to reflect the angle of the contact face (in the model these negatives are captured by the signs of λ_{P1} and λ_O).

$$\boxed{\left(\vec{\boldsymbol{F}}^{N1}_{PS^*}\right)^W + \left(\vec{\boldsymbol{F}}^{N2}_{PS^*}\right)^W + \boldsymbol{\mathcal{F}}^{k_{P1}} + \frac{\left(m^{P1}_S\right)\left(\|\vec{\boldsymbol{v}}^*_{P1}\|^2\right)}{\rho^{P1}_S} = 0} \tag{4.14}$$

$\left(\vec{\boldsymbol{F}}^{N1}_{PS^*}\right)^W$ = W-component of Normal Force #1 (acts on the Inner Planet block).

$\left(\vec{\boldsymbol{F}}^{N2}_{PS^*}\right)^W$ = W-component of Normal Force #2 (acts on the Inner Planet block).

$\boldsymbol{\mathcal{F}}^{k_{P1}}$ = Inner Planet block preload force, applied via preload spring.

$\left(\frac{m^{P1}_S\|\vec{\boldsymbol{v}}^*_{P1}\|^2}{\rho^{P1}_S}\right)$ = Inner Planet block inertial force (UVW is a non-inertial frame).

m^{P1}_S = Inner Planet block mass.

$\|\vec{\boldsymbol{v}}^*_{P1}\|$ = Speed of the Inner Planet block (in global coordinates).

ρ^{P1}_S = Radial distance from the Inner Planet block's center-of-mass to the Planet center.

For the Orbit block:

$$\boxed{\left(\vec{\boldsymbol{F}}^{N7}_{OS^*}\right)^W + \left(\vec{\boldsymbol{F}}^{N8}_{OS^*}\right)^W + \boldsymbol{\mathcal{F}}^{k_O} + \frac{\left(m^O_S\right)\left(\|\vec{\boldsymbol{v}}^*_O\|^2\right)}{\rho^O_S} = 0} \tag{4.15}$$

Where:

$\left(\vec{\boldsymbol{F}}^{N7}_{OS^*}\right)^W$ = W-component of Normal Force #7 (acts on the Orbit block).

$\left(\vec{\boldsymbol{F}}^{N8}_{OS^*}\right)^W$ = W-component of Normal Force #8 (acts on the Orbit block).

$\boldsymbol{\mathcal{F}}^{k_O}$ = Orbit block preload force, applied via preload spring.

$\left(\frac{m^O_S\|\vec{\boldsymbol{v}}^*_O\|^2}{\rho^O_S}\right)$ = Orbit block inertial force (UVW is a non-inertial frame).

m^O_S = Orbit block mass.

$\|\vec{\boldsymbol{v}}^*_O\|$ = Speed of the Orbit block (in global coordinates).

ρ^O_S = Radial distance from the Orbit block's center-of-mass to the Planet center.

The preload equations can then be rewritten to factor out the normal force magnitudes:

$$\boxed{\begin{aligned} &\boldsymbol{\mathcal{F}}^{N1}\left(\vec{\boldsymbol{F}}^{N1}_{PS^*}\right)^W + \boldsymbol{\mathcal{F}}^{N2}\left(\vec{\boldsymbol{F}}^{N2}_{PS^*}\right)^W + \boldsymbol{\mathcal{F}}^{k_{P1}} + \frac{\left(m_S^{P1}\right)\left(\|\vec{\boldsymbol{v}}^*_{P1}\|^2\right)}{\rho_S^{P1}} = 0 && (4.16)\\ &\boldsymbol{\mathcal{F}}^{N7}\left(\vec{\boldsymbol{F}}^{N7}_{OS^*}\right)^W + \boldsymbol{\mathcal{F}}^{N8}\left(\vec{\boldsymbol{F}}^{N8}_{OS^*}\right)^W + \boldsymbol{\mathcal{F}}^{kO} + \frac{\left(m_S^{O}\right)\left(\|\vec{\boldsymbol{v}}^*_{O}\|^2\right)}{\rho_S^{O}} = 0 && (4.17)\end{aligned}}$$

4.4 Equilibrium Equation Matrix

At this stage, the equilibrium equations can finally be assembled into matrices. As a reminder, the eight normal force magnitudes are the unknowns in these equations. The most general expression for the system of equations is given in Equation (4.18):

$$\boxed{\underset{(8x8)}{\mathbb{C}}\;\underset{(8x1)}{\mathbb{F}^N} = \underset{(8x1)}{\mathbb{A}}} \tag{4.18}$$

In this form, it is clear that the unknowns comprising $\mathbb{F}^N$ can be determined using matrix division:

$$\boxed{\mathbb{F}^N = \mathbb{A}/\mathbb{C}} \tag{4.19}$$

So, the forces can be found once the matrices $\mathbb{A}$ and $\mathbb{C}$ are assembled. Consider Equation (4.20):

$$\boxed{\begin{bmatrix} \cdots & \underset{(3x8)}{\mathbb{C}^F} & \cdots \\ \cdots & \underset{(3x8)}{\mathbb{C}^M} & \cdots \\ \cdots & \underset{(1x8)}{\mathbb{C}^{k_{P1}}} & \cdots \\ \cdots & \underset{(1x8)}{\mathbb{C}^{k_O}} & \cdots \end{bmatrix} \begin{bmatrix} \vdots \\ \underset{(8x1)}{\mathbb{F}^N} \\ \vdots \end{bmatrix} = \begin{bmatrix} \underset{(3x1)}{\mathbb{A}^{(ma)}} \\ \underset{(3x1)}{\mathbb{A}^{(I\alpha)}} \\ \underset{(1x1)}{\mathbb{A}^{k_{P1}}} \\ \underset{(1x1)}{\mathbb{A}^{k_O}} \end{bmatrix}} \tag{4.20}$$

The matrices $\mathbb{C}$, $\mathbb{F}^N$, and $\mathbb{A}$ contain the coefficients for the equations of linear equilibrium, the equations of angular equilibrium, and the two preload equations. All of these have been previously defined, and only need to be collected together at this stage. The various entries are given in the following equations:

$$\underset{(3x8)}{\mathbb{C}^{F}} = \begin{bmatrix} \vdots & \vdots & \vdots & \vdots & \vdots & \vdots & \vdots & \vdots \\ \underset{(3x1)}{\mathbb{C}^{F1}} & \underset{(3x1)}{\mathbb{C}^{F2}} & \underset{(3x1)}{\mathbb{C}^{F3}} & \underset{(3x1)}{\mathbb{C}^{F4}} & \underset{(3x1)}{\mathbb{C}^{F5}} & \underset{(3x1)}{\mathbb{C}^{F6}} & \underset{(3x1)}{\mathbb{C}^{F7}} & \underset{(3x1)}{\mathbb{C}^{F8}} \\ \vdots & \vdots & \vdots & \vdots & \vdots & \vdots & \vdots & \vdots \end{bmatrix} \tag{4.21}$$

$$\underset{(3x8)}{\mathbb{C}^{M}} = \begin{bmatrix} \vdots & \vdots & \vdots & \vdots & \vdots & \vdots & \vdots & \vdots \\ \underset{(3x1)}{\mathbb{C}^{M1}} & \underset{(3x1)}{\mathbb{C}^{M2}} & \underset{(3x1)}{\mathbb{C}^{M3}} & \underset{(3x1)}{\mathbb{C}^{M4}} & \underset{(3x1)}{\mathbb{C}^{M5}} & \underset{(3x1)}{\mathbb{C}^{M6}} & \underset{(3x1)}{\mathbb{C}^{M7}} & \underset{(3x1)}{\mathbb{C}^{M8}} \\ \vdots & \vdots & \vdots & \vdots & \vdots & \vdots & \vdots & \vdots \end{bmatrix} \tag{4.22}$$

Where:

$$\mathbb{C}^{F1} = \vec{\boldsymbol{F}}^{N1}_{PS^*} + \vec{\boldsymbol{F}}^{f1}_{PS^*} \tag{4.23}$$
$$\mathbb{C}^{F2} = \vec{\boldsymbol{F}}^{N2}_{PS^*} + \vec{\boldsymbol{F}}^{f2}_{PS^*} \tag{4.24}$$
$$\mathbb{C}^{F3} = \vec{\boldsymbol{F}}^{N3}_{PS^*} + \vec{\boldsymbol{F}}^{f3}_{PS^*} \tag{4.25}$$
$$\mathbb{C}^{F4} = \vec{\boldsymbol{F}}^{N4}_{PS^*} + \vec{\boldsymbol{F}}^{f4}_{PS^*} \tag{4.26}$$
$$\mathbb{C}^{F5} = \vec{\boldsymbol{F}}^{N5}_{PS^*} + \vec{\boldsymbol{F}}^{f5}_{PS^*} \tag{4.27}$$
$$\mathbb{C}^{F6} = \vec{\boldsymbol{F}}^{N6}_{PS^*} + \vec{\boldsymbol{F}}^{f6}_{PS^*} \tag{4.28}$$
$$\mathbb{C}^{F7} = \vec{\boldsymbol{F}}^{N7}_{OS^*} + \vec{\boldsymbol{F}}^{f7}_{OS^*} \tag{4.29}$$
$$\mathbb{C}^{F8} = \vec{\boldsymbol{F}}^{N8}_{OS^*} + \vec{\boldsymbol{F}}^{f8}_{OS^*} \tag{4.30}$$

$$\mathbb{C}^{M1} = \vec{\boldsymbol{M}}^{N1}_{PS^*} + \vec{\boldsymbol{M}}^{f1}_{PS^*} \tag{4.31}$$
$$\mathbb{C}^{M2} = \vec{\boldsymbol{M}}^{N2}_{PS^*} + \vec{\boldsymbol{M}}^{f2}_{PS^*} \tag{4.32}$$
$$\mathbb{C}^{M3} = \vec{\boldsymbol{M}}^{N3}_{PS^*} + \vec{\boldsymbol{M}}^{f3}_{PS^*} \tag{4.33}$$
$$\mathbb{C}^{M4} = \vec{\boldsymbol{M}}^{N4}_{PS^*} + \vec{\boldsymbol{M}}^{f4}_{PS^*} \tag{4.34}$$
$$\mathbb{C}^{M5} = \vec{\boldsymbol{M}}^{N5}_{PS^*} + \vec{\boldsymbol{M}}^{f5}_{PS^*} \tag{4.35}$$
$$\mathbb{C}^{M6} = \vec{\boldsymbol{M}}^{N6}_{PS^*} + \vec{\boldsymbol{M}}^{f6}_{PS^*} \tag{4.36}$$
$$\mathbb{C}^{M7} = \vec{\boldsymbol{M}}^{N7}_{OS^*} + \vec{\boldsymbol{M}}^{f7}_{OS^*} \tag{4.37}$$
$$\mathbb{C}^{M8} = \vec{\boldsymbol{M}}^{N8}_{OS^*} + \vec{\boldsymbol{M}}^{f8}_{OS^*} \tag{4.38}$$

$$\underset{(1x8)}{\mathbb{C}^{k_{P1}}} = \begin{bmatrix} \left(\vec{\boldsymbol{F}}^{N1}_{PS^*}\right)^W & \left(\vec{\boldsymbol{F}}^{N2}_{PS^*}\right)^W & 0 & 0 & 0 & 0 & 0 & 0 \end{bmatrix} \tag{4.39}$$

$$\underset{(1x8)}{\mathbb{C}^{k_{O}}} = \begin{bmatrix} 0 & 0 & 0 & 0 & 0 & 0 & \left(\vec{\boldsymbol{F}}^{N7}_{OS^*}\right)^W & \left(\vec{\boldsymbol{F}}^{N8}_{OS^*}\right)^W \end{bmatrix} \tag{4.40}$$

$$\boxed{\underset{(8x1)}{\mathbb{F}^{N}} = \begin{bmatrix} \boldsymbol{\mathcal{F}}^{N1} \\ \boldsymbol{\mathcal{F}}^{N2} \\ \boldsymbol{\mathcal{F}}^{N3} \\ \boldsymbol{\mathcal{F}}^{N4} \\ \boldsymbol{\mathcal{F}}^{N5} \\ \boldsymbol{\mathcal{F}}^{N6} \\ \boldsymbol{\mathcal{F}}^{N7} \\ \boldsymbol{\mathcal{F}}^{N8} \end{bmatrix}} \tag{4.41}$$

$$\boxed{\underset{(3x1)}{\mathbb{A}^{(ma)}} = \begin{bmatrix} (m_S)\left(a^{U}_{S*}\right) \\ (m_S)\left(a^{V}_{S*}\right) \\ (m_S)\left(a^{W}_{S*}\right) \end{bmatrix}} \tag{4.42}$$

$$\boxed{\underset{(3x1)}{\mathbb{A}^{(I\alpha)}} = \begin{bmatrix} \left(I^{UU}_S\right)\left(\alpha^{U}_{S*}\right) \\ \left(I^{VV}_S\right)\left(\alpha^{V}_{S*}\right) \\ \left(I^{WW}_S\right)\left(\alpha^{W}_{S*}\right) \end{bmatrix}} \tag{4.43}$$

Note that, because the Satellite Orbit block rotates separately about W, it is excluded from the calculation for I^{WW}_S.

$$\boxed{\underset{(1x1)}{\mathbb{A}^{k_{P1}}} = -\left(\boldsymbol{\mathcal{F}}^{k_{P1}} + \frac{\left(m^{P1}_S\right)\left(\|\vec{\boldsymbol{v}}^{*}_{P1}\|^2\right)}{\rho^{P1}_S}\right)} \tag{4.44}$$

$$\boxed{\underset{(1x1)}{\mathbb{A}^{k_O}} = -\left(\boldsymbol{\mathcal{F}}^{kO} + \frac{\left(m^{O}_S\right)\left(\|\vec{\boldsymbol{v}}^{*}_{O}\|^2\right)}{\rho^{O}_S}\right)} \tag{4.45}$$

4.5 Forces: Solutions to the Equilibrium Equations

4.5.1 Valid and Invalid Solutions

The matrix division in Equation (4.19) solves for the eight force coefficients ($\boldsymbol{\mathcal{F}}^{N1} \dots \boldsymbol{\mathcal{F}}^{N8}$). As mentioned previously, a valid solution requires all eight entries of $\mathbb{F}^N$ to be positive, meaning all surfaces maintain some contact pressure at all times. One or more negative entries in $\mathbb{F}^N$ indicates either (a) loss of contact or (b) system lockup (wherein the mathematical solution corresponds to "negative friction"). This criterion makes it easy to identify whether the solution found is valid – one must simply verify that all entries of $\mathbb{F}^N$ are positive. Assuming they are, the values can then be plugged into the Satellite force vectors

(Table 4.3) to obtain numerical expressions for each.

4.5.2 Reaction Loads on Planet & Orbit in UVW Coordinates

Discussion so far has focused on the forces acting on a Satellite by the Planet/Orbit. In terms of characterizing overall coupling performance, the reaction loads – *i.e.* the loads "seen" by Planet and Orbit – are now important to find. Luckily this process is trivial as each load acting on the Planet/Orbit is exactly equal and opposite to the associated load acting on the Satellite:

$$\boxed{\begin{aligned}
\vec{\boldsymbol{F}}^{N1}_{S^*P} &= -\vec{\boldsymbol{F}}^{N1}_{PS^*} \quad (4.46)\\
\vec{\boldsymbol{F}}^{N2}_{S^*P} &= -\vec{\boldsymbol{F}}^{N2}_{PS^*} \quad (4.47)\\
\vec{\boldsymbol{F}}^{N3}_{S^*P} &= -\vec{\boldsymbol{F}}^{N3}_{PS^*} \quad (4.48)\\
\vec{\boldsymbol{F}}^{N4}_{S^*P} &= -\vec{\boldsymbol{F}}^{N4}_{PS^*} \quad (4.49)\\
\vec{\boldsymbol{F}}^{N5}_{S^*P} &= -\vec{\boldsymbol{F}}^{N5}_{PS^*} \quad (4.50)\\
\vec{\boldsymbol{F}}^{N6}_{S^*P} &= -\vec{\boldsymbol{F}}^{N6}_{PS^*} \quad (4.51)\\
\vec{\boldsymbol{F}}^{N7}_{S^*O} &= -\vec{\boldsymbol{F}}^{N7}_{OS^*} \quad (4.52)\\
\vec{\boldsymbol{F}}^{N8}_{S^*O} &= -\vec{\boldsymbol{F}}^{N8}_{OS^*} \quad (4.53)
\end{aligned}}$$

$$\boxed{\begin{aligned}
\vec{\boldsymbol{F}}^{f1}_{S^*P} &= -\vec{\boldsymbol{F}}^{f1}_{PS^*} \quad (4.54)\\
\vec{\boldsymbol{F}}^{f2}_{S^*P} &= -\vec{\boldsymbol{F}}^{f2}_{PS^*} \quad (4.55)\\
\vec{\boldsymbol{F}}^{f3}_{S^*P} &= -\vec{\boldsymbol{F}}^{f3}_{PS^*} \quad (4.56)\\
\vec{\boldsymbol{F}}^{f4}_{S^*P} &= -\vec{\boldsymbol{F}}^{f4}_{PS^*} \quad (4.57)\\
\vec{\boldsymbol{F}}^{f5}_{S^*P} &= -\vec{\boldsymbol{F}}^{f5}_{PS^*} \quad (4.58)\\
\vec{\boldsymbol{F}}^{f6}_{S^*P} &= -\vec{\boldsymbol{F}}^{f6}_{PS^*} \quad (4.59)\\
\vec{\boldsymbol{F}}^{f7}_{S^*O} &= -\vec{\boldsymbol{F}}^{f7}_{OS^*} \quad (4.60)\\
\vec{\boldsymbol{F}}^{f8}_{S^*O} &= -\vec{\boldsymbol{F}}^{f8}_{OS^*} \quad (4.61)
\end{aligned}}$$

Note that the coordinate locations of the original and reaction loads are identical.

4.5.3 Reaction Loads on Planet & Orbit in Global Coordinates

Next, the Planet/Orbit loads must be transformed from local UVW coordinates to global XYZ coordinates, allowing the net torque and bearing loads on the device as a whole to be found. The (1) location (coordinate) and (2) orientation (direction) of each force must be separately transformed.

The coordinate location of each force is transformed to XYZ-space following Equation (3.73), which uses the rotation matrix ${}^{\boldsymbol{S}}\boldsymbol{H}_{\boldsymbol{S^*}}$ (Equation (3.74)) and translation matrix ${}^{\boldsymbol{S}}\boldsymbol{H}^{\boldsymbol{XYZ}}_{\boldsymbol{S^*}}$ (Equation (3.75)):

$$\boxed{\begin{bmatrix} \vec{\boldsymbol{r}}^{\{i\}}_{S} \\ \\ 1 \end{bmatrix} = \left({}^{\boldsymbol{S}}\boldsymbol{H}^{\boldsymbol{XYZ}}_{\boldsymbol{S^*}}\right)\left({}^{\boldsymbol{S}}\boldsymbol{H}_{\boldsymbol{S^*}}\right)\begin{bmatrix} \vec{\boldsymbol{r}}^{\{i\}}_{S^*} \\ \\ 1 \end{bmatrix}} \tag{4.62}$$

The orientation of each force is transformed to XYZ-space using Equation (3.72), which requires only the rotation matrix ${}^{\boldsymbol{S}}\boldsymbol{H}_{\boldsymbol{S^*}}$ (Equation (3.74)):

$$\boxed{\begin{bmatrix} \vec{\boldsymbol{F}}_{S}^{\{i\}} \\ \\ 1 \end{bmatrix} = \left({}^{\boldsymbol{S}}\boldsymbol{H}_{\boldsymbol{S^*}}\right) \begin{bmatrix} \vec{\boldsymbol{F}}_{S^*}^{\{i\}} \\ \\ 1 \end{bmatrix}} \tag{4.63}$$

Expressions for the Planet/Orbit normal and friction forces are listed in Table 4.5.

The effective moments of the normal and friction forces acting on the Planet/Satellite can then be calculated in a similar fashion to the process used for the Satellites. They are listed in Table 4.6.[1]

4.5.4 Planet/Orbit Net Torque & Bearing Loads

The forces and moments acting on the Planet/Orbit can be summed to determine the net force and moment acting on each:

$$\vec{\boldsymbol{F}}_{SP} = \left(\sum_{i=1}^{6} \vec{\boldsymbol{F}}_{SP}^{N\{i\}}\right) + \left(\sum_{i=1}^{6} \vec{\boldsymbol{F}}_{SP}^{f\{i\}}\right) \tag{4.64}$$

$$\overrightarrow{\boldsymbol{M}}_{SP} = \left(\sum_{i=1}^{6} \overrightarrow{\boldsymbol{M}}_{SP}^{N\{i\}}\right) + \left(\sum_{i=1}^{6} \overrightarrow{\boldsymbol{M}}_{SP}^{f\{i\}}\right) \tag{4.65}$$

$$\vec{\boldsymbol{F}}_{SO} = \left(\sum_{i=7}^{8} \vec{\boldsymbol{F}}_{SO}^{N\{i\}}\right) + \left(\sum_{i=7}^{8} \vec{\boldsymbol{F}}_{SO}^{f\{i\}}\right) \tag{4.66}$$

$$\overrightarrow{\boldsymbol{M}}_{SO} = \left(\sum_{i=7}^{8} \overrightarrow{\boldsymbol{M}}_{SO}^{N\{i\}}\right) + \left(\sum_{i=7}^{8} \overrightarrow{\boldsymbol{M}}_{SO}^{f\{i\}}\right) \tag{4.67}$$

Expressed in vector form, the torque on the Planet/Orbit in the coupling's direction of rotation is:

$$\vec{\boldsymbol{T}}_{S1P} = \left(\overrightarrow{\boldsymbol{M}}_{SP} \odot \hat{\mathbf{X}}\right) \tag{4.68}$$

$$\vec{\boldsymbol{T}}_{S1O} = \left(\overrightarrow{\boldsymbol{M}}_{SO} \odot \hat{\mathbf{X}}\right) \tag{4.69}$$

Here, the notation $(A \odot B)$ represents the element-wise product of A and B.

The other components of $\vec{\boldsymbol{F}}_{SP}, \overrightarrow{\boldsymbol{M}}_{SP}, \vec{\boldsymbol{F}}_{SO}$, and $\overrightarrow{\boldsymbol{M}}_{SO}$ represent the Planet/Orbit bearing loads. **As a reminder, Chapter 4's calculations up to this point reflect the instantaneous results at a**

[1] To reduce the likelihood of mistakes, is recommended that moments not be transformed between coordinate frames. Instead, forces should be transformed and moments calculated in the new frame using the appropriate vector $\vec{\boldsymbol{r}}$.

Table 4.5 – Planet & Orbit Reaction Forces in XYZ

Contact Point:	IHC Component Acted On:	Contact Location in XYZ:	Normal Force in XYZ:	Friction Force in XYZ:
1	**Planet**	$\begin{bmatrix}\vec{\boldsymbol{r}}_{S}^{\{1\}}\\1\end{bmatrix}=\left({}^{S}\boldsymbol{H}_{S^*}^{XYZ}\right)\left({}^{S}\boldsymbol{H}_{S^*}\right)\begin{bmatrix}\vec{\boldsymbol{r}}_{S^*}^{\{1\}}\\1\end{bmatrix}$	$\begin{bmatrix}\vec{\boldsymbol{F}}_{SP}^{N1}\\1\end{bmatrix}=\left({}^{S}\boldsymbol{H}_{S^*}\right)\begin{bmatrix}\vec{\boldsymbol{F}}_{S^*P}^{N1}\\1\end{bmatrix}$	$\begin{bmatrix}\vec{\boldsymbol{F}}_{SP}^{f1}\\1\end{bmatrix}=\left({}^{S}\boldsymbol{H}_{S^*}\right)\begin{bmatrix}\vec{\boldsymbol{F}}_{S^*P}^{f1}\\1\end{bmatrix}$
2	**Planet**	$\begin{bmatrix}\vec{\boldsymbol{r}}_{S}^{\{2\}}\\1\end{bmatrix}=\left({}^{S}\boldsymbol{H}_{S^*}^{XYZ}\right)\left({}^{S}\boldsymbol{H}_{S^*}\right)\begin{bmatrix}\vec{\boldsymbol{r}}_{S^*}^{\{2\}}\\1\end{bmatrix}$	$\begin{bmatrix}\vec{\boldsymbol{F}}_{SP}^{N2}\\1\end{bmatrix}=\left({}^{S}\boldsymbol{H}_{S^*}\right)\begin{bmatrix}\vec{\boldsymbol{F}}_{S^*P}^{N2}\\1\end{bmatrix}$	$\begin{bmatrix}\vec{\boldsymbol{F}}_{SP}^{f2}\\1\end{bmatrix}=\left({}^{S}\boldsymbol{H}_{S^*}\right)\begin{bmatrix}\vec{\boldsymbol{F}}_{S^*P}^{f2}\\1\end{bmatrix}$
3	**Planet**	$\begin{bmatrix}\vec{\boldsymbol{r}}_{S}^{\{3\}}\\1\end{bmatrix}=\left({}^{S}\boldsymbol{H}_{S^*}^{XYZ}\right)\left({}^{S}\boldsymbol{H}_{S^*}\right)\begin{bmatrix}\vec{\boldsymbol{r}}_{S^*}^{\{3\}}\\1\end{bmatrix}$	$\begin{bmatrix}\vec{\boldsymbol{F}}_{SP}^{N3}\\1\end{bmatrix}=\left({}^{S}\boldsymbol{H}_{S^*}\right)\begin{bmatrix}\vec{\boldsymbol{F}}_{S^*P}^{N3}\\1\end{bmatrix}$	$\begin{bmatrix}\vec{\boldsymbol{F}}_{SP}^{f3}\\1\end{bmatrix}=\left({}^{S}\boldsymbol{H}_{S^*}\right)\begin{bmatrix}\vec{\boldsymbol{F}}_{S^*P}^{f3}\\1\end{bmatrix}$
4	**Planet**	$\begin{bmatrix}\vec{\boldsymbol{r}}_{S}^{\{4\}}\\1\end{bmatrix}=\left({}^{S}\boldsymbol{H}_{S^*}^{XYZ}\right)\left({}^{S}\boldsymbol{H}_{S^*}\right)\begin{bmatrix}\vec{\boldsymbol{r}}_{S^*}^{\{4\}}\\1\end{bmatrix}$	$\begin{bmatrix}\vec{\boldsymbol{F}}_{SP}^{N4}\\1\end{bmatrix}=\left({}^{S}\boldsymbol{H}_{S^*}\right)\begin{bmatrix}\vec{\boldsymbol{F}}_{S^*P}^{N4}\\1\end{bmatrix}$	$\begin{bmatrix}\vec{\boldsymbol{F}}_{SP}^{f4}\\1\end{bmatrix}=\left({}^{S}\boldsymbol{H}_{S^*}\right)\begin{bmatrix}\vec{\boldsymbol{F}}_{S^*P}^{f4}\\1\end{bmatrix}$
5	**Planet**	$\begin{bmatrix}\vec{\boldsymbol{r}}_{S}^{\{5\}}\\1\end{bmatrix}=\left({}^{S}\boldsymbol{H}_{S^*}^{XYZ}\right)\left({}^{S}\boldsymbol{H}_{S^*}\right)\begin{bmatrix}\vec{\boldsymbol{r}}_{S^*}^{\{5\}}\\1\end{bmatrix}$	$\begin{bmatrix}\vec{\boldsymbol{F}}_{SP}^{N5}\\1\end{bmatrix}=\left({}^{S}\boldsymbol{H}_{S^*}\right)\begin{bmatrix}\vec{\boldsymbol{F}}_{S^*P}^{N5}\\1\end{bmatrix}$	$\begin{bmatrix}\vec{\boldsymbol{F}}_{SP}^{f5}\\1\end{bmatrix}=\left({}^{S}\boldsymbol{H}_{S^*}\right)\begin{bmatrix}\vec{\boldsymbol{F}}_{S^*P}^{f5}\\1\end{bmatrix}$
6	**Planet**	$\begin{bmatrix}\vec{\boldsymbol{r}}_{S}^{\{6\}}\\1\end{bmatrix}=\left({}^{S}\boldsymbol{H}_{S^*}^{XYZ}\right)\left({}^{S}\boldsymbol{H}_{S^*}\right)\begin{bmatrix}\vec{\boldsymbol{r}}_{S^*}^{\{6\}}\\1\end{bmatrix}$	$\begin{bmatrix}\vec{\boldsymbol{F}}_{SP}^{N6}\\1\end{bmatrix}=\left({}^{S}\boldsymbol{H}_{S^*}\right)\begin{bmatrix}\vec{\boldsymbol{F}}_{S^*P}^{N6}\\1\end{bmatrix}$	$\begin{bmatrix}\vec{\boldsymbol{F}}_{SP}^{f6}\\1\end{bmatrix}=\left({}^{S}\boldsymbol{H}_{S^*}\right)\begin{bmatrix}\vec{\boldsymbol{F}}_{S^*P}^{f6}\\1\end{bmatrix}$
7	**Orbit**	$\begin{bmatrix}\vec{\boldsymbol{r}}_{S}^{\{7\}}\\1\end{bmatrix}=\left({}^{S}\boldsymbol{H}_{S^*}^{XYZ}\right)\left({}^{S}\boldsymbol{H}_{S^*}\right)\begin{bmatrix}\vec{\boldsymbol{r}}_{S^*}^{\{7\}}\\1\end{bmatrix}$	$\begin{bmatrix}\vec{\boldsymbol{F}}_{SO}^{N7}\\1\end{bmatrix}=\left({}^{S}\boldsymbol{H}_{S^*}\right)\begin{bmatrix}\vec{\boldsymbol{F}}_{S^*O}^{N7}\\1\end{bmatrix}$	$\begin{bmatrix}\vec{\boldsymbol{F}}_{SO}^{f7}\\1\end{bmatrix}=\left({}^{S}\boldsymbol{H}_{S^*}\right)\begin{bmatrix}\vec{\boldsymbol{F}}_{S^*O}^{f7}\\1\end{bmatrix}$
8	**Orbit**	$\begin{bmatrix}\vec{\boldsymbol{r}}_{S}^{\{8\}}\\1\end{bmatrix}=\left({}^{S}\boldsymbol{H}_{S^*}^{XYZ}\right)\left({}^{S}\boldsymbol{H}_{S^*}\right)\begin{bmatrix}\vec{\boldsymbol{r}}_{S^*}^{\{8\}}\\1\end{bmatrix}$	$\begin{bmatrix}\vec{\boldsymbol{F}}_{SO}^{N8}\\1\end{bmatrix}=\left({}^{S}\boldsymbol{H}_{S^*}\right)\begin{bmatrix}\vec{\boldsymbol{F}}_{S^*O}^{N8}\\1\end{bmatrix}$	$\begin{bmatrix}\vec{\boldsymbol{F}}_{SO}^{f8}\\1\end{bmatrix}=\left({}^{S}\boldsymbol{H}_{S^*}\right)\begin{bmatrix}\vec{\boldsymbol{F}}_{S^*O}^{f8}\\1\end{bmatrix}$

Table 4.6 – Planet & Orbit Reaction Moments in XYZ

Contact Point:	IHC Component Acted On:	Contact Location in XYZ:	Normal Moment in XYZ:	Friction Moment in XYZ:
1	**Planet**	$\vec{\boldsymbol{r}}_S^{\{1\}}$	$\vec{\boldsymbol{M}}_{SP}^{N1} = \vec{\boldsymbol{r}}_S^{\{1\}} \times \vec{\boldsymbol{F}}_{SP}^{N1}$	$\vec{\boldsymbol{M}}_{SP}^{f1} = \vec{\boldsymbol{r}}_S^{\{1\}} \times \vec{\boldsymbol{F}}_{SP}^{f1}$
2	**Planet**	$\vec{\boldsymbol{r}}_S^{\{2\}}$	$\vec{\boldsymbol{M}}_{SP}^{N2} = \vec{\boldsymbol{r}}_S^{\{2\}} \times \vec{\boldsymbol{F}}_{SP}^{N2}$	$\vec{\boldsymbol{M}}_{SP}^{f2} = \vec{\boldsymbol{r}}_S^{\{2\}} \times \vec{\boldsymbol{F}}_{SP}^{f2}$
3	**Planet**	$\vec{\boldsymbol{r}}_S^{\{3\}}$	$\vec{\boldsymbol{M}}_{SP}^{N3} = \vec{\boldsymbol{r}}_S^{\{3\}} \times \vec{\boldsymbol{F}}_{SP}^{N3}$	$\vec{\boldsymbol{M}}_{SP}^{f3} = \vec{\boldsymbol{r}}_S^{\{3\}} \times \vec{\boldsymbol{F}}_{SP}^{f3}$
4	**Planet**	$\vec{\boldsymbol{r}}_S^{\{4\}}$	$\vec{\boldsymbol{M}}_{SP}^{N4} = \vec{\boldsymbol{r}}_S^{\{4\}} \times \vec{\boldsymbol{F}}_{SP}^{N4}$	$\vec{\boldsymbol{M}}_{SP}^{f4} = \vec{\boldsymbol{r}}_S^{\{4\}} \times \vec{\boldsymbol{F}}_{SP}^{f4}$
5	**Planet**	$\vec{\boldsymbol{r}}_S^{\{5\}}$	$\vec{\boldsymbol{M}}_{SP}^{N5} = \vec{\boldsymbol{r}}_S^{\{5\}} \times \vec{\boldsymbol{F}}_{SP}^{N5}$	$\vec{\boldsymbol{M}}_{SP}^{f5} = \vec{\boldsymbol{r}}_S^{\{5\}} \times \vec{\boldsymbol{F}}_{SP}^{f5}$
6	**Planet**	$\vec{\boldsymbol{r}}_S^{\{6\}}$	$\vec{\boldsymbol{M}}_{SP}^{N6} = \vec{\boldsymbol{r}}_S^{\{6\}} \times \vec{\boldsymbol{F}}_{SP}^{N6}$	$\vec{\boldsymbol{M}}_{SP}^{f6} = \vec{\boldsymbol{r}}_S^{\{6\}} \times \vec{\boldsymbol{F}}_{SP}^{f6}$
7	**Orbit**	$\vec{\boldsymbol{r}}_S^{\{7\}}$	$\vec{\boldsymbol{M}}_{SO}^{N7} = \vec{\boldsymbol{r}}_S^{\{7\}} \times \vec{\boldsymbol{F}}_{SO}^{N7}$	$\vec{\boldsymbol{M}}_{SO}^{f7} = \vec{\boldsymbol{r}}_S^{\{7\}} \times \vec{\boldsymbol{F}}_{SO}^{f7}$
8	**Orbit**	$\vec{\boldsymbol{r}}_S^{\{8\}}$	$\vec{\boldsymbol{M}}_{SO}^{N8} = \vec{\boldsymbol{r}}_S^{\{8\}} \times \vec{\boldsymbol{F}}_{SO}^{N8}$	$\vec{\boldsymbol{M}}_{SO}^{f8} = \vec{\boldsymbol{r}}_S^{\{8\}} \times \vec{\boldsymbol{F}}_{SO}^{f8}$

single moment in time. This process must be repeated across each timestep in the model for complete results.

4.6 Visualizing the Location and Direction of Contact Forces

A useful tip for verifying the correctness of the force derivations is to plot or animate their locations. With so many transforms between various coordinate systems, visual checks prove extremely helpful. In the event of a software bug, plotting and animation tools make it much easier to identify the root cause. Figure 4-9 is a screenshot of such a tool developed to animate the directions and locations of all contact forces in both XYZ and UVW space.

4.7 Extending the Results to Multiple Satellites

4.7.1 Inter-Satellite Time Delay

Thus far, all kinematics and force calculations have only considered a single Satellite, yet the IHC prototype uses six. Luckily, it is not necessary to repeat all of this effort for each Satellite in the system. A "shortcut" of sorts – enabled by having modeled the system at steady-state operation – can be exploited. In short, the results from the first Satellite will be copied to the others with a time-shift applied. Recall that:

- All Satellites are identical
- All Planet slots are identical and evenly-spaced
- At steady-state operation, the slip rate (ω_{OP}) is constant

As a result of these assumptions, all Satellites maintain constant and uniform spacing in the time-domain. That is, the period between subsequent Satellites crossing the same location on the Orbit ring is always the same. For $n_S = 6$ satellites, this time is exactly 1/6 the period of a "slip-rotation." The time-shift between neighboring satellites is:

$$\boxed{\Delta t_S = \frac{2\pi}{(n_S)(\omega_{OP})}} \tag{4.70}$$

Therefore, the results for Satellites 2-6 do not need to be calculated directly. Instead, the data from Satellite 1 can simply be copied over and the time vector shifted by Δt_S, $2\Delta t_S$, $3\Delta t_S$, $4\Delta t_S$, or $5\Delta t_S$.

The aggregate results for the entire IHC can then be found by summing the time-aligned Satellite data together, where the subscript $\mathbb{S}$ is used to denote the combined effect of all Satellites. **Care should be taken when summing the results from multiple Satellites, especially for any expressions**

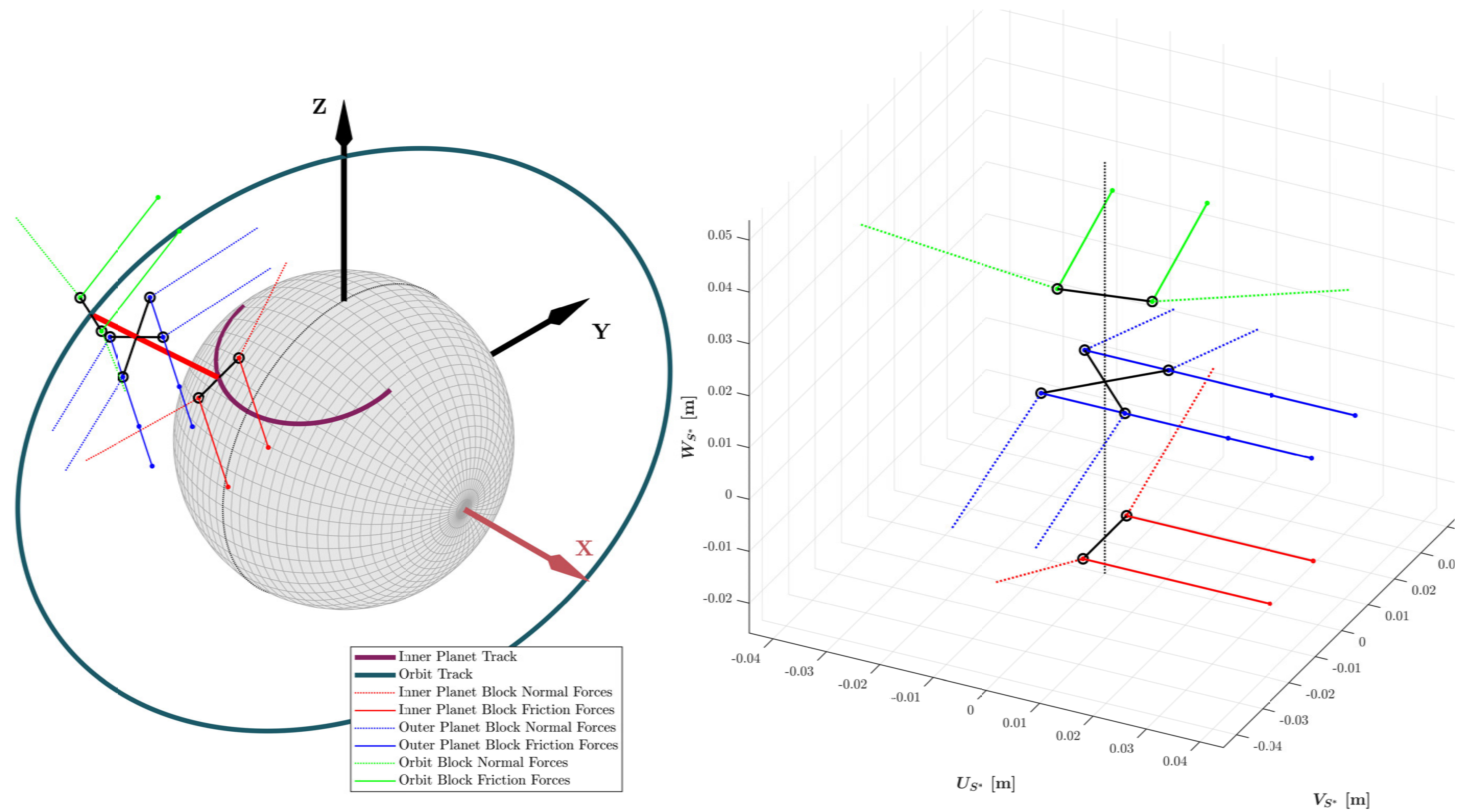

Figure 4-9 – Screenshot of the ihcMATLAB Satellite Contact Force Animator. This tool shows the location and direction of all Satellite forces and proves very useful for confirming the coded transformations and geometry are working correctly.

involving absolute values. Vector forms should always be used, allowing Satellites that act in opposite directions to properly negate one another. The total Planet and Orbit torques transmitted by multiple satellites at once are:

$$\boxed{\begin{aligned} \vec{\boldsymbol{T}}_{\mathbb{S}P} &= \vec{\boldsymbol{T}}_{S1P} + \vec{\boldsymbol{T}}_{S2P} + \vec{\boldsymbol{T}}_{S3P} + \vec{\boldsymbol{T}}_{S4P} + \vec{\boldsymbol{T}}_{S5P} + \vec{\boldsymbol{T}}_{S6P} && (4.71) \\ \vec{\boldsymbol{T}}_{\mathbb{S}O} &= \vec{\boldsymbol{T}}_{S1O} + \vec{\boldsymbol{T}}_{S2O} + \vec{\boldsymbol{T}}_{S3O} + \vec{\boldsymbol{T}}_{S4O} + \vec{\boldsymbol{T}}_{S5O} + \vec{\boldsymbol{T}}_{S6O} && (4.72) \end{aligned}}$$

The time-average vectors $\overline{\vec{\boldsymbol{T}}}_{\mathbb{S}P}$ and $\overline{\vec{\boldsymbol{T}}}_{\mathbb{S}O}$ are equal and opposite, with their magnitudes being the amount of torque transmitted across the coupling:

$$\boxed{\overline{\mathcal{T}}_{\boldsymbol{IHC}} = \left\| \overline{\vec{\boldsymbol{T}}}_{\mathbb{S}P} \right\| = \left\| \overline{\vec{\boldsymbol{T}}}_{\mathbb{S}O} \right\|} \tag{4.73}$$

The total vectorized forces and moments acting on the Planet/Orbit are:

$$\boxed{\begin{aligned} \vec{\boldsymbol{F}}_{\mathbb{S}P} &= \vec{\boldsymbol{F}}_{S1P} + \vec{\boldsymbol{F}}_{S2P} + \vec{\boldsymbol{F}}_{S3P} + \vec{\boldsymbol{F}}_{S4P} + \vec{\boldsymbol{F}}_{S5P} + \vec{\boldsymbol{F}}_{S6P} && (4.74) \\ \vec{\boldsymbol{F}}_{\mathbb{S}O} &= \vec{\boldsymbol{F}}_{S1O} + \vec{\boldsymbol{F}}_{S2O} + \vec{\boldsymbol{F}}_{S3O} + \vec{\boldsymbol{F}}_{S4O} + \vec{\boldsymbol{F}}_{S5O} + \vec{\boldsymbol{F}}_{S6O} && (4.75) \\ \vec{\boldsymbol{M}}_{\mathbb{S}P} &= \vec{\boldsymbol{M}}_{S1P} + \vec{\boldsymbol{M}}_{S2P} + \vec{\boldsymbol{M}}_{S3P} + \vec{\boldsymbol{M}}_{S4P} + \vec{\boldsymbol{M}}_{S5P} + \vec{\boldsymbol{M}}_{S6P} && (4.76) \\ \vec{\boldsymbol{M}}_{\mathbb{S}O} &= \vec{\boldsymbol{M}}_{S1O} + \vec{\boldsymbol{M}}_{S2O} + \vec{\boldsymbol{M}}_{S3O} + \vec{\boldsymbol{M}}_{S4O} + \vec{\boldsymbol{M}}_{S5O} + \vec{\boldsymbol{M}}_{S6O} && (4.77) \end{aligned}}$$

4.8 Power Calculations

The power transmitted from the Planet/Orbit to their attached equipment is:

$$\boxed{\begin{aligned} \boldsymbol{\mathcal{P}}_{\mathbb{S}P} &= \vec{\boldsymbol{T}}_{\mathbb{S}P} \cdot \vec{\boldsymbol{\omega}}_P && (4.78) \\ \boldsymbol{\mathcal{P}}_{\mathbb{S}O} &= \vec{\boldsymbol{T}}_{\mathbb{S}O} \cdot \vec{\boldsymbol{\omega}}_O && (4.79) \end{aligned}}$$

The subscripts ($\mathbb{S}P,\ \mathbb{S}O$) convey that the direction of power transmission is from Satellite to Planet/Orbit. Thus, a positive value for $\boldsymbol{\mathcal{P}}_{\mathbb{S}P}$ or $\boldsymbol{\mathcal{P}}_{\mathbb{S}O}$ corresponds to power output from the Planet or Orbit to the connected loads. Negative values correspond to power input.

Although $\overline{\vec{\boldsymbol{T}}}_{\mathbb{S}P}$ and $\overline{\vec{\boldsymbol{T}}}_{\mathbb{S}O}$ are equal and opposite, the direction of power flow still depends on the signs of $\vec{\boldsymbol{\omega}}_P$ and $\vec{\boldsymbol{\omega}}_O$. If the calculations thus far are performed correctly, the sum of the time-averaged power outputs $\left(\overline{\boldsymbol{\mathcal{P}}}_{\mathbb{S}P} + \overline{\boldsymbol{\mathcal{P}}}_{\mathbb{S}O}\right)$ will be either zero or negative to obey conservation of energy.[1] Negative values correspond to power dissipation in the coupling, the average value of which is:

$$\boxed{\overline{\boldsymbol{\mathcal{P}}}^{\boldsymbol{\{diss\}}}_{\boldsymbol{IHC}} = \overline{\boldsymbol{\mathcal{T}}}_{\boldsymbol{IHC}} \| \vec{\boldsymbol{\omega}}_P - \vec{\boldsymbol{\omega}}_O \|} \tag{4.80}$$

Power dissipation can also be considered using the friction contact forces and local sliding velocities. In Equation (3.81) the local Planet/Satellite velocity $\vec{\boldsymbol{v}}_{PS^*}$ was defined for a theoretical Satellite, but this did not consider that the "real" IHC has two Planet blocks (thus requiring two sliding speeds). The speeds of the actual blocks are:

$$\vec{\boldsymbol{v}}_{P_2S^*} = \vec{\boldsymbol{v}}_{PS^*} \qquad \textit{Outer Planet Sliding Velocity (Contact Points \#3-6)} \tag{4.81}$$

$$\vec{\boldsymbol{v}}_{P_1S^*} = \left(\frac{\rho_{P_1}}{\rho_{P_2}}\right) \vec{\boldsymbol{v}}_{P_2S^*} \qquad \textit{Inner Planet Sliding Velocity (Contact Points \#1-2)} \tag{4.82}$$

The instantaneous power dissipation rates at the eight contact points are therefore:

$$\boldsymbol{\mathcal{P}}^{\{1,diss\}}_{PS} = \left\|\vec{\boldsymbol{F}}^{f1}_{PS^*}\right\| \left\|\vec{\boldsymbol{v}}_{P_1S^*}\right\| \tag{4.83}$$

$$\boldsymbol{\mathcal{P}}^{\{2,diss\}}_{PS} = \left\|\vec{\boldsymbol{F}}^{f2}_{PS^*}\right\| \left\|\vec{\boldsymbol{v}}_{P_1S^*}\right\| \tag{4.84}$$

$$\boldsymbol{\mathcal{P}}^{\{3,diss\}}_{PS} = \left\|\vec{\boldsymbol{F}}^{f3}_{PS^*}\right\| \left\|\vec{\boldsymbol{v}}_{P_2S^*}\right\| \tag{4.85}$$

$$\boldsymbol{\mathcal{P}}^{\{4,diss\}}_{PS} = \left\|\vec{\boldsymbol{F}}^{f4}_{PS^*}\right\| \left\|\vec{\boldsymbol{v}}_{P_2S^*}\right\| \tag{4.86}$$

$$\boldsymbol{\mathcal{P}}^{\{5,diss\}}_{PS} = \left\|\vec{\boldsymbol{F}}^{f5}_{PS^*}\right\| \left\|\vec{\boldsymbol{v}}_{P_2S^*}\right\| \tag{4.87}$$

$$\boldsymbol{\mathcal{P}}^{\{6,diss\}}_{PS} = \left\|\vec{\boldsymbol{F}}^{f6}_{PS^*}\right\| \left\|\vec{\boldsymbol{v}}_{P_2S^*}\right\| \tag{4.88}$$

$$\boldsymbol{\mathcal{P}}^{\{7,diss\}}_{OS} = \left\|\vec{\boldsymbol{F}}^{f7}_{OS^*}\right\| \left\|\vec{\boldsymbol{v}}_{OS^*}\right\| \tag{4.89}$$

$$\boldsymbol{\mathcal{P}}^{\{8,diss\}}_{OS} = \left\|\vec{\boldsymbol{F}}^{f8}_{OS^*}\right\| \left\|\vec{\boldsymbol{v}}_{OS^*}\right\| \tag{4.90}$$

4.9 Thermal Flux & Heat Accumulation

Although there are eight Contact Points modeled, each Satellite only has six contact surfaces (the top Planet blocks have two Contact Points each). Correspondingly, each Satellite interfaces with four Planet surfaces and two Orbit surfaces. Assuming the power dissipated in Equations (4.83) to (4.90) flows directly into the contacting surfaces, the heat flux can be estimated. At any one interface, half the dissipation power is allocated to each of the contacting surfaces.

For this model, contact areas are estimated by treating Satellite surfaces as flat:[2]

[1] On an instantaneous basis things are more complicated due to the continual cycle of Satellite kinetic energy storage/release. It would be more correct to say $\boldsymbol{\mathcal{P}}_{\mathbb{S}P} + \boldsymbol{\mathcal{P}}_{\mathbb{S}O} + \sum \dot{E}^K_S \leq 0$, where E^K_S is each Satellite's kinetic energy. On a time-averaged basis the $\dot{E}$ terms vanish.

[2] Curvature, due to non-zero β_P for example, could be incorporated in future models for greater accuracy.

$$\boxed{\begin{aligned} A_{PS}^{\{1,2\}} &= \frac{(h_{S,P1})(L_{S,P1})}{\cos(\lambda_{P1})} && (4.91)\\ A_{PS}^{\{3,4,5,6\}} &= \frac{(h_{S,P2})(L_{S,P2})}{\cos(\lambda_{P2})} && (4.92)\\ A_{OS}^{\{7,8\}} &= \frac{(h_{S,O})(L_{S,O})}{\cos(\lambda_{O})} && (4.93)\end{aligned}}$$

In these equations, the superscripts in braces indicate which contact points each surface area corresponds to. The thermal fluxes into the six Satellite surfaces are then:

$$\dot{\boldsymbol{Q}}_S^{\{1\}} = \frac{\left(\boldsymbol{\mathcal{P}}_{PS}^{\{1,diss\}}\right)}{2\left(A_{PS}^{\{1,2\}}\right)} \tag{4.94}$$

$$\dot{\boldsymbol{Q}}_S^{\{2\}} = \frac{\left(\boldsymbol{\mathcal{P}}_{PS}^{\{2,diss\}}\right)}{2\left(A_{PS}^{\{1,2\}}\right)} \tag{4.95}$$

$$\dot{\boldsymbol{Q}}_S^{\{3,4\}} = \frac{\left(\boldsymbol{\mathcal{P}}_{PS}^{\{3,diss\}}\right) + \left(\boldsymbol{\mathcal{P}}_{PS}^{\{4,diss\}}\right)}{2\left(A_{PS}^{\{3,4,5,6\}}\right)} \tag{4.96}$$

$$\dot{\boldsymbol{Q}}_S^{\{5,6\}} = \frac{\left(\boldsymbol{\mathcal{P}}_{PS}^{\{5,diss\}}\right) + \left(\boldsymbol{\mathcal{P}}_{PS}^{\{6,diss\}}\right)}{2\left(A_{PS}^{\{3,4,5,6\}}\right)} \tag{4.97}$$

$$\dot{\boldsymbol{Q}}_S^{\{7\}} = \frac{\left(\boldsymbol{\mathcal{P}}_{OS}^{\{7,diss\}}\right)}{2\left(A_{OS}^{\{7,8\}}\right)} \tag{4.98}$$

$$\dot{\boldsymbol{Q}}_S^{\{8\}} = \frac{\left(\boldsymbol{\mathcal{P}}_{OS}^{\{8,diss\}}\right)}{2\left(A_{OS}^{\{7,8\}}\right)} \tag{4.99}$$

Again, half the thermal load is assumed to go to each interface surface, so the thermal fluxes into the Planet/Orbit surfaces are the same as those for the Satellites:

$$\dot{\boldsymbol{Q}}_P^{\{1\}} = \dot{\boldsymbol{Q}}_S^{\{1\}} \tag{4.100}$$

$$\dot{\boldsymbol{Q}}_P^{\{2\}} = \dot{\boldsymbol{Q}}_S^{\{2\}} \tag{4.101}$$

$$\dot{\boldsymbol{Q}}_P^{\{3,4\}} = \dot{\boldsymbol{Q}}_S^{\{3,4\}} \tag{4.102}$$

$$\dot{\boldsymbol{Q}}_P^{\{5,6\}} = \dot{\boldsymbol{Q}}_S^{\{5,6\}} \tag{4.103}$$

$$\dot{\boldsymbol{Q}}_O^{\{7\}} = \dot{\boldsymbol{Q}}_S^{\{7\}} \tag{4.104}$$

$$\dot{\boldsymbol{Q}}_O^{\{8\}} = \dot{\boldsymbol{Q}}_S^{\{8\}} \tag{4.105}$$

4.9.1 Tracking Planet Heat Accumulation

While the entirety of each Satellite surface is always in sliding contact, only part of the Planet and Orbit surfaces are. This makes it trickier to track the average thermal flux for these surfaces over time. To solve this, arrays representing the surfaces of Planet/Orbit tracks are created, with each index corresponding to a fraction of the total surface length. This allows heat flux across the entirety of each of the Planet/Orbit surfaces to be tracked and stored during the simulation.

First, the Planet intersect position ($\vec{\boldsymbol{r}}^*_P$, from Table 3.4) is compared against the Planet position array ($\boldsymbol{S_P}$), whose two closest points $\vec{\boldsymbol{S}}_P^A$ and $\vec{\boldsymbol{S}}_P^B$ are identified (the associated indices of these two points are $\{i\}_P^A$ and $\{i\}_P^B$, respectively). The exact Planet intersection location falls somewhere in between these two and its corresponding "fractional position index" $\left(\{i\}_P^S\right)$ can be calculated using linear interpolation:[1]

$$\boxed{\{i\}_P^S = \left(\frac{\left\|\vec{\boldsymbol{r}}_P^* - \vec{\boldsymbol{S}}_P^A\right\|}{\left\|\vec{\boldsymbol{S}}_P^B - \vec{\boldsymbol{S}}_P^A\right\|}\right)\left(\{i\}_P^B - \{i\}_P^A\right) + \{i\}_P^A} \tag{4.106}$$

The "coverage ratio" for each segment can be found as the ratio of Planet track length (L_{P1} and L_{P2}) to Satellite block length ($L_{S,P1}$ and $L_{S,P2}$):

$$\mathfrak{f}^{\{1,2\}} = \frac{(L_{S,P1})}{(L_{P1})} \tag{4.107}$$

$$\mathfrak{f}^{\{3,4,5,6\}} = \frac{(L_{S,P2})}{(L_{P2})} \tag{4.108}$$

The "length" of the indices in contact is:

$$n_P^{\{1,2\}} = (n_P)\left(\mathfrak{f}^{\{1,2\}}\right) \tag{4.109}$$

$$n_P^{\{3,4,5,6\}} = (n_P)\left(\mathfrak{f}^{\{3,4,5,6\}}\right) \tag{4.110}$$

The vectors $\vec{\boldsymbol{n}}_P^{\{1,2\}*}$ and $\vec{\boldsymbol{n}}_P^{\{3,4,5,6\}*}$ are created, representing the specific Planet indices in contact with the Satellite.[2] They are size $\left(\left\lceil n_P^{\{1,2\}}\right\rceil + 1\right)$ and $\left(\left\lceil n_P^{\{3,4,5,6\}}\right\rceil + 1\right)$ respectively, where $\lceil\ \rceil$ is the ceiling (round-up) operation. Their entries are:

$$\begin{aligned}
\vec{\boldsymbol{n}}_P^{\{1,2\}*} &= \left[\left(\{i\}_P^S - \tfrac{n_P^{\{1,2\}}}{2}\right),\ \left(\{i\}_P^S - \tfrac{n_P^{\{1,2\}}}{2} + 1\right),\ \left(\{i\}_P^S - \tfrac{n_P^{\{1,2\}}}{2} + 2\right),\ \cdots\right] \\
\vec{\boldsymbol{n}}_P^{\{3,4,5,6\}*} &= \left[\left(\{i\}_P^S - \tfrac{n_P^{\{3,4,5,6\}}}{2}\right),\ \left(\{i\}_P^S - \tfrac{n_P^{\{3,4,5,6\}}}{2} + 1\right),\ \left(\{i\}_P^S - \tfrac{n_P^{\{3,4,5,6\}}}{2} + 2\right),\ \cdots\right]
\end{aligned} \tag{4.111}$$

The last entries in $\vec{\boldsymbol{n}}_P^{\{1,2\}*}$ and $\vec{\boldsymbol{n}}_P^{\{3,4,5,6\}*}$ are:

[1] The same index is used for both the inner and outer Planet surfaces.

[2] This derivation assumes the entire Satellite remains within the bounds of the Planet tracks – in other words, the Satellite's ends never cross the ends of the Planet tracks. If this is violated (because the Satellite block is long and/or travels very near the ends of the Satellite track), special accommodations must be made. One potential approach is to create separate Planet track geometry that is used only for thermal tracking.

$$\vec{\boldsymbol{n}}_P^{\{1,2\}*}(end) = \left(\{i\}_P^S - \frac{n_P^{\{1,2\}}}{2} + \left\lceil n_P^{\{1,2\}} \right\rceil \right) \tag{4.112}$$

$$\vec{\boldsymbol{n}}_P^{\{3,4,5,6\}*}(end) = \left(\{i\}_P^S - \frac{n_P^{\{3,4,5,6\}}}{2} + \left\lceil n_P^{\{3,4,5,6\}} \right\rceil \right) \tag{4.113}$$

The values of $\vec{\boldsymbol{n}}_P^{\{1,2\}*}$ and $\vec{\boldsymbol{n}}_P^{\{3,4,5,6\}*}$ are all then **rounded down** ($\lfloor\ \rfloor$) to the nearest whole number:

$$\begin{aligned} \vec{\boldsymbol{n}}_P^{\{1,2\}} &= \left[\left\lfloor \{i\}_P^S - \tfrac{n_P^{\{1,2\}}}{2} \right\rfloor, \ \left\lfloor \{i\}_P^S - \tfrac{n_P^{\{1,2\}}}{2} + 1 \right\rfloor, \ \left\lfloor \{i\}_P^S - \tfrac{n_P^{\{1,2\}}}{2} + 2 \right\rfloor, \ \cdots \right] \\ \vec{\boldsymbol{n}}_P^{\{3,4,5,6\}} &= \left[\left\lfloor \{i\}_P^S - \tfrac{n_P^{\{3,4,5,6\}}}{2} \right\rfloor, \ \left\lfloor \{i\}_P^S - \tfrac{n_P^{\{3,4,5,6\}}}{2} + 1 \right\rfloor, \ \left\lfloor \{i\}_P^S - \tfrac{n_P^{\{3,4,5,6\}}}{2} + 2 \right\rfloor, \ \cdots \right] \end{aligned} \tag{4.114}$$

Weighting vectors are then created, where each entry reflects the "coverage ratio" of that particular line segment in $\vec{\boldsymbol{n}}_P^{\{1,2\}}$ and $\vec{\boldsymbol{n}}_P^{\{3,4,5,6\}}$. The weighting vectors are:

$$\vec{\boldsymbol{\mathfrak{W}}}_P^{\{1,2\}} = \left(\frac{1}{n_P^{\{1,2\}}} \right) \left[\ \mathfrak{w}_{P1}^{\{A\}}, \quad 1, \quad 1, \quad \cdots, \quad 1, \quad 1, \quad \mathfrak{w}_{P1}^{\{B\}} \ \right] \tag{4.115}$$

$$\vec{\boldsymbol{\mathfrak{W}}}_P^{\{3,4,5,6\}} = \left(\frac{1}{n_P^{\{3,4,5,6\}}} \right) \left[\ \mathfrak{w}_{P2}^{\{A\}}, \quad 1, \quad 1, \quad \cdots, \quad 1, \quad 1, \quad \mathfrak{w}_{P2}^{\{B\}} \ \right] \tag{4.116}$$

All entries within the brackets are 1, except for the first and last, whose weightings are:

$$\mathfrak{w}_{P1}^{\{A\}} = 1 - \left(\left(\{i\}_P^S - \frac{n_P^{\{1,2\}}}{2} \right) - \left\lfloor \{i\}_P^S - \frac{n_P^{\{1,2\}}}{2} \right\rfloor \right) \tag{4.117}$$

$$\mathfrak{w}_{P1}^{\{B\}} = \left(n_P^{\{1,2\}} - \left\lfloor n_P^{\{1,2\}} \right\rfloor - \mathfrak{w}_{P1}^{\{A\}} \right) \tag{4.118}$$

$$\mathfrak{w}_{P2}^{\{A\}} = 1 - \left(\left(\{i\}_P^S - \frac{n_P^{\{3,4,5,6\}}}{2} \right) - \left\lfloor \{i\}_P^S - \frac{n_P^{\{3,4,5,6\}}}{2} \right\rfloor \right) \tag{4.119}$$

$$\mathfrak{w}_{P2}^{\{B\}} = \left(n_P^{\{3,4,5,6\}} - \left\lfloor n_P^{\{3,4,5,6\}} \right\rfloor - \mathfrak{w}_{P2}^{\{A\}} \right) \tag{4.120}$$

The power dissipation at each of the Planet indices $\vec{\boldsymbol{n}}_P^{\{1,2\}}$ is then:

$$\boxed{\begin{aligned}
\vec{\dot{\mathfrak{Q}}}_P^{\{1\}} &= \frac{1}{2}\Big(\boldsymbol{\mathcal{P}}_{PS}^{\{1,diss\}}\Big)\vec{\mathfrak{W}}_P^{\{1,2\}} && (4.121)\\
\vec{\dot{\mathfrak{Q}}}_P^{\{2\}} &= \frac{1}{2}\Big(\boldsymbol{\mathcal{P}}_{PS}^{\{2,diss\}}\Big)\vec{\mathfrak{W}}_P^{\{1,2\}} && (4.122)\\
\vec{\dot{\mathfrak{Q}}}_P^{\{3,4\}} &= \frac{1}{2}\Big(\boldsymbol{\mathcal{P}}_{PS}^{\{3,diss\}} + \boldsymbol{\mathcal{P}}_{PS}^{\{4,diss\}}\Big)\vec{\mathfrak{W}}_P^{\{3,4,5,6\}} && (4.123)\\
\vec{\dot{\mathfrak{Q}}}_P^{\{5,6\}} &= \frac{1}{2}\Big(\boldsymbol{\mathcal{P}}_{PS}^{\{5,diss\}} + \boldsymbol{\mathcal{P}}_{PS}^{\{6,diss\}}\Big)\vec{\mathfrak{W}}_P^{\{3,4,5,6\}} && (4.124)
\end{aligned}}$$

Finally, the total energy dissipated at the Planet index locations is the product of the power dissipations and the simulation timestep size Δt_{OP}:

$$\boxed{\begin{aligned}
\vec{\mathfrak{Q}}_P^{\{1\}} &= \vec{\dot{\mathfrak{Q}}}_P^{\{1\}}\Delta t_{OP} && (4.125)\\
\vec{\mathfrak{Q}}_P^{\{2\}} &= \vec{\dot{\mathfrak{Q}}}_P^{\{2\}}\Delta t_{OP} && (4.126)\\
\vec{\mathfrak{Q}}_P^{\{3,4\}} &= \vec{\dot{\mathfrak{Q}}}_P^{\{3,4\}}\Delta t_{OP} && (4.127)\\
\vec{\mathfrak{Q}}_P^{\{5,6\}} &= \vec{\dot{\mathfrak{Q}}}_P^{\{5,6\}}\Delta t_{OP} && (4.128)
\end{aligned}}$$

The values in $\vec{\mathfrak{Q}}_P^{\{\}}$ can be stored in separate arrays and tracked across the simulation duration. Four arrays are used, corresponding to total energy dissipation along the four Planet surfaces. Each array is length n_P, and at each timestep the entries of $\vec{\mathfrak{Q}}_P^{\{\}}$ are added to the stored values at the corresponding index locations $\vec{\boldsymbol{n}}_P^{\{\}}$ to keep track of the total heat dissipation.

4.9.2 Planet Track Example Calculation

As an example, suppose:

- The Planet curve has 99 indices
- The Satellite coverage ratio is $\mathfrak{f}^{\{1,2\}} = 0.08$ *(the Lower Planet block covers 8% of the length of the Planet curve)*
- The fractional position index is $\Big(\{i\}_P^S\Big) = 34.2$ *(the Planet intercept point is 1/5 of the way between the coordinates of Planet indices 34 and 35)*
- Total power dissipation at the Planet surface $\{1\}$ is 10 watts *(5 watts to the Planet and 5 watts to the Satellite)*
- The model timestep is 0.01 seconds

Then:

$$\boxed{\begin{aligned}
n_P^{\{1,2\}} &= (0.08)(99) = 7.92 && (4.129)\\
\vec{\boldsymbol{n}}_P^{\{1,2\}*} &= [30.24,\ 31.24,\ 32.24,\ 33.24,\ 34.24,\ 35.24,\ 36.24,\ 37.24,\ 38.24] && (4.130)\\
\vec{\boldsymbol{n}}_P^{\{1,2\}} &= [30,\ 31,\ 32,\ 33,\ 34,\ 35,\ 36,\ 37,\ 38] && (4.131)\\
\mathfrak{w}_{P1}^{\{A\}} &= 1 - (30.24 - 30) = 0.76 && (4.132)\\
\mathfrak{w}_{P1}^{\{B\}} &= 7.92 - 7 - 0.76 = 0.16 && (4.133)\\
\mathfrak{W}_P^{\{1,2\}} &= \left(\frac{1}{7.92}\right)[0.76,\ 1,\ 1,\ 1,\ 1,\ 1,\ 1,\ 1,\ 0.16] && (4.134)\\
\dot{\vec{\mathfrak{Q}}}_P^{\{1\}} &\approx [0.48,\ 0.63,\ 0.63,\ 0.63,\ 0.63,\ 0.63,\ 0.63,\ 0.63,\ 0.10] \text{ watts} && (4.135)\\
\vec{\mathfrak{Q}}_P^{\{1\}} &\approx (0.01)[0.48,\ 0.63,\ 0.63,\ 0.63,\ 0.63,\ 0.63,\ 0.63,\ 0.63,\ 0.10] \text{ joules} && (4.136)
\end{aligned}}$$

In this example, the values in $\vec{\mathfrak{Q}}_P^{\{1\}}$ would be added to the heat storage vector for this track surface at the indices $\vec{\boldsymbol{n}}_P^{\{1,2\}}$. As a consistency check, summing $\dot{\vec{\mathfrak{Q}}}_P^{\{1\}}$ should return the original power dissipation of ~5 watts (in this example, it gives 4.99 watts due to numerical roundoff). Also, the sum of all elements in the weighting vector $\mathfrak{W}_P^{\{1,2\}}$ should equal 1, as is the case here.

4.9.3 Tracking Orbit Heat Accumulation

The process for tracking heat dissipation in the Orbit tracks is essentially the same as it was for the Planet tracks. **However, the implementation must take care to properly handle index wrap-around due to the fact the Orbit track is a loop.**

The Orbit "fractional position index" is:

$$\boxed{\{i\}_O^S = \left(\frac{\left\|\vec{\boldsymbol{r}}_O^* - \vec{\boldsymbol{S}}_O^A\right\|}{\left\|\vec{\boldsymbol{S}}_O^B - \vec{\boldsymbol{S}}_O^A\right\|}\right)\left(\{i\}_O^B - \{i\}_O^A\right) + \{i\}_O^A} \tag{4.137}$$

The "coverage ratio," where L_O is the length of the Orbit track and $L_{S,O}$ is the length of the Satellite Orbit block, is:

$$\boxed{\mathfrak{f}^{\{7,8\}} = \frac{(L_{S,O})}{(L_O)}} \tag{4.138}$$

The "length" of the indices in contact is:

$$\boxed{n_O^{\{7,8\}} = (n_O)\Big(\mathfrak{f}^{\{7,8\}}\Big)} \tag{4.139}$$

The unrounded Orbit index vector is:

$$\boxed{\vec{\boldsymbol{n}}_O^{\{7,8\}*} \quad = \quad \left[\left(\{i\}_O^S - \frac{n_O^{\{7,8\}}}{2}\right),\ \ \left(\{i\}_O^S - \frac{n_O^{\{7,8\}}}{2} + 1\right),\ \ \left(\{i\}_O^S - \frac{n_O^{\{7,8\}}}{2} + 2\right),\ \ \cdots\ \right]} \tag{4.140}$$

The rounded-down Orbit index vector is:

$$\boxed{\vec{\boldsymbol{n}}_O^{\{7,8\}} \quad = \quad \left[\left\lfloor\{i\}_O^S - \frac{n_O^{\{7,8\}}}{2}\right\rfloor,\ \ \left\lfloor\{i\}_O^S - \frac{n_O^{\{7,8\}}}{2} + 1\right\rfloor,\ \ \left\lfloor\{i\}_O^S - \frac{n_O^{\{7,8\}}}{2} + 2\right\rfloor,\ \ \cdots\ \right]} \tag{4.141}$$

The weighting vector is:

$$\boxed{\vec{\mathfrak{W}}_O^{\{7,8\}} = \left(\frac{1}{n_O^{\{7,8\}}}\right)\left[\ \mathfrak{w}_O^{\{A\}},\quad 1,\quad 1,\quad \cdots,\quad 1,\quad 1,\quad \mathfrak{w}_O^{\{B\}}\ \right]} \tag{4.142}$$

The first and last weights are:

$$\mathfrak{w}_O^{\{A\}} = 1 - \left(\left(\{i\}_O^S - \frac{n_O^{\{7,8\}}}{2}\right) - \left\lfloor\{i\}_O^S - \frac{n_O^{\{7,8\}}}{2}\right\rfloor\right) \tag{4.143}$$

$$\mathfrak{w}_O^{\{B\}} = \left(n_O^{\{7,8\}} - \left\lfloor n_O^{\{7,8\}}\right\rfloor - \mathfrak{w}_O^{\{A\}}\right) \tag{4.144}$$

The power dissipation at each of the Orbit indices $\vec{\boldsymbol{n}}_O^{\{7,8\}}$ is then:

$$\vec{\dot{\mathfrak{Q}}}_O^{\{7\}} = \frac{1}{2}\Big(\boldsymbol{\mathcal{P}}_{OS}^{\{7,diss\}}\Big)\vec{\mathfrak{W}}_O^{\{7,8\}} \tag{4.145}$$

$$\vec{\dot{\mathfrak{Q}}}_O^{\{8\}} = \frac{1}{2}\Big(\boldsymbol{\mathcal{P}}_{OS}^{\{8,diss\}}\Big)\vec{\mathfrak{W}}_O^{\{7,8\}} \tag{4.146}$$

Finally, the total energy dissipated is:

$$\boxed{\begin{aligned} \vec{\mathcal{Q}}_O^{\{7\}} &= \dot{\vec{\mathcal{Q}}}_O^{\{7\}} \Delta t_{OP} && (4.147) \\ \vec{\mathcal{Q}}_O^{\{8\}} &= \dot{\vec{\mathcal{Q}}}_O^{\{8\}} \Delta t_{OP} && (4.148) \end{aligned}}$$

The values $\vec{\mathcal{Q}}_O^{\{\}}$ are stored in two arrays, corresponding to total energy dissipation along the two Orbit surfaces. Each array is length n_O, and at each timestep the entries of $\vec{\mathcal{Q}}_O^{\{\}}$ are added to the stored values at the corresponding index locations $\vec{\boldsymbol{n}}_O^{\{\}}$ to keep track of the total heat dissipation.

4.10 IHC Parameters for ihcBENCH Prototype

ihcMATLAB proved critical in choosing the parameters for the IHC prototype ("ihcBENCH") presented in Chapter 5. Keeping in mind the many unknowns involved in building the first IHC prototype, risk mitigation was by far the most important goal. Performance optimization was considered secondary to practical concerns related to building the prototype. It was far more important to ensure the design could be realistically fabricated, assembled, adjusted, and finally tested without encountering a catastrophic issue along the way. Ultimately the design was driven by fabrication/assembly/*etc.* concerns, then the viability of parameters checked with ihcMATLAB.

The various parameters defining the prototype Planet, Orbit, and Satellite geometries are given in Tables 4.7 and 4.8.

4.11 Model Predictions using ihcBENCH Parameters

Of all the ihcMATLAB parameters, the estimated friction coefficient presented by far the greatest project risk. While the IHC principle relies on non-zero friction to operate, the value must still be sufficiently low to avoid binding, particularly with a pseudo-kinematic design. To mitigate the risk of friction coefficient uncertainty it was necessary to ensure other parameters could be adjusted to achieve a successful result in the event the friction coefficient proved higher than expected. This was accomplished by preparing a "contingency design," for which certain parameters were adjusted to accommodate this outcome. **The prototype parameters which (a) could be adjusted later at minimal cost/difficulty and (b) could effectively "counteract" excessive friction were: the Orbit preload force $\left(\boldsymbol{\mathcal{F}}^{\boldsymbol{k_O}}\right)$, the Planet Preload force $\left(\boldsymbol{\mathcal{F}}^{\boldsymbol{k_{P1}}}\right)$, and the Orbit contact radius ($\boldsymbol{\rho_O}$).** The preloads are easily adjusted by changing the Satellite shim and spring sets. Modifying the Orbit contact point requires more work but is still straightforward. The easiest option is to simply swap the Satellite Orbit blocks for a new design with lower sidewalls (resulting in a lower contact point). If needed, new Orbit tracks could also be swapped in to aid this. Of course, the real system could be adjusted anywhere between the nominal and

Table 4.7 – ihcBENCH Coupling Geometry Parameters

Radius, Sat. Inner Planet Block	$\boldsymbol{\rho_{P1}}$	45 mm	**Height,** Sat. Inner Planet Block	$\boldsymbol{t_{P1}}$	8.0 mm
Radius, Sat. Outer Planet Block	$\boldsymbol{\rho_{P2}}$	74 mm	**Height,** Sat. Outer Planet Block	$\boldsymbol{t_{P2}}$	8.0 mm
Radius, Sat. Orbit Block	$\boldsymbol{\rho_{O}}$	87 mm	**Height,** Sat. Orbit Block	$\boldsymbol{t_{O}}$	9.5 mm
Length, Sat. Inner Planet Block	$\boldsymbol{l_{P1}}$	11 mm	**Width,** Sat. Inner Planet Block	$\boldsymbol{w_{P1}}$	14 mm
Length, Sat. Outer Planet Block	$\boldsymbol{l_{P2}}$	16 mm	**Width,** Sat. Outer Planet Block	$\boldsymbol{w_{P2}}$	14 mm
Length, Sat. Orbit Block	$\boldsymbol{l_{O}}$	35 mm	**Width,** Sat. Orbit Block	$\boldsymbol{w_{O}}$	15 mm
Contact Angle, Sat. Inner Planet Block	$\boldsymbol{\lambda_{P1}}$	$-20°$ (Upwards Taper)	**Shape Parameter,** Planet	$\boldsymbol{\beta_{P}}$	53°
Contact Angle, Sat. Outer Planet Block	$\boldsymbol{\lambda_{P2}}$	$+15°$ (Downwards Taper)	**Preload Force,** Outer Planet Block	$\boldsymbol{\mathcal{F}^{k_{P1}}}$	185 N
Contact Angle, Sat. Orbit Block	$\boldsymbol{\lambda_{O}}$	$-12°$ (Upwards Taper)	**Preload Force,** Orbit Block	$\boldsymbol{\mathcal{F}^{k_{O}}}$	22 N

Table 4.8 – ihcBENCH Physical Parameter Estimates

Radius, Sat. Center-of-Mass	ρ_S	64 mm
Total Mass, Per Satellite	m_S	50 g
Mass Moment of Inertia, About Satellite U axis	I_{UU}	2.0×10^{-5} kg-m^2
Mass Moment of Inertia, About Satellite V axis	I_{VV}	1.9×10^{-5} kg-m^2
Mass Moment of Inertia, About Satellite W axis	I_{WW}	2.5×10^{-6} kg-m^2
Coefficient of Friction, Planet-Sat Interface, Estimate	μ_{PS}	0.03
Coefficient of Friction, Orbit-Sat, Estimate	μ_{OS}	0.03

contingency designs.

Figure 4-10 shows the characteristic maps for the nominal ihcBENCH design, as well as a contingency design for use in the event of higher-than-expected friction coefficients. In the contingency case, the Planet preload is halved and the Orbit contact radius brought inwards by ~12 mm. This allowed a very similar characteristic plot to be achieved despite the difference in friction coefficient. In other words, the Planet preload and Orbit contact radius could effectively compensate for differences in friction coefficient.

Friction sensitivity plots are shown in Figure 4-11. In both cases, the goal was to ensure the test system could confidently achieve torque modulation (*i.e.* a demonstrable relationship between β_O and torque) without the β_O stroke range becoming prohibitively small.

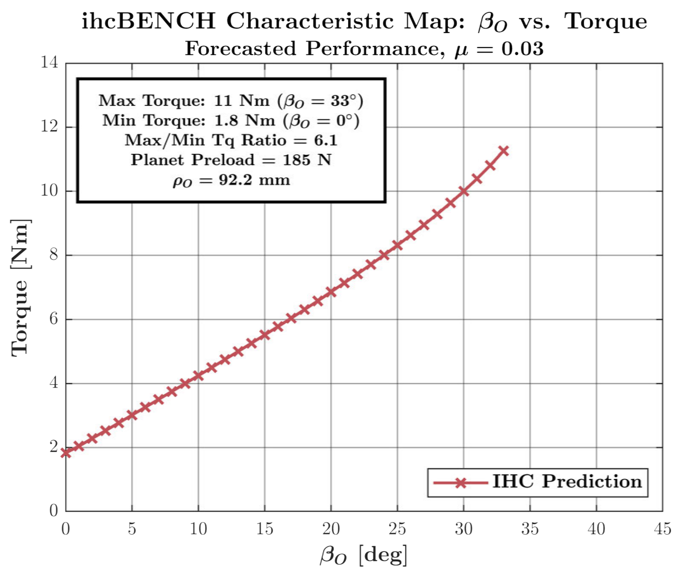

(a) Nominal IHC Design

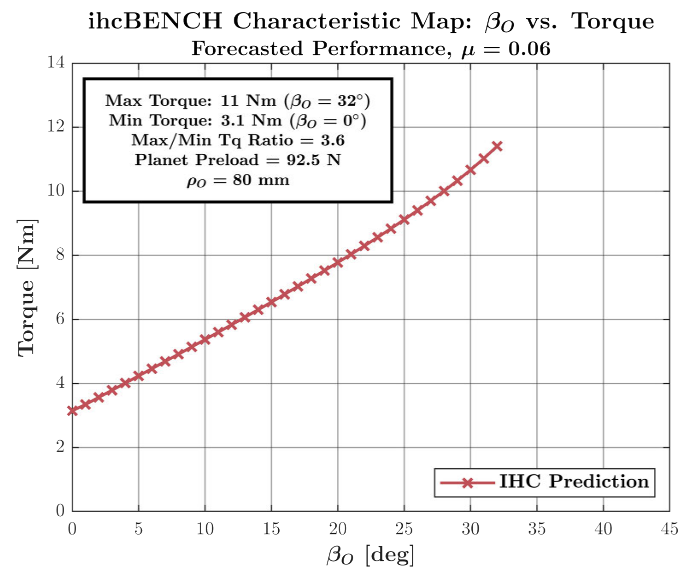

(b) High-μ Contingency IHC Design

Figure 4-10 – IHC Characteristic Maps for the projected nominal IHC design ($\mu \approx 0.03$) and the contingency design ($\mu \approx 0.06$). The ability to adjust the IHC preloads and Orbit contact position greatly mitigated the potential risks associated with contact friction.

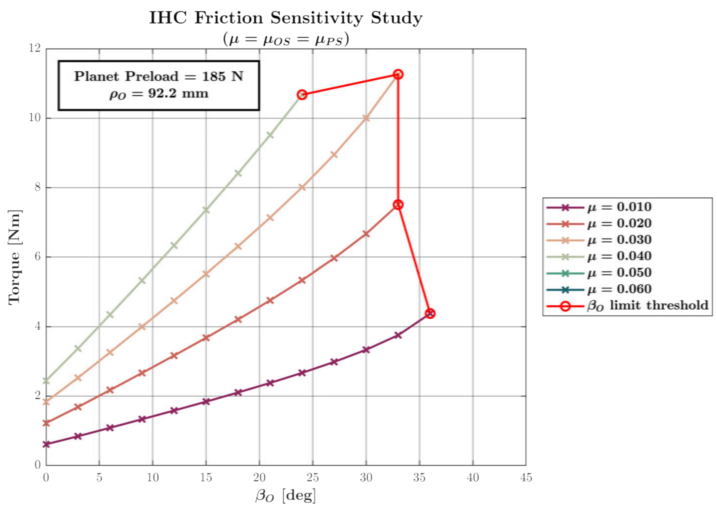

(a) Nominal IHC Design

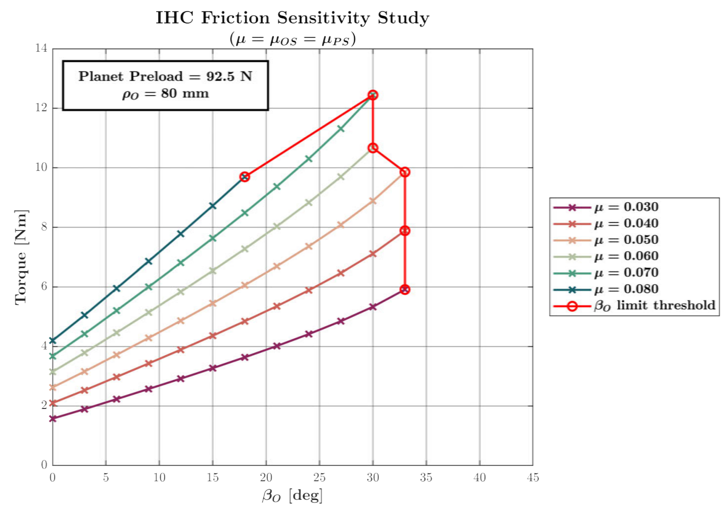

(b) High-μ Contingency IHC Design

Figure 4-11 – Sensitivity study plots for the nominal and contingency IHC designs. Note that some friction values are indicated in the figure legends but do not have corresponding data appearing on the plots. This is because these cases have no valid pseudokinematic operating points regardless of the β_O value.

Chapter 5

Test System Design

5.1 Scope, Goals, & Requirements for ihcBENCH Test System

5.1.1 Motivation & High-Level Goals

To “close-the-loop” on the work laid out in the earlier chapters, substantial testing and validation of a real-world IHC was needed. Although simple hand-scale prototypes had been built early on in the project timeline, these only provided qualitative feedback via manual, hands-on interaction. True validation of the IHC concept required a robust prototype capable of subjecting an IHC to repeated testing and collecting reliable performance data. This chapter discusses the design of that system, termed **“ihcBENCH.”** Its major high-level goals are summarized in Table 5.1. Photographs of early and final IHC prototypes can be seen in Figure 5-1.

Table 5.1 – ihcBench Testing Goals

1	Prove that the motions and degrees-of-freedom of the real system match the expectations from theory and earlier prototypes.
2	Demonstrate the ability to vary torque transmission by modulating the Orbit clutch angle.
3	Demonstrate IHC lockup by moving the Orbit ring to/past a critical lockup angle.
4	Gather performance data to assess the accuracy of the predictive model in steady-state operation.
5	Summarize important takeaways and suggestions for designing, building, and testing future IHC prototypes.

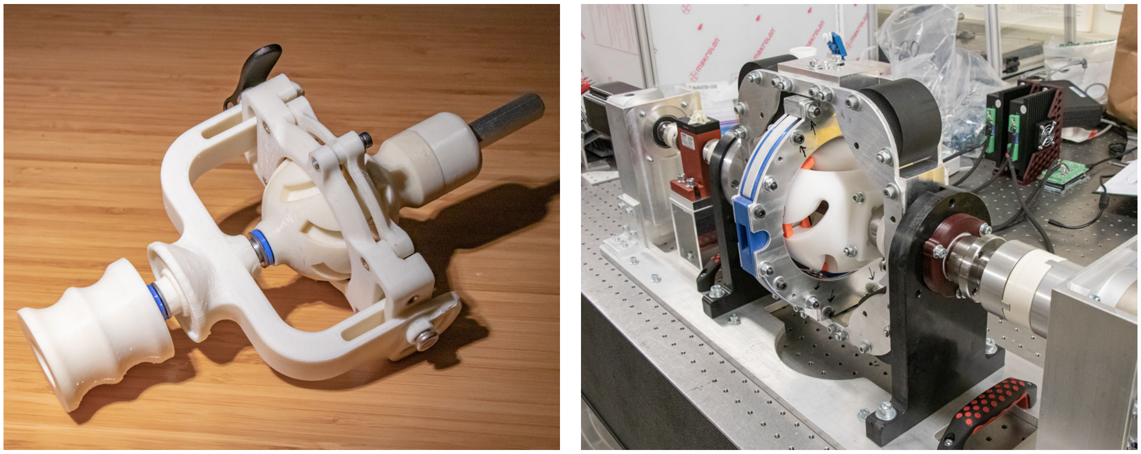

(a) (b)

Figure 5-1 – Photographs of early and final IHC prototypes. The early prototype in (5-1a) is 2” (∼50mm) in diameter and built to conduct hands-on qualitative testing of the core IHC principles. The later prototype, shown in (5-1b), is the prototype system discussed throughout this chapter.

To successfully fulfill all goals listed in Table 5.1 it was imperative that major mistakes and design errors be avoided. ihcBENCH would need to be both fully-functional and reliable in its first iteration. Keeping in mind that ihcBENCH was a ground-up design of a brand new mechanism, avoiding unnecessary risk and carefully managing scope creep was paramount. Major goals beyond those in Table 5.1 – such as maximizing torque density – were relegated to future work to avoid over-complicating this first-generation prototype.

5.1.2 ihcBENCH Functional Requirements

ihcBENCH was a ground-up design with no predecessor from which baseline targets could be drawn. The test system’s Functional Requirements (FRs) were therefore largely driven by:

- The specifications of the lab’s torque sensor (FUTEK FSH02567)
- The suite of validation tests planned
- The predicted performance from ihcMATLAB
- A focus on simplicity, modularity, manufacturability, and ease-of-assembly

The complete system-level Functional Requirements are given in Table 5.2.

5.1.3 ihcBENCH Design Requirements

In addition to the Functional Requirements, a number of Design Requirements also guided the design process – see Table 5.3.

Table 5.2 – ihcBENCH Functional Requirements

FR #	Functional Requirement (FR)	FR Value	Constraint	Value Achieved	Description & Reasoning
1	Nominal Planet Diameter	6 in	±20%	6.00 in	A planet diameter of approx. 6 inches would avoid excessively small parts (especially in the Satellites) without making any components unduly large. This value was specified based on reasonable component sizes and fits from early CAD models.
2	Torque Capacity	50 Nm	Minimum	—	The torque capacity of load-bearing components in the torque path. 50 Nm was chosen as it is the peak continuous torque rating for the torque sensor used (FUTEK FSH02567).
3	Maximum Motor Torque Output	50 Nm	Maximum	∼42 Nm	The peak torque output of the drive system (before efficiency losses) must not exceed the target torque capacity.
4	IHC Peak Torque Output (Before Lockup)	10 Nm	Minimum	>13 Nm	Design target to guide the selection of IHC parameters. The IHC should transmit at least this much torque before locking up. This value would facilitate clear and distinct measurements while leaving plenty of headroom in the event the IHC significantly deviated from model predictions.
5	Torque Measurement Accuracy	±0.5 Nm	Maximum	±0.15 Nm	Given **FR #4**, this ensures errors are small relative to the torque measurements themselves.
6	Achievable Clutch Angle β_O	35°	Minimum	∼40°	Ensures the orbit subassembly has sufficient sweep angle to achieve lockup without encountering mechanical interference. This value was specified based on reasonable component sizes and fits from early CAD models.
7	Target Planet Angle β_P	50°	Minimum	53°	The range of practically attainable β_O values is limited in a real system. The Planet track must therefore be significantly tilted to ensure a Satellite can still reach its extremities; this target was specified based on reasonable component sizes and fits in early CAD models.
8	Target Lockup Angle β_O	30° − 40°	Range	∼37°	The IHC should be able to achieve lockup before reaching its terminal clutch angle β_O.

Table 5.3 – ihcBench Design Requirements

1	Simplify construction as much as possible. Most custom parts were to be fabricated in-house by the author.
2	Implement modularity so parts could be replaced in the event of unexpected problems.
3	The Planet, Orbit, and Satellite positions should be adjustable (via shims) so alignment errors could be corrected.
4	Satellite preload forces and block axial offsets should be individually adjustable.
5	Satellites should be accessible for adjustment without removing the entire Orbit subassembly.
6	IHC motions should be fully automated during tests to ensure precise motion and repeatable data collection.
7	The clutch angle β_O should be manually adjustable, measurable, and lockable.
8	The system should be transportable for meetings and demonstrations.

5.2 Overview of ihcBENCH

ihcBENCH is a system of hardware, electronics, and software – Figures 5-3 to 5-4 show the system flowchart and photographs of key components. At the core of ihcBENCH is the prototype Inertial Hysteresis Coupling itself, which is driven by two stepper motors. The Planet and Orbit speeds are independently controllable via a software user interface. An in-line sensor measures and logs the torque developed across the IHC. This process is then repeated and the coupling parameters (particularly β_O) varied to explore the coupling's performance envelope. Numerous results, such as the IHC characteristic plot, were collected this way.

5.2.1 ihcBENCH Motion

Mechanically, the system consists of two rotating subassemblies organized along a common rotation axis (see Figure 5-5). The Inertial Hysteresis Coupling is centrally located and supported on either side by bearing uprights that resemble tombstones. Geared stepper motors are mounted at either end of the system and each drives one of the rotating subassemblies. Figure 5-6 contains side-views of ihcBENCH, with each rotating subassembly color-coded for clarity. In these diagrams, the "RIGHT" motor drives the Planet by means of a splined driveshaft. The "LEFT" motor drives both the in-line torque sensor and the Orbit subassembly. ihcBENCH is mounted upon a baseplate that bolts down to an optical table during testing. However, the baseplate can be unbolted so the entire system can be easily transported for

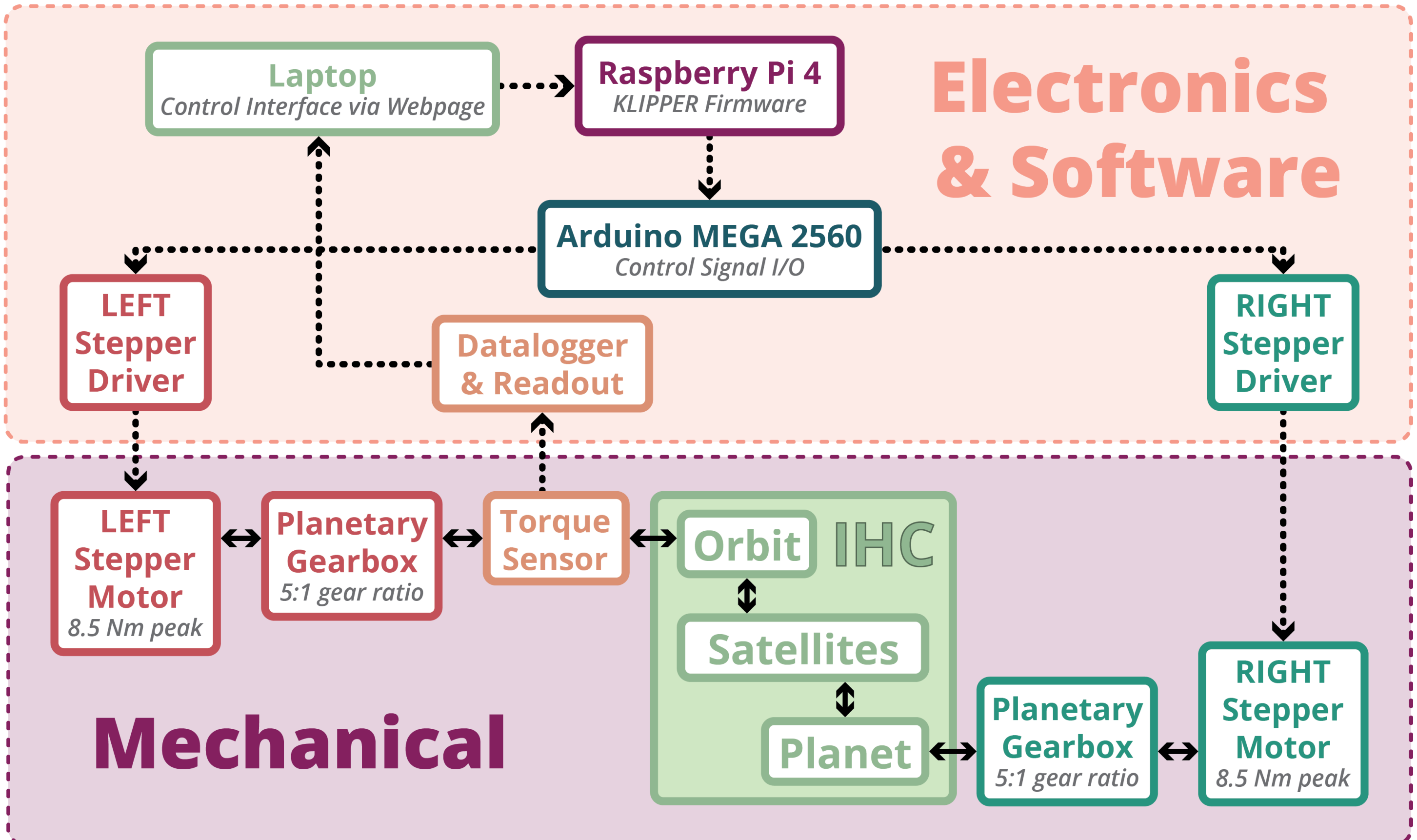

Figure 5-2 – ihcBENCH System Layout Block Diagram.

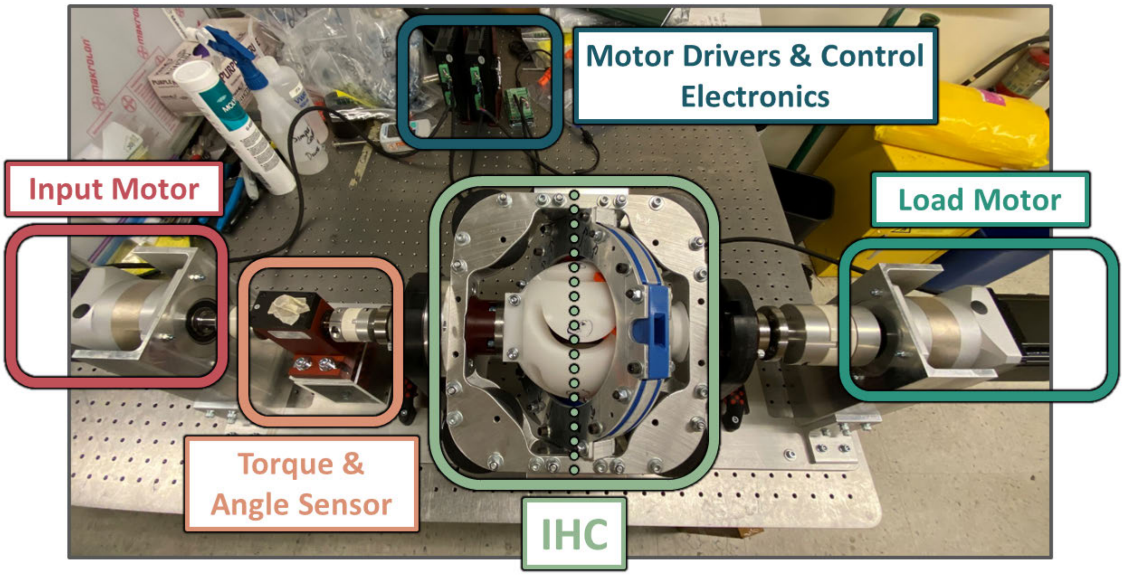

Figure 5-3 – Photograph of ihcBENCH with major components labeled.

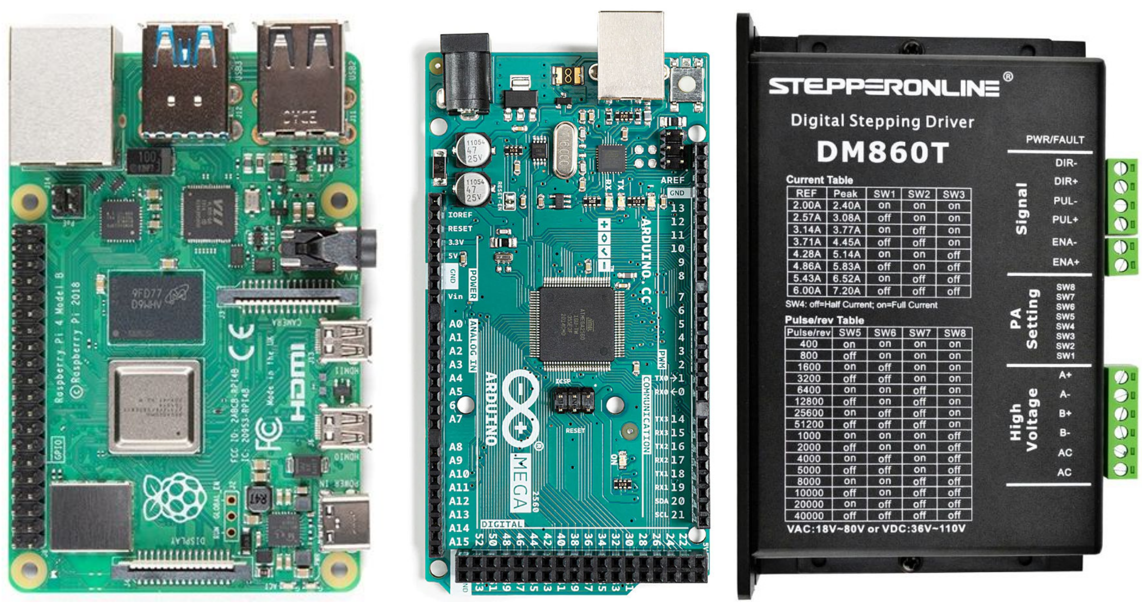

(a) Raspberry Pi 4B [37] (Command & Motion Processor)

(b) Arduino Mega 2560 [38] (I/O Microcontroller)

(c) STEPPERONLINE DM860T [39] (NEMA34 Stepper Driver)

Figure 5-4 – Product images of the major electrical components for driving the ihcBENCH stepper motors.

meetings, demonstrations, *etc.*

A variety of bearings guide and constrain the motion of the two rotating assemblies (see Figure 5-6). The chosen bearing layout satisfies a few important criteria:

1. **Single-DOF Constraint:** The two rotating subassemblies are each constrained to only a single degree-of-freedom – rotation about the driveline axis.
2. **Doubly-Supported Shafts:** The Planet and Orbit components are each supported on both sides of the IHC, allowing loads from the Satellites to be reacted symmetrically. Compared to a cantilever approach this not only provides substantially greater stiffness, but also naturally aligns the subassemblies' rotating axes. In this layout, the non-driven end of the Planet driveshaft is mounted inside the "LEFT" end of the Orbit outer frame.
3. **Adjustability:** The relative axial positions of the Planet and Orbit can easily be adjusted by means of shims and spacers.
4. **Universal Axial Preloading:** Axial preload can be applied to all bearings simultaneously using a single process. This greatly eases assembly/disassembly and is explained further in Figure 5-6.

An additional crucial degree-of-freedom – modulation of the clutch angle β_O – is built into the Orbit subassembly (see Figure 5-7). Mounted on 3/8" dowel pins, the Orbit ring swivels to change the clutch angle β_O. Once the desired position is found, four 1/4"-20 bolts are tightened to lock the clutch angle for testing under load.

5.2.2 Torque Sensor – FUTEK TRS705

From the start, ihcBENCH was designed to use the lab's existing FUTEK TRS705 torque sensor (Figure 5-8). It is a non-contact, shaft-to-shaft rotary torque sensor with 50 Nm capacity (see Table 5.4 for additional specs). This sensor is easy to interface with as it can be placed directly in-line with the IHC. System torque is measured as it passes directly through. The incorporated encoder also permits angular position and speed measurements to be recorded. However, due to coupling slip, only the Orbit-side position/velocity can be logged on ihcBENCH. To interface with the sensor a FUTEK IHH500 Elite handheld readout is used. It provides the actual datalogging capabilities (via laptop over USB) and has a display for showing real-time measurements.

5.2.3 Measurement Errors

ihcBENCH measurement errors are primarily associated with (a) measured torque, and (b) the measured clutch angle β_O. Sources of error, as well as the combined measurement uncertainties, are given in Table 5.5.

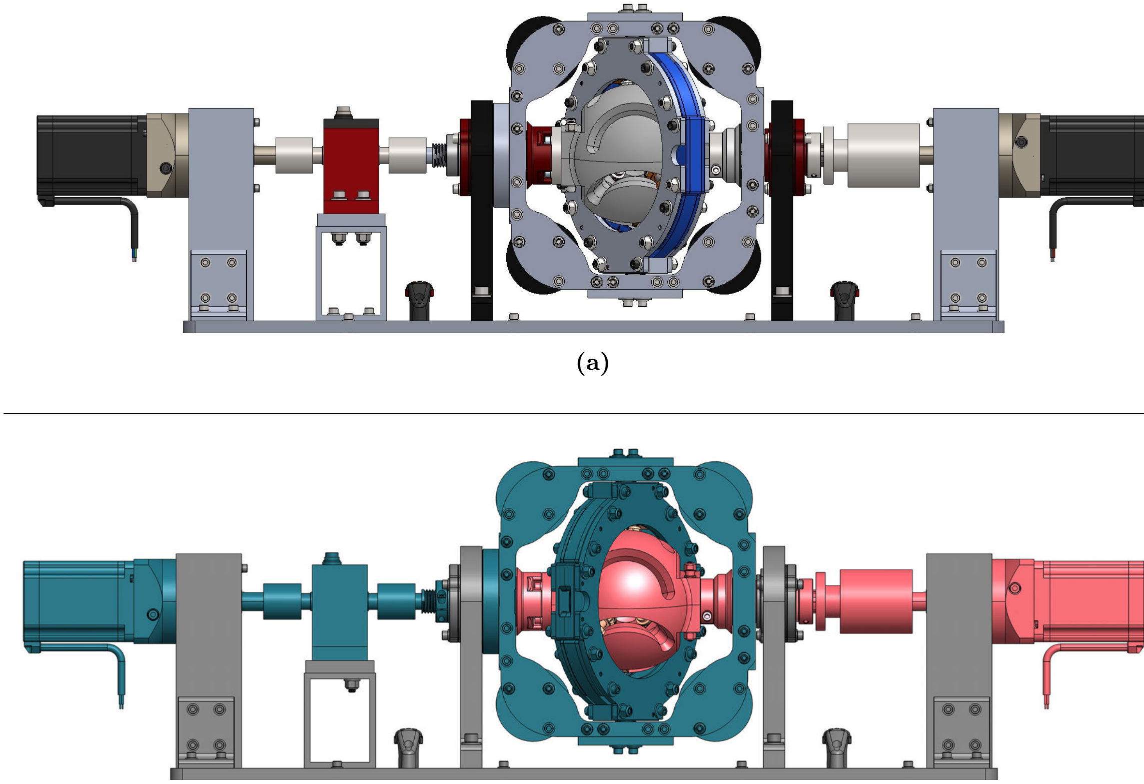

(a)

(b)

Figure 5-5 – Screenshots of ihcBENCH in CAD (Side View). Two versions of the system are shown (one above the other) to help illustrate which components move together. Each component in Figure 5-5b takes one of three colors: green for the Orbit subassembly, salmon for the Planet subassembly, or gray for stationary components.

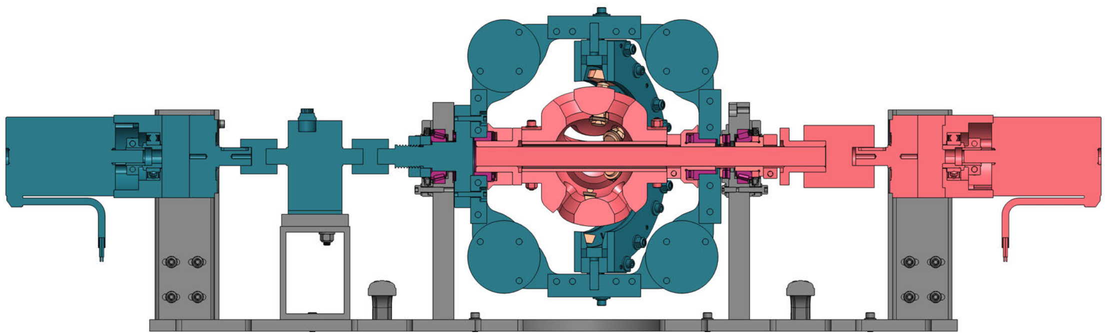

(a)

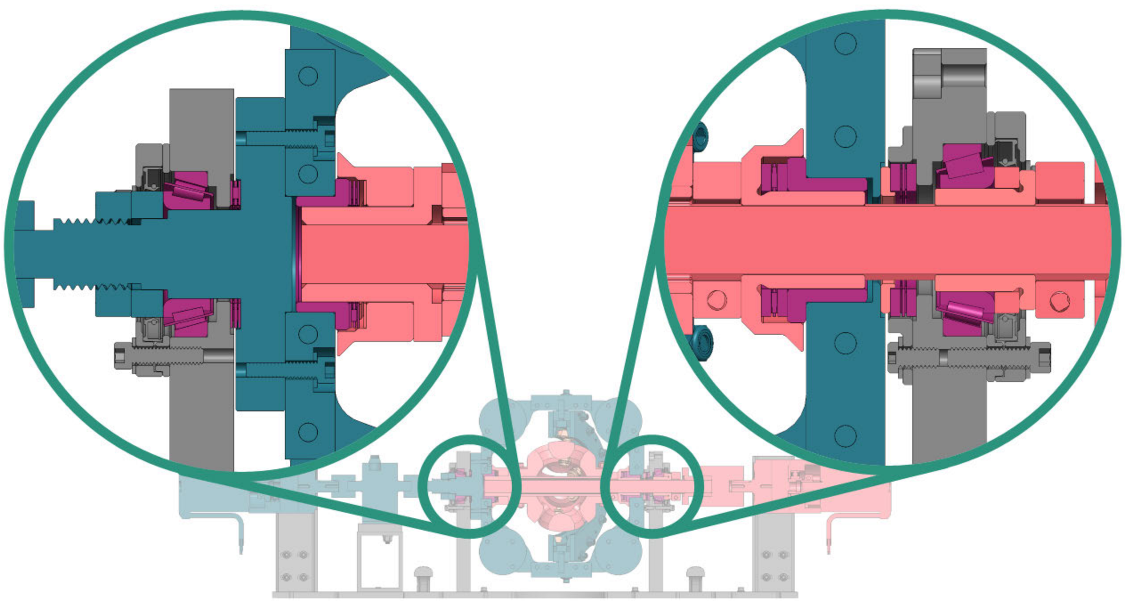

(b)

Figure 5-6 – Cutaway side views of ihcBENCH with bearing components color-coded purple. Tapered roller bearings support the IHC assembly via the uprights just outside of the Orbit's rectangular outer frame. The Planet and Orbit components use a collection of needle thrust bearings and plain bearings for thrust and radial constraint. The entire subassembly can be preloaded in a single operation: when one block of the Orbit is unfastened, the nut backing the leftmost tapered roller bearing can be tightened, thereby preloading every other bearing axially (the Orbit block is then re-tightened to secure the preload). All bearings and bearing surfaces were greased (Molykote P/N G-4500 FM) during first assembly.

Table 5.4 – Specifications – FUTEK Torque Sensor

Manufacturer:	FUTEK Advanced Sensor Technology, Inc.
Model:	TRS705 (50 Nm)
Part Number:	FSH02567
Nominal Torque Rating:	50 Nm
Nonlinearity:	±0.1 Nm
Hysteresis:	±0.05 Nm
Nonrepeatability:	±0.1 Nm
Max Rotation Speed:	7000 rpm
Encoder Pulses-Per-Rev:	720

Table 5.5 – Measurement Uncertaintiess

Sources of Torque Measurement Error:	±0.1 Nm (Sensor Nonlinearity) ±0.05 Nm (Sensor Hysteresis) ±0.1 Nm (Sensor Nonrepeatability)
Combined Torque Uncertainty: ($\boldsymbol{\ell_2}$ norm of errors)	**±0.15 Nm**
Sources of β_O Angle Measurement Error:	±0.3° (Angle Finder Accuracy) ±0.5° (Manual Measurement Repeatability)
Combined β_O Angle Uncertainty: ($\boldsymbol{\ell_2}$ norm of errors)	**±0.6°**

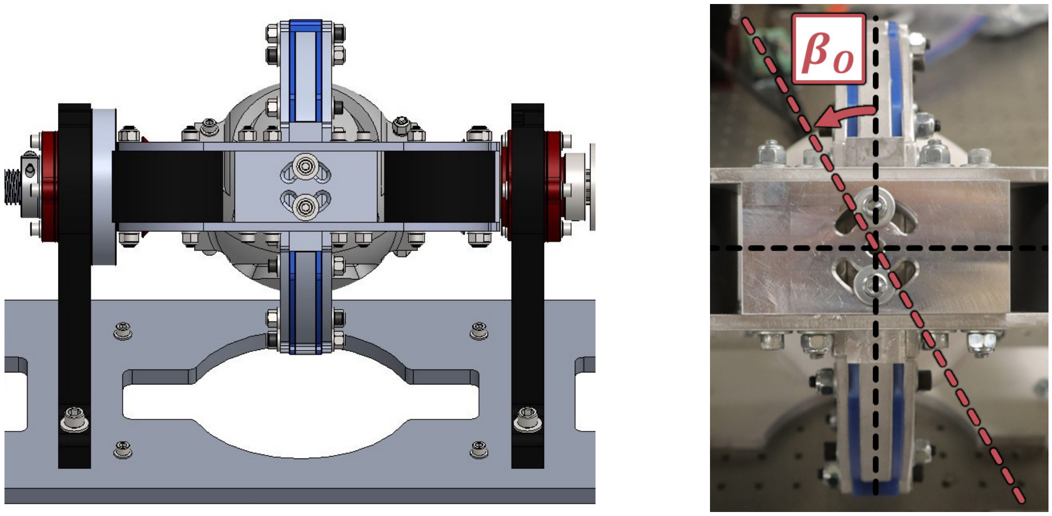

(a) (b)

Figure 5-7 – Screenshot and photograph of the Orbit clutch angle (β_O) adjustment mechanism. Two fasteners on either side are loosened to free the Orbit ring to rotate. It is then manually repositioned, measured, and locked in place once more.

5.2.4 ihcBENCH Motion Sequences

The motion of the IHC is quite difficult to visualize without observing it in person or on video. However, for purposes of this thesis, a number of motion sequences are shown in Figures 5-9 to 5-12. These contain video snapshots of the Planet, Orbit, Satellites, and other hardware moving under a variety of conditions.

5.3 IHC Planet Design

At the core of ihcBENCH is the Planet – by far the most difficult component to fabricate and the only custom component not made on-site at MIT.[1] With a diameter of 6 inches, the Planet is comprised of two identical half-spheres joined together via alignment pins and four 1/4”-20 fasteners. These fasteners clamp the Planet halves together through rectangular hubs protruding from either end of the Planet (along its rotation axis). See Figures 5-13 and 5-14 for photographs and CAD cross-section views of these components.

5.3.1 Planet Slot Geometry & Fabrication

The difficulty of Planet fabrication is driven largely by the geometry of the Satellite slots, of which each Sphere half has three. This is largely due to three factors:

- **Slot Orientation** – The bore of each slot is a real-world analog to the Satellite intercept

[1] The Planet halves were machined by SuNPe Limited.

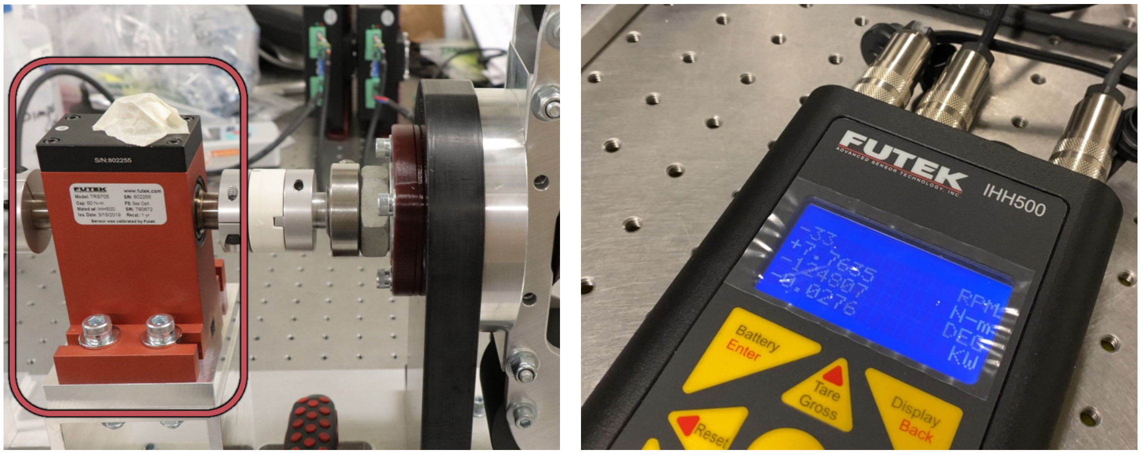

(a) **(b)**

Figure 5-8 – Photographs of the FUTEK TRS705 (50 Nm) torque sensor and IHH500 datalogger. This combination of sensor and datalogger facilitated electronic data collection during testing and provided immediate readouts of torque, position, and speed via the handheld display.

line introduced in Chapter 3. Just as the Satellite intercept line must always intersect the Planet's centerpoint, so too must the axis of each slot's bore. Practically speaking, this requires the associated milling operations to always keep the cutting axis directly in-line with the sphere center, a constraint that requires a 5-axis CNC machine.

- **Slot Taper** – Each slot has both internal and external tapers (λ_{P1} and λ_{P2}, respectively). The inner taper in particular presents a challenge as the geometry is difficult to reach when approached from the Planet's interior (see Figure 5-15). It cannot be reached from the Planet's exterior side with standard tooling (see Figure 5-15).
- **External Spherical Geometry** – The tight clearance between the Planet's exterior surface and the Orbit ring requires the Planet to remain approximately spherical.

The Planet's Shape Parameter of $\beta_P = 53°$ is driven by real-world constraints – in particular, practical limits on the achievable clutch angle β_O. Clearance must be maintained between the Orbit ring and Planet hubs, both of which must be of meaningful size. The Planet hub must be large enough to support the required torque and the Orbit ring sidewalls be thick enough to react the lateral loads from the Satellite Orbit blocks. In ihcBENCH, β_O is geometrically limited to a maximum of approximately 40°. With this in mind, $\beta_P = 53°$ was chosen. This value balances four considerations: (a) utilizing as much of the Planet's non-hub surface area as possible; (b) achieving high Satellite-Planet contact angles (γ_S); (c) maintaining reasonable wall thicknesses (especially with respect to the half-sphere parting surface); and (d) remaining practical to fabricate and assemble.

In CAD, the Satellite slot geometry is generated using a carefully-specified Cut-Revolve operation (see

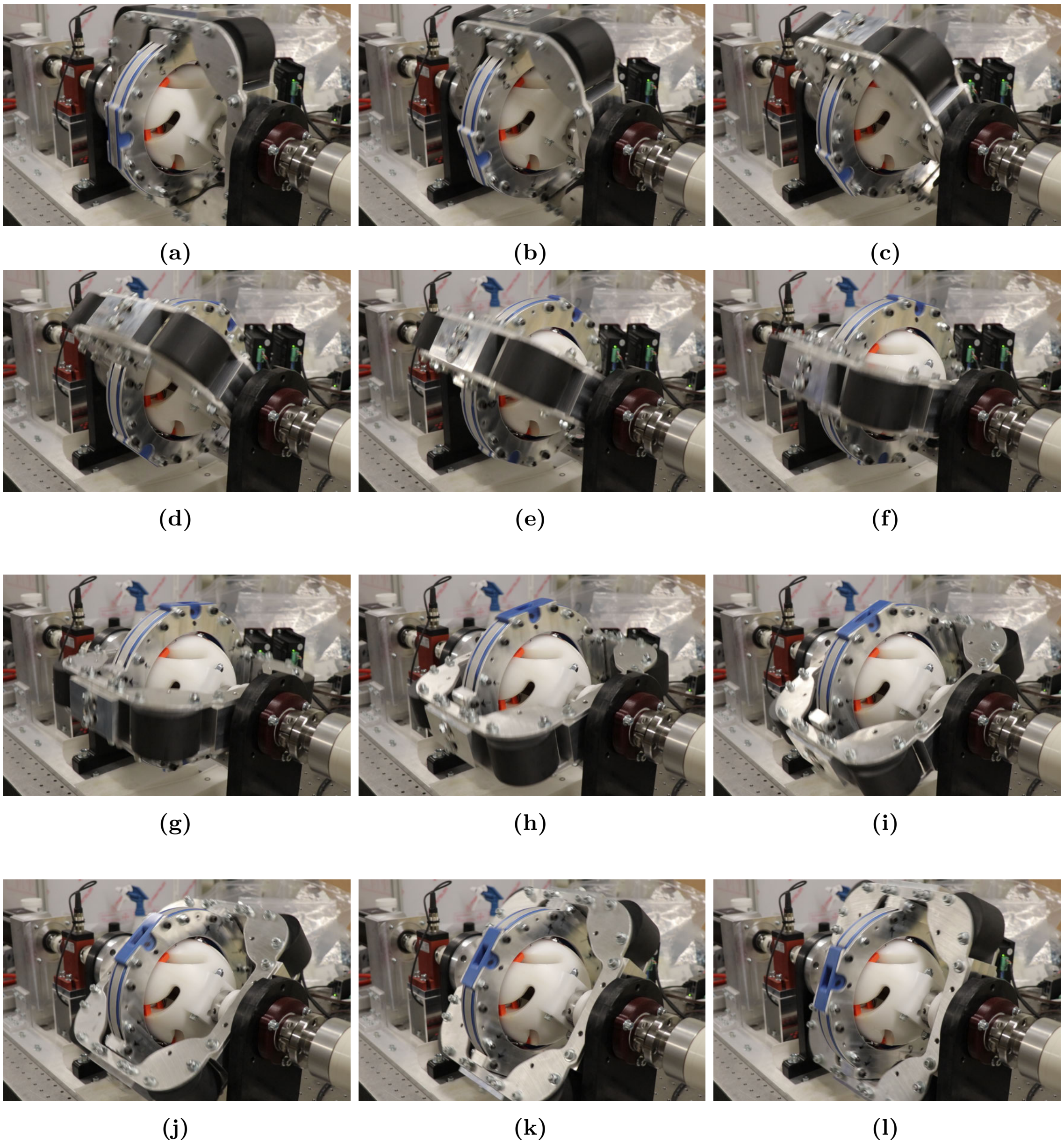

(a) (b) (c) (d) (e) (f) (g) (h) (i) (j) (k) (l)

Figure 5-9 – Example IHC Motion Sequence #1. These photographs show IHC motion where only the Orbit subassembly rotates. In this case, it moves counter-clockwise relative to the camera. The Planet is held stationary. The Satellites slip through the Orbit ring.

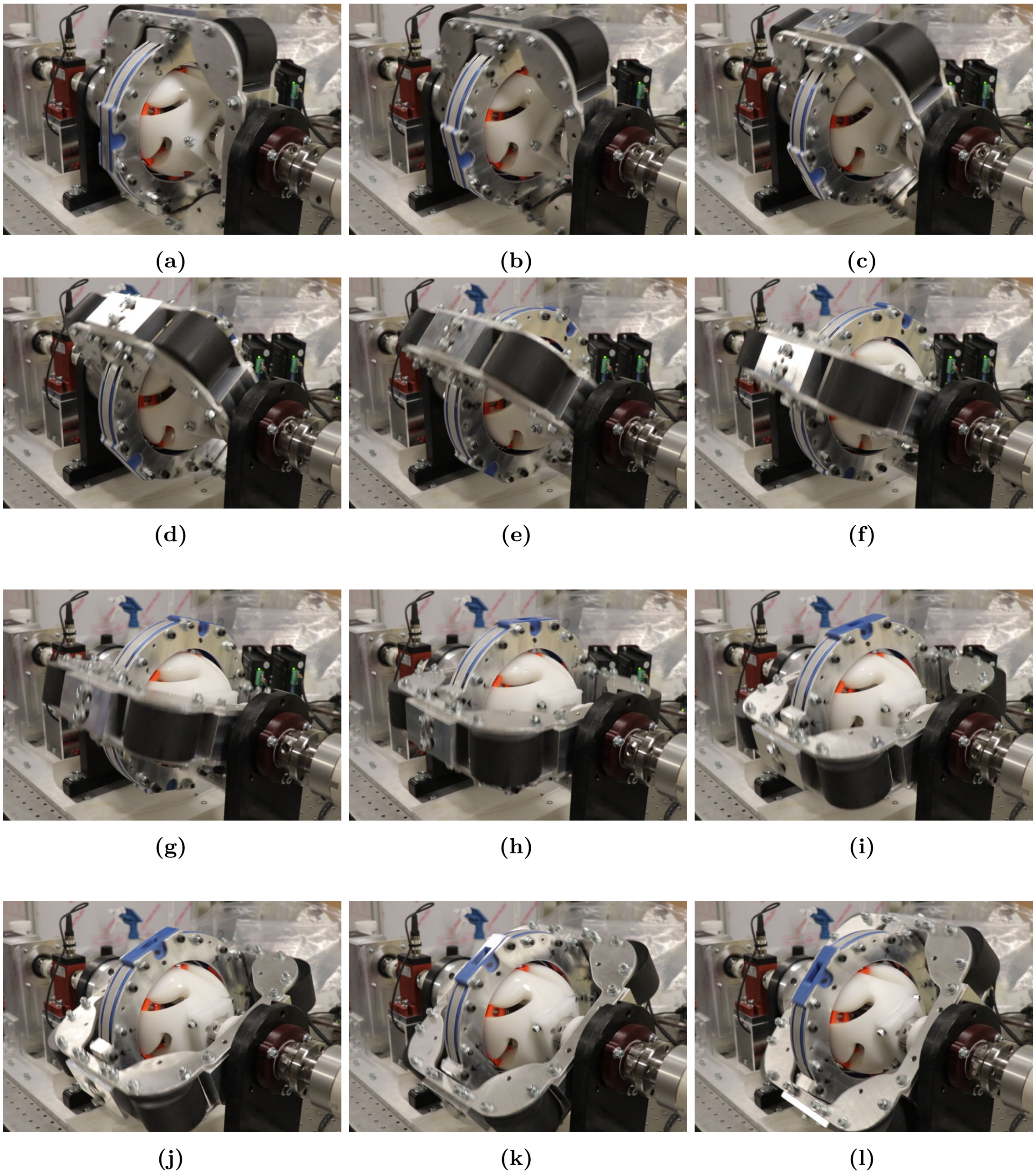

Figure 5-10 – Example IHC Motion Sequence #2. These photographs show IHC motion where both the Orbit and Planet subassemblies rotate in the same direction, but at different rates. The Orbit subassembly rotates much more quickly than the Planet. The Planet motion is subtle, but can be seen by observing the gradual "appearance" of a Planet slot between images 5-10g and 5-10l.

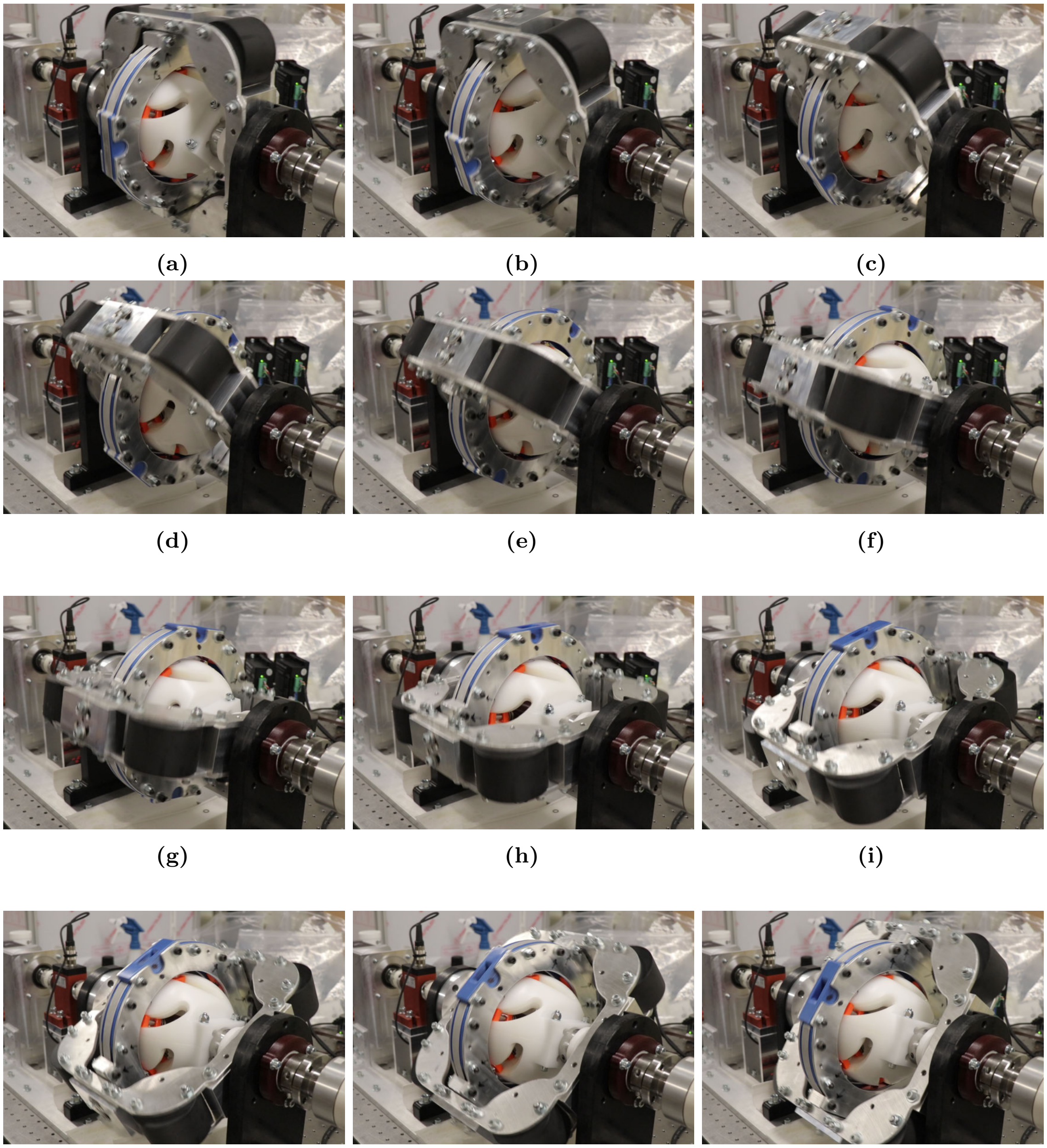

(a) **(b)** **(c)** **(d)** **(e)** **(f)** **(g)** **(h)** **(i)** **(j)** **(k)** **(l)**

Figure 5-11 – Example IHC Motion Sequence #3. These photographs show IHC motion where both the Orbit and Planet subassemblies rotate, but in opposite directions. This sequence demonstrates the wide variety of Planet and Orbit speed combinations that can be queried. As mentioned previously, the *slip rate* is the crucial speed parameter.

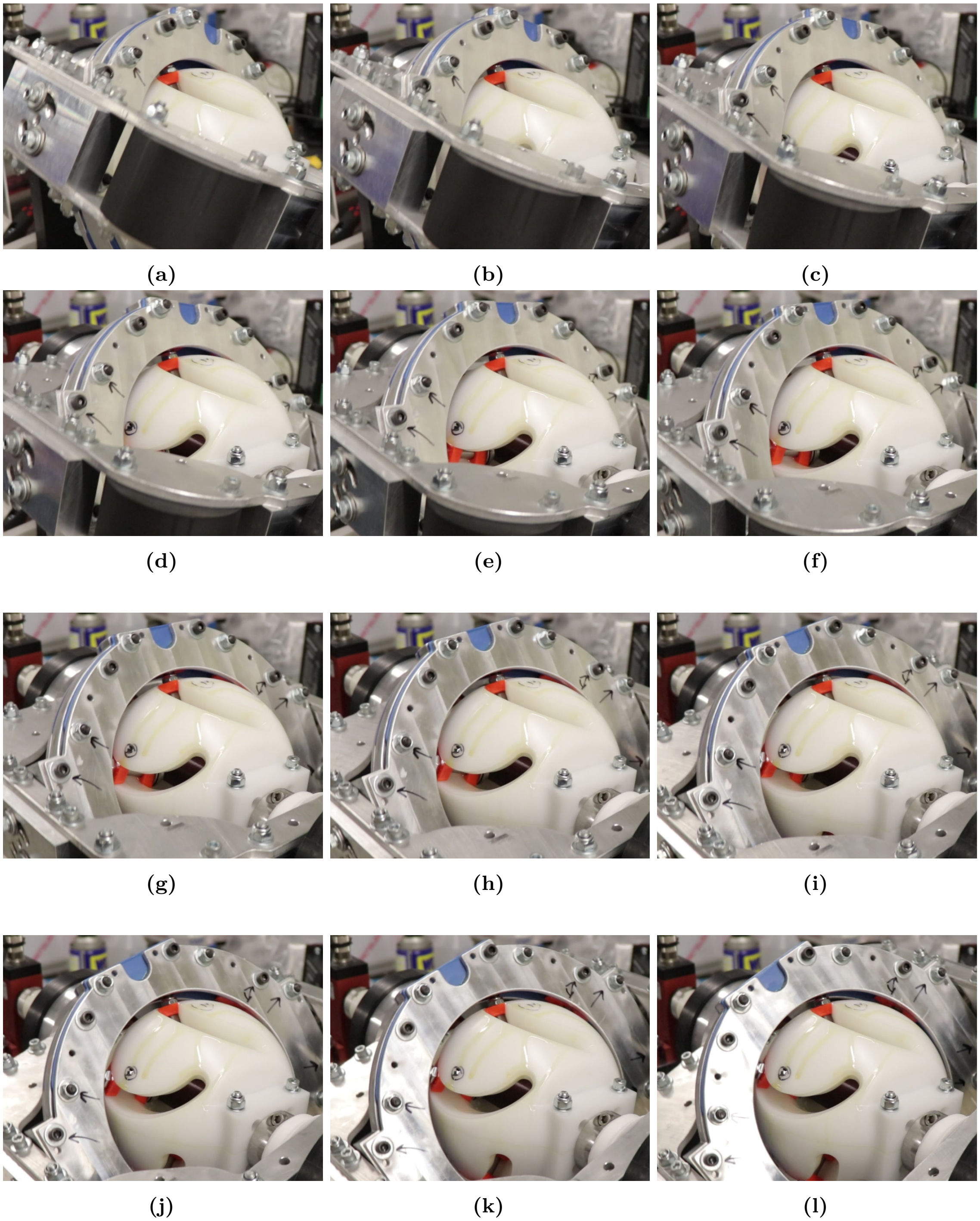

Figure 5-12 – Example IHC Motion Sequence #4. Narrow-angle photographs showing IHC motions at high clutch angle values ($\beta_O = 33°$). In this image sequence, the lower Satellite (first "revealed" in image 5-12e) traverses its Planet slot from right-to-left. At the same time, the Satellite above it reaches the end of its Planet slot and begins to reverse directions.

Figure 5-14). First, the slot cross-section geometry is sketched on the Planet's equatorial plane. The Cut-Revolve axis is then specified. It passes through the centerpoint of the Planet and is inclined from "horizontal" by β_O.

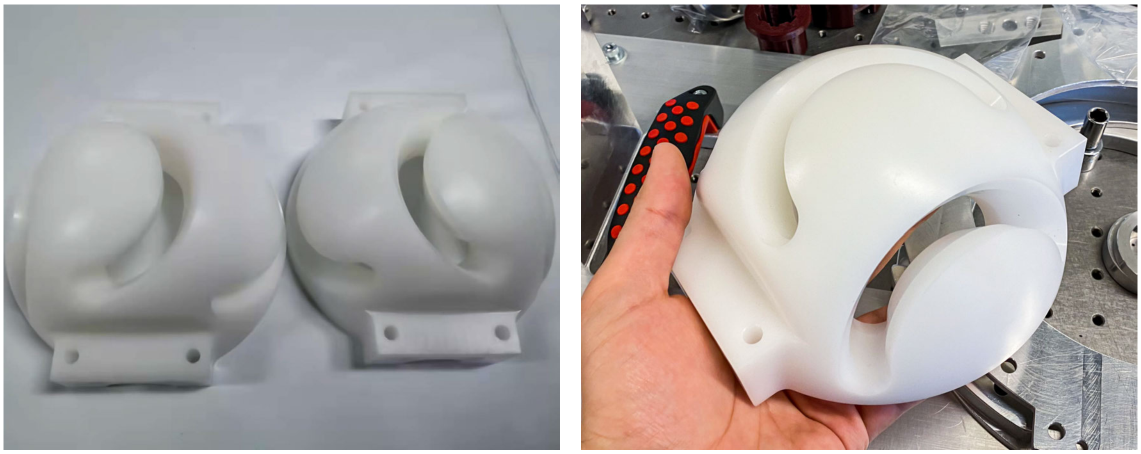

(a) (b)

Figure 5-13 – Photographs of the Planet half-spheres (a) upon completion of machining by the manufacturer, and (b) upon reception at MIT.

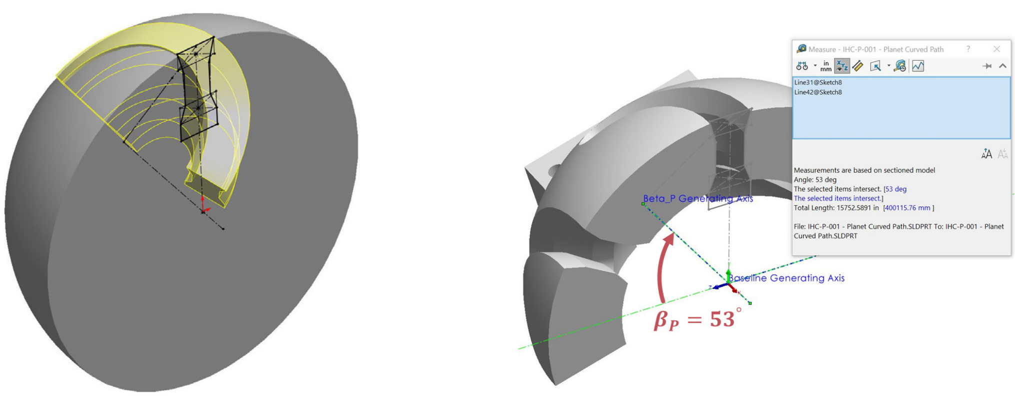

(a) (b)

Figure 5-14 – Screenshots demonstrating the generation of the Planet slot geometry in CAD. The desired slot cross-section shape is first sketched at the center plane, then revolve-cut about an axis inclined by β_P (this axis intercepts the Planet origin).

5.3.2 Planet Material Selection

From discussions with SuNPe (who machined the Planet parts), six materials were considered:[1]

- A3 Tool Steel

[1] Both practical factors (lead time and stock material availability) and material properties (stiffness, strength, lubricity, and wear/abrasion resistance) were considered.

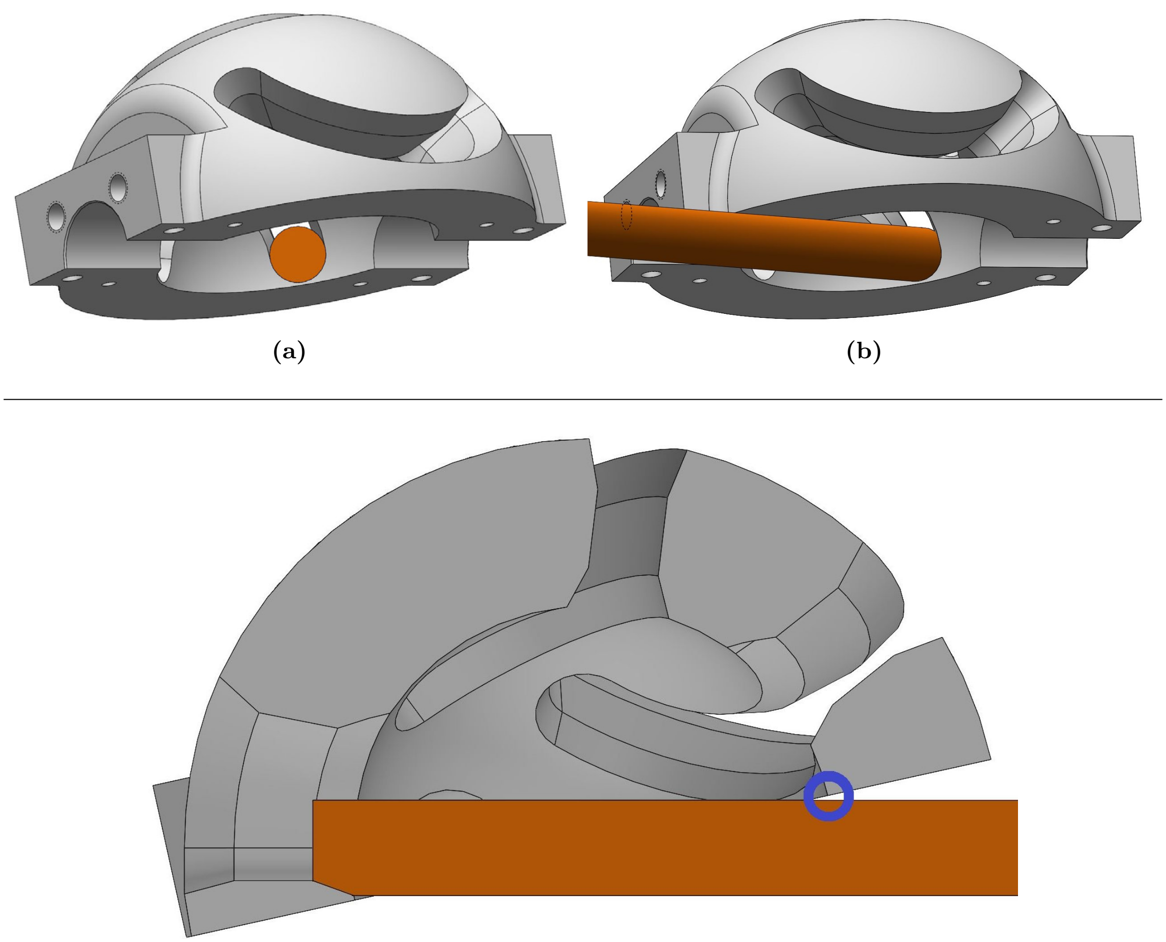

(a) (b) (c)

Figure 5-15 – Screenshot to help visualize the difficulty in machining the inner tapers of the Planet slots. The cylinders shown in orange represent the axis of the cutting tool, with a diameter equal to the slot width at its outermost point. The blue circle highlights the tight clearances involved with successfully machining this taper.

- M303E High-Chromium Steel (Corrosion-resistant but not stainless)
- POM (Polyoxymethylene[1])
- PBT (Polybutylene Terephthalate)
- PA6 Nylon (Polyamide)
- PA66 Nylon (Polyamide)

Of these, POM was chosen. The A3 and M303E steels were rejected on the basis of price, costing more than twice as much as the plastics. Plastic greatly mitigated the risk associated with unexpected Planet damage or an unforeseen design mistake as a replacement could be obtained at much lower cost (this was, thankfully, not necessary). Of the four plastics, POM was chosen for its combination of desirable properties: its excellent lubricity (low coefficient of friction), excellent wear and abrasion resistance, non-hygroscopic nature (aversion to moisture absorption), and excellent chemical resistance (compatibility with a wide range of lubricants and cleaning products).

It should be emphasized that the dissipation of waste heat is expected to be a major consideration in future IHC generations. The thermal properties of the Planet, Orbit, and Satellite are likely to take high priority in the material selection process. However, this was not necessary for ihcBENCH as the relative thermal loads are small ($\sim 10W$).

5.3.3 Planet Spacers & Splined Coupling

The hole pattern on the "LEFT" Planet hub mates to a splined flange coupling,[2] which in turn drives a 25mm six-groove splined shaft.[3] This connects the Planet with its driveshaft. The coupling-shaft connection can sustain 200+ Nm of torque – well in excess of the 50 Nm requirement[4] and leaving ample headroom for use in a future 2nd-generation prototype. Unlike a set screw or machine key, the six splines transfer load in a radially-symmetric fashion, greatly reducing the risk of unexpected damage to the Planet in the event of shock loading. Steel threaded inserts[5] were used for the four threaded holes comprising the Planet-coupling connection. This allowed much larger M10x1.5 threads to be tapped into the (plastic) Planet parts to reduce the likelihood of accidental thread damage during assembly or operation. The Planet-coupling connection is made using four M6x1.0 fasteners. The Planet-driveshaft connection and its components can be seen in Figure 5-16.

A red 3D printed splined spacer[6] can be seen in Figure 5-16. This spacer is used for radial support between the Planet and its driveshaft. Being 3D printed, the spacer easily accomplishes interfacing with

[1] Also known as acetal or polyacetal and often referred to by the trade name "Delrin." Delrin is a registered trademark of DuPont de Nemours, Inc.
[2] A2Z Metric P/N SFH21-ST
[3] A2Z Metric P/N S21-ST
[4] This particular shaft/coupling pair were used to lay out the initial prototype geometry before Functional Requirements were finalized. Smaller shafts did not offer significant cost savings so these parts were ultimately not changed.
[5] E-Z LOK P/N 450-6. The original threadlocker was stripped from the inserts as it is not plastic-compatible. Vibra-Tite VC-3 threadmate was used instead.
[6] Printed in carbon-fiber infused PETG (PETG-CF) from Atomic Filament (https://atomicfilament.com/)

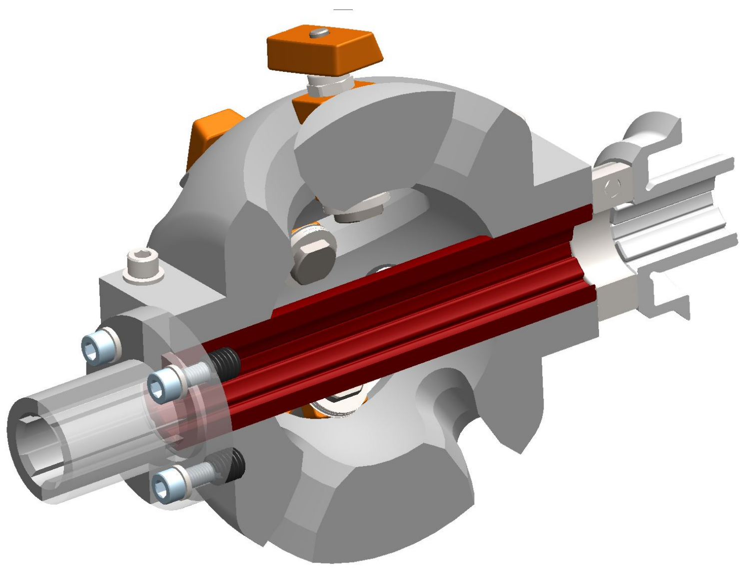

Figure 5-16 – Hybrid cutaway screenshot of the Planet subassembly. Visible in this screenshot are the inner Planet splined spacer (red), the splined coupling and associated fasteners (at left), and a custom 3D-printed splined plain bearing (at right). The splined bearing was printed using IGUS iglide I150-PF tribo-filament.

the six grooves of the splined shaft. The spacer's geometry can be fine-tuned to achieve the desired Planet/driveshaft fits. Additionally, the radial faces of the Planet-spacer interface can be shimmed if needed to correct for any unexpected Planet rotational eccentricity.

5.4 IHC Satellite Design

As the components responsible for actually transmitting torque from input to output, the Satellites (pictured in Figure 5-17) must be granted their fair share of design attention. The most difficult aspect of Satellite design is working within the very limited packaging envelope available. Each Satellite must not only support its blocks during operation, but must also supply two independent preload forces (to the Orbit and outer Planet blocks), be easily adjustable, and be easily manufactured & assembled.

5.4.1 Satellite Components

At the core of each Satellite is a stepped shaft machined from AISI 303 stainless steel. The shaft base is a wide flange on which sits a wave spring, a stack of shims, and the inner Planet block. The bottoming force of this spring determines the preload force applied to the lower Planet block. The shims allow adjustment of the shaft position so the protrusion of its shoulder and thread can be fine-tuned. At the end of the lower shoulder section sits the outer Planet block, which must engage with the shoulder to support the lateral loads endured in operation. Directly backing the outer Planet block is a low-profile nylon-insert

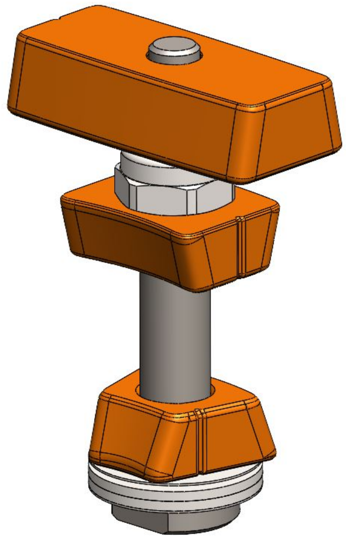

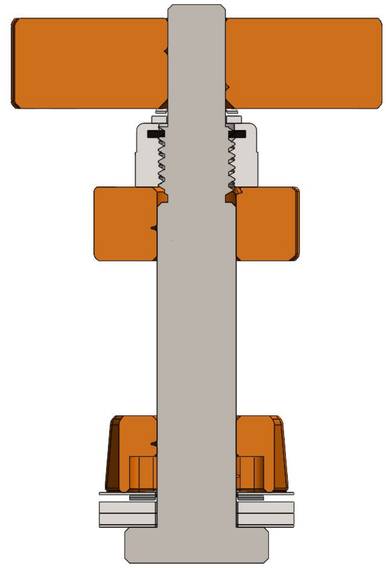

(a) (b)

Figure 5-17 – Isometric and cutaway views of the ihcBENCH Satellite design in CAD. Two shim-and-spring stacks are used to tune the Satellite preloads – one at the base of the Satellite shaft and the other directly beneath the Orbit block (near the top).

locknut which is tightened onto a short section of M8x1.25mm thread. Directly above the locknut is a second spring and stack of shims. The spring provides the Orbit block preload force, but this is sensitive to the relative position of the locknut and the Orbit block. Since the Orbit block will follow the Orbit track, its exact position is subject to various associated geometric and fitment errors. The second shim stack is included for this reason – it allows the spring position to be adjusted to compensate for these positional errors.

The combination of Satellite contact angles $\lambda_{P1} = -20°, \lambda_{P2} = +15°$, and $\lambda_O = -12°$ were chosen for several reasons:

- The pseudo-kinematic constraint layout described in Chapter 4 is satisfied.
- The results of ihcMATLAB calculations, which suggested successful testing outcomes with reasonable margins-of-error.
- The Planet and Orbit preloads are both reacted by the rigidly-mounted outer Planet block. Therefore they do not affect one another and can be set/adjusted independently.
- The "back-to-back" mounting of the Planet blocks increases their effective center distance to enhance moment stiffness.
- All contact angles are comfortably large enough to prevent wedging/seizing of any Planet

block within its track.[1]

- Negative λ_{P1} firmly retains the Satellite shaft so neither cannot be easily ejected outwards in the event of a catastrophic failure at high speed.
- Negative λ_O firmly retains the Orbit block so it cannot be easily ejected in the event of a catastrophic failure at high speed. Likewise, the outer Orbit block cannot be easily ejected as it would need to travel through the Orbit block.

Initially, the Satellite blocks were planned to be CNC machined from 954 aluminum-bronze. However, 3D printed PETG[2] mockup blocks were tested first – the results proved very favorable and the extra design flexibility of 3D printing was much appreciated, so these were retained for this generation of ihcBENCH. For example, complete sets of Satellite blocks could be printed with the inner diameter dimensions gradually stepping up in increments of 0.001". This allowed each Satellite shaft to be hand-matched with the best-fitting blocks.

Photographs of example 3D printed satellite blocks are shown in Figure 5-18. The 3D printer used is the author's own proprietary design.

5.4.2 Satellite Block Lubrication

To achieve sufficiently low sliding coefficients of friction it is absolutely crucial to lubricate the Planet/Satellite/Orbit contact surfaces. Mobil Vactra #4, applied manually via syringe, was used for this purpose. Mobil Vactra is a slideway oil, expressly designed to lubricate sliding bearing surfaces and to maintain consistent frictional properties (*i.e.* seeking to minimize stick-slip, chatter, and variation in the effective coefficient-of-friction). The #4 variant is the thickest option (grade ISO 220) in the Vactra product family. It is well-suited for use on vertical and inclined surfaces where thinner oils tend to drain away. As an anecdotal observation, the lubricant drastically reduced the friction in the system compared to the unlubricated state when moving the system by hand – the perceived resistance dropped by well over 50%.

5.5 IHC Orbit Design

The ihcBENCH Orbit is comprised of the two subassemblies seen in Figure 5-19: the Orbit ring itself and an outer frame in which the Orbit ring is mounted. Both subassemblies use "sandwich" construction to reduce costs and manufacturing complexity. Aluminum 6061-T6 plates, cut using a waterjet, serve as the outer plates.

[1] A friction coefficient of 0.20 corresponds to a critical friction angle of $\sim 11.3°$. 0.20 is substantially above both the expected, and observed, values for operational lubricated friction coefficients.
[2] PETG from Atomic Filament (https://atomicfilament.com/)

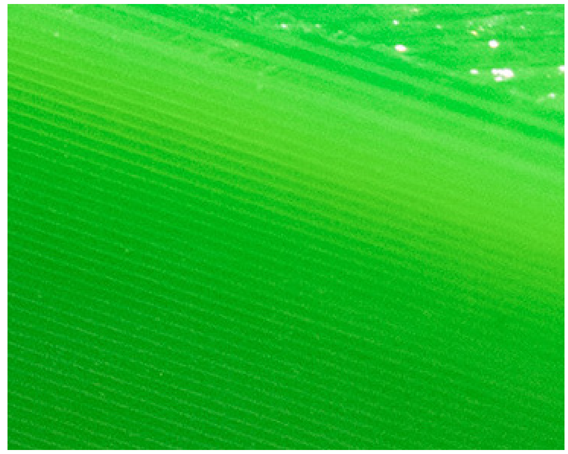

(a) **(b)**

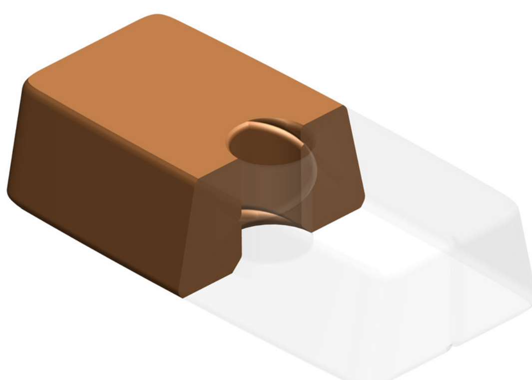

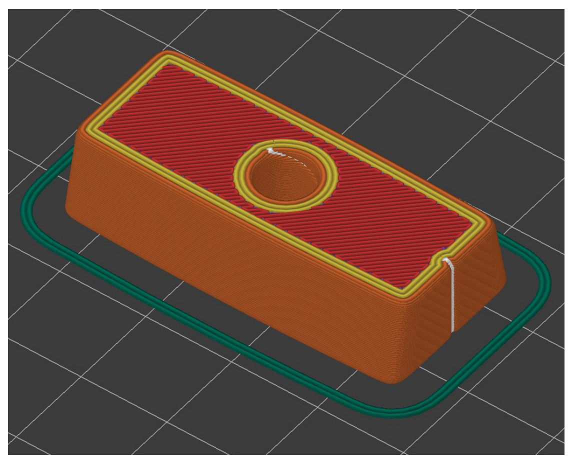

(c) **(d)**

Figure 5-18 – Photographs and screenshots of 3D printed Satellite blocks. The first two images demonstrate the surface finishes achieved. In the last two images, a helix can be seen wrapping around the central hole. The layer seam (from 3D printing) was recessed into this helix to avoid interfering with the shaft fit. The helix itself (vs a vertical seam recess) ensures the shaft/block interface is adequately supported from all sides.

Beneath the Orbit ring's outer plates are a set of 3D printed Orbit tracks.[1] Like the Satellites, the 3D printed Orbit tracks proved successful in testing and so were never replaced (the alternative was to CNC-machine the tracks from a lubricant-impregnated nylon 6/6; this was ultimately unnecessary). 3D printing also allowed various other small features to be easily incorporated, such as regularly-spaced pockets in the tracks for retaining lubricant.

A key feature of the Orbit ring design is the removable track section shown in Figure 5-20. This block provides much-needed access to the Satellites: the low-profile nuts can be adjusted, shim stacks modified, preload springs exchanged, and Orbit blocks installed/removed. When this section of track is replaced, care must be taken to ensure its track surfaces are set flush with the others.

The Orbit ring and its outer frame connect via swivel blocks at their tops and bottoms. This degree-of-freedom – modulation of the IHC clutch angle β_O – is provided by a pair of 3/8" diameter dowel pins. Four screws (two per side) allow the clutch angle to be locked in place for testing under load. β_O is measured manually using a handheld digital protractor. The protractor is laid against the aluminum plates of the Orbit ring and the outer frame and the angle reading recorded. This is repeated at each corner on both the front and back of the Orbit assembly, giving eight total measurements. For a manual process, this yields acceptably repeatable measurements. For any single measurement, repeatability is better than $\pm 0.6°$.

Torque to/from the Orbit ring is transmitted via a custom output shaft, shown in Figure 5-19b.

5.6 Other Mechanical Design Details

ihcBENCH is intended to characterize couplings by subjecting them to predetermined input/output speed combinations and measuring the resulting torque developed. This is fundamentally a "position-input, torque-output" process and the actuation scheme must reflect this. NEMA 34 stepper motors[2] and 5:1 planetary gearboxes[3] were chosen to drive ihcBENCH (the same motor and gearbox are used on both ends). This combination produces nearly 40 Nm of peak torque (after losses), which falls right in line with the system Functional Requirements. Stepper motors are inexpensive and are inherently position-control devices, making them particularly well-suited for this application. The motors are mounted via their gearboxes using custom brackets machined from 5"-wide aluminum C-channel.

Three Oldham couplings are used in ihcBENCH. These complete the following three connections while accommodating misalignment between the components:

- LEFT Motor/Gearbox ↔[4] Torque Sensor

[1] PETG from Atomic Filament (https://atomicfilament.com/)
[2] StepperOnline P/N 34HS46-6004S1
[3] StepperOnline P/N EG34-G5 (formerly, P/N PLE34-G5)
[4] Coupling: MISUMI P/N MOR-38C-17-BT-20-BT

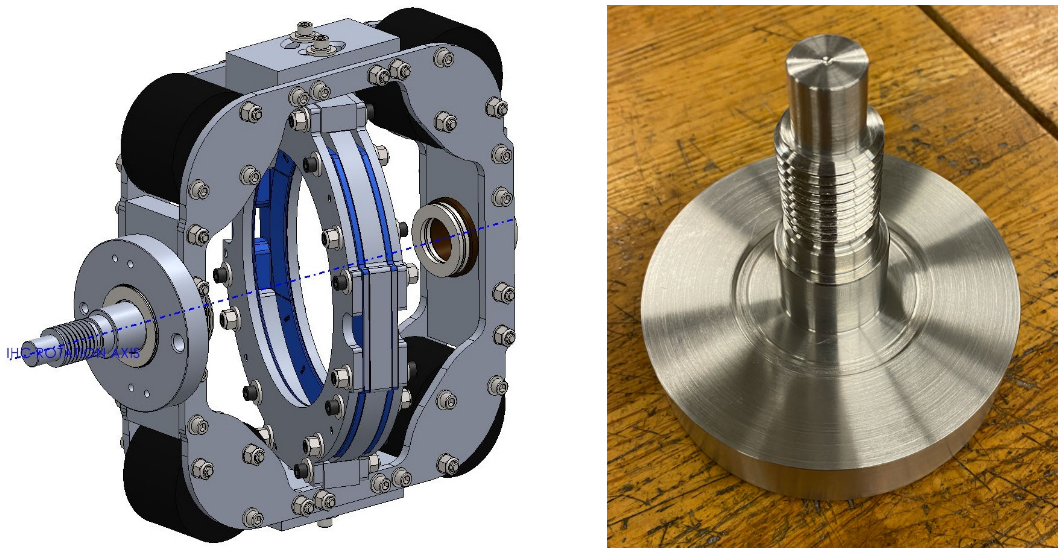

(a) (b)

Figure 5-19 – 5-19a: Screenshot of the Orbit frame subassembly with rotation axis shown.
5-19b: Photograph of the Orbit frame's custom output shaft component, partway through fabrication. This component passes torque along torque from Orbit frame; it is the component that mates to the torque sensor.

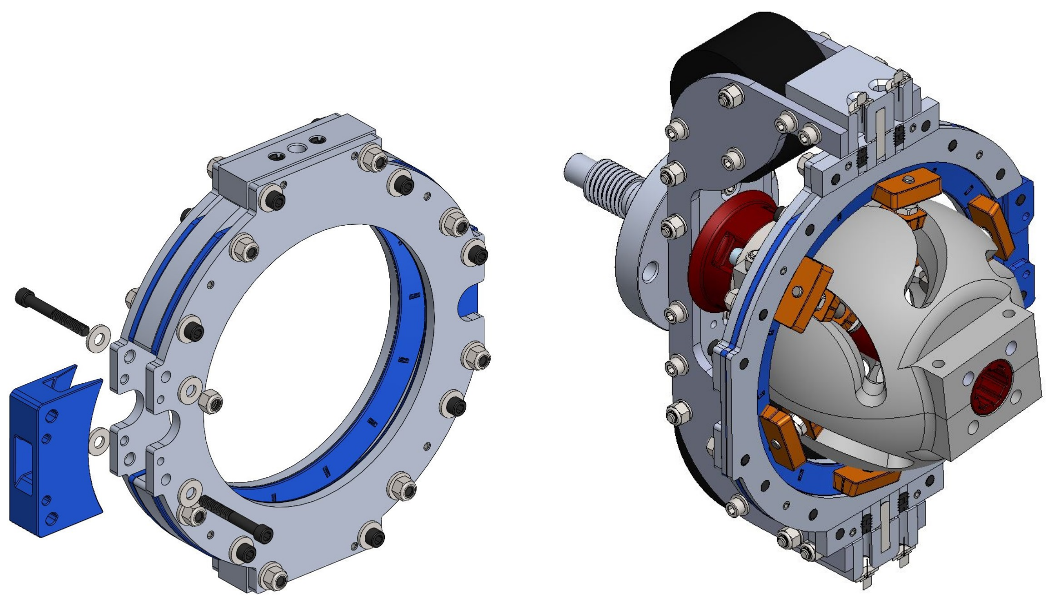

(a) (b)

Figure 5-20 – CAD screenshots of (a) the removable Orbit track section, and (b) a cutaway view of the Satellites traveling along the Orbit track.

- Torque Sensor ↔[1] IHC
- IHC ↔[2] RIGHT Motor/Gearbox

5.7 Firmware and Control Interface

In terms of software, ihcBENCH runs on a heavily-customized configuration of Klipper [40]. Klipper is a popular open-source 3D printer firmware with a particular focus on motion accuracy and precise I/O timing. The related open-source project "Mainsail" serves as the graphical user interface (GUI) [41]. The GUI is hosted as a webpage on a local network and is accessed via browser on a laptop or mobile device. Klipper/Mainsail were selected for their established track record of motion reliability, their compatibility with inexpensive hardware, and the author's personal familiarity from prior unrelated projects.

The Klipper and Mainsail configurations were heavily customized for this application. A screenshot of the Mainsail GUI can be seen in Figure 5-21 and the Klipper configuration file can be found in Appendix A.

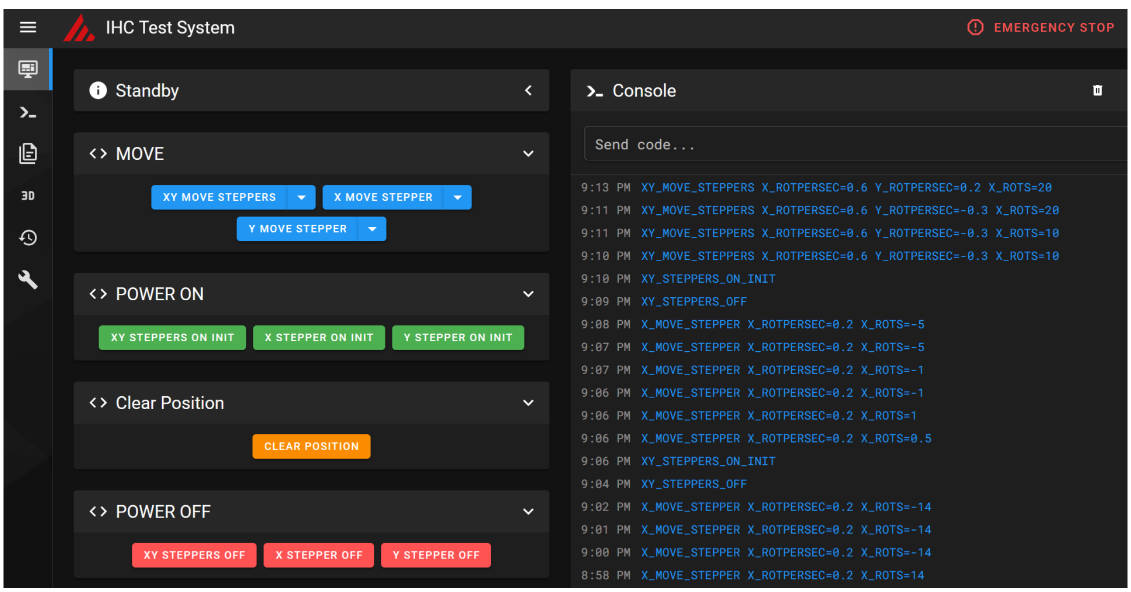

Figure 5-21 – Screenshot of the Mainsail interface for controlling the test system. This interface makes it easy to execute custom G-Code macros for testing, to monitor machine status, and to issue manual G-Code commands via the console.

[1] Coupling: MISUMI P/N MOR-38C-17-BT-17-BT
[2] Coupling: MISUMI P/N MOR-68C-20-34-BT

5.8 Electronics

5.8.1 ihcBENCH Control

The Klipper firmware was configured to use two pieces of equipment for stepper motor control. A "parent" motion processor[1] calculates motion commands based on supplied G-Codes. Then, a "child" microcontroller[2] executes these commands as precisely-timed I/O events[3]. A screw-terminal "shield" module is installed on the Arduino Mega to facilitate simple and clean wiring. All electrical connections are shielded and are terminated with crimped ferrules.

Driving each stepper motor is a dedicated stepper driver.[4] This driver is rated for up to 7.2A output, meaning the motors (rated for 6.0A) can be fully harnessed. The microstepping multiplier on each driver can be adjusted. Increasing this multiplier improves positional resolution and smoothness of motion, but requires a faster step-rate to maintain the same rotation speed. ihcBENCH is I/O-limited by the Arduino Mega 2560 – a safe max stepping rate (controlling two motors at once) was found to be approximately 20,000 steps/sec. Given this, a 16x microstepping multiplier was chosen. With the motors' 200 steps/rev and the 5:1 gearboxes, this corresponds to a motion resolution of 16000 steps per revolution ($\sim$80 arcsec per step) and a peak no-load speed of approximately 1.25 rev/s (75 rpm).

5.8.2 Datalogging

FUTEK's "SENSIT" software was used to log measurements from each test. This software interfaces with the FUTEK IHH500 unit via USB and allows test data to be exported in various formats.

[1] Raspberry Pi 4B (4GB)
[2] Arduino Mega 2560 Rev3
[3] Step events are scheduled and executed with a precision of 25 μs or better [42].
[4] StepperOnline P/N DM860T v3.0

THIS PAGE INTENTIONALLY LEFT BLANK

Chapter 6

Key Test Results

Discussion in this chapter will focus first on the standard testing methodology and the most important results – specifically, the demonstration of IHC torque modulation and coupling lockup. Some one-way / overrunning behavior is also demonstrated.

6.1 ihcBENCH Testing Methodology

A consistent procedure was followed when collecting ihcBENCH test data. The following parameters were used unless specified otherwise in a particular test:

- The "LEFT" motor drives the system, while the "RIGHT" motor holds position (behaving as a non-moving load)
- Each trial run consisted of 60 seconds of data collection
- Earlier torque data was collected at 5 Hz; later data was sampled at 100 Hz[1]
- Trials were nominally conducted at 12 RPM (0.2 rev/sec)
- Steady-state readings were extracted from the middle of each test to avoid start-up transients
- Trials were repeated three times to confirm run-to-run consistency

An example 60-second data collection run can be seen in Figure 6-1.

[1] After software and settings updates.

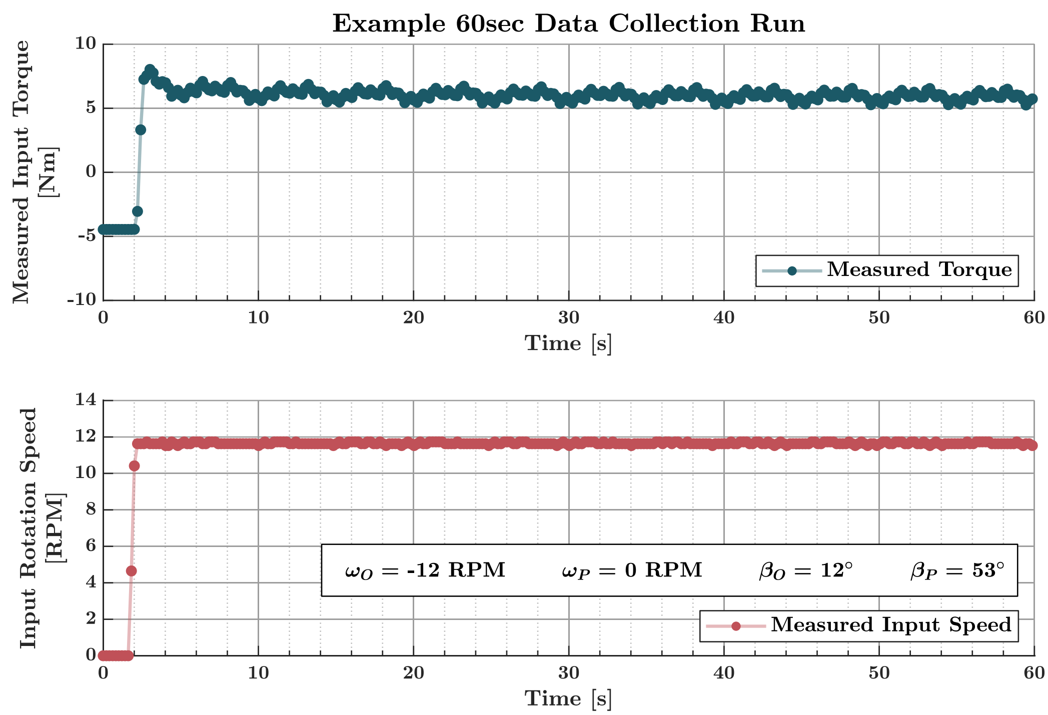

Figure 6-1 – Example data collected over a full 60 second test. Before each test begins, the stepper motors are already energized and holding position. This, plus some compliance in the driveline, leads to a non-zero "pre-test" torque. Approximately 2s into data collection the motors begin driving the system and torque/speed quickly stabilize. Some torque ripple is observed across the duration of the test.

6.2 β_O vs Torque, Characteristic Maps, & Lockup

6.2.1 Performance with Varying β_O

The effect of β_O-modulation on torque transmission was measured in tests corresponding to the data in Figures 6-2 and 6-3 (one plot contains raw data, while the other applies a 1-second moving-average). In both figures it is immediately apparent that the clutch angle β_O can be used to control torque transmission through the IHC. As expected, higher clutch engagement angles β_O correspond to increases in transmitted torque. The behavior is also quite linear, and essentially the entire β_O stroke can used. Aside from crossing the lockup threshold, there are no regions that are particularly sensitive or insensitive to β_O. For reference, bearing drag was measured by fully locking the IHC clutch angle (β_O) and removing the RIGHT motor's Oldham coupling. In this configuration, bearing drag is the only torque opposing the motion induced by the LEFT motor.

The effectiveness of β_O for modulating torque transmission is a crucial result as it demonstrates the IHC's capacity to behave as a variable-slip coupling. Verifying this behavior was a key goal of this project.

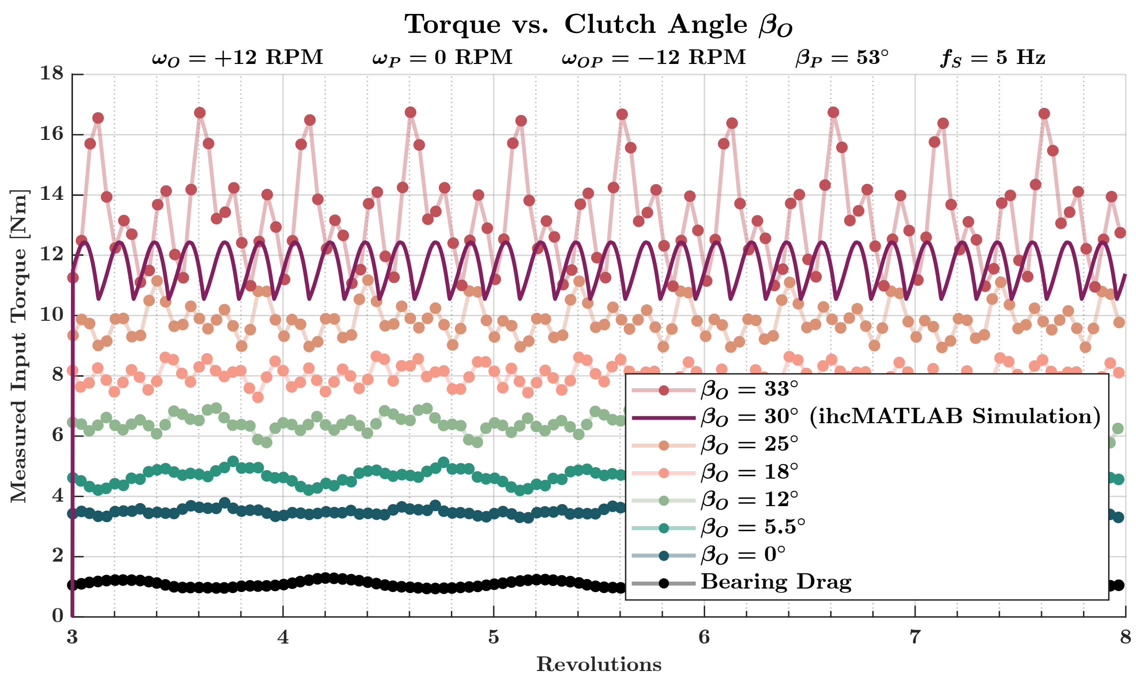

Figure 6-2 – Torque-vs-time data from ihcBENCH at a variety of β_O settings, plus ihcMATLAB simulation results at $\beta_O = 30°$.

One ihcMATLAB simulation result ($\beta_O = 30°$) is plotted alongside the ihcBENCH measurements in Figures 6-2 and 6-3. The simulated performance falls right where it would be expected – directly between the ihcBENCH test results for $\beta_O = 25°$ and $\beta_O = 33°$. The modeled performance and measured results

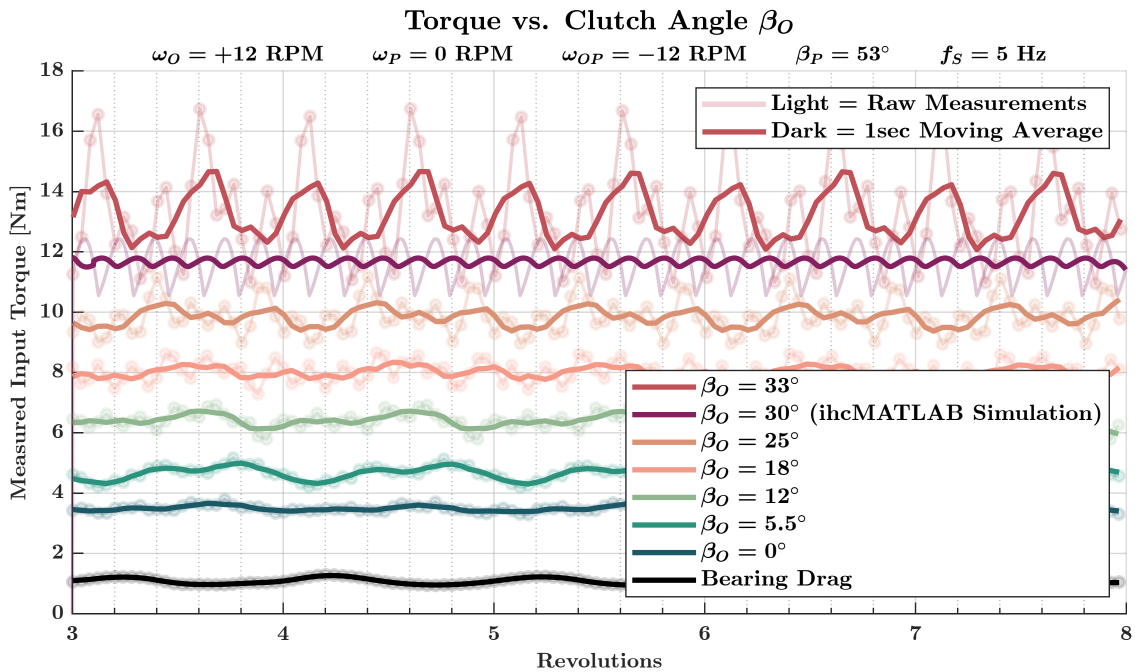

Figure 6-3 – Torque-vs-time data from ihcBENCH and ihcMATLAB, with a 1-second moving average applied to more clearly see the average behavior.

agree very closely, particularly for a first exploration into this device.

Also visible in these tests is torque ripple, the magnitude of which increases alongside the clutch angle β_O. This torque ripple is actually an expected result and is predicted by the ihcMATLAB simulation. While optimizing the IHC design for torque ripple was not a design priority (it is a task left for future work), once again the model and test data exhibit remarkably close agreement. Regardless, additional testing at higher sampling rates was performed to further investigate this phenomenon. Figure 6-4 shows data collected using a 100 Hz sampling frequency, a slower rotation speed (6 RPM), and a high clutch angle ($\beta_O = 26.9°$). Two dominant periodic behaviors are seen:

- Torque fluctuates with every 1/6 slip-rotation, *i.e.* at 6x the slip rate. This frequency is in direct agreement with the simulated behavior in Figures 6-2 and 6-3 and corresponds to variations in the torque delivered by the six Satellites traversing the Orbit ring.
- Twice per slip rotation (or, after every third gray line) the total coupling torque briefly peaks.

Recall the friction coefficient sensitivity analysis in Chapter 4 – specifically, the fact that an IHC's point-of-transition into lockup is sensitive to (a) higher-than-expected coefficients of friction and (b) variations in the Orbit contact radius ρ_O. Both of these can vary in practice – the friction conditions are uncertain, and the actual pressure distribution on the Orbit block can shift the apparent ρ_O location. Consider that, as β_O approaches the lockup threshold, individual Satellites would likely not perform identically and some would begin to lock up earlier than others. Also consider that each Satellite should experience two instances of peak loading in each slip-rotation – one for each time it reverses direction within its Planet slot. Given these points, the observed behaviors match what would be expected if one Satellite were locking up early (whether due to manufacturing, assembly, and/or preload variations). That is, the amplitude of torque ripple increases with β_O and notable torque peaks appear twice per slip-rotation.

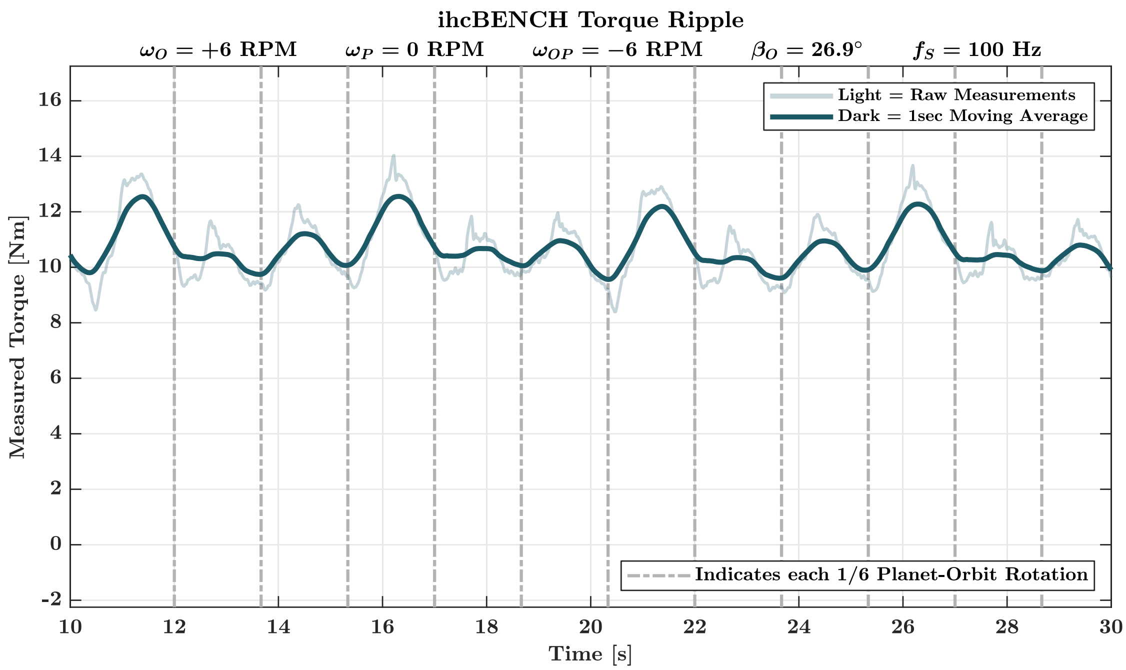

Figure 6-4 – Plot of Observed Torque Ripple on ihcBENCH. As expected from ihcMATLAB, torque fluctuates every 1/6 slip-rotation in correspondence with the number of Satellites in the system. Additional peaking is observed every 1/2 rotation, suggesting one Satellite is beginning to lock up earlier than the others.

6.2.2 ihcBENCH Characteristic Map

The time-averaged data from these runs was then collected together to produce the ihcBENCH characteristic maps. Two versions are shown in Figures 6-5 and 6-6 – one that includes measurement variation and errorbars, and a second that compares the measured performance against ihcMATLAB predictions. Some tabulated results are also given in Table 6.1.

First, the characteristic maps confirm the linearity of the relationship between β_O and torque transmission. Second, the forecasted performance again agrees closely with the measured results with respect to multiple factors:

- Minimum Torque (at $\beta_O = 0$)
- Threshold angle β_O before transition to lockup

- Trajectory of the β_O/Torque contour across nearly the entire β_O sweep range

Results from three simulations are presented in Figure 6-6. Two of these results assume the Planet/Satellite and Orbit/Satellite friction coefficients are the same, while the third treats them separately. Recall that ihcBENCH's Orbit tracks are 3D printed and its Planet is machined from POM. Given the substantial difference in surface finish of these two processes, it is reasonable to expect the effective coefficients of friction to differ. The Planet's much smoother, machined-POM surface may contribute to a reduced effective friction coefficient via a number of potential mechanisms:

- The Planet's fine surface finish more easily supports a lubrication film without asperities protruding through.
- The Planet has no meaningful surface texture which could interact with the Satellite blocks' 3D printed layer lines. Meanwhile, the Orbit tracks and Satellite blocks were printed in orientations that cause their layer lines to align in operation. This means it is likely their edges can slightly catch on one another.
- The Planet and Satellites use dissimilar materials (POM vs PETG), which generally produces a reduced friction coefficient. Meanwhile, the Orbit and Satellites are both PETG.

Counteracting these mechanisms is the fact that the local Planet/Satellite surface speed is much lower than the Orbit/Satellite surface speed.[1] Despite this, in total, the Planet/Satellite interface is observed to exhibit the lower friction coefficient of the two.

Table 6.1 – By the Numbers:
ihcBENCH β_O vs Torque

Minimum Torque Transmitted: (Time-Avg)	~3.5 Nm
Maximum Torque Transmitted: (Time-Avg)	~13 Nm
Max/Min Torque Ratio:	~3.8
Approximate μ_{PS}: (Planet/Satellite Friction Coefficient)	0.032
Approximate μ_{OS}: (Orbit/Satellite Friction Coefficient)	0.040
Useful Clutch Sweep Angle β_O:	$> 33°$

[1] In general, higher surface speeds contribute to the development of a supportive hydrodynamic lubricant film at the sliding interface.

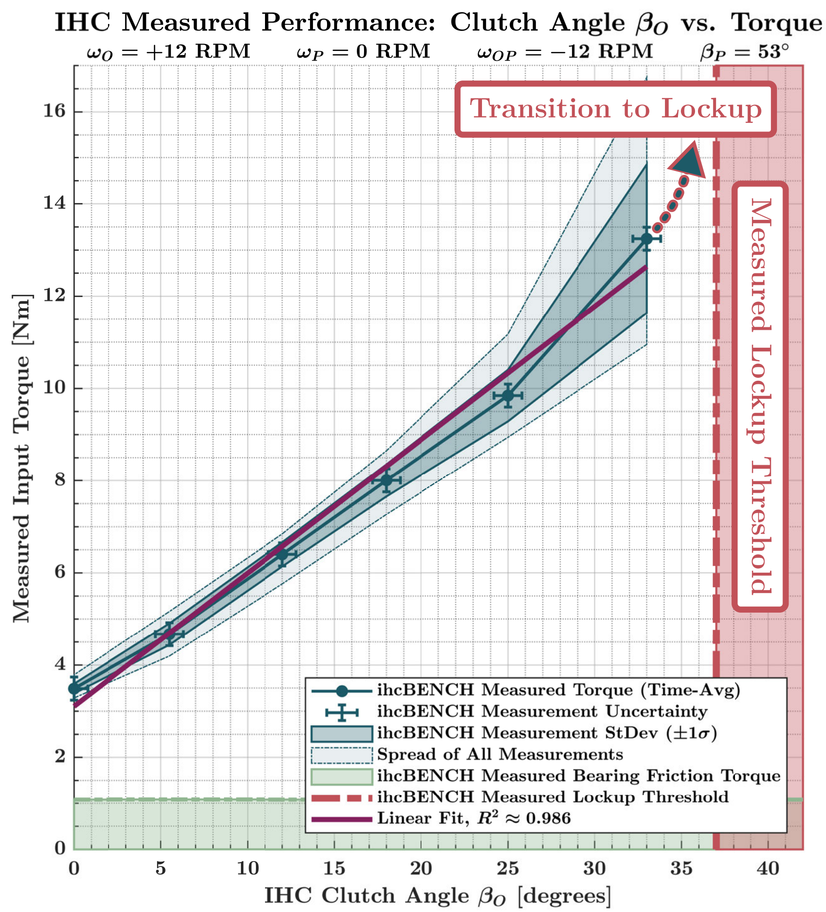

Figure 6-5 – Measured ihcBENCH Characteristic Plot: β_O vs Torque.

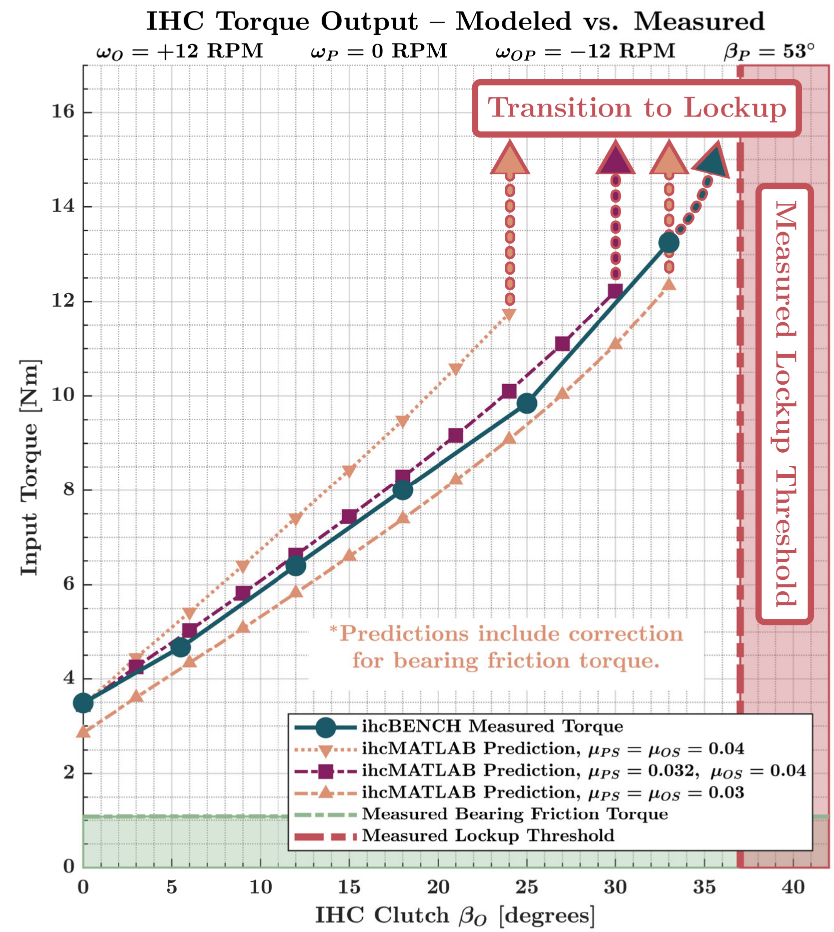

Figure 6-6 – Measured (ihcBENCH) vs Modeled (ihc-MATLAB) Characteristic Plots.

6.2.3 ihcBENCH Lockup

Pushing β_O to its extreme values, a critical threshold is reached at approximately 37°, wherein ihcBENCH enters a "jam" state and repeatedly drives the IHC in a hammering motion. This is the manifestation of IHC lockup, *i.e.* the transition to complete coupling engagement. A sequence of video screenshots showing this behavior can be seen in Figure 6-7.

This behavior is a sort of "soft lockup", where input and output shafts are not strictly positively engaged. The stalling stepper motors repeatedly induce the aforementioned "hammering" (reminiscent of an impact driver). At the same time, the sprung Satellites and tapered contact surfaces mean that, with serendipitous timing, individual Satellites can "sneak past" their jam positions. This allows the mechanism to advance by a fraction of a rotation before jamming again.

ihcBENCH's "soft lockup" – as opposed to strict positive engagement – is not a disappointing result. It was actually an expected outcome, given the sprung Satellites and tapered contact surfaces. This result implies that IHC designers can target different lockup behaviors depending on the intended application. A "soft lockup" design similar to ihcBENCH could, for example, function as a torque limiter. On the other hand, when strict positive engagement is required, it is anticipated that non-sprung, non-kinematic IHCs will prove fruitful. **Regardless, the successful results of lockup testing at $\boldsymbol{\beta_O = 37^\circ}$ represents the fulfillment of a second critical deliverable – demonstrating that IHCs can transition from variable-slip operation into lockup without the need for any separate mechanisms or complications.**

6.3 ihcBENCH Self-Lockup & Self-Centering

This thesis has so far treated the clutch angle β_O as being deterministically controlled. In terms of performing the functions of a variable-slip coupling, this makes good sense. However, the utility of IHCs can potentially be extended by lifting this restriction. One consequence of tilting the Planet track by β_P is that moment loads are developed on the Orbit ring about its clutch axis, *i.e.* in the direction of β_O modulation. If β_O is not firmly set and is instead acted on by compliant elements (springs/dampers), it can potentially deliver its own mechanical feedback control.

While this area has not been substantially explored yet, some early tests were performed using ihcBENCH. The β_O retaining screws were released to permit the Orbit ring to swivel freely on its mounting pins. Then, ihcBENCH could be operated in the usual fashion and the β_O response, if any, observed.

In short, the results demonstrated the capability of an IHC to function as a one-way clutch:

- **$\boldsymbol{\omega_{OP} < 0}$ (Figures 6-8 and 6-9):**

    At negative slip rates ($\omega_P < \omega_O$), β_O is self-stabilizing and will readily return to center

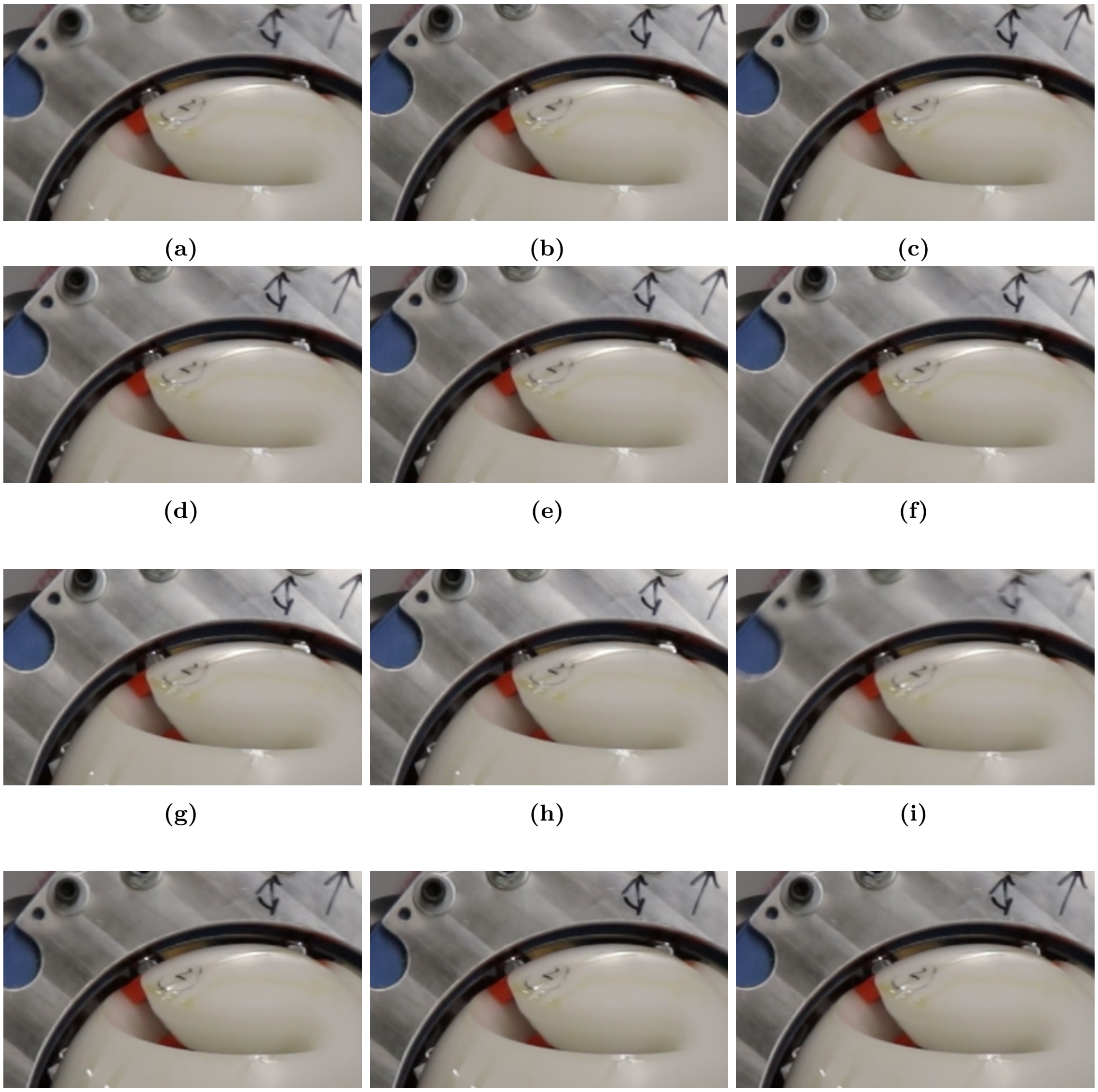

(a) **(b)** **(c)** **(d)** **(e)** **(f)** **(g)** **(h)** **(i)** **(j)** **(k)** **(l)**

Figure 6-7 – A series of screenshots where ihcBENCH "hammers" due to lockup. Though the motions between these screenshots are subtle, the arrow at the top-right of each screenshot helps identify them. It begins just to the left of the screenshot corner, gradually shifts to the right over a number of frames, then snaps back in screenshot (i). This motion corresponds with coupling lockup and "hammering" by the stepper motors.

($\beta_O = 0$). This is true regardless of its initial position – it will readily "unlock" the coupling from even the most tightly jammed scenarios (where IHC lockup has caused β_O to be immovable by hand).

- **$\boldsymbol{\omega_{OP} > 0}$ and $\boldsymbol{\beta_O \lessapprox 15°}$:**

  ihcBENCH unlocks, though not as quickly as in the $\omega_{OP} < 0$ case.
- **$\boldsymbol{\omega_{OP} > 0}$ and $\boldsymbol{\beta_O \gtrapprox 21°}$ (Figures 6-10 and 6-11):**[1]

  At positive slip rates ($\omega_O < \omega_P$) and moderate clutch angles β_O, ihcBENCH is self-locking. β_O will readily diverge to its extreme values, fully engaging and locking up the coupling.

One-way couplings see widespread use throughout industry. Yet, to the author's knowledge, there has previously existed no coupling that singlehandedly achieves all three of the following behaviors:

1. One-way torque transmission
2. Positive engagement when fully locked
3. Speed-synchronization (*i.e.* the ability to engage smoothly and gradually, and to transmit torque under partial slip)

For example, the vast majority of existing one-way couplings (such as sprag clutches and ratcheting couplings) are dual-mode by nature – they are either fully engaged or not at all and speed synchronization must be facilitated externally. While a complete demonstration of true IHC positive engagement must wait for future prototype revisions, the preliminary results provide a strong indication that IHCs may be able to realize all three of the characteristics listed above.

6.4 Varying Planet/Orbit Speed at Constant Slip Rate

The final set of tests discussed in this thesis considers IHC operation at different ω_P/ω_O speeds while keeping the slip rate (ω_{OP}) constant. Two sets of raw and time-averaged results are provided in Figures 6-12 and 6-13.

The results of theses tests are initially quite unexpected – at such low speeds[2] these tests would be expected to give very similar results to one another. Instead, average torque transmission appears to drop as the coupling speeds become more negative.

A deeper look at the results suggests that this behavior is likely attributable to separate effects rather than being an intrinsic IHC behavior. Examination of the torque profiles in Figure 6-13b shows that, for $\omega_O > 0$, the very-long-term average torques differ minimally from one another. Instead, there is an

[1] For $\boldsymbol{\omega_{OP} > 0}$ the transition from self-locking to self-stabilizing has been observed to be between $\boldsymbol{\beta_O}$ values of 15 and 21 degrees, though a distinct threshold has not yet been quantified. Outside of this range the self-locking / self-unlocking behaviors are highly consistent and repeatable.

[2] Where Satellite inertial effects are minimal.

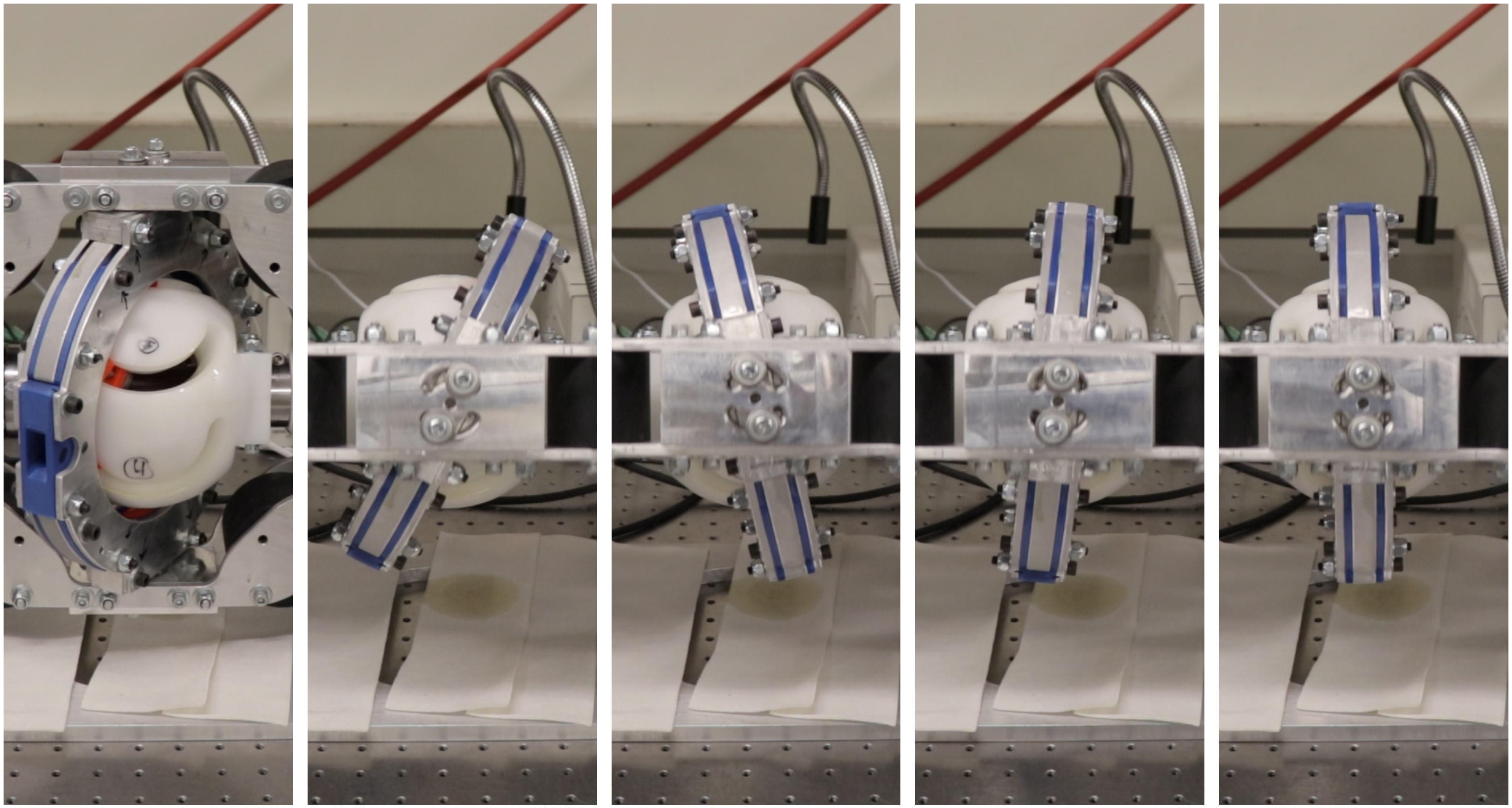

(a) Initial position
(0 Orbit rotations)
($t \lessapprox 6.4s$ in Figure 6-11)

(b) First on-axis snapshot
(+0.15 Orbit rotations)
($t \approx 7.2s$ in Figure 6-11)

(c) Second on-axis snapshot
(+0.65 Orbit rotations)
($t \approx 9.2s$ in Figure 6-11)

(d) Third on-axis snapshot
(+1.15 Orbit rotations)
($t \approx 11.2s$ in Figure 6-11)

(e) Fourth on-axis snapshot
(+1.65 Orbit rotations)
($t \approx 13.2s$ in Figure 6-11)

Figure 6-8 – Sequence of screenshots that show ihcBENCH self-unlocking.

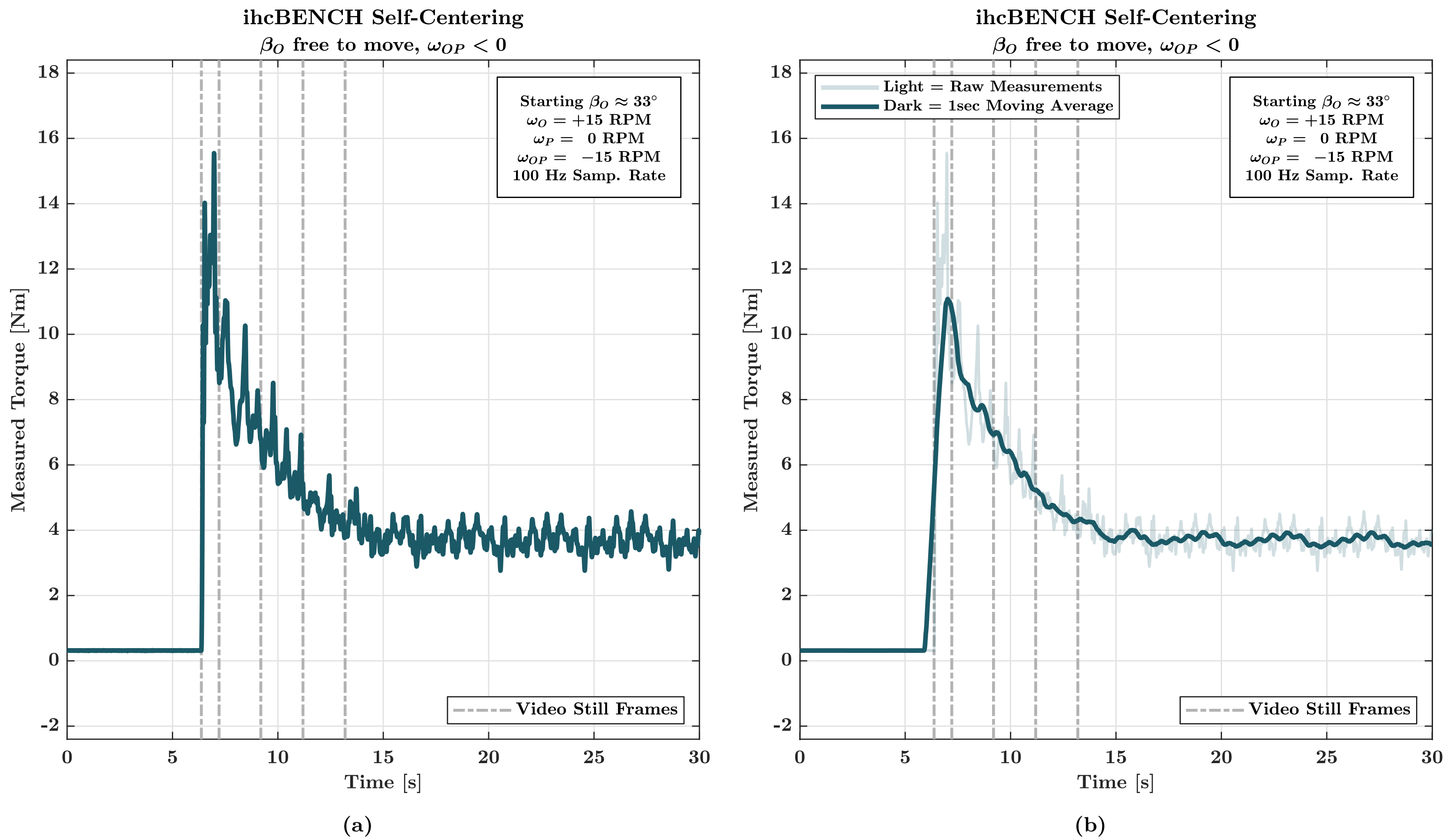

Figure 6-9 – Raw and moving-average torque profiles during an IHC self-unlocking event. The coupling begins the test at a high clutch angle. Once load is applied, the Orbit ring quickly centers itself and the torque transmitted drops off.

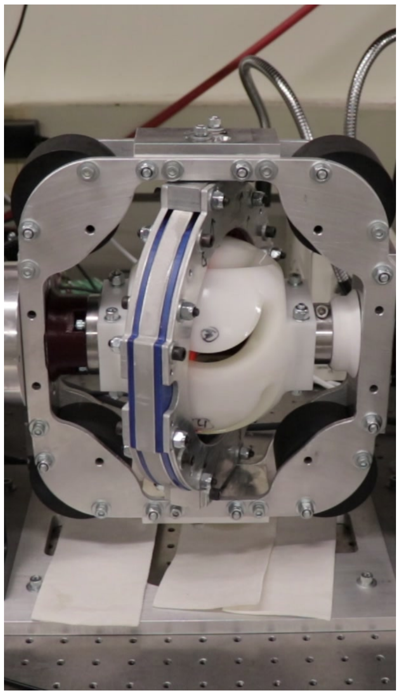

(a) Initial position (0 Orbit rotations) ($t \lessapprox 1.9s$ in Figure 6-11)

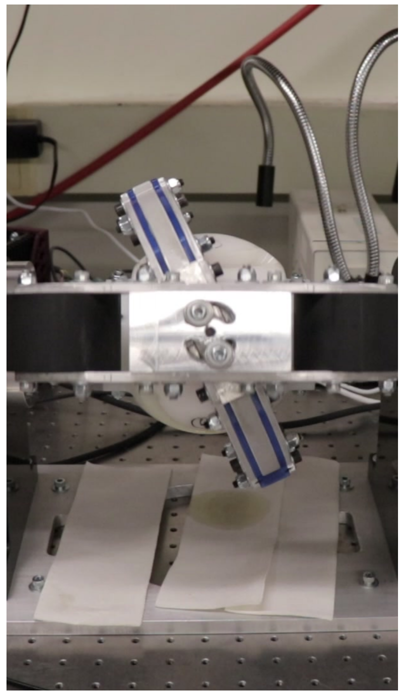

(b) First on-axis snapshot (-0.3 Orbit rotations) ($t \approx 3.0s$ in Figure 6-11)

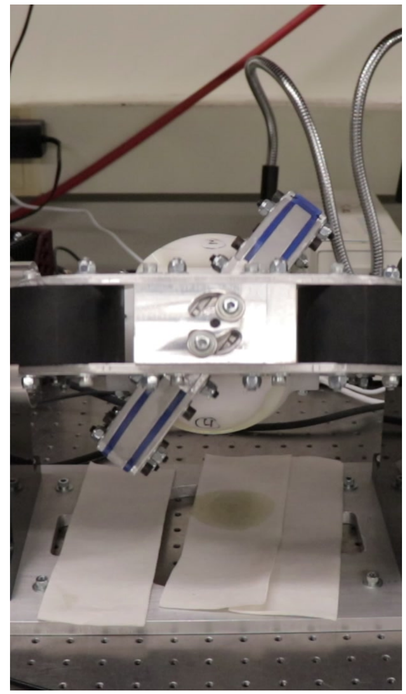

(c) Second on-axis snapshot (-0.8 Orbit rotations) ($t \approx 4.8s$ in Figure 6-11)

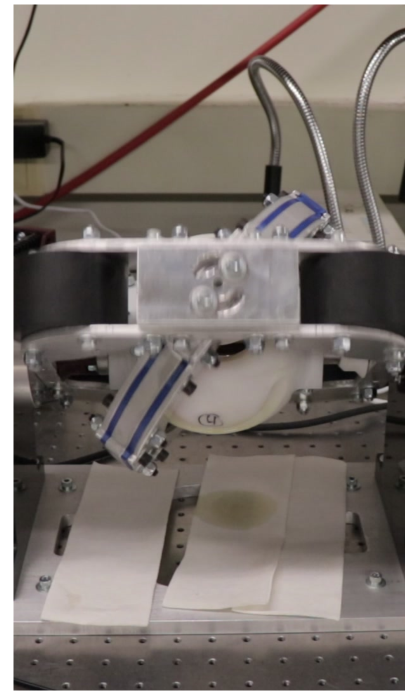

(d) Moment before lockup ($t \approx 4.9s$ in Figure 6-11)

Figure 6-10 – Sequence of screenshots that show ihcBENCH self-locking.

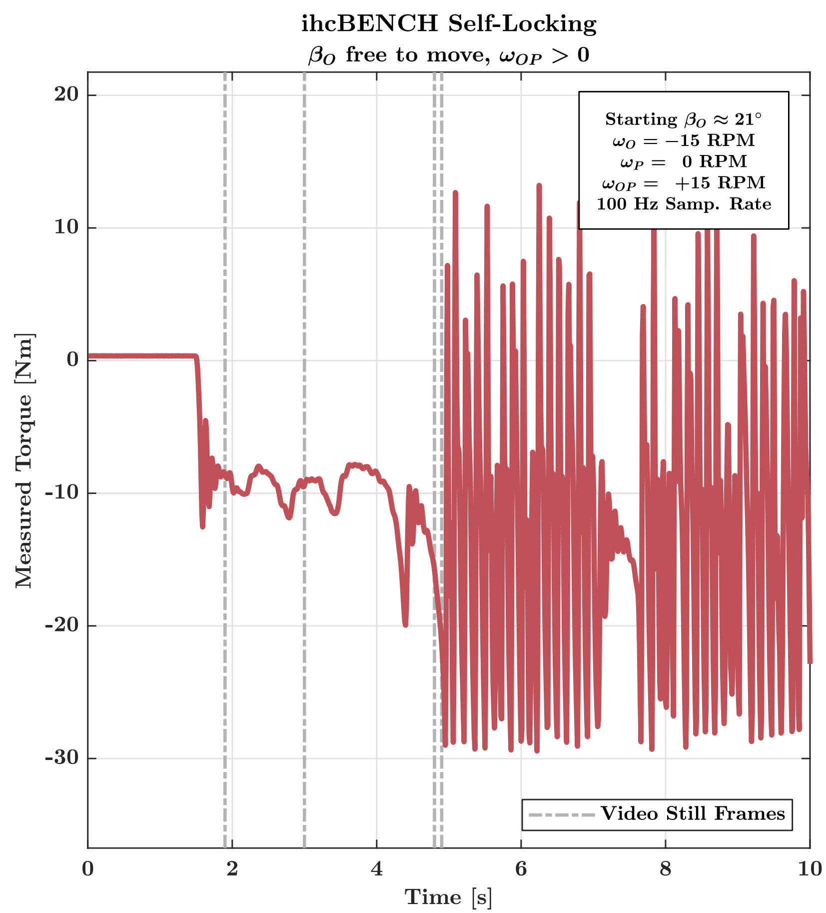

(a)

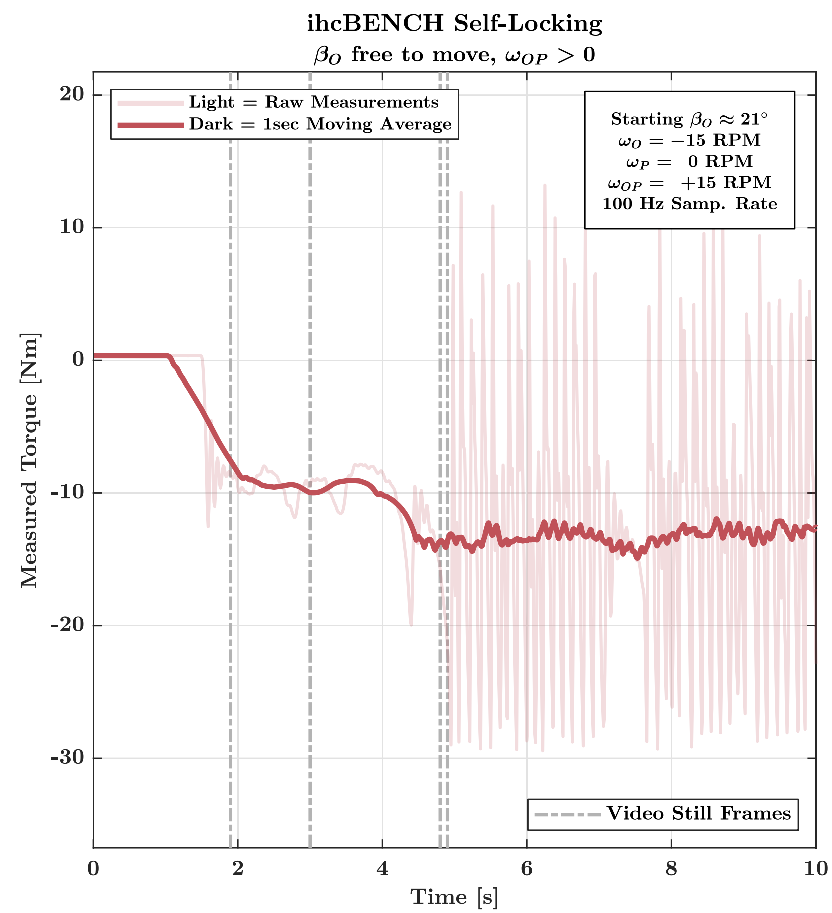

(b)

Figure 6-11 – Raw and moving-average torque profiles during an IHC self-locking event. The test itself begins just before the first gray line near $t = 2s$. When loaded, the coupling initially transmits some load but continues to slip. However, the clutch angle β_O quickly begins to diverge away from center. This does not happen in one fell swoop – β_O cycles a bit, before fully locking at roughly $t = 4.9$s. The torque spikes after $t = 4.9$s correspond to the "hammering" motion previously described.

underlying torque ripple that occurs synchronously with ω_O. Also, the torque at low speeds (such as $\omega_O = 3$ RPM) varies so slowly that the results can appear to be at different levels simply by choosing a small x-axis window size. The likely culprit here is believed to be uneven preloading on one or both primary tapered roller bearings. This particular issue was previously diagnosed and mostly mitigated – though not completely eliminated – during the ihcBENCH assembly and calibration process. Varying reaction loads on the Planet/Orbit and/or undiagnosed mechanism backlash (such as play at any Satellite block/shaft fit) may also be contributing to the ω_O directional bias observed.

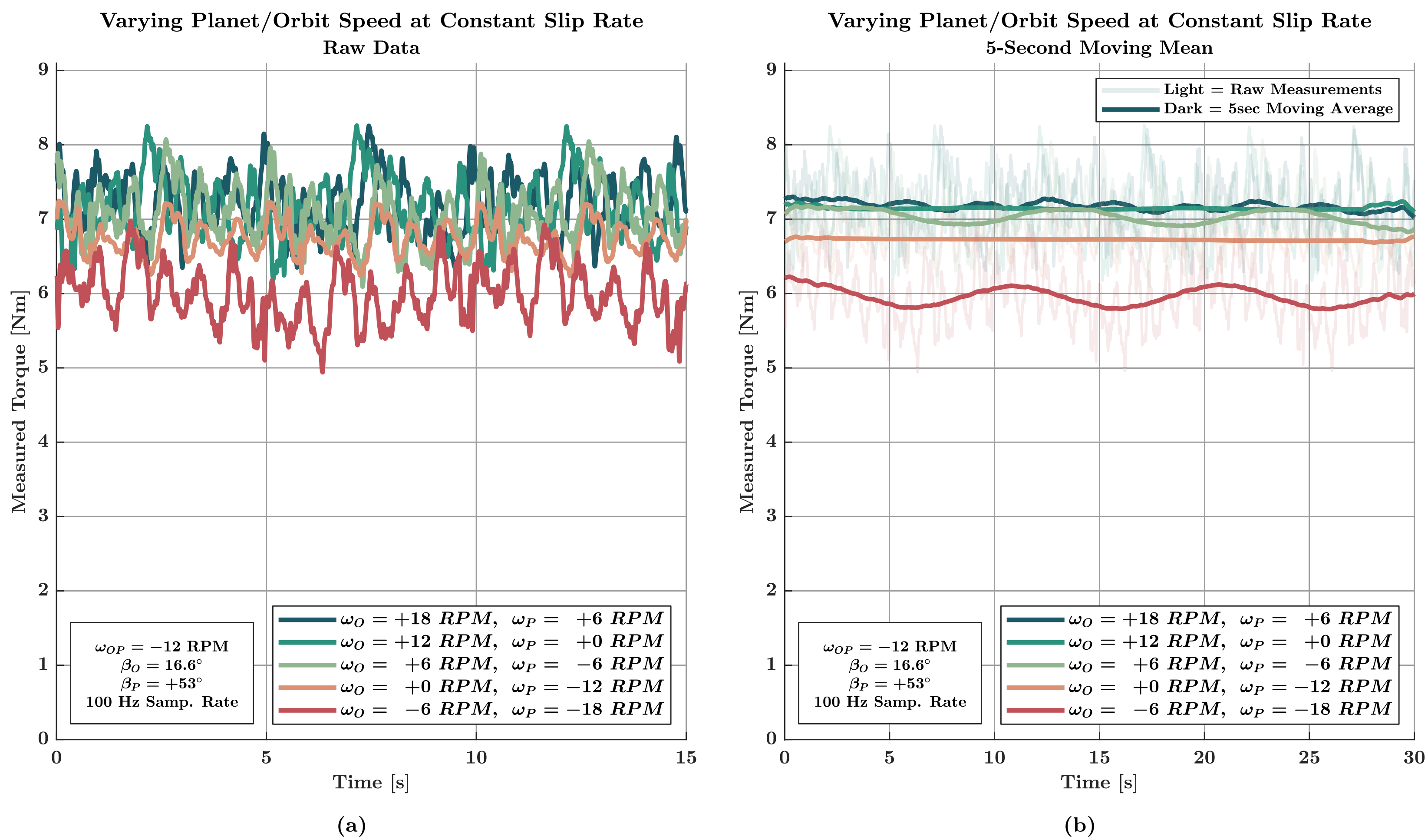

Figure 6-12 – Constant slip rate tests spanning symmetric values of ω_O, ω_P.

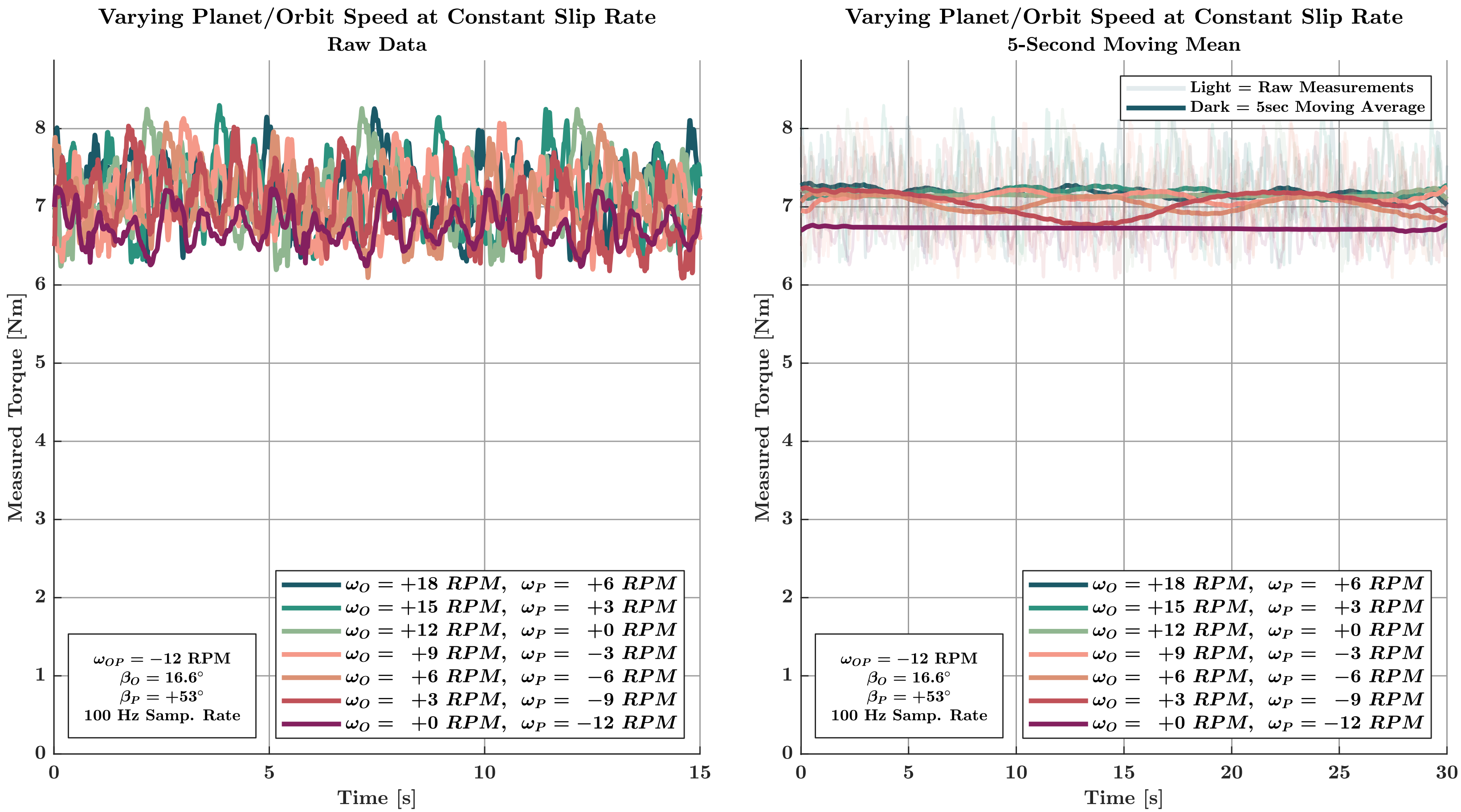

(a) (b)

Figure 6-13 – Constant slip rate tests focusing on values where $0 \leq \omega_O$.

THIS PAGE INTENTIONALLY LEFT BLANK

Chapter 7

Conclusions & Future Work

7.1 Project Conclusions

Despite the challenges and risks of this project, substantial progress has been made in laying the groundwork for future IHC development. The most important goals of the project were all satisfied:

- Create a model that accurately predicts IHC performance
- Demonstrate modulation of torque transmission via β_O
- Demonstrate that an IHC is intrinsically capable of transitioning from slip to lockup

Additional testing further demonstrated the potential capability for IHCs to function as speed-synchronizing one-way clutches. Together, these results demonstrate beyond reasonable doubt the viability of the IHC concept, and it is the author's hope that future work will continue to expand on this framework.

7.2 Research Contributions Revisited

The key high-level research contributions are reprised in Figure 7-1.

7.3 Future Work

With the core IHC principles now firmly demonstrated, a wide variety of potential paths are available for future IHC development. These include:

- Investigation of non-kinematic designs with a goal of realizing substantial increases in torque density. By moving away from a pseudo-kinematic design, lateral and axial forces can be fully decoupled from one another.

Concept Synthesis	• IHC Synthesis • Determine degrees of freedom / constraint / actuation • Identify key opportunities (torque density, overload protection)
Mathematical Modeling	• Mathematical descriptions of geometry & motion • Definitions for coordinate frames & coordinate transforms • Deterministic approach for solving kinematics • Derivation of equilibrium equations incl. friction
Simulation Package	• Comprehensive MATLAB implementation of analytical models • Estimates vibration, wear, & thermal effects • Presents instantaneous and time-averaged results • Numerous visualizations & animations to aid communication
Test System Design	• Identify concerns for manufacturability & assembly • Major design, fabrication, assembly, and testing takeaways
Validation Testing	• Prove working principle via operation • Validation of analytical and numerical models • Observe important expected & unexpected behaviors

Figure 7-1 – Summary of key research contributions.

- Operation at higher speeds and with greater Satellite mass to take advantage of the inertial effects.
- Active actuation of the clutch angle β_O in operation rather than requiring manual adjustment. This could be achieved with a swashplate-like mechanism.
- Active preload control, where contact pressures can be tuned in-situ. One approach would be to use hydraulic pressure to modulate Satellite preload on-demand.
- Plumbed lubricant paths, where pressurized oil is pumped through the Satellites and out the faces of their contact surfaces to produce a hydrostatic bearing effect.
- Thermal considerations for high-power-dissipation scenarios, including material properties, cooling system design, immersion in an oil bath, etc. Given the high potential torque density of IHCs, effective system cooling is expected to become an increasingly important factor. It is important to note that, at high slip rates (under heavy thermal load), existing fluid couplings are limited by their thermal performance rather than their torque capacity ceiling. Similar thermal constraints are reasonable to expect for IHCs operating at high slip rates.
- Further exploration of one-way clutching and other behaviors via internal mechanical feedback, *i.e.* where β_O can vary based on the instantaneous torque transmitted and relative rotation rates.
- Alternate Planet path shapes, such as the intentional introduction of geometric asymmetries.
- Using multiple Planet shapes in a single mechanism. For example, alternating the Planet shapes may provide an approach for mitigating torque ripple.

∞

THIS PAGE INTENTIONALLY LEFT BLANK

Appendix A

ihcBENCH Klipper Config Code

```
############################################################################################################
# ----------------------------------------------------------------------------------------------------------
#
#  INERTIAL HYSTERESIS COUPLING - IHCBENCH TEST SYSTEM
#  KLIPPER FIRMWARE CONFIGURATION FILE
#  REV: 2023-MAY-10
#  BY: CHARLIE WHEELER
#
#  I/O BOARD: Arduino MEGA 2560 (ATMEGA2560 MCU)
#  Note: The StepperOnline DM860T drivers require signal line "HI" levels of 5V. The Arduino MEGA 2560 is
#       5V, but many other microcontrollers are only 3.3v, so a level shifter is required if a different
#       MCU is used in the future.
#
############################################################################################################


# ----------------------------------------------------------------------------------------------------------
#  MAINSAIL GUI
# ----------------------------------------------------------------------------------------------------------
[include mainsail-utils.cfg]


# ----------------------------------------------------------------------------------------------------------
#  MICROCONTROLLER UNIT (MCU)
# ----------------------------------------------------------------------------------------------------------
[mcu]
serial: /dev/serial/by-id/usb-Arduino__www.arduino.cc__0042_850363135303513142D0-if00


# ----------------------------------------------------------------------------------------------------------
#  PRINTER KINEMATICS
#       To achieve precise simultaneous motion from both motors, we "fake" having a cartesian X/Y/Z 3D
#       printer (with the two ihcBENCH motors being "X" and "Y"). This requires some manual pre-processing
#       of commands since only a single "combined" feedrate is specified. For a planar cartesian 3D
#       printer this is the total feedrate, ie the L2 Norm of the X/Y speeds:
#       F = sqrt( (vX)^2 + (vY)^2 )
#
#       This approach is currently used as a workaround. Klipper does have a "None" kinematics option that
#       is intended to facilitate simultaneous independent control of multiple motors. However, the
#       implementation is not fully complete and currently only one axis can be controlled at a time.
#       A better workaround for this would be to write custom "machine kinematics" code specific to
#       ihcBENCH, but the current approach is sufficient at present.
# ----------------------------------------------------------------------------------------------------------
[printer]
kinematics: cartesian   # X/Y motors are Motors 1/2 respectively
max_velocity: 1.25      # [rot / s]         Velocity ceiling
max_accel: 2.5          # [rot / s^2]       Acceleration ceiling


# ----------------------------------------------------------------------------------------------------------
#  MOTOR 1 - X - LEFT SIDE / TORQUE SENSOR SIDE
# ----------------------------------------------------------------------------------------------------------
[stepper_x]

dir_pin: DIGI_52                #   DIGI_50 must be pulled to ground
step_pin: DIGI_33               #   DIGI_32 must be pulled to ground
enable_pin: !DIGI_27            #   DIGI_25 and DIGI_26 must be pulled to ground
step_pulse_duration: 0.000003   #   DM860T stepper driver requires pulse width >=2.5 us (using 3 us)

full_steps_per_rotation: 200    #   Stepper motor has 200 steps per rotation PLUS gear ratio
gear_ratio: 5:1
microsteps: 16                  #   16x microstepping provides good resolution without outrunning MCU
rotation_distance: 1            #   [revolutions] Rotation units definition. One rotation = 1 revolution
                                #           (For 3D printers this is a rotational <--> linear conversion,
                                #           eg 16mm/rev)
```

```
endstop_pin: DIGI_49            #   DUMMY value
position_endstop: 0
position_min: -999999
position_max: 999999
homing_positive_dir: true


# ------------------------------------------------------------------------------------------------------
#  MOTOR 2 - Y - RIGHT SIDE
#
#   NOTE: Direction pin has been flipped since motors face head-on. This causes both motors to spin in the
#       same direction when fed the same rotation speed command.
# ------------------------------------------------------------------------------------------------------
[stepper_y]

dir_pin: !DIGI_35               #   DIGI_37 must be pulled to ground
step_pin: DIGI_34               #   DIGI_36 must be pulled to ground
enable_pin: !DIGI_28            #   DIGI_29 and DIGI_30 must be pulled to ground
step_pulse_duration: 0.000003   #   DM860T stepper driver requires pulse width >=2.5 us (using 3 us)

full_steps_per_rotation: 200    #   Stepper motor has 200 steps per rotation PLUS gear ratio
gear_ratio: 5:1
microsteps: 16                  #   16x microstepping provides good resolution without outrunning MCU
rotation_distance: 1            #   [revolutions] Rotation units definition. One rotation = 1 revolution
                                #           (For 3D printers this is a rotational <--> linear conversion,
                                #           eg 16mm/rev)

endstop_pin: DIGI_51            #   DUMMY value
position_endstop: 0
position_min: -999999
position_max: 999999
homing_positive_dir: true


# ------------------------------------------------------------------------------------------------------
#  DUMMY MOTOR - Z
# ------------------------------------------------------------------------------------------------------
[stepper_z]                     #   Dummy motor, but must be defined for cartesian kinematics firmware to run

dir_pin: DIGI_41                #   DIGI_37 must be pulled to ground
step_pin: DIGI_43               #   DIGI_36 must be pulled to ground
enable_pin: !DIGI_45            #   DIGI_29 and DIGI_30 must be pulled to ground
step_pulse_duration: 0.000003   #   DM860T stepper driver requires pulse width >=2.5 us (using 3 us)

full_steps_per_rotation: 200    #   Stepper motor is a standard configuration with 200 steps/rev
microsteps: 16                  #   16x microstepping provides good resolution without outrunning MCU
rotation_distance: 1            #   [revolutions] Rotation units definition. One rotation = 1 revolution
                                #           (For 3D printers this is a rotational <--> linear conversion,
                                #           eg 16mm/rev)

endstop_pin: DIGI_53            #   DUMMY value
position_endstop: 0
position_min: -999999
position_max: 999999
homing_positive_dir: true


# ------------------------------------------------------------------------------------------------------
#  SAFETY
# ------------------------------------------------------------------------------------------------------
[idle_timeout]
gcode:
    M84     # Disable all steppers
timeout:
    600     # seconds


# ------------------------------------------------------------------------------------------------------
#  MACROS
# ------------------------------------------------------------------------------------------------------
[gcode_macro XY_STEPPERS_ON]
gcode:
    SET_STEPPER_ENABLE STEPPER=stepper_x ENABLE=1
    SET_STEPPER_ENABLE STEPPER=stepper_y ENABLE=1
    G28


[gcode_macro X_STEPPER_ON]
gcode:
    SET_STEPPER_ENABLE STEPPER=stepper_x ENABLE=1
    G28
    CLEAR_POSITION


[gcode_macro Y_STEPPER_ON]
gcode:
    SET_STEPPER_ENABLE STEPPER=stepper_y ENABLE=1
    G28
    CLEAR_POSITION


[gcode_macro XY_STEPPERS_OFF]
gcode:
    X_STEPPER_OFF
    Y_STEPPER_OFF


[gcode_macro X_STEPPER_OFF]
gcode:
    SET_STEPPER_ENABLE STEPPER=stepper_x ENABLE=0


[gcode_macro Y_STEPPER_OFF]
gcode:
    SET_STEPPER_ENABLE STEPPER=stepper_y ENABLE=0
```

```


[gcode_macro CLEAR_POSITION]
gcode:
    G92 X0 Y0 Z0


[gcode_macro XY_MOVE_STEPPERS]
gcode:
    {% set X_DIST = params.X_DIST | default(1) | float %}
    {% set Y_DIST = params.Y_DIST | default(1) | float %}
    {% set TOTAL_SPD = params.HYPOTENUSE_ROTPERSEC | default(0.2) | float %}
        #   Calculate "Hypotenuse Speed" separately using a spreadsheet or similar. This is required
        #   currently as Klipper macros can only perform basic arithmetic (they do not support functions
        #   like "sqrt" by default). F = sqrt( (desired_X_speed)^2 + (desired_Y_speed)^2 )

    G0 X{X_DIST} Y{Y_DIST} F{TOTAL_SPD * 60}        # TOTAL_SPD units are rot-per-sec, F units are RPM
    M400                                            # Wait for move to finish
    CLEAR_POSITION                                  # Reset position readings to 0


# ------------------------------------------------------------------------------------------------------------
#  OVERRIDE HOMING ROUTINE W/ RESET POSITION
# ------------------------------------------------------------------------------------------------------------
[homing_override]
gcode:
axes: xyz
set_position_x: 0
set_position_y: 0
set_position_z: 0


# ------------------------------------------------------------------------------------------------------------
#  SET GROUND PINS AT STARTUP
# ------------------------------------------------------------------------------------------------------------
[output_pin dir_x_gnd]
pin: DIGI_50
pwm: true
static_value: 0

[output_pin step_x_gnd]
pin: DIGI_32
pwm: false
static_value: 0

[output_pin enable_x_ground]
pin: DIGI_26
pwm: false
static_value: 0

[output_pin shield_x_ground]
pin: DIGI_25
pwm: false
static_value: 0

[output_pin dir_y_gnd]
pin: DIGI_37
pwm: true
static_value: 0

[output_pin step_y_gnd]
pin: DIGI_36
pwm: false
static_value: 0

[output_pin enable_y_ground]
pin: DIGI_29
pwm: false
static_value: 0

[output_pin shield_y_ground]
pin: DIGI_30
pwm: false
static_value: 0

[output_pin dir_z_gnd]
pin: DIGI_40
pwm: true
static_value: 0

[output_pin step_z_gnd]
pin: DIGI_42
pwm: false
static_value: 0

[output_pin enable_z_ground]
pin: DIGI_44
pwm: false
static_value: 0

[output_pin shield_z_ground]
pin: DIGI_46
pwm: false
static_value: 0


# ------------------------------------------------------------------------------------------------------------
#  BOARD PIN ALIASES
# ------------------------------------------------------------------------------------------------------------
[board_pins arduino_mega]

aliases:

    # For Arduino Mega Riser Pins (Numbered on side)
    # Notes:
    #  - "Communication" pins are subset of digital pins
```

```
    #  - Pins numbered on screw terminal shield as "A##" are analog, all others are digital
    #  - See Arduino documentation for general digital I/O pins vs. PWM

    ANLG_0 = PF0,
    ANLG_1 = PF1,
    ANLG_2 = PF2,
    ANLG_3 = PF3,
    ANLG_4 = PF4,
    ANLG_5 = PF5,
    ANLG_6 = PF6,
    ANLG_7 = PF7,
    ANLG_8 = PK0,
    ANLG_9 = PK1,
    ANLG_10 = PK2,
    ANLG_11 = PK3,
    ANLG_12 = PK4,
    ANLG_13 = PK5,
    ANLG_14 = PK6,
    ANLG_15 = PK7,

    DIGI_0_RX = PE0,
    DIGI_1_TX = PE1,
    DIGI_2_PWM = PE4,
    DIGI_3_PWM = PE5,
    DIGI_4_PWM = PG5,
    DIGI_5_PWM = PE3,
    DIGI_6_PWM = PH3,
    DIGI_7_PWM = PH4,
    DIGI_8_PWM = PH5,
    DIGI_9_PWM = PH6,
    DIGI_10_PWM = PB4,
    DIGI_11_PWM = PB5,
    DIGI_12_PWM = PB6,
    DIGI_13_PWM = PB7,
    DIGI_14_TX = PJ1,
    DIGI_15_RX = PJ0,
    DIGI_16_TX = PH1,
    DIGI_17_RX = PH0,
    DIGI_18_TX = PD3,
    DIGI_19_RX = PD2,
    DIGI_20_SDA = PD1,
    DIGI_21_SCL = PD0,
    DIGI_22 = PA0,
    DIGI_23 = PA1,
    DIGI_24 = PA2,
    DIGI_25 = PA3,
    DIGI_26 = PA4,
    DIGI_27 = PA5,
    DIGI_28 = PA6,
    DIGI_29 = PA7,
    DIGI_30 = PC7,
    DIGI_31 = PC6,
    DIGI_32 = PC5,
    DIGI_33 = PC4,
    DIGI_34 = PC3,
    DIGI_35 = PC2,
    DIGI_36 = PC1,
    DIGI_37 = PC0,
    DIGI_38 = PD7,
    DIGI_39 = PG2,
    DIGI_40 = PG1,
    DIGI_41 = PG0,
    DIGI_42 = PL7,
    DIGI_43 = PL6,
    DIGI_44 = PL5,
    DIGI_45 = PL4,
    DIGI_46 = PL3,
    DIGI_47 = PL2,
    DIGI_48 = PL1,
    DIGI_49 = PL0,
    DIGI_50 = PB3,
    DIGI_51 = PB2,
    DIGI_52 = PB1,
    DIGI_53 = PB0

    # Other digital pins with no input screw terminal
    # ar54=PF0, ar55=PF1, ar56=PF2, ar57=PF3, ar58=PF4, ar59=PF5,
    # ar60=PF6, ar61=PF7, ar62=PK0, ar63=PK1, ar64=PK2, ar65=PK3,
    # ar66=PK4, ar67=PK5, ar68=PK6, ar69=PK7

# ----------------------------------------------------------------------------------------------------------
############################################################################################################
```

All References

[1] J. R. Mancuso, *Couplings and Joints: Design, Selection, & Application*, Second Edition, L. L. Faulkner, Ed. 270 Madison Avenue, New York, NY 10016: Marcel Dekker, Inc., 1999, ISBN: 978-0-824-79950-2.

[2] Industry Nine, Inc., *Industry Nine Hydra Mountain Hub*, Digital Image.
URL: https://industrynine.com/
ARCHIVED URL: https://web.archive.org/web/20230418022010/https://industrynine.com/

[3] C. Culler, *Photo of San Francisco Cable Car Power House*, Digital Image.
URL: https://en.wikipedia.org/wiki/File:San_Francisco_Cable_Car_Power_House.jpg
ARCHIVED URL: https://web.archive.org/web/20230418022927/https://en.wikipedia.org/wiki/File:San_Francisco_Cable_Car_Power_House.jpg

[4] "Autoset Application: Levelers in Hot Strip Mill," The Voith Group, Heidenheim, Germany, Case Study, 2019.

[5] Eaton Corporation, *New Eaton electronic limited slip differential improves traction, performance and fuel economy*, Webpage.
URL: https://www.eaton.com/Eaton/OurCompany/NewsEvents/NewsReleases/PCT_211712
ARCHIVED URL: https://web.archive.org/web/20230418021317/https://www.eaton.com/Eaton/OurCompany/NewsEvents/NewsReleases/PCT_211712

[6] "Fluid Couplings with Constant Fill," The Voith Group, Heidenheim, Germany, Catalog, 2019.
URL: https://voith.com/corp-en/products-services/connection-components-couplings/fluid-couplings/downloads-publications.html
ARCHIVED URL: https://web.archive.org/web/20230509043405/https://voith.com/corp-en/products-services/connection-components-couplings/fluid-couplings/downloads-publications.html

[7] "National Thermal Power Corporation (NTPC) India," MagnaDrive Corporation, Case Study.
URL: http://www.magnadrive.com/custom_post/ntpc/
ARCHIVED URL: https://web.archive.org/web/20230418022216/https://magnadrive.com/case-studies/ntpc/

[8] W. C. Orthwein, *Clutches and Brakes: Design and Selection*, Second Edition. 270 Madison Avenue, New York, NY 10016, USA: Marcel Dekker, Inc., 2004, ISBN: 978-0-824-74876-0.

[9] "Flender Standard Couplings," Flender GmbH, Catalog MD 10.1, 2015.

[10] "Flender Fluid Couplings – Fludex," Flender GmbH, Catalog FLE 10.4, 2022.

[11] "Voith Variable Speed Fluid Couplings," The Voith Group, Heidenheim, Germany, Catalog.
URL: https://voith.com/corp-en/drives-transmissions/variable-speed-drives/variable-speed-fluid

-couplings.html
ARCHIVED URL: https://web.archive.org/web/20230509043928/https://voith.com/corp-en/drives-transmissions/variable-speed-drives/variable-speed-fluid-couplings.html

[12] "Pneumatic Clutches and Brakes (Catalog)," Wichita Clutch, Altra Industrial Motion, Catalog, 2018.

[13] MagnaDrive Corporation, *MagnaDrive Synchra 200-800 Series*, Specifications Sheet.
URL: https://www.magnadrive.com/products/synchra/
ARCHIVED URL: https://web.archive.org/web/20230418022304/https://magnadrive.com/products/synchra/

[14] MagnaDrive Corporation, *MagnaDrive Adjustable Speed Drive Standard Dimensions and Design Characteristics*, Specifications Sheet.
URL: https://www.magnadrive.com/products/adjustable-speed-drive/the-magnadrive-adjustable-speed-drive-specifications/
ARCHIVED URL: https://web.archive.org/web/20230418022350/https://magnadrive.com/products/adjustable-speed-drive/the-magnadrive-adjustable-speed-drive-specifications/

[15] B. Obsieger, *Voith Power Transmission: 100 Years of the Föttinger Principle*. Springer-Verlag, 2005, ISBN: 978-3-540-68784-9.

[16] B. D. Cullity and C. D. Graham, "Introduction to Magnetic Materials," in Second Edition. Hoboken, New Jersey: John Wiley & Sons, Inc., 2009, ISBN: 978-0-471-47741-9.

[17] B. Obsieger, *Couplings and Clutches*, Second Edition. Croatia: Juraj Dobrila University of Pula, Department for Technical Studies, 2021, ISBN: 979-8-519-49104-4.

[18] "Overrunning, Indexing, Backstopping Clutches," Formsprag Clutch, Altra Industrial Motion, Catalog P-956-FC.
URL: https://www.formsprag.com/
ARCHIVED URL: https://web.archive.org/web/20230418021522/https://www.formsprag.com/

[19] J. Nicholson, *The Millwright's Guide: A Practical Treatise on the Construction of All Kinds of Mill Work, and the Application of the Power of Wind and Water*. Paternoster Row: Sherwood, Gilbert, and Piper, 1830.

[20] US National Park Service, *Photo of Boott Cotton Mills Museum Weave Room*, Digital Image.
URL: https://www.nps.gov/lowe/planyourvisit/boott-cotton-mills-museum.htm
ARCHIVED URL: https://web.archive.org/web/20230509043219/https://www.nps.gov/lowe/planyourvisit/boott-cotton-mills-museum.htm

[21] SSS Gears Limited, *Exploded View Rendering of an SSS Clutch*, Digital Image.
URL: http://www.sssclutch.com/
ARCHIVED URL: https://web.archive.org/web/20230509042913/http://www.sssclutch.com/

[22] M. Hendry, "US Navy Experience with SSS (Synchro-Self-Shifting) Clutches," *Mechanical Engineering*, vol. 132, no. 08, pp. 54–55, 2010.

[23] "Pneumatic and Hydraulic Clutches and Brakes," Industrial Clutch, Altra Industrial Motion, Catalog P-7045-IC.
URL: https://www.indclutch.com/
ARCHIVED URL: https://web.archive.org/web/20230418021741/https://www.indclutch.com/

[24] J. Clarkson, R. Hammond, and J. May, *The Grand Tour (Season 2, Episode 5): "Up, Down and*

Round the Farm", 2018.

[25] "Cleetus McFarland" (YouTube Channel), *I'm Selling My 70mph Duramax Luxury Tank... It Ain't Cheap!!!* 2022.
URL: https://www.youtube.com/watch?v=7BYg_SM7ZRM

[26] K. Ramanathan, "Global Industrial Coupling Factbook," Frost & Sullivan, Market Research Report PD18-17, 2022.

[27] AUDI AG, *Audi quattro drive with Sport differential*, Webpage.
URL: https://www.audi-mediacenter.com/en/photos/detail/audi-quattro-drive-with-sport-differential-15823
ARCHIVED URL: https://web.archive.org/web/20230530114652/https://www.audi-mediacenter.com/en/photos/detail/audi-quattro-drive-with-sport-differential-15823

[28] AUDI AG, *Audi quattro drive with Sport differential*, Webpage.
URL: https://www.audi-mediacenter.com/en/photos/detail/audi-quattro-drive-with-sport-differential-15822
ARCHIVED URL: https://web.archive.org/web/20230526075611/https://www.audi-mediacenter.com/en/photos/detail/audi-quattro-drive-with-sport-differential-15822

[29] M. Jacko, P. Tsang, and S. Rhee, "Automotive friction materials evolution during the past decade," *Wear*, vol. 100, no. 1-3, pp. 503–515, 1984.

[30] J. Wheals, M. Deane, S. Drury, *et al.*, "Design and simulation of a torque vectoring™ rear axle," in *SAE Technical Paper Series*, SAE International, 2006-04. DOI: 10.4271/2006-01-0818.
URL: https://doi.org/10.4271/2006-01-0818

[31] KMP Drivetrain Solutions, *Blog – Tripod vs. Rzeppa Joint*, Digital Image.
URL: https://www.kmpdrivetrain.com/wp-content/uploads/2020/08/Parts-in-a-Rzeppa-joint-for-motorsport.png
ARCHIVED URL: https://web.archive.org/web/20220316155641/https://www.kmpdrivetrain.com/wp-content/uploads/2020/08/Parts-in-a-Rzeppa-joint-for-motorsport.png

[32] "Hydrodynamic Couplings: Principles, Features, Benefits," Voith Turbo GmbH & Co. KG, 74564 Crailsheim, Germany, White Paper, 2015.
URL: https://voith.com/corp-en/products-services/connection-components-couplings/fluid-couplings/downloads-publications.html
ARCHIVED URL: https://web.archive.org/web/20230509043405/https://voith.com/corp-en/products-services/connection-components-couplings/fluid-couplings/downloads-publications.html

[33] M. V. ("Mvolz"), *Photo of a Bead Rollercoaster / Bead-and-Wire Maze*, Digital Image.
URL: https://en.wikipedia.org/wiki/File:Bead_roller_coaster.jpg
ARCHIVED URL: https://web.archive.org/web/20230418022840/https://en.wikipedia.org/wiki/File:Bead_roller_coaster.jpg

[34] T. V. Group, "Hydrodynamic Couplings," Tech. Rep.

[35] *ISO 80000-2:2019: Quantities and Units – Part 2: Mathematical Signs and Symbols to be Used in the Natural Sciences and Technology*, ISO Standard, International Organization for Standardization, 2019.
URL: https://www.iso.org/standard/64973.html

[36] L. D. Landau and E. M. Lifshitz, *Course of Theoretical Physics, Volume 1 – Mechanics*, Third Edition. Oxford, England: Butterworth-Heinemann, 2000, Translated from the 3rd revised and

enlarged edition of *Medkanika*, by L.D. Landau and E.M. Lifschitz, Nauka, Moscow, 1993.

[37] SparkFun Electronics, *Raspberry Pi 4 Model B (4 GB)*.
URL: https://www.sparkfun.com/products/15447
ARCHIVED URL: https://web.archive.org/web/20230502140933/https://www.sparkfun.com/products/15447

[38] Arduino S.r.l., *Arduino Mega 2560 Rev3*, Webpage.
URL: https://store-usa.arduino.cc/products/arduino-mega-2560-rev3
ARCHIVED URL: https://web.archive.org/web/20230502135637/https://store-usa.arduino.cc/products/arduino-mega-2560-rev3

[39] STEPPERONLINE, *DM860T – Digital Stepper Driver 2.4-7.2A 18-80VAC or 36-110VDC for Nema 34 Motor*, Webpage.
URL: https://www.omc-stepperonline.com/digital-stepper-driver-2-4-7-2a-18-80vac-or-36-110vdc-for-nema-34-motor-dm860t
ARCHIVED URL: https://web.archive.org/web/20230502134948/https://www.omc-stepperonline.com/digital-stepper-driver-2-4-7-2a-18-80vac-or-36-110vdc-for-nema-34-motor-dm860t

[40] Klipper Development Team, *Klipper GitHub Repository*, Webpage.
URL: https://github.com/Klipper3d/klipper
ARCHIVED URL: https://web.archive.org/web/20230509042648/https://github.com/Klipper3d/klipper

[41] *Mainsail GitHub Repository*, Webpage.
URL: https://github.com/mainsail-crew/mainsail
ARCHIVED URL: https://web.archive.org/web/20230509042741/https://github.com/mainsail-crew/mainsail

[42] *Klipper Documentation: Features*, Webpage.
URL: https://www.klipper3d.org/Features.html
ARCHIVED URL: https://web.archive.org/web/20230509042545/https://www.klipper3d.org/Features.html